

AD-A253 186

A standard linear barcode is positioned horizontally across the page, consisting of vertical black lines of varying widths on a white background.

MENTATION PAGE

Form Approved
OMB No. 0704-0188

estimated to average 1 hour per response, including the time for reviewing instructions, searching existing data sources, and completing the collection of information. Send comments regarding this burden estimate or any other aspect of this burden to Washington Headquarters Services, Directorate for Information Operations and Reports, 1215 Jefferson in the Office of Management and Budget, Paperwork Reduction Project (0704-0188), Washington, DC 20503.

1. AGENCY USE ONLY (Leave Blank)	2. REPORT DATE	3. REPORT TYPE AND DATES COVERED Final Report 01 Mar 90 to 29 Feb 92
4. TITLE AND SUBTITLE Polarized light scattering from perfect and perturbed surfaces and fundamental scattering systems		5. FUNDING NUMBERS 2306/A3
6. AUTHOR(S) Professor William S. Bickel		
7. PERFORMING ORGANIZATION NAME(S) AND ADDRESS(ES) University of Arizona Department of Physics Tucson, AZ 85721		8. PERFORMING ORGANIZATION REPORT NUMBER AFOSR-TR-92 0671
9. SPONSORING / MONITORING AGENCY NAME(S) AND ADDRESS(ES) AFOSR/NE Bldg 410 BOLLING AFB WASHINGTON DC 20332-6448		10. SPONSORING / MONITORING AGENCY REPORT NUMBER AFOSR-90-0243
11. SUPPLEMENTARY NOTES		DTIC S ELECTE JUL 24 1992 D
12a. DISTRIBUTION / AVAILABILITY STATEMENT APPROVED FOR PUBLIC RELEASE: DISTRIBUTION IS UNLIMITED		12b. DISTRIBUTION CODE C

The following 12 papers and two Graduate Theses report work done under the Air Force grant 90-NE-020 during the period March 1, 1990 to February 29, 1992.

92-19920

92 7 23 039

14. SUBJECT TERMS		15. NUMBER OF PAGES	
		16. PRICE CODE	
17. SECURITY CLASSIFICATION OF REPORT	18. SECURITY CLASSIFICATION OF THIS PAGE	19. SECURITY CLASSIFICATION OF ABSTRACT	20. LIMITATION OF ABSTRACT
UNCLASSIFIED	UNCLASSIFIED	UNCLASSIFIED	UL (UNLIMITED)

POLARIZED LIGHT SCATTERING FROM PERFECT AND PERTURBED SURFACES
AND FUNDAMENTAL SCATTERING SYSTEMS

Final Report

William S. Bickel
Physics department
University of Arizona
Tucson, Arizona 85721

Attention: Dr. Harold Weinstock
Department of the Air Force
Air Force Office of Scientific Research
Bolling Air Force Base. DC 20332-6448

Dr. Tom Moran
WRDC/ML
Wright Patterson AFB, OH 45433

Accession For	
Ref. Serial	<input checked="" type="checkbox"/>
Pub. No.	<input type="checkbox"/>
Classification	<input type="checkbox"/>
By	
Distribution/	
Availability Codes	
Dist	Avail and/or Special
A-1	

The following 12 papers and two Graduate Theses report work done under the Air Force grant 90-NE-020 during the period March 1, 1990 to February 29, 1992.

1. Light Scattering from a Sphere On or Near a Surface
Gorden Videen
J. Opt. Soc. Am. A, Vol. 8, No. 3, p. 483 (1991).
2. Light Scattering from a Sphere On or Near a Surface: Errata
Gorden Videen
J. Opt. Soc. Am. A, Vol. 9, No. 5, p. 844 (1992).
3. Coherent Fluorescent Emission and Scattering from a Uniform Cylinder
Gorden Videen, William S. Bickel, and Joseph M. Boyer
Physical Review A, Vol. 43, No. 10, p. 5656 (1991).
4. Coherent Fluorescent Emission and Scattering from a Uniform Sphere
Gorden Videen, William S. Bickel, and Joseph M. Boyer
Physical Review A, Vol. 44, No. 2, p. 1358 (1991).
5. Light-scattering Mueller Matrix from a Fiber as a Function of MgO Contamination
Gorden Videen and William S. Bickel
Applied Optics, Vol. 30, No. 27, p. 3880 (1991).

6. Experimental Light-scattering Mueller Matrix for a Fiber on a Reflecting Optical Surface as a Function of Incident Angle
Gorden Videen, William S. Bickel, Vincent Iafelice, and David Abromson
J. Opt. Soc. Am. A, Vol. 9, No. 2, p. 312 (1992).

7. Light-scattering Resonances in Small Spheres
Gorden Videen and William S. Bickel
Physical Review A, Vol. 45, No. 8, p. 6008 (1992).

8. Polarized Light Scattered from Rough Surfaces
Gorden Videen, Jiunn-Yann Hsu, William S. Bickel, and William L. Wolfe
J. Opt. Soc. Am. A, Vol. 9, No. 7, p. 1 (1992).

9. Scattering from a Small Sphere Near a Surface
Gorden Videen, Mary G. Turner, Vincent J. Iafelice, William S. Bickel, and William L. Wolfe
J. Opt. Soc. Am. A, submitted.

10. Stokes Vectors, Mueller Matrices and Polarized Scattered Light: Experimental Applications to Optical Surfaces and All Other Scatterers
William S. Bickel and Gorden Videen
SPIE Vol. 1530 Optical Scatter: Applications, Measurement, and Theory (1991).

11. The Light-Scattering Mueller Matrix for a Surface Contaminated by a Single Particle in the Rayleigh Limit
Gorden Videen, William L. Wolfe, and William S. Bickel
J. Opt. Soc. Am. A, submitted.

12. Electromagnetic Scattering from a Sphere:
The Near Field Region
Gorden Videen, Joseph M. Boyer, and William S. Bickel
J. Opt. Soc. Am. A, submitted.

Light Scattering from a Sphere On or Near an Interface
Gorden Wayne Videen
Dissertation, University of Arizona, 1992.

The Polarized Light Scattering Matrix Elements for Rough Surfaces
Jiunn-Yann Hsu
Thesis, University of Arizona, 1992.

Two papers are in preparation.
A paper will be presented at the July SPIE meeting in San Diego this summer

The work done the past two years with Air force support has been very productive with regard to research done, papers published and students trained.

I am proud to say that two students working in my laboratory on these light scattering problems have received advanced degrees.

Gorden Videen defended his PhD Dissertation in March getting his doctorate from the University of Arizona Optical Sciences Center. Please note that he is a co-author on all of the above papers. He was totally responsible for the theoretical work and took full responsibility for their publication. He now rates among the very best small particle light scattering (electromagnetic) theorists in the country. He now has a Post-Doctorate position in the Physics Department at Dalhousie University in Halifax Nova Scotia.

Jiunn (June) Yann Shu will defend his MS thesis in few days. Jiunn has done most of the experimental work for the program. He is a very careful and clever experimentalist. His careful work in preparing samples and making the measurements stands as a great credit and something he can be proud of. He is one of the few good small particle experimentalist around.

A number of High school students, undergraduates, graduates and other personnel have gained valuable experience helping with the work. The research group consisted of the following:

William S. Bickel	Principal Investigator
Gorden Videen	Graduate student in Optical Sciences
James Dugan	Graduate student in Atmospheric Physics
Joseph M. Boyer	Visiting Senior Scientist
Jim Gilmore	Honors undergraduate in Physics
June Yann Shu	Graduate student in Physics
John Pattison	Graduate student technician (physics)
Steve Robinson	Graduate student in Physics
John Petti	High School Professional Intern
Daniel	High School Professional Intern
Jon Haas	Undergraduate in Physics
Eric Fest	Undergraduate in Engineering-Physics
also	8 Independent Studies Students

We are thankful to William L. Wolfe of the Optical Sciences Center for many helpful discussions.

The Air Force Support for this two-year project was \$49,000. I do not have a big laboratory or a big program. Consequently I don't need much money. However I am fortunate to attract good students who are interested in this area of physics and are willing to work hard. There is a growing need to train students in the basics of experimental science. This modest AF program has contributed to the education of many potential scientists.

Light scattering from a sphere on or near a surface

Gorden Videen

Optical Sciences Center, University of Arizona, Tucson, Arizona 85721

Received April 27, 1990; accepted October 30, 1990

The light-scattering problem of a sphere on or near a plane surface is solved by using an extension of the Mie theory. The approach taken is to solve the boundary conditions at the sphere and at the surface simultaneously and to develop the scattering amplitude and Mueller scattering matrices. This is performed by projecting the fields in the half-space region not including the sphere multiplied by an appropriate Fresnel reflection coefficient onto the half-space region including the sphere. An assumption is that the scattered fields from the sphere, reflecting off the surface and interacting with the sphere, are incident upon the surface at near-normal incidence. The exact solution is asymptotically approached when either the sphere is a large distance from the surface or the refractive index of the surface approaches infinity.

INTRODUCTION

Light scattering from a cylinder was solved independently by Lord Rayleigh¹ in 1881 and by von Ignatowsky² in 1905. A few years later, Mie³ solved the scattering from a sphere. Liang and Lo⁴ extended this theory for two spheres. Kattawar and Dean⁵ confirmed the existence of resonances discovered by Wang *et al.*,⁶ who measured microwave scattering from two dielectric spheres. Bobbert and Vlieger⁷ used operators to solve for the scattering of a small sphere near a surface. Younis⁸ solved for the scattering from two parallel cylinders and recently solved for the scattering from a cylinder on a surface. Younis's results have been verified experimentally by comparing his theory to the light-scattering Mueller matrix elements measured for a cylinder on a surface.⁹ His approach to the problem of a cylinder on a surface has been adopted to solve the scattering of a sphere on or near a surface. The approach is similar to that taken by Rao and Barakat,¹⁰ who calculated the scatter by a conducting cylinder partially buried in a conducting medium.

The method used to calculate the electromagnetic radiation scattered by the system is to address how the radiation may interact with the sphere. The incident plane wave strikes the sphere either directly or after interacting with the medium at the surface, in which case it is an image plane wave. Far-field radiation is a result of a superposition of fields either directly from the sphere or from the image sphere. The fields emanating from the sphere may also reflect off the surface and interact with the sphere again. The magnitude and phase of the fields about the image sphere are altered by the reflections that take place at the surface by the Fresnel coefficients. One assumption is that the scattered fields from the sphere, reflecting off the surface and interacting with the sphere, are incident on the surface at near-normal incidence. The exact solution is asymptotically approached when either the sphere is a large distance from the surface or the refractive index of the surface approaches infinity.

Figure 1 shows the geometry of the scattering system. A sphere of radius a is located on the z axis a distance d below a plane surface bounding two media of different refractive indices oriented perpendicular to the z axis. The incident

radiation is a plane wave traveling in the $x-z$ plane, oriented at angle α with respect to the z axis. The wavelength and wave vector for the plane wave in the nonabsorbing, nonmagnetic incident medium below the substrate are λ and \mathbf{k} , respectively. The complex wave vectors for a plane wave of the same frequency in the sphere and the medium above the surface are \mathbf{k}_{sp} and \mathbf{k}_{med} , respectively.

SOLUTION

The solution to the light scattering from a sphere on or near a surface is treated here in several subsections. In Subsection 1 the scalar wave equation is solved, and the vector wave functions and Debye potentials are developed. In Subsection 2 the scattering coefficients are solved for a general case. In Subsection 3 the specific case of a sphere-surface system illuminated with plane-wave incident radiation is solved. Finally, in Subsection 4 the Mueller matrix elements are derived from the scattering coefficients.

1. Wave Equations

The starting point for this scattering problem is the vector wave equation, which is derived in almost any text on electromagnetic theory¹¹:

$$\nabla^2 \mathbf{E} - \mu \epsilon \frac{\partial^2 \mathbf{E}}{\partial t^2} - \mu \sigma \frac{\partial \mathbf{E}}{\partial t} = 0, \\ \nabla^2 \mathbf{H} - \mu \epsilon \frac{\partial^2 \mathbf{H}}{\partial t^2} - \mu \sigma \frac{\partial \mathbf{H}}{\partial t} = 0, \quad (1.1)$$

where \mathbf{E} and \mathbf{H} are the electric and magnetic field vectors, respectively. With the assumption of a time dependence of the form $\exp(-i\omega t)$ these equations can be used for deriving the scalar wave equation, which in spherical polar coordinates may be expressed as

$$\frac{1}{r^2} \frac{\partial}{\partial r} \left(r^2 \frac{\partial u}{\partial r} \right) + \frac{1}{r^2 \sin \theta} \frac{\partial}{\partial \theta} \left(\sin \theta \frac{\partial u}{\partial \theta} \right) + \frac{1}{r^2 \sin^2 \theta} \frac{\partial^2 u}{\partial \phi^2} + k^2 u = 0 \quad (1.2)$$

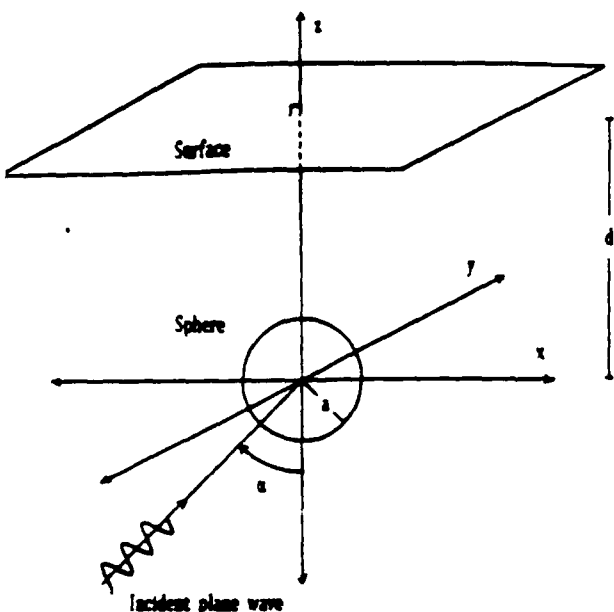


Fig. 1. Geometry of scattering system. A sphere of radius a is located a distance d from a surface. A plane wave travels in the x - z plane at angle α with respect to the z axis.

A separable solution of the following form is assumed:

$$u(r, \vartheta, \varphi) = R(r)\Theta(\vartheta)\Phi(\varphi). \quad (1.3)$$

The particular functions satisfying Eqs. (1.2) and (1.3) are

$$\begin{aligned} \Phi(\varphi) &= \exp(im\varphi), \\ \Theta(\vartheta) &= P_n^m(\cos \vartheta) = \left[\frac{(2n+1)(n-m)!}{2(n+m)!} \right]^{1/2} P_n^m(\cos \vartheta), \\ R(r) &= z_n(kr) = \left(\frac{\pi}{2r} \right)^{1/2} Z_{n+1/2}(kr), \end{aligned} \quad (1.4)$$

where $P_n^m(\cos \vartheta)$ are associated Legendre polynomials and $z_n(kr)$ are either spherical Bessel functions of the first kind, $j_n(kr)$, or spherical Hankel functions of the first kind, $h_n^{(1)}(kr)$. The electric and magnetic fields may be expanded in terms of the vector wave functions $M_{nm}^{(i)}$ and $N_{nm}^{(i)}$ ($i = 1$ corresponds to $j_n(kr)$'s being used and $i = 3$ corresponds to $h_n^{(1)}(kr)$'s being used):

$$\begin{aligned} \mathbf{E} &= \sum_{n,m} p_{nm} M_{nm}^{(i)} + q_{nm} N_{nm}^{(i)} \\ \mathbf{H} &= \frac{k}{i\omega\mu} \sum_{n,m} p_{nm} N_{nm}^{(i)} + q_{nm} M_{nm}^{(i)}. \end{aligned} \quad (1.5)$$

The vector wave functions $M_{nm}^{(i)}$ and $N_{nm}^{(i)}$ assume the following form:

$$\begin{aligned} M_{nm}^{(i)} &= \hat{\phi} \left[\frac{im}{\sin \vartheta} z_n(kr) P_n^m(\cos \vartheta) \exp(im\varphi) \right] \\ &\quad - \hat{\phi} \left\{ z_n(kr) \frac{d}{d\vartheta} [P_n^m(\cos \vartheta)] \exp(im\vartheta) \right\}, \end{aligned}$$

$$\begin{aligned} N_{nm}^{(i)} &= \hat{\phi} \left[\frac{1}{kr} z_n(kr) n(n+1) P_n^m(\cos \vartheta) \exp(im\varphi) \right] \\ &\quad + \hat{\phi} \left\{ \frac{1}{kr} \frac{d}{dr} [rz_n(kr)] \frac{d}{d\vartheta} [P_n^m(\cos \vartheta)] \exp(im\vartheta) \right\} \\ &\quad + \hat{\phi} \left\{ \frac{1}{kr} \frac{d}{dr} [rz_n(kr)] \frac{im}{\sin \vartheta} P_n^m(\cos \vartheta) \exp(im\vartheta) \right\}. \end{aligned} \quad (1.6)$$

Rather than expanding the electric and magnetic fields in terms of the vector wave functions as in Eq. (1.2), it is often convenient to expand the fields in terms of the Debye potentials:

$$\begin{aligned} \mathbf{E} &= \sum_{n,m} \nabla \times (k p_{nm} u_{nm}^{(i)}) + \frac{1}{k} \nabla \times \nabla \times (k q_{nm} u_{nm}^{(i)}), \\ \mathbf{H} &= \frac{k}{i\omega\mu} \sum_{n,m} \nabla \times (k q_{nm} u_{nm}^{(i)}) + \frac{1}{k} \nabla \times \nabla \times (k p_{nm} u_{nm}^{(i)}). \end{aligned} \quad (1.7)$$

The Debye potentials are $p_{nm}u_{nm}^{(i)}$ and $q_{nm}u_{nm}^{(i)}$. The coefficients p_{nm} and q_{nm} are common to both potentials and vector wave functions, making it convenient to consider the scattering problem from either perspective.

2. Scattering Coefficients

The general case for scattering from a sphere on or near a surface can be treated by representing the incident field on the sphere as a superposition of terms in the expansion given by Eq. (1.5):

$$\begin{aligned} \mathbf{E}^{\text{inc}} &= \sum_{n=0}^{\infty} \sum_{m=-n}^n a_{nm} M_{nm}^{(1)} + b_{nm} N_{nm}^{(1)} \\ \mathbf{H}^{\text{inc}} &= \frac{k}{i\omega\mu} \sum_{n=0}^{\infty} \sum_{m=-n}^n b_{nm} M_{nm}^{(1)} + a_{nm} N_{nm}^{(1)}. \end{aligned} \quad (2.1)$$

The coefficients a_{nm} and b_{nm} will be solved for the special case of an incident plane wave in Subsection 3. The radial functions used in expanding the vector functions for the incident radiation are the spherical Bessel functions $j_n(kr)$. In this section the scattering coefficients will be solved in terms of these coefficients. The scattered field is also expanded:

$$\begin{aligned} \mathbf{E}^{\text{scat}} &= \sum_{n=0}^{\infty} \sum_{m=-n}^n c_{nm} M_{nm}^{(3)} + f_{nm} N_{nm}^{(3)}, \\ \mathbf{H}^{\text{scat}} &= \frac{k}{i\omega\mu} \sum_{n=0}^{\infty} \sum_{m=-n}^n f_{nm} M_{nm}^{(3)} + c_{nm} N_{nm}^{(3)}. \end{aligned} \quad (2.2)$$

The radial functions are the spherical Hankel functions of the first kind $h_n^{(1)}(kr)$. The fields inside the sphere are also expanded:

$$\begin{aligned} \mathbf{E}^{\text{inh}} &= \sum_{n=0}^{\infty} \sum_{m=-n}^n c_{nm} M_{nm}^{(1)} + d_{nm} N_{nm}^{(1)}, \\ \mathbf{H}^{\text{inh}} &= \frac{k_{\text{inh}}}{i\omega\mu_{\text{inh}}} \sum_{n=0}^{\infty} \sum_{m=-n}^n d_{nm} M_{nm}^{(1)} + c_{nm} N_{nm}^{(1)}. \end{aligned} \quad (2.3)$$

The radial functions for the internal fields are the spherical Bessel functions $j_n(k_{sph}r)$. To this point, the analysis is identical to those given by Refs. 11-14 for the case of a single sphere (Mie theory), except that here the coefficients a_{nm} and b_{nm} will include a reflection from the surface. In addition to the three fields described by Eqs. (2.1)-(2.3), a fourth field is incident upon the sphere. The field is a result of the scattered field of the sphere's reflecting off the surface and striking the sphere. This interacting field is also expanded:

$$\mathbf{E}^{int} = \sum_{n=0}^{\infty} \sum_{m=-n}^n g_{nm} \mathbf{M}_{nm}^{(1)} + h_{nm} \mathbf{N}_{nm}^{(1)},$$

$$\mathbf{H}^{int} = \frac{k}{i\omega\mu} \sum_{n=0}^{\infty} \sum_{m=-n}^n h_{nm} \mathbf{M}_{nm}^{(1)} + g_{nm} \mathbf{N}_{nm}^{(1)}. \quad (2.4)$$

The radial functions used for the interacting field are the spherical Bessel functions $j_n(kr)$.

The next step is to apply the boundary conditions at the surface of the sphere. The coefficients for the internal fields, c_{nm} and d_{nm} , can be eliminated, and the scattering coefficients can be solved:

$$c_{nm} = -(a_{nm} + g_{nm})$$

$$\times \frac{k_{sph} \mu \psi_n(k_{sph}a) \psi_n(ka) - k \mu_{sph} \psi_n(ka) \psi_n(k_{sph}a)}{k_{sph} \mu \psi_n'(k_{sph}a) \xi_n(ka) - k \mu_{sph} \xi_n(ka) \psi_n(k_{sph}a)}$$

$$= (a_{nm} + g_{nm}) Q_n^m,$$

$$f_{nm} = -(b_{nm} + h_{nm})$$

$$\times \frac{k_{sph} \mu \psi_n(ka) \psi_n(k_{sph}a) - k \mu_{sph} \psi_n(k_{sph}a) \psi_n(ka)}{k_{sph} \mu \xi_n(ka) \psi_n(k_{sph}a) - k \mu_{sph} \psi_n(k_{sph}a) \xi_n(ka)}$$

$$= (b_{nm} + h_{nm}) Q_n^m, \quad (2.5)$$

where $\psi(r)$ and $\xi(r)$ are the Riccati-Bessel functions defined by

$$\psi_n(r) = r j_n(r), \quad \xi_n(r) = r h_n^{(1)}(r), \quad (2.6)$$

and the primes denote derivatives with respect to the argument.

The interaction coefficients can be solved by using the relationship between the scattered field and the interaction field. The interaction field is due to the scattered field's reflecting off the surface and striking the sphere. The interaction field is the image of the scattered field. Identically, the interaction potential is the image of the scattered potential.

Figure 2 shows the two coordinate systems, one centered about the real sphere and one at an image location of the coordinate system, a distance of $2d$ along the positive z axis. It is easiest to consider potentials when solving for the interaction coefficients. The interaction potentials are the scattering potentials centered about the image coordinate. The interaction coefficients, however, are inverted and undergo a reflection at the surface. The inversion can be explained by taking advantage of the nature of the associated Legendre polynomials that make up the potentials; i.e.,

$$P_n^m[\cos(\pi - \vartheta)] = (-1)^{n+m} P_n^m[\cos(\vartheta)]. \quad (2.7)$$

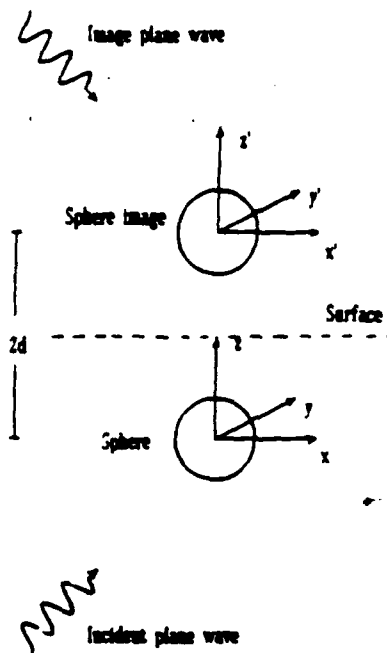


Fig. 2. Image coordinate surface is located a distance $2d$ from the sphere coordinate system along the positive z axis. Fields in the image coordinate system are inverted; e.g., the image of the incident plane wave travels in the x - z plane at angle $\pi - \alpha$ with respect to the z axis.

An approximation is made in order to account for the interaction. The interacting radiation is assumed to strike the surface at normal incidence. A Fresnel reflection at normal incidence is then used to account for the reflection loss at the surface. This same approximation was used by Yousif to solve for the scattering from a cylinder on a surface that has been verified by experiment. Justification for this approximation can be seen by tracing rays from the image coordinate system to the edges of the sphere, as in Fig. 3. The maximum angle at which a ray emanating from the center of the image coordinate system strikes the surface is 30° , and the Fresnel coefficients are fairly constant from normal incidence out to this angle for most optical materials. For highly conducting optical surfaces, such as mirrors, the Fresnel coefficients are nearly constant from 0° to 90° , and, as the refractive index approaches ∞ , the Fresnel coefficients are constants and there is no approximation. The Fresnel reflection and transmission coefficients for this system can be written as follows:

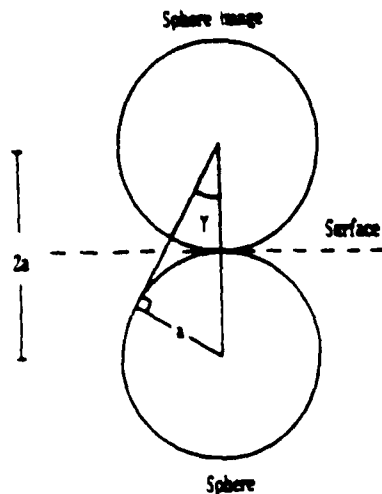
$$R_{TE}(\vartheta_i) = \frac{Z_2 \cos \vartheta_i - Z_1 [1 - (n_1/n_2)^2 \sin^2 \vartheta_i]^{1/2}}{Z_2 \cos \vartheta_i + Z_1 [1 - (n_1/n_2)^2 \sin^2 \vartheta_i]^{1/2}},$$

$$T_{TE}(\vartheta_i) = \frac{2Z_2 \cos \vartheta_i}{Z_2 \cos \vartheta_i + Z_1 [1 - (n_1/n_2)^2 \sin^2 \vartheta_i]^{1/2}},$$

$$R_{TM}(\vartheta_i) = - \frac{Z_1 \cos \vartheta_i - Z_2 [1 - (n_1/n_2)^2 \sin^2 \vartheta_i]^{1/2}}{Z_1 \cos \vartheta_i + Z_2 [1 - (n_1/n_2)^2 \sin^2 \vartheta_i]^{1/2}},$$

$$T_{TM}(\vartheta_i) = \frac{2Z_2 \cos \vartheta_i}{Z_1 \cos \vartheta_i + Z_2 [1 - (n_1/n_2)^2 \sin^2 \vartheta_i]^{1/2}}, \quad (2.8)$$

where



Maximum angle of incidence on the surface γ for an intersecting ray occurs for a ray traced from the image coordinate system (at the center of the image sphere) to the edge of the sphere (the ray touches the surface). This angle can be no greater than 30° . Fresnel equations are fairly constant near normal incidences.

$$\frac{1}{2} = \frac{\mu_1 k_2}{\mu_2 k_1}, \quad (2.9)$$

TE and TM subscripts pertain to the transverse electric and transverse magnetic cases, and the subscripts 1 and 2 refer to the optical parameters of the media below and above surface, respectively. The interaction terms can be expressed in the image coordinate system as

$$\begin{aligned} f_{nm} u_{nm}^{(3)} &= R(0^\circ) (-1)^{n+m} e_{nm} u_{nm}^{(3)}, \\ f_{nm} u_{nm}^{(3)} &= R(0^\circ) (-1)^{n+m} f_{nm} u_{nm}^{(3)}, \end{aligned} \quad (2.10)$$

where the primes denote quantities in the image coordinate system. Note that $R_{TE}(0^\circ) = R_{TM}(0^\circ) = R(0^\circ)$. At this point the scattering coefficients are essentially fixed, but they are coefficients of functions in a different coordinate system. The next step is to find a representation of the functions in the unprimed coordinate system. Each of the primed functions can be expanded in terms of functions in the unprimed system; i.e.,

$$\begin{aligned} f_{nm} u_{nm}^{(3)} &= R(0^\circ) (-1)^{n+m} e_{nm} \sum_{n'=0}^{\infty} c_{n'}^{(n,m)} u_{n'm}^{(1)}, \\ f_{nm} u_{nm}^{(3)} &= R(0^\circ) (-1)^{n+m} f_{nm} \sum_{n'=0}^{\infty} c_{n'}^{(n,m)} u_{n'm}^{(1)}. \end{aligned} \quad (2.11)$$

The interaction coefficients can be solved by extending summations over n and m . Collecting like terms yields

$$\begin{aligned} g_{nm} &= R(0^\circ) \sum_{n'=0}^{\infty} (-1)^{n+m} e_{n'm} c_{n'}^{(n,m)}, \\ h_{nm} &= R(0^\circ) \sum_{n'=0}^{\infty} (-1)^{n+m} f_{n'm} c_{n'}^{(n,m)}. \end{aligned} \quad (2.12)$$

Substituting these expressions into Eqs. (2.5) yields

$$\begin{aligned} e_{nm} &= \left[a_{nm} + R(0^\circ) \sum_{n'=0}^{\infty} (-1)^{n+m} e_{n'm} c_{n'}^{(n',m)} \right] Q_e^n, \\ f_{nm} &= \left[b_{nm} + R(0^\circ) \sum_{n'=0}^{\infty} (-1)^{n+m} f_{n'm} c_{n'}^{(n',m)} \right] Q_f^n. \end{aligned} \quad (2.13)$$

The only unknowns are the translation coefficients $c_{n'}^{(n',m)}$. These were solved by Bobbert and Vlieger by way of recursion relations. In this paper the translation is along the positive z axis rather than the negative z axis. This creates some minor differences. The coefficients can be determined by using the following equations:

$$c_n^{(0,0)} = (2n+1)^{1/2} h_n^{(1)}(2kd), \quad (2.14)$$

while

$$c_n^{(-1,0)} = -(2n+1)^{1/2} h_n^{(1)}(2kd), \quad (2.15)$$

$$\begin{aligned} [(n'-m+1)(n'+m)(2n+1)]^{1/2} c_n^{(n',m)} &= [(n-m+1)(n+m)(2n+1)]^{1/2} c_n^{(n',m-1)} \\ &- 2kd \left[\frac{(n-m+2)(n-m+1)}{(2n+3)} \right]^{1/2} c_{n+1}^{(n',m-1)} \\ &- 2kd \left[\frac{(n+m)(n+m-1)}{(2n-1)} \right]^{1/2} c_{n-1}^{(n',m-1)}, \end{aligned} \quad (2.16)$$

$$c_n^{(n',m)} = c_n^{(n',-m)}, \quad (2.17)$$

$$\begin{aligned} n' c_n^{(n'-1,0)} \left(\frac{2n+1}{2n'-1} \right)^{1/2} - (n'+1) c_n^{(n'+1,0)} \left(\frac{2n+1}{2n'+3} \right)^{1/2} &= (n+1) c_{n+1}^{(n',0)} \left(\frac{2n'+1}{2n+3} \right)^{1/2} - n c_{n-1}^{(n',0)} \left(\frac{2n'+1}{2n-1} \right)^{1/2}. \end{aligned} \quad (2.18)$$

With the use of these equations, the translation coefficients can be determined, and the only remaining unknowns in Eqs. (2.12) are the coefficients for the incident field. In Subsection 3 these coefficients will be solved for the particular case of an arbitrarily incident plane wave.

3. The Case of Plane-Wave Incident Radiation

The incident radiation on the sphere can be separated into two parts. One part strikes the sphere directly, and the other part reflects off the surface before striking the sphere. The part that reflects off the surface will undergo a Fresnel reflection on striking the surface, and it will also be out of phase by an amount $\exp(i2kd \cos \alpha)$. The Fresnel reflection term depends on whether the plane wave is TE or TM with respect to the plane of incidence (the z - s plane). Both cases must be considered separately. Equations (2.1) must be separated into two parts: one for the TE case and one for the TM case. The fields can be expressed by including both parts of the incident radiation as follows:

$$E_{TE}^{inc} = [1 + R_{TE}(\alpha) \exp(2ikd \cos \alpha) (-1)^{n+m}]$$

$$\times \sum_{n=0}^{\infty} \sum_{m=-n}^n a_{nm}^{TE} M_{nm}^{(1)} + b_{nm}^{TE} N_{nm}^{(1)}$$

$$\begin{aligned}
 \mathbf{H}_{TE}^{inc} &= \frac{k}{i\omega\mu} [1 + R_{TE}(\alpha) \exp(2ikd \cos \alpha) (-1)^{n+m}] \\
 &\quad \times \sum_{n=0}^{\infty} \sum_{m=-n}^n b_{nm}^{TE} M_{nm}^{(1)} + a_{nm}^{TE} N_{nm}^{(1)}, \\
 \mathbf{E}_{TM}^{inc} &= [1 + R_{TM}(\alpha) \exp(2ikd \cos \alpha) (-1)^{n+m}] \\
 &\quad \times \sum_{n=0}^{\infty} \sum_{m=-n}^n a_{nm}^{TM} M_{nm}^{(1)} + b_{nm}^{TM} N_{nm}^{(1)}, \\
 \mathbf{H}_{TM}^{inc} &= \frac{k}{i\omega\mu} [1 + R_{TM}(\alpha) \exp(2ikd \cos \alpha) (-1)^{n+m}] \\
 &\quad \times \sum_{n=0}^{\infty} \sum_{m=-n}^n b_{nm}^{TM} M_{nm}^{(1)} + c_{nm}^{TM} N_{nm}^{(1)}. \quad (3.1)
 \end{aligned}$$

The factor of $(-1)^{n+m}$ is a result of Eq. (2.7), since the reflected plane wave is traveling in the $x-z$ plane at an angle $\pi - \alpha$ with respect to the z axis. Coefficients a_{nm}^{TE} , a_{nm}^{TM} , b_{nm}^{TE} , and b_{nm}^{TM} are now the coefficients for a plane wave traveling in the $x-z$ plane at an angle α with respect to the z axis. The path to the solution is outlined by Stratton¹⁰ (the case for $\alpha = 0^\circ$ is solved). The result, after much algebra, is

$$\begin{aligned}
 b_{nm}^{TE} &= \frac{i^n}{n(n+1)} [(n-m)(n+m+1)]^{1/2} P_n^{m+1}(\cos \alpha) \\
 &\quad - [(n-m+1)(n+m)]^{1/2} P_n^{m-1}(\cos \alpha) \\
 &= \frac{2i^{n+2}}{n(n+1)} \frac{\partial P_n^m(\cos \alpha)}{\partial \alpha}, \quad (3.2)
 \end{aligned}$$

$$\begin{aligned}
 b_{nm}^{TM} &= \frac{i^{n+2}(2n+1)}{n(n+1)} \left\{ P_{n+1}^{m-1}(\cos \alpha) \right. \\
 &\quad \times \left[\frac{(n-m+1)(n-m+2)}{(2n+1)(2n+3)} \right]^{1/2} + P_{n+1}^{m+1}(\cos \alpha) \\
 &\quad \times \left[\frac{(n+m+1)(n+m+2)}{(2n+1)(2n+3)} \right]^{1/2} \left. \right\} \\
 &= \frac{2i^{n+2}}{n(n+1)} \frac{m P_n^m(\cos \alpha)}{\sin \alpha}, \quad (3.3)
 \end{aligned}$$

$$a_{nm}^{TM} = i b_{nm}^{TE}, \quad (3.4)$$

$$b_{nm}^{TM} = i a_{nm}^{TE}. \quad (3.5)$$

From these expressions, Eqs. (2.5) take on the following form:

$$\begin{aligned}
 a_{nm}^{TE} &= \left\{ [1 + R_{TE}(\alpha) (-1)^{n+m} \exp(2ikd \cos \alpha)] a_{nm}^{TE} \right. \\
 &\quad \left. + R_{TE}(0^\circ) \sum_{n'=n}^{\infty} (-1)^{n'+m} e_{n'm}^{TE} c_n^{(n',m)} \right\} Q_n^{\alpha}, \quad (3.6)
 \end{aligned}$$

$$\begin{aligned}
 a_{nm}^{TM} &= \left\{ [1 + R_{TM}(\alpha) (-1)^{n+m} \exp(2ikd \cos \alpha)] a_{nm}^{TM} \right. \\
 &\quad \left. + R_{TM}(0^\circ) \sum_{n'=n}^{\infty} (-1)^{n'+m} e_{n'm}^{TM} c_n^{(n',m)} \right\} Q_n^{\alpha}. \quad (3.7)
 \end{aligned}$$

$$\begin{aligned}
 f_{nm}^{TE} &= \left\{ [1 + R_{TE}(\alpha) (-1)^{n+m} \exp(2ikd \cos \alpha)] b_{nm}^{TE} \right. \\
 &\quad \left. + R_{TE}(0^\circ) \sum_{n'=n}^{\infty} (-1)^{n'+m} f_{n'm}^{TE} c_n^{(n',m)} \right\} Q_n^{\alpha}, \\
 f_{nm}^{TM} &= \left\{ [1 + R_{TM}(\alpha) (-1)^{n+m} \exp(2ikd \cos \alpha)] b_{nm}^{TM} \right. \\
 &\quad \left. + R_{TM}(0^\circ) \sum_{n'=n}^{\infty} (-1)^{n'+m} f_{n'm}^{TM} c_n^{(n',m)} \right\} Q_n^{\alpha}. \quad (3.6)
 \end{aligned}$$

In practice the infinite number of terms in these equations are not needed. Experimental precision determines the number of terms needed. In any case the scattering coefficients may be solved, since there always remains an equivalent number of equations and unknowns. The next step in this analysis is to develop the Mueller scattering matrix.

4. The Mueller Scattering Matrix

Two axes are used for determining the Mueller scattering matrix, one perpendicular to the plane of incidence (ϕ) and one parallel to the plane of incidence (ψ). The matrix will also be derived for the far-field solution, where $kr \gg n^2$. In this limit the spherical Hankel functions reduce to spherical waves:

$$h_n^{(1)}(kr) \sim \frac{(-i)^n}{ikr} e^{ikr}. \quad (4.1)$$

The field below the surface is composed of two parts. One part results from the sphere directly. The other part results from the field reflecting off the surface. This part is centered about the image coordinate system and is, in fact, the interaction term. In the far field the contributions of spherical waves can be added without translating the image coordinate system. This image field will contain a Fresnel reflection term, a phase term equivalent to $\exp(-2ikd \cos \psi)$, and an inversion term equivalent to $(-1)^{n+m}$. The field above the surface results only from the scattering directly from the sphere that is reduced by the Fresnel transmission factor when passing through the surface.

The starting point for calculating the Mueller scattering matrix is the amplitude scattering matrix, which is defined by

$$\begin{bmatrix} E_{\phi}^{inc} \\ E_{\phi}^{rec} \end{bmatrix} = \frac{e^{ikr}}{-ikr} \begin{bmatrix} S_2 & S_3 \\ S_4 & S_1 \end{bmatrix} \begin{bmatrix} E_{TM}^{inc} \\ E_{TE}^{inc} \end{bmatrix}. \quad (4.2)$$

The scattering amplitude matrix elements are solved by expanding the scattered electric fields in terms of the vector wave functions and then expanding the vector wave functions in terms of the polarization directions by using Eqs. (1.6). The scattering amplitude matrix elements for $|\psi| > \pi/2$ assume the following form:

$$\begin{aligned}
 S_1 &= \sum_{n=0}^{\infty} \sum_{m=-n}^n (-i)^n e^{im\psi} \\
 &\quad \times [1 + R_{TE}(\pi - \psi) (-1)^{n+m} \exp(-2ikd \cos \psi)] \\
 &\quad \times \left[\frac{f_{nm}^{TE}}{\sin \psi} P_n^m(\cos \psi) + e_{nm}^{TE} \frac{\partial}{\partial \psi} P_n^m(\cos \psi) \right].
 \end{aligned}$$

$$\begin{aligned}
 &= -i \sum_{n=0}^{\infty} \sum_{m=-n}^n (-i)^n e^{im\vartheta} \\
 &\quad \times [1 + R_{TM}(\pi - \vartheta) (-1)^{n+m} \exp(-2ikd \cos \vartheta)] \\
 &\quad \times \left[\frac{e_{nm}^{TMm}}{\sin \vartheta} P_n^m(\cos \vartheta) + f_{nm}^{TM} \frac{\partial}{\partial \vartheta} P_n^m(\cos \vartheta) \right], \\
 &= -i \sum_{n=0}^{\infty} \sum_{m=-n}^n (-i)^n e^{im\vartheta} \\
 &\quad \times [1 + R_{TM}(\pi - \vartheta) (-1)^{n+m} \exp(-2ikd \cos \vartheta)] \\
 &\quad \times \left[\frac{e_{nm}^{TEm}}{\sin \vartheta} P_n^m(\cos \vartheta) + f_{nm}^{TE} \frac{\partial}{\partial \vartheta} P_n^m(\cos \vartheta) \right], \\
 &= \sum_{n=0}^{\infty} \sum_{m=-n}^n (-i)^n e^{im\vartheta} \\
 &\quad \times [1 + R_{TE}(\pi - \vartheta) (-1)^{n+m} \exp(-2ikd \cos \vartheta)] \\
 &\quad \times \left[\frac{f_{nm}^{TMm}}{\sin \vartheta} P_n^m(\cos \vartheta) + e_{nm}^{TM} \frac{\partial}{\partial \vartheta} P_n^m(\cos \vartheta) \right]. \quad (4.3)
 \end{aligned}$$

The elements behind the surface ($|\vartheta| < \pi/2$) take on the form

$$\begin{aligned}
 S_1 &= \sum_{n=0}^{\infty} \sum_{m=-n}^n (-i)^n e^{im\vartheta} T_{TE}(\vartheta) \\
 &\quad \times \left[\frac{f_{nm}^{TEm}}{\sin \vartheta} P_n^m(\cos \vartheta) + e_{nm}^{TE} \frac{\partial}{\partial \vartheta} P_n^m(\cos \vartheta) \right], \\
 S_2 &= -i \sum_{n=0}^{\infty} \sum_{m=-n}^n (-i)^n e^{im\vartheta} T_{TM}(\vartheta) \\
 &\quad \times \left[\frac{e_{nm}^{TMm}}{\sin \vartheta} P_n^m(\cos \vartheta) + f_{nm}^{TM} \frac{\partial}{\partial \vartheta} P_n^m(\cos \vartheta) \right], \\
 S_3 &= -i \sum_{n=0}^{\infty} \sum_{m=-n}^n (-i)^n e^{im\vartheta} T_{TM}(\vartheta) \\
 &\quad \times \left[\frac{e_{nm}^{TEm}}{\sin \vartheta} P_n^m(\cos \vartheta) + f_{nm}^{TE} \frac{\partial}{\partial \vartheta} P_n^m(\cos \vartheta) \right], \\
 S_4 &= \sum_{n=0}^{\infty} \sum_{m=-n}^n (-i)^n e^{im\vartheta} T_{TE}(\vartheta) \\
 &\quad \times \left[\frac{f_{nm}^{TMm}}{\sin \vartheta} P_n^m(\cos \vartheta) + e_{nm}^{TM} \frac{\partial}{\partial \vartheta} P_n^m(\cos \vartheta) \right]. \quad (4.4)
 \end{aligned}$$

For the transmission case, ϑ is the angle incident upon the surface. The actual field inside the surface is determined from Snell's law. Most measurements are taken by placing a detector in air on the opposite side of a thin slab of the bulk material. If the rear surface of the bulk material is antireflection coated, these are the elements that would result. The Mueller scattering matrix can be determined directly from these elements by using relations given by Bohren and Huffman.

A few symmetries that exist simplify the calculations. A careful examination of Eqs. (3.6) reveals that

$$\begin{aligned}
 e_{nm}^{TE} &= (-1)^m e_{nm}^{TE}, \\
 e_{nm}^{TM} &= (-1)^{m+1} e_{nm}^{TM}, \\
 f_{nm}^{TE} &= (-1)^{m+1} f_{nm}^{TE}, \\
 f_{nm}^{TM} &= (-1)^m f_{nm}^{TM}, \quad (4.5)
 \end{aligned}$$

where $m = -n$. If the Mueller scattering matrix is measured in the plane of incidence ($\varphi = 0^\circ$), then from these symmetries and Eqs. (4.3) and (4.4), S_3 and S_4 reduce to zero, since for the normalized associated Legendre polynomials

$$P_n^{-m}(x) = (-1)^m P_n^m(x). \quad (4.6)$$

Of the Mueller scattering matrix elements, only four remain that are not zero or simple multiples of another element. These may be determined with the following relations:

$$\begin{aligned}
 S_{11} &= \frac{1}{2} (|S_1|^2 + |S_2|^2), \\
 S_{12} &= \frac{1}{2} (|S_2|^2 - |S_1|^2), \\
 S_{33} &= \text{Re}(S_1 S_2^*), \\
 S_{34} &= \text{Im}(S_2 S_1^*). \quad (4.7)
 \end{aligned}$$

In the plane of incidence these four matrix elements are sufficient to categorize the light scattering from a sphere on or near a plane surface.

CONCLUSION

Relations for calculating the light-scattering Mueller matrix for a sphere of arbitrary size and optical parameters on or near a surface of arbitrary complex refractive index, illuminated by light of arbitrary wavelength and incident angle, are provided. When the matrix is determined in the plane of incidence, the Mueller matrix can be characterized by four elements.

The particular functions used in the derivation facilitate the calculation of the matrix elements. Incorporating Eqs. (2.7), (4.5), and (4.6) into a scattering program will significantly reduce the number of calculations and the run time.

ACKNOWLEDGMENTS

The author thanks William L. Wolfe and William S. Bickel for their support and encouragement. He also thanks Mary Turner, Paul Spyak, and Lowell Lamb for many helpful discussions. This research was partly supported by a fellowship from Itek Optical Systems.

REFERENCES

1. Lord Rayleigh, "On the electromagnetic theory of light," Philos. Mag. 12, 81-101 (1881).
2. W. von Ignatowsky, "Reflexion elektromagnetischer Wellen an einem Draht," Ann. Phys. (Leipzig) 18, 496-522 (1905).
3. G. Mie, "Beiträge zur Optik trüber Medien speziell kolloidaler Metallösungen," Ann. Phys. (Leipzig) 28, 377-445 (1908).
4. C. Liang and Y. T. Lo, "Scattering by two spheres," Radio Sci. 1, 1481-1495 (1967).
5. G. W. Kettawar and C. E. Dean, "Electromagnetic scattering from two dielectric spheres: comparison between theory and experiment," Opt. Lett. 8, 48-52 (1983).
6. R. T. Wang, J. M. Greenberg, and D. W. Schuerman, "Experimental results of dependent light scattering by two spheres," Opt. Lett. 8, 543-546 (1983).

A. Bobbert and J. Vlieger, "Light scattering by a sphere on a substrate," *Physica* **137A**, 209-241 (1996).

Yousaf, "Light scattering from parallel tilted fibers," Ph.D. dissertation (Department of Physics, University of Arizona, Tucson, Ariz., 1987).

Lamb, Department of Physics, University of Arizona, Tucson, Ariz. 85721 (personal communication).

C. Rao and R. Barakat, "Plane-wave scattering by a conducting cylinder partially buried in a ground plane. 1. TM case," *J. Opt. Soc. Am. A* **6**, 1270-1280 (1989).

11. J. A. Stratton, *Electromagnetic Theory* (McGraw-Hill, New York, 1941).
12. C. F. Bohren and D. R. Huffman, *Absorption and Scattering of Light by Small Particles* (Wiley, New York, 1983).
13. H. C. van de Hulst, *Light Scattering by Small Particles* (Wiley, New York, 1967).
14. M. Kerker, *The Scattering of Light and Other Electromagnetic Radiation* (Academic, New York, 1969).

ERRATA

Light scattering from a sphere on or near a surface: errata

Gorden Videen

Optical Sciences Center, University of Arizona, Tucson, Arizona 85721

A few errors in the far-field expressions for the light scattered from a sphere on or near a surface are corrected in these errata. The equations for the interference coefficients are

$$\begin{aligned} g_{nm}^{(1)} u_{nm}^{(3)} &= -R(0^\circ) (-1)^{n+m} e_{nm} u_{nm}^{(3)}, \\ h_{nm}^{(1)} u_{nm}^{(3)} &= R(0^\circ) (-1)^{n+m} f_{nm} u_{nm}^{(3)}. \end{aligned} \quad (2.10)$$

The interference coefficients must be translated by means of the vector wave functions.^{2,3} This interference field may be expressed as

$$\begin{aligned} \mathbf{E}^{int} &= \sum_{n=0}^{\infty} \sum_{m=-n}^n e_{nm} (-1)^{n+m+1} R(0^\circ) \mathbf{M}_{nm}^{(3)} \\ &\quad + f_{nm} (-1)^{n+m} R(0^\circ) \mathbf{N}_{nm}^{(3)} \\ &= \sum_{n=0}^{\infty} \sum_{m=-n}^n \left\{ e_{nm} (-1)^{n+m+1} R(0^\circ) \right. \\ &\quad \times \left[\sum_{n'=m}^n C_{n'}^{(n,m)} \mathbf{M}_{nm}^{(1)} + D_{n'}^{(n,m)} \mathbf{N}_{nm}^{(1)} \right] \\ &\quad + f_{nm} (-1)^{n+m} R(0^\circ) \\ &\quad \times \left[\sum_{n'=m}^n D_{n'}^{(n,m)} \mathbf{M}_{nm}^{(1)} + C_{n'}^{(n,m)} \mathbf{N}_{nm}^{(1)} \right] \} \\ &= \sum_{n=0}^{\infty} \sum_{m=-n}^n \sum_{n'=m}^n (-1)^{n+m} R(0^\circ) \\ &\quad \times \{ [f_{nm} D_{n'}^{(n,m)} - e_{nm} C_{n'}^{(n,m)}] \mathbf{M}_{nm}^{(1)} \\ &\quad + [f_{nm} C_{n'}^{(n,m)} - e_{nm} D_{n'}^{(n,m)}] \mathbf{N}_{nm}^{(1)} \}, \end{aligned} \quad (2.11a)$$

where

$$\begin{aligned} C_{n'}^{(n,m)} &= c_n^{(n,m)} - \frac{2kd}{2n+3} \frac{n+m+1}{n+1} c_{n-1}^{(n,m)} \\ &\quad - \frac{2kd}{2n-1} \frac{n-m}{n} c_{n+1}^{(n,m)}, \\ D_{n'}^{(n,m)} &= \frac{-2ikd}{n(n+1)} m c_{n'}^{(n,m)} \end{aligned} \quad (2.11b)$$

are given in Refs. 2 and 3. Equations (2.11) lead to

$$\begin{aligned} g_{nm} &= \sum_{n=-m}^{\infty} R(0^\circ) (-1)^{n+m} [f_{nm} D_{n'}^{(n,m)} - e_{nm} C_{n'}^{(n,m)}], \\ h_{nm} &= \sum_{n=-m}^{\infty} R(0^\circ) (-1)^{n+m} [f_{nm} C_{n'}^{(n,m)} - e_{nm} D_{n'}^{(n,m)}], \end{aligned} \quad (2.12)$$

$$\begin{aligned} e_{nm} &= \left\{ a_{nm} - \sum_{n=-m}^{\infty} R(0^\circ) (-1)^{n+m} \right. \\ &\quad \times [f_{nm} D_{n'}^{(n,m)} - e_{nm} C_{n'}^{(n,m)}] \} Q_1^2, \\ f_{nm} &= \left\{ b_{nm} + \sum_{n=-m}^{\infty} R(0^\circ) (-1)^{n+m} \right. \\ &\quad \times [f_{nm} C_{n'}^{(n,m)} - e_{nm} D_{n'}^{(n,m)}] \} Q_1^2. \end{aligned} \quad (2.13)$$

The expressions for the incident fields are

$$\begin{aligned} \mathbf{E}_{TE}^{TE} &= \sum_{n=0}^{\infty} \sum_{m=-n}^n a_{nm}^{TE} [1 - R_{TE}(\alpha) \\ &\quad \times \exp(2ikd \cos \alpha) (-1)^{n+m}] \mathbf{M}_{nm}^{(1)} \\ &\quad + b_{nm}^{TE} [1 + R_{TE}(\alpha) \exp(2ikd \cos \alpha) (-1)^{n+m}] \mathbf{N}_{nm}^{(1)}, \\ \mathbf{H}_{TE}^{TE} &= \frac{k}{i\omega\mu} \sum_{n=0}^{\infty} \sum_{m=-n}^n b_{nm}^{TE} [1 + R_{TE}(\alpha) \\ &\quad \times \exp(2ikd \cos \alpha) (-1)^{n+m}] \mathbf{M}_{nm}^{(1)} \\ &\quad + a_{nm}^{TE} [1 - R_{TE}(\alpha) \exp(2ikd \cos \alpha) (-1)^{n+m}] \mathbf{N}_{nm}^{(1)}, \\ \mathbf{E}_{TM}^{TM} &= \sum_{n=0}^{\infty} \sum_{m=-n}^n a_{nm}^{TM} [1 - R_{TM}(\alpha) \\ &\quad \times \exp(2ikd \cos \alpha) (-1)^{n+m}] \mathbf{M}_{nm}^{(1)} \\ &\quad + b_{nm}^{TM} [1 + R_{TM}(\alpha) \exp(2ikd \cos \alpha) (-1)^{n+m}] \mathbf{N}_{nm}^{(1)}, \\ \mathbf{H}_{TM}^{TM} &= \frac{k}{i\omega\mu} \sum_{n=0}^{\infty} \sum_{m=-n}^n b_{nm}^{TM} [1 + R_{TM}(\alpha) \\ &\quad \times \exp(2ikd \cos \alpha) (-1)^{n+m}] \mathbf{M}_{nm}^{(1)} \\ &\quad + a_{nm}^{TM} [1 - R_{TM}(\alpha) \exp(2ikd \cos \alpha) (-1)^{n+m}] \mathbf{N}_{nm}^{(1)}. \end{aligned} \quad (3.1)$$

The scattering coefficients are

$$\begin{aligned} e_{nm}^{TE} &= \left\{ [1 - R_{TE}(\alpha) (-1)^{n+m} \exp(2ikd \cos \alpha)] a_{nm}^{TE} \right. \\ &\quad \left. + R_{TE}(0^\circ) \sum_{n=-m}^{\infty} (-1)^{n+m} [f_{nm}^{TE} D_{n'}^{(n,m)} - e_{nm}^{TE} C_{n'}^{(n,m)}] \right\} Q_1^2, \\ e_{nm}^{TM} &= \left\{ [1 - R_{TM}(\alpha) (-1)^{n+m} \exp(2ikd \cos \alpha)] a_{nm}^{TM} \right. \\ &\quad \left. + R_{TM}(0^\circ) \sum_{n=-m}^{\infty} (-1)^{n+m} [f_{nm}^{TM} D_{n'}^{(n,m)} - e_{nm}^{TM} C_{n'}^{(n,m)}] \right\} Q_1^2. \end{aligned}$$

$$\begin{aligned} f_{nm}^{TE} &= \left\{ [1 + R_{TE}(\alpha) (-1)^{n+m} \exp(2ikd \cos \alpha)] b_{nm}^{TE} \right. \\ &\quad \left. + R_{TE}(0^\circ) \sum_{n=-m}^{\infty} (-1)^{n+m} [f_{nm}^{TE} C_{n'}^{(n,m)} - e_{nm}^{TE} D_{n'}^{(n,m)}] \right\} Q_1^2. \end{aligned}$$

$$f_{4m}^{TM} = \left\{ [1 + R_{TM}(\alpha)(-1)^{n+m} \exp(2ikd \cos \alpha)] b_{4m}^{TM} \right. \\ \left. + R_{TM}(0^\circ) \sum_{n=-m}^m (-1)^{n+m} [f_{4m}^{TM} C_{4,n}^{TM} - e_{4m}^{TM} D_{4,n}^{TM}] \right\} Q_2. \quad (3.6)$$

The scattering amplitude matrix elements below the surface ($\vartheta > \pi/2$) are

$$S_1 = \sum_{n=0}^{\infty} \sum_{m=-n}^n (-i)^n \exp(im\varphi) \\ \times \left\{ [1 + R_{TE}(\pi - \vartheta)(-1)^{n+m} \exp(-2ikd \cos \vartheta)] \right. \\ \times \frac{f_{4m}^{TE} m}{\sin \vartheta} \tilde{P}_n^m(\cos \vartheta) + [1 - R_{TE}(\pi - \vartheta)(-1)^{n+m} \\ \left. \times \exp(-2ikd \cos \vartheta)] e_{4m}^{TE} \frac{\partial}{\partial \vartheta} \tilde{P}_n^m(\cos \vartheta) \right\},$$

$$S_2 = -i \sum_{n=0}^{\infty} \sum_{m=-n}^n (-i)^n \exp(im\varphi) \\ \times \left\{ [1 - R_{TM}(\pi - \vartheta)(-1)^{n+m} \exp(-2ikd \cos \vartheta)] \right. \\ \times \frac{e_{4m}^{TM} m}{\sin \vartheta} \tilde{P}_n^m(\cos \vartheta) + [1 + R_{TM}(\pi - \vartheta)(-1)^{n+m} \\ \left. \times \exp(-2ikd \cos \vartheta)] f_{4m}^{TM} \frac{\partial}{\partial \vartheta} \tilde{P}_n^m(\cos \vartheta) \right\},$$

$$S_3 = -i \sum_{n=0}^{\infty} \sum_{m=-n}^n (-i)^n \exp(im\varphi) \\ \times \left\{ [1 - R_{TM}(\pi - \vartheta)(-1)^{n+m} \exp(-2ikd \cos \vartheta)] \right. \\ \times \frac{e_{4m}^{TM} m}{\sin \vartheta} \tilde{P}_n^m(\cos \vartheta) + [1 + R_{TM}(\pi - \vartheta)(-1)^{n+m} \\ \left. \times \exp(-2ikd \cos \vartheta)] f_{4m}^{TE} \frac{\partial}{\partial \vartheta} \tilde{P}_n^m(\cos \vartheta) \right\},$$

$$S_4 = \sum_{n=0}^{\infty} \sum_{m=-n}^n (-i)^n \exp(im\varphi) \\ \times \left\{ [1 + R_{TE}(\pi - \vartheta)(-1)^{n+m} \exp(-2ikd \cos \vartheta)] \right. \\ \times \frac{f_{4m}^{TE} m}{\sin \vartheta} \tilde{P}_n^m(\cos \vartheta) + [1 - R_{TE}(\pi - \vartheta)(-1)^{n+m} \\ \left. \times \exp(-2ikd \cos \vartheta)] e_{4m}^{TE} \frac{\partial}{\partial \vartheta} \tilde{P}_n^m(\cos \vartheta) \right\}. \quad (4.3)$$

REFERENCES

1. G. Videen, "Light scattering from a sphere on or near a surface," *J. Opt. Soc. Am. A* **8**, 483-489 (1991).
2. S. Stein, "Addition theorems for spherical wave functions," *Q. Appl. Math.* **19**, 15-24 (1961).
3. O. R. Cruzan, "Translational addition theorems for spherical vector wave functions," *Q. Appl. Math.* **20**, 33-40 (1962).

Coherent fluorescent emission and scattering from a uniform cylinder

Gorden Videen, William S. Bickel, and Joseph M. Boyer
 Department of Physics, University of Arizona, Tucson, Arizona 85721
 (Received 11 October 1990)

The coherent light inelastically scattered from an ideal fluorescent cylinder illuminated by an arbitrary electromagnetic wave is analyzed using an extension of Rayleigh's theory. Scattering coefficients are solved specifically for a plane wave illuminating the cylinder normal to the axis of the cylinder. The resulting inelastically scattered radiation is not entirely unlike that of elastically scattered radiation from a perfect cylinder. These results are illustrated by numerical calculations for several specific, but arbitrary, cases.

I. INTRODUCTION

Inelastically scattered light is subject to the morphology and optical properties of the particle that interacts with the incident electromagnetic radiation. Experimentally, morphology-dependent resonances have been observed in the elastically scattered light emitted from glass fibers coated with fluorescent dyes by Owen *et al.*¹ Fluorescence enhancement by a uniform cylinder was studied by Sekerak² and Abramson.³ Uniform spherical particles were examined by Biswas *et al.*⁴ and Benner *et al.*⁵ Theoretically, Raman and fluorescent emission by a molecule embedded in a dielectric cylinder has been derived by Chew, Cooke, and Kerker.⁶ Kerker and Druger⁷ theoretically studied fluorescent molecules embedded in spheres. Das and Metiu⁸ took a quantum-mechanical approach in examining fluorescence enhancement. Ching, Lai, and Young examined microspheres as optical cavities.⁹ For a uniform distribution of molecules within a cylinder, the coherent process can be treated by adding the resulting amplitudes, molecule by molecule, over the cross section of the cylinder. A shortcut to this summation may be achieved by examining the polarization induced at the new frequency within the cylinder. This is the method used in this paper.

In this paper we derive and examine the effects of coherent, inelastic scattering due to the geometry imposed by an infinitely-long, circular cylinder composed of fluorescing material. The approach taken in this paper is an extension of Rayleigh's solution to the elastically scattered light from an infinitely-long, circular cylinder.¹⁰ The derivation closely follows Bohren and Huffman's derivation, and we represent the final scattered and radiated fields in terms of Mueller matrix elements.¹¹

Inelastic scattering occurring in particles is a process which may be solved in three parts. First, the boundary conditions of the particle are used to determine the internal electromagnetic fields within the particle. Second, these internal fields are used to determine the fields produced by the fluorescing medium. And third, the boundary conditions of the particle are used to determine the inelastic fields emitted.

The fluorescence process outlined here is very similar to coherent, Raman processes. For incoherent Raman processes, the internal fields are not intense enough to

stimulate the individual molecules to emit as they are for coherent Raman processes where more intense internal fields are generated, often by employing a second laser. Although our theory is limited as a model for Raman scatter because it incorporates only an incident field of one frequency, an extension of it to multiple-field interactions would follow the same basic procedure. However, we expect the main qualitative features of the scatter generated with this simplified model to remain unchanged.

Knowledge of the interaction of the incident electric fields and the fluorescing medium which produces the emitted fields is necessary to accurately determine the inelastically scattered radiation. We assume that the polarization within the fluorescing medium is proportional to the internal electric fields due to the incident electromagnetic field. We also assume all media are isotropic, homogeneous. With these assumptions, the derivation is straightforward.

II. THEORY

The starting point is to derive the internal fields within the uniform, fluorescing cylinder having the same fre-

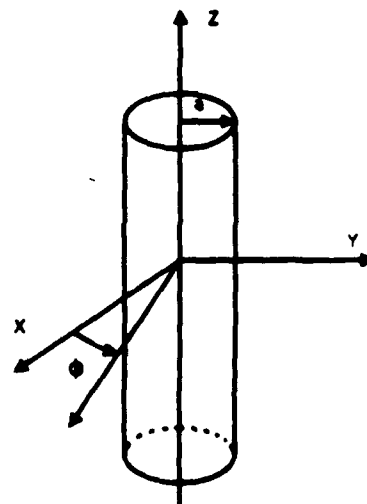


FIG. 1. The scattering geometry showing the fluorescing cylinder of radius a , centered on the origin, oriented parallel to the z axis.

quency of the incident radiation. This is done by applying the boundary conditions of the cylinder on the electromagnetic field and follows the same procedure used to derive the scattered field.

A. The fields for the incident wavelength

Figure 1 shows the scattering geometry of the system. A cylinder of radius a , centered on the origin is parallel to the z axis. The first step is to derive the internal electric fields of the cylinder. For wavelength λ_1 , the complex refractive index of the cylinder is m_1 . The illuminat-

ing fields of the incident radiation may be expanded as follows (see Bohren and Huffman, for instance):

$$\mathbf{E}_{\text{inc},1} = \sum_{n=-\infty}^{\infty} a_{n,1} \mathbf{M}_{n,\rho_1}^{(1)} + b_{n,1} \mathbf{N}_{n,\rho_1}^{(1)}, \quad (1a)$$

$$\mathbf{H}_{\text{inc},1} = \frac{-ik_1}{\omega_1 \mu_1} \sum_{n=-\infty}^{\infty} a_{n,1} \mathbf{N}_{n,\rho_1}^{(1)} + b_{n,1} \mathbf{M}_{n,\rho_1}^{(1)}, \quad (1b)$$

where $k_1 = 2\pi/\lambda_1$ is the wave number, ω_1 is the angular frequency, and μ_1 is the permeability of the incident medium at λ_1 . The vectors $\mathbf{M}_{n,\rho_1}^{(1)}$ and $\mathbf{N}_{n,\rho_1}^{(1)}$ are given by

$$\mathbf{M}_{n,\rho_1}^{(1)} = (k_1^2 - h^2)^{1/2} \left[in \frac{Z_n^{(1)}(\rho_1)}{\rho_1} \hat{\mathbf{e}}_r - Z_n^{(1)}(\rho_1) \hat{\mathbf{e}}_\phi \right] e^{i(n\phi + hz)}, \quad (2a)$$

$$\mathbf{N}_{n,\rho_1}^{(1)} = (k_1^2 - h^2)^{1/2} / k_1 \left[ih Z_n^{(1)}(\rho_1) \hat{\mathbf{e}}_r - hn \frac{Z_n^{(1)}(\rho_1)}{\rho_1} \hat{\mathbf{e}}_\phi + (k_1^2 - h^2)^{1/2} Z_n^{(1)}(\rho_1) \hat{\mathbf{e}}_z \right] e^{i(n\phi + hz)}. \quad (2b)$$

The superscript identifies the Bessel functions used to represent the fields. For example, $i=1$ corresponds with the use of the functions $Z_n^{(1)}(\rho) = J_n(\rho)$, $i=2$ corresponds with the use of the functions $Z_n^{(2)}(\rho) = Y_n(\rho)$, and $i=3$ corresponds with the use of the functions $Z_n^{(3)}(\rho) = H_n^{(1)}(\rho) = J_n(\rho) + iY_n(\rho)$. The functions representing the incident radiation are of the form $u_{n,\text{inc}} = J_n(\rho_1) e^{in\phi} e^{ih_1 z}$. The internal fields are also generated:

$$\mathbf{E}_{\text{int},1} = \sum_{n=-\infty}^{\infty} c_{n,1} \mathbf{M}_{n,\rho_1}^{(1)} + d_{n,1} \mathbf{N}_{n,\rho_1}^{(1)}, \quad (3a)$$

$$\mathbf{H}_{\text{int},1} = \frac{-ik'_1}{\omega_1 \mu_1} \sum_{n=-\infty}^{\infty} c_{n,1} \mathbf{N}_{n,\rho_1}^{(1)} + d_{n,1} \mathbf{M}_{n,\rho_1}^{(1)}, \quad (3b)$$

where $k'_1 = k_1 m_1$ is the wave number inside the cylinder

medium for wavelength λ_1 and μ'_1 is the permeability of the cylinder medium at wavelength λ_1 . The functions representing the internal fields are of the form $u_{n,\text{int}} = J_n(\rho'_1) e^{in\phi} e^{ih_1 z}$. The scattered fields are

$$\mathbf{E}_{\text{sc},1} = \sum_{n=-\infty}^{\infty} e_{n,1} \mathbf{M}_{n,\rho_1}^{(3)} + f_{n,1} \mathbf{N}_{n,\rho_1}^{(3)}, \quad (4a)$$

$$\mathbf{H}_{\text{sc},1} = \frac{-ik_1}{\omega_1 \mu_1} \sum_{n=-\infty}^{\infty} e_{n,1} \mathbf{N}_{n,\rho_1}^{(3)} + f_{n,1} \mathbf{M}_{n,\rho_1}^{(3)}. \quad (4b)$$

The functions representing the scattered fields are of the form $u_{n,\text{sc}} = H_n^{(1)}(\rho_1) e^{in\phi} e^{ih_1 z}$.

Setting $\mu_{r,1} = \mu'_1/\mu_1$, $\xi_1 = x_1 \sin\theta_0$, $\eta_1 = x_1 (m_1^2 - \cos^2\theta_0)^{1/2}$, and $x_1 = k_1 a$, four boundary conditions on \mathbf{E} and \mathbf{H} must be satisfied:

$$a_{n,1} \xi_1 J'_n(\xi_1) + b_{n,1} h_1 n J_n(\xi_1) / k_1 + e_{n,1} \xi_1 [H_n^{(1)}(\xi_1)]' + f_{n,1} h_1 n H_n^{(1)}(\xi_1) / k_1 = c_{n,1} \eta_1 J'_n(\eta_1) + d_{n,1} h_1 n J_n(\eta_1) / m_1 k_1. \quad (5a)$$

$$b_{n,1} \xi_1^2 J_n(\xi_1) + f_{n,1} \xi_1^2 H_n^{(1)}(\xi_1) = d_{n,1} \eta_1^2 J_n(\eta_1) / m_1. \quad (5b)$$

$$b_{n,1} \xi_1 J'_n(\xi_1) + a_{n,1} h_1 n J_n(\xi_1) / k_1 + f_{n,1} \xi_1 [H_n^{(1)}(\xi_1)]' + e_{n,1} h_1 n H_n^{(1)}(\xi_1) / k_1 = d_{n,1} m_1 \eta_1 J'_n(\eta_1) / \mu_{r,1} + c_{n,1} h_1 n J_n(\eta_1) / k_1 \mu_{r,1}. \quad (5c)$$

$$= d_{n,1} m_1 \eta_1 J'_n(\eta_1) / \mu_{r,1} + c_{n,1} h_1 n J_n(\eta_1) / k_1 \mu_{r,1}. \quad (5d)$$

and

$$a_{n,1} \xi_1^2 J_n(\xi_1) + e_{n,1} \xi_1^2 H_n^{(1)}(\xi_1) = c_{n,1} \eta_1^2 J_n(\eta_1) / \mu_{r,1}. \quad (5d)$$

B. Plane-wave illumination

When the coefficients $a_{n,1}$ and $b_{n,1}$ are known, then the other field components of Eq. (5) can be solved. For the case of plane-wave illumination, $h_1 = -k_1 \cos\theta_0$, $\rho_1 = k_1 r \sin\theta_0$, and $\rho'_1 = k'_1 r (m_1^2 - \cos^2\theta_0)^{1/2}$ where θ_0 is the angle of incidence measured from the z axis. We consider first the expansion of a plane wave of the form $\mathbf{E} = \hat{\mathbf{e}}_x E_0 e^{-i(k_1 x + \omega_1 t)}$ traveling along the negative x axis. The expansion coefficients for the TM case are

$$b_{n,1} = 0, \quad a_{n,1} = -i E_0 (-i)^n / k_1 \sin\theta_0.$$

For the case of a normally incident plane wave ($\theta_0 = \pi/2$), many of the terms in Eqs. (5a)-(5d) are

(since $h_1 = 0$). The internal and scattered field coefficients are simple expressions. For the TE case (incident electric field parallel to the z axis),

$$d_{n,1} = b_{n,1} \frac{J_n(\xi_1)H'_n(\xi_1) - J'_n(\xi_1)H_n(\xi_1)}{m_1 J_n(\eta_1)H'_n(\xi_1) - m_1^2 J'_n(\eta_1)H_n(\xi_1)}, \quad (8a)$$

$$f_{n,1} = -b_{n,1} \frac{m_1 J_n(\xi_1)J'_n(\eta_1) - J'_n(\xi_1)J_n(\eta_1)}{m_1 H_n(\xi_1)J'_n(\eta_1) - H'_n(\xi_1)J_n(\eta_1)}, \quad (8b)$$

$$c_{n,1} = e_{n,1} = 0. \quad (8c)$$

For the TM case (incident magnetic field parallel to the z axis),

$$c_{n,1} = a_{n,1} \frac{J_n(\xi_1)H'_n(\xi_1) - J'_n(\xi_1)H_n(\xi_1)}{m_1 J_n(\eta_1)H'_n(\xi_1) - m_1 J'_n(\eta_1)H_n(\xi_1)}, \quad (9a)$$

$$e_{n,1} = -a_{n,1} \frac{J_n(\xi_1)J'_n(\eta_1) - m_1 J'_n(\xi_1)J_n(\eta_1)}{H_n(\xi_1)J'_n(\eta_1) - m_1 H'_n(\xi_1)J_n(\eta_1)}, \quad (9b)$$

$$d_{n,1} = f_{n,1} = 0. \quad (9c)$$

C. The fluorescent medium

The absorption of light in the fluorescent medium is proportional to the magnitude of the electromagnetic field. We agree with the assumption of Chew, Cooke, and Kerker that the transmitted electric field within the cylinder induces a polarization within the medium oscillating at a shifted frequency, ω_2 ; i.e., the distribution of excited fluorescent molecules emitting a particular wavelength λ_2 is given as follows:

$$P(r, \phi, z, t) = \alpha E_{int,1}(r, \phi, z) e^{-i\omega_2 t}, \quad (10)$$

where α is an excitation characteristic of the fluorescent

medium (in the case of Raman scatter, α corresponds to a gain term). We consider the coherent field produced having the specific characteristic wavelength, angular frequency, permeability, and wave number in the incident medium, of λ_2 , ω_2 , μ_2 , and k_2 , respectively. The refractive index, wave number, and permeability of the cylinder at λ_2 are m_2 , k'_2 , and μ'_2 , respectively. We first expand the field oscillating at ω_2 into its components,

$$\mathbf{E}_{n,2} = \sum_{n'=-\infty}^{\infty} a_{n,2} \mathbf{M}_{n',\rho_1}^{(3)} + b_{n,2} \mathbf{N}_{n',\rho_1}^{(3)}, \quad (11a)$$

$$\mathbf{H}_{n,2} = \frac{-ik'_2}{\omega_2 \mu'_2} \sum_{n'=-\infty}^{\infty} a_{n,2} \mathbf{N}_{n',\rho_1}^{(3)} + b_{n,2} \mathbf{M}_{n',\rho_1}^{(3)}. \quad (11b)$$

In order for the fields to behave as expanding cylindrical waves, the functions of the fields created by fluorescence are of the form $u_{n,2} = H_n^{(1)}(\rho'_2) e^{i(n\phi + \omega_2 t)}$. The source of these fields is the electric polarization expressed in Eq. (10). The coefficients $a_{n,2}$ and $b_{n,2}$ can be solved for by expanding the electric polarization in terms of the vector harmonics of generating function $u_{n,2}$. Since the electric polarization is composed of vector harmonics of generating function $u_{n,int}$, we can start by expanding the internal electric field vector harmonics in terms of the electric field vector harmonics oscillating at ω_2 :

$$\mathbf{M}_{n',\rho_1}^{(1)} = \sum_{n''} A_{n'} \mathbf{M}_{n'',\rho_1}^{(3)} + B \mathbf{N}_{n'',\rho_1}^{(3)}, \quad (12a)$$

$$\mathbf{N}_{n',\rho_1}^{(1)} = \sum_{n''} C_{n'} \mathbf{M}_{n'',\rho_1}^{(3)} + D_{n'} \mathbf{N}_{n'',\rho_1}^{(3)}. \quad (12b)$$

As outlined in Stratton,¹² we first develop orthogonal relationships for the vector harmonics by introducing two new sets of vector harmonics:

$$(\mathbf{M}_{n',\rho_1}^{(1)})^* = (k_j^2 - h^2)^{1/2} \left[-in \frac{Z_n^{(i)}(\rho_j)}{\rho_j} \hat{\mathbf{e}}_r - Z_n^{(i)*}(\rho_j) \hat{\mathbf{e}}_r \right] e^{-i(n\phi + \omega_2 t)}, \quad (13a)$$

$$(\mathbf{N}_{n',\rho_1}^{(1)})^* = (k_j^2 - h^2)^{1/2} / k_j \left[-ih Z_n^{(i)*}(\rho_j) \hat{\mathbf{e}}_r - hn \frac{Z_n^{(i)}(\rho_j)}{\rho_j} \hat{\mathbf{e}}_r + (k_j^2 - h^2)^{1/2} Z_n^{(i)}(\rho_j) \hat{\mathbf{e}}_z \right] e^{-i(n\phi + \omega_2 t)}. \quad (13b)$$

The generating functions for these vectors are of the form $u_{n,2} = J_n(\rho'_2) e^{i(n\phi + \omega_2 t)}$. The orthogonal relationships are

$$\int_0^{2\pi} \mathbf{M}_{n',\rho_1}^{(1)} \cdot (\mathbf{M}_{n'',\rho_1}^{(1)})^* d\phi = \delta_{n,n'} \pi (k_1^2 - h_1^2)^{1/2} (k_2^2 - h_2^2)^{1/2} [J_{n-1}(\rho'_1)J_{n-1}(\rho'_2) + J_{n+1}(\rho'_1)J_{n+1}(\rho'_2)], \quad (14a)$$

$$\begin{aligned} \int_0^{2\pi} \mathbf{N}_{n',\rho_1}^{(1)} \cdot (\mathbf{N}_{n'',\rho_1}^{(1)})^* d\phi &= \delta_{n,n'} \frac{2\pi}{k_1' k_2'} (k_1^2 - h_1^2)^{1/2} (k_2^2 - h_2^2)^{1/2} \\ &\times \left[-\frac{h_1 h_2}{2} [J_{n-1}(\rho'_1)J_{n-1}(\rho'_2) + J_{n+1}(\rho'_1)J_{n+1}(\rho'_2)] \right. \\ &\left. + (k_1^2 - h_1^2)^{1/2} (k_2^2 - h_2^2)^{1/2} J_n(\rho'_1)J_n(\rho'_2) \right], \end{aligned} \quad (14b)$$

$$\begin{aligned} \int_0^{2\pi} \mathbf{M}_{n',\rho_1}^{(2)} \cdot (\mathbf{N}_{n'',\rho_1}^{(1)})^* d\phi &= \int_0^{2\pi} \mathbf{N}_{n',\rho_1}^{(2)} \cdot (\mathbf{M}_{n'',\rho_1}^{(1)})^* d\phi \\ &= \delta_{n,n'} \frac{\pi h_2}{k_2'} (k_2^2 - h_2^2) [J_{n-1}(\rho'_1)H_{n-1}(\rho'_2) - J_{n+1}(\rho'_1)H_{n+1}(\rho'_2)]. \end{aligned} \quad (14c)$$

By scalar multiplying (12a) and (12b) by $(\mathbf{M}_{n,\rho_2}^{(1)})^*$ and integrating both equations over the fluorescing cylinder, then repeating the process with $(\mathbf{N}_{n,\rho_2}^{(1)})^*$ we can solve for the following coefficients:

$$A_n = \delta_{h_2, h_1} \frac{\int_0^a \mathbf{M}_{n,\rho_1}^{(1)} \cdot (\mathbf{M}_{n,\rho_2}^{(1)})^* r dr \int_0^a \mathbf{N}_{n,\rho_2}^{(2)} \cdot (\mathbf{N}_{n,\rho_2}^{(1)})^* r dr - \int_0^a \mathbf{M}_{n,\rho_1}^{(1)} \cdot (\mathbf{N}_{n,\rho_2}^{(1)})^* r dr \int_0^a \mathbf{N}_{n,\rho_2}^{(2)} \cdot (\mathbf{M}_{n,\rho_2}^{(1)})^* r dr}{\int_0^a \mathbf{M}_{n,\rho_2}^{(2)} \cdot (\mathbf{M}_{n,\rho_2}^{(1)})^* r dr \int_0^a \mathbf{N}_{n,\rho_2}^{(1)} \cdot (\mathbf{N}_{n,\rho_2}^{(1)})^* r dr - \int_0^a \mathbf{N}_{n,\rho_2}^{(2)} \cdot (\mathbf{M}_{n,\rho_2}^{(1)})^* r dr \int_0^a \mathbf{M}_{n,\rho_2}^{(2)} \cdot (\mathbf{N}_{n,\rho_2}^{(1)})^* r dr}, \quad (15a)$$

$$B_n = \delta_{h_2, h_1} \frac{\int_0^a \mathbf{M}_{n,\rho_2}^{(2)} \cdot (\mathbf{M}_{n,\rho_2}^{(1)})^* r dr \int_0^a \mathbf{N}_{n,\rho_1}^{(1)} \cdot (\mathbf{N}_{n,\rho_2}^{(1)})^* r dr - \int_0^a \mathbf{M}_{n,\rho_1}^{(1)} \cdot (\mathbf{M}_{n,\rho_2}^{(1)})^* r dr \int_0^a \mathbf{M}_{n,\rho_2}^{(2)} \cdot (\mathbf{N}_{n,\rho_2}^{(1)})^* r dr}{\int_0^a \mathbf{M}_{n,\rho_2}^{(2)} \cdot (\mathbf{M}_{n,\rho_2}^{(1)})^* r dr \int_0^a \mathbf{N}_{n,\rho_2}^{(2)} \cdot (\mathbf{N}_{n,\rho_2}^{(1)})^* r dr - \int_0^a \mathbf{N}_{n,\rho_2}^{(2)} \cdot (\mathbf{M}_{n,\rho_2}^{(1)})^* r dr \int_0^a \mathbf{M}_{n,\rho_2}^{(2)} \cdot (\mathbf{N}_{n,\rho_2}^{(1)})^* r dr}, \quad (15b)$$

$$C_n = \delta_{h_2, h_1} \frac{\int_0^a \mathbf{N}_{n,\rho_1}^{(1)} \cdot (\mathbf{M}_{n,\rho_2}^{(1)})^* r dr \int_0^a \mathbf{N}_{n,\rho_2}^{(2)} \cdot (\mathbf{N}_{n,\rho_2}^{(1)})^* r dr - \int_0^a \mathbf{N}_{n,\rho_2}^{(2)} \cdot (\mathbf{M}_{n,\rho_2}^{(1)})^* r dr \int_0^a \mathbf{N}_{n,\rho_1}^{(1)} \cdot (\mathbf{N}_{n,\rho_2}^{(1)})^* r dr}{\int_0^a \mathbf{M}_{n,\rho_2}^{(2)} \cdot (\mathbf{M}_{n,\rho_2}^{(1)})^* r dr \int_0^a \mathbf{N}_{n,\rho_2}^{(2)} \cdot (\mathbf{N}_{n,\rho_2}^{(1)})^* r dr - \int_0^a \mathbf{N}_{n,\rho_2}^{(2)} \cdot (\mathbf{M}_{n,\rho_2}^{(1)})^* r dr \int_0^a \mathbf{M}_{n,\rho_2}^{(2)} \cdot (\mathbf{N}_{n,\rho_2}^{(1)})^* r dr}, \quad (15c)$$

$$D_n = \delta_{h_2, h_1} \frac{\int_0^a \mathbf{M}_{n,\rho_2}^{(2)} \cdot (\mathbf{M}_{n,\rho_2}^{(1)})^* r dr \int_0^a \mathbf{N}_{n,\rho_1}^{(1)} \cdot (\mathbf{N}_{n,\rho_2}^{(1)})^* r dr - \int_0^a \mathbf{N}_{n,\rho_1}^{(1)} \cdot (\mathbf{M}_{n,\rho_2}^{(1)})^* r dr \int_0^a \mathbf{M}_{n,\rho_2}^{(2)} \cdot (\mathbf{N}_{n,\rho_2}^{(1)})^* r dr}{\int_0^a \mathbf{M}_{n,\rho_2}^{(2)} \cdot (\mathbf{M}_{n,\rho_2}^{(1)})^* r dr \int_0^a \mathbf{N}_{n,\rho_2}^{(2)} \cdot (\mathbf{N}_{n,\rho_2}^{(1)})^* r dr - \int_0^a \mathbf{N}_{n,\rho_2}^{(2)} \cdot (\mathbf{M}_{n,\rho_2}^{(1)})^* r dr \int_0^a \mathbf{M}_{n,\rho_2}^{(2)} \cdot (\mathbf{N}_{n,\rho_2}^{(1)})^* r dr}. \quad (15d)$$

The result that $h_1 = h_2$ has some interesting consequences. For plane-wave illumination, the result $h_1 = h_2 = k_1 \cos \theta_0 = k_2 \cos \theta_2$ means that the scattered light of wavelength λ_2 will not travel along the path of the light of wavelength λ_1 unless the light is normally incident on the cylinder. As shown in Fig. 2, a cylinder illuminated by a plane wave scatters light elastically into a cone at angle θ_0 with respect to the z axis. The inelastically scattered light travels along a cone at angle θ_2 with respect to the z axis.

When $h_1 = 0$, which is the case of a plane wave at normal incidence, the coefficients are greatly reduced, since the orthogonality condition forces (14c) to zero:

$$A_n = \delta_{h_2, h_1} \frac{\int_0^a \mathbf{M}_{n,\rho_1}^{(1)} \cdot (\mathbf{M}_{n,\rho_2}^{(1)})^* r dr}{\int_0^a \mathbf{M}_{n,\rho_2}^{(2)} \cdot (\mathbf{M}_{n,\rho_2}^{(1)})^* r dr} = \frac{k'_1 \int_0^a [J_{n-1}(k'_1 r) J_{n-1}(k'_2 r) + J_{n+1}(k'_1 r) J_{n+1}(k'_2 r)] r dr}{k'_2 \int_0^a [H_{n-1}(k'_2 r) J_{n-1}(k'_2 r) + H_{n+1}(k'_2 r) J_{n+1}(k'_2 r)] r dr}, \quad (16a)$$

$$D_n = \delta_{h_2, h_1} \frac{\int_0^a \mathbf{N}_{n,\rho_1}^{(1)} \cdot (\mathbf{N}_{n,\rho_2}^{(1)})^* r dr}{\int_0^a \mathbf{N}_{n,\rho_2}^{(2)} \cdot (\mathbf{N}_{n,\rho_2}^{(1)})^* r dr} = \frac{k'_1 \int_0^a J_n(k'_1 r) J_n(k'_2 r) r dr}{k'_2 \int_0^a H_n(k'_2 r) J_n(k'_2 r) r dr}, \quad (16b)$$

$$B_n = C_n = 0. \quad (16c)$$

The integrals in Eqs. (16a) and (16b) are Lommel's integrals and have the following solutions:¹³

$$\int_0^a x J_n(k'_2 x) J_n(k'_1 x) dx = \frac{a}{(k'_1)^2 - (k'_2)^2} [k'_2 J'_n(k'_2 a) J_n(k'_1 a) - k'_1 J'_n(k'_1 a) J_n(k'_2 a)], \quad (17a)$$

$$\int_0^a x J_n(k'_2 x) H_n(k'_2 x) dx = \frac{1}{2} \left[a^2 J'_n(k'_1 a) H'_n(k'_2 a) - \left(a^2 - \frac{n^2}{k'_2^2} \right) H_n(k'_2 a) J_n(k'_1 a) - \frac{3i|n|}{\pi k'_2^2} \right]. \quad (17b)$$

The coefficients of the emitted electromagnetic fields may be written as

$$a_{n,2} = -\frac{\alpha}{\epsilon'_2} c_{n,1} A_n, \quad (18a)$$

$$b_{n,2} = -\frac{\alpha}{\epsilon'_2} d_{n,1} D_n, \quad (18b)$$

where ϵ'_2 is the cylinder permittivity at the emitted frequency. An induced field within the cylinder is needed to

satisfy the boundary conditions. This field corresponds to the field created by fluorescence reflecting off the inner surface of the cylinder. Using functions of the form $u_{n,1,ind,2} = J_n(\rho_2) e^{in\varphi} e^{ik_2 z}$, the induced field may be expressed as

$$\mathbf{E}_{ind,2} = \sum_{n=-\infty}^{\infty} c_{n,2} \mathbf{M}_{n,\rho_2}^{(1)} + d_{n,2} \mathbf{N}_{n,\rho_2}^{(1)}, \quad (19a)$$

$$\mathbf{H}_{ind,2} = \frac{-ik_2}{\omega_2 \mu_2} \sum_{n=-\infty}^{\infty} c_{n,2} \mathbf{N}_{n,\rho_2}^{(1)} + d_{n,2} \mathbf{M}_{n,\rho_2}^{(1)}. \quad (19b)$$

Finally, the scattered fields may be expressed as

$$\mathbf{E}_{sca,2} = \sum_{n=-\infty}^{\infty} e_{n,2} \mathbf{M}_{n,\rho_2}^{(3)} + f_{n,2} \mathbf{N}_{n,\rho_2}^{(3)}, \quad (20a)$$

$$\mathbf{H}_{sca,2} = \frac{-ik_2}{\omega_2 \mu_2} \sum_{n=-\infty}^{\infty} e_{n,2} \mathbf{N}_{n,\rho_2}^{(3)} + f_{n,2} \mathbf{M}_{n,\rho_2}^{(3)}. \quad (20b)$$

The generating functions of the scattered fields are of the form $u_{n,sca,2} = H_n^{(1)}(\rho_2) e^{in\varphi} e^{ik_2 z}$.

D. Boundary conditions at the wavelength of fluorescence

Setting $\mu_{r,2} = \mu'_2 / \mu_2$, $\xi_2 = x_2 \sin\theta_2$, $\eta_2 = x_2 (m_2^2 - \cos^2\theta_2)$, and $x_2 = k_2 a$, four boundary conditions on \mathbf{E} and \mathbf{H} must be satisfied:

$$a_{n,2} \eta_2 [H_n^{(1)}(\eta_2)]' + c_{n,2} \eta_2 J_n'(\eta_2) + b_{n,2} h_2 n / (m_2 k_2) H_n^{(1)}(\eta_2) + d_{n,2} h_2 n / (m_2 k_2) J_n(\eta_2)$$

$$= e_{n,2} \xi_2 [H_n^{(1)}(\xi_2)]' + f_{n,2} h_2 n H_n'(\xi_2) / k_2, \quad (21a)$$

$$b_{n,2} \eta_2^2 H_n^{(1)}(\eta_2) / m_2 + d_{n,2} \eta_2^2 J_n(\eta_2) / m_2 = f_{n,2} \xi_2^2 H_n^{(1)}(\xi_2), \quad (21b)$$

$$b_{n,2} m_2 \eta_2 [H_n^{(1)}(\eta_2)]' / \mu_{r,2} + d_{n,2} m_2 \eta_2 J_n'(\eta_2) / \mu_{r,2} + a_{n,2} h_2 n H_n^{(1)}(\eta_2) / (k_2 \mu_{r,2}) + c_{n,2} h_2 n J_n(\eta_2) / k_2 \mu_{r,2}$$

$$= f_{n,2} \xi_2 [H_n^{(1)}(\xi_2)]' + e_{n,2} h_2 n H_n^{(1)}(\xi_2) / k_2, \quad (21c)$$

$$a_{n,2} \eta_2^2 H_n^{(1)}(\eta_2) / \mu_{r,2} + c_{n,2} \eta_2^2 J_n(\eta_2) / \mu_{r,2} = e_{n,2} \xi_2^2 H_n^{(1)}(\xi_2). \quad (21d)$$

For the case of a normally incident plane wave ($\theta_0 = \pi/2$), many of the terms in Eqs. (21a)–(21d) are zero, and the scattering amplitude coefficients are simple expressions. For the TE case,

$$f_{n,2} = b_{n,2} \frac{m_2^2 J_n'(\eta_2) H_n(\eta_2) - m_2^2 J_n(\eta_2) H_n'(\eta_2)}{m_2 H_n(\xi_2) J_n'(\eta_2) - J_n(\eta_2) H_n'(\xi_2)}, \quad (22a)$$

$$e_{n,2} = 0. \quad (22b)$$

For the TM case,

$$e_{n,2} = a_{n,2} \frac{m_2^2 J_n'(\eta_2) H_n(\eta_2) - m_2^2 J_n(\eta_2) H_n'(\eta_2)}{H_n(\xi_2) J_n'(\eta_2) - m_2 J_n(\eta_2) H_n'(\xi_2)}, \quad (23a)$$

$$f_{n,2} = 0. \quad (23b)$$

It can be shown that the following relationship holds for these coefficients:

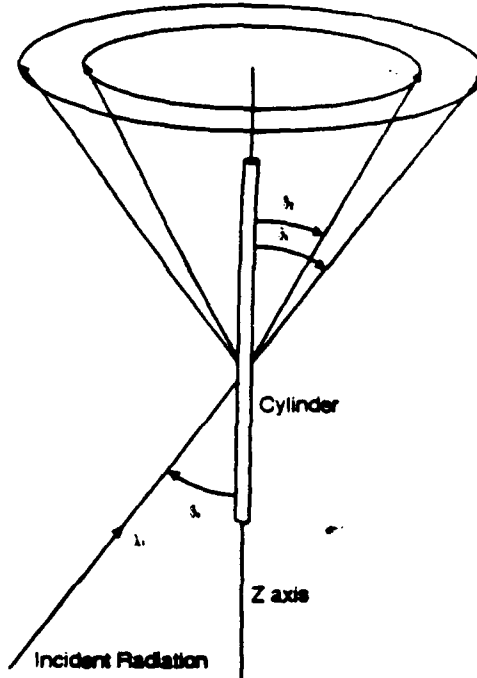


FIG. 2. The scattered radiation from a cylinder illuminated by a plane wave traveling in the x - z plane at an angle θ_0 with respect to the z axis. Elastically scattered light travels in a cone at angle θ_0 with respect to the z axis. Inelastically scattered light travels in a cone at angle θ_1 with respect to the z axis determined by $k_1 \cos\theta_0 = k_2 \cos\theta_1$.

$$e_{-n,2} = (-1)^n e_{n,2}, \quad (24a)$$

$$f_{-n,2} = (-1)^n f_{n,2}. \quad (24b)$$

With analytical expressions for these coefficients, the solution to the scattered field from a coherently fluorescing cylinder is complete. Analytical expressions may be derived for any illuminating radiation expressed by the coefficients $a_{n,1}$ and $b_{n,1}$ by solving the simultaneous equations (5a)–(5d) and (21a)–(21d).

For large arguments, the first-order Hankel function is given asymptotically by the following:

$$H_n^{(1)}(\rho) \sim \left[\frac{2}{\pi \rho} \right]^{1/2} e^{i\rho} (-i)^n e^{-i\pi/4}, \quad |\rho| \gg n^2. \quad (25)$$

At large distances from the cylinder ($k_1 r \sin\theta_1 \gg 1$), the scattered electric field may be expressed as follows:

$$E_{\text{exc},2} = \left[\frac{2(k_2^2 - h_2^2)}{\pi \rho_2} \right]^{1/2} e^{i(\rho_2 + h_2 z - \pi/4)} \sum_n e^{in\varphi} (-i)^n \left[-ie_{n,2} \hat{e}_\rho + \frac{h_2}{k_2} f_{n,2} \hat{e}_\rho + \frac{(k_2^2 - h_2^2)^{1/2}}{k_2} f_{n,2} \hat{e}_z \right]. \quad (26)$$

E. Scattered light for normally incident plane-wave illumination

We now look at the specific case of light scattered in the far field from a fluorescing cylinder illuminated by a normally incident plane wave. We examine the light in two separate polarization states: the TE state corresponds with light polarized along the vector \hat{e}_z , and the TM state corresponds with light polarized along the vector $-\hat{e}_\rho$. The amplitude scattering matrix is given in the far field by

$$\begin{bmatrix} E_{\text{TE,scs}} \\ E_{\text{TM,scs}} \end{bmatrix} = E_0 \left[\frac{2}{\pi k_2 r} \right]^{1/2} e^{i(k_2 r - \pi/4)} \times \begin{bmatrix} T_1 & T_4 \\ T_3 & T_2 \end{bmatrix} \begin{bmatrix} E_{\text{TE,inc}} \\ E_{\text{TM,inc}} \end{bmatrix}, \quad (27)$$

where

$$T_1 = \sum_{n=-\infty}^{\infty} \frac{k_2}{E_0} (-i)^n e^{in\varphi} f_{n,2} = \frac{k_2}{E_0} \left[f_{0,2} + 2 \sum_{n=1}^{\infty} (-i)^n f_{n,2} \cos(n\varphi) \right], \quad (28a)$$

$$T_2 = \sum_{n=-\infty}^{\infty} i \frac{k_2}{E_0} (-i)^n e^{in\varphi} e_{n,2} = i \frac{k_2}{E_0} \left[e_{0,2} + 2 \sum_{n=1}^{\infty} (-i)^n e_{n,2} \cos(n\varphi) \right], \quad (28b)$$

$$T_3 = T_4 = 0. \quad (28c)$$

The four independent, nonzero Mueller matrix elements may be expressed by

$$T_{11} = \frac{1}{2} (|T_1|^2 + |T_2|^2), \quad (29a)$$

$$T_{12} = \frac{1}{2} (|T_1|^2 - |T_2|^2)/T_{11}, \quad (29b)$$

$$T_{33} = \text{Re}(T_1 T_2^*)/T_{11}, \quad (29c)$$

$$T_{34} = \text{Im}(T_1 T_2^*)/T_{11}. \quad (29d)$$

III. RESULTS

The numerical results presented here are for plane-wave incident radiation with the waves traveling along the negative x axis. The detector plane is the x - y plane. The scattering angle $\theta = \pi - \varphi$, so that $\theta = 0^\circ$ is the forward-scattered light and $\theta = 180^\circ$ is the backscattered light. We study in detail a few specific, but arbitrary, cases. Since photons of wavelength λ_1 are absorbed to create photons of wavelength λ_2 , it is unrealistic to consider the cylinder to be composed of a dielectric medium. The imaginary part of the complex refractive index (which corresponds to the Einstein B coefficient) for the cylinders we calculated is set at the arbitrary value of $\text{Im}(m_1) = \text{Im}(m_2) = 0.001$.

The program used to calculate the inelastically scattered electromagnetic fields requires the calculation of the cylindrical Bessel and Hankel functions of complex arguments. Some of the subroutines used to calculate

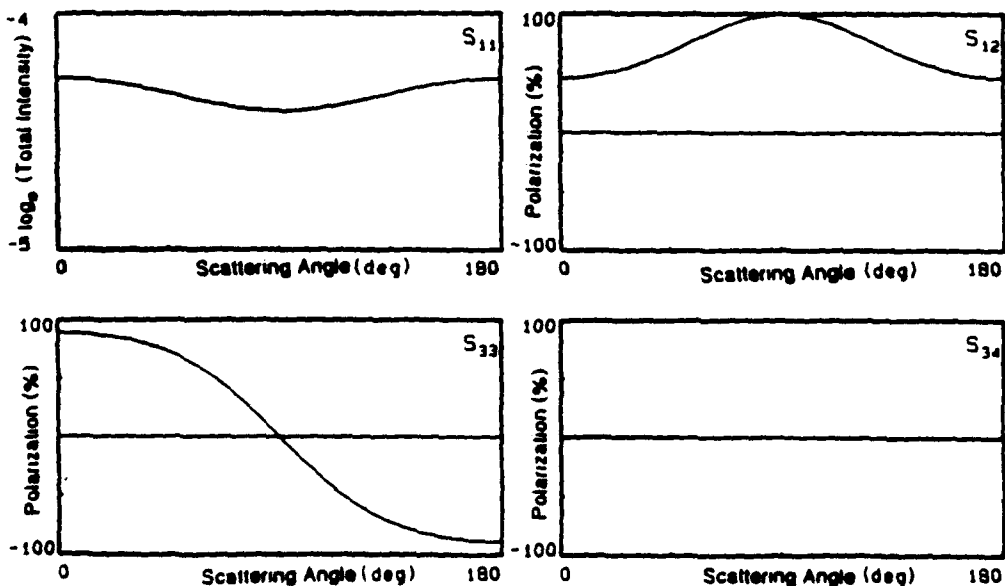


FIG. 3. The elastic Mueller scattering matrix for a small fiber: $a = 0.015\lambda$, $m = 1.50 + 0.001i$.

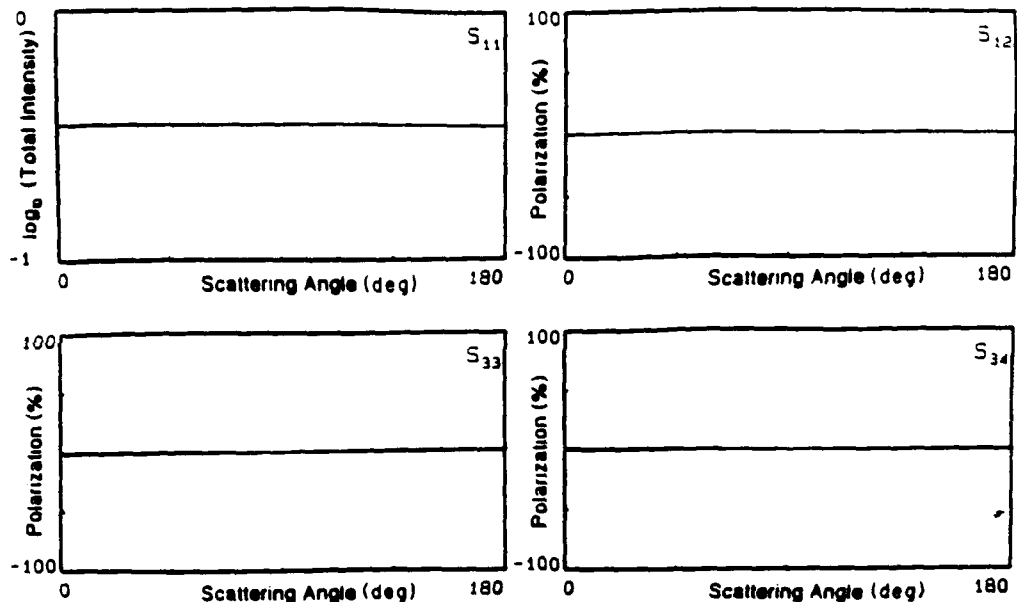


FIG. 4. The inelastic Mueller scattering matrix for a small fiber: $a = 0.015\lambda_1$, $\lambda_2 = 1.2\lambda_1$, $m_1 = m_2 = 1.50 + 0.001i$.

these functions are modifications of those provided in Ref. 14, and all of them were checked using relationships and values given in Ref. 15. Furthermore, the subroutines were first used to calculate the elastically scattered radiation, which was compared with the matrix elements calculated using the program listed in Ref. 11. This program was then modified to calculate the inelastically scattered radiation.

Calculations of the scattered electromagnetic fields are quite involved. The exact solution [Eqs. (20a) and (20b)] requires the summation of an infinite number of terms. Criteria for terminating the series are discussed in Ref. 11 for the elastically scattering case, but these criteria do not

necessarily apply for the inelastically scattering case. In most cases examined, these criteria were adequate.

A. A small cylinder

It is instructive to consider the scattering from a cylinder of small $k_1 a$ (one whose fields do not change appreciably throughout its cross section) since the number of cylindrical harmonics needed to describe the fields are greatly reduced. Figure 3 shows the elastic light-scattering Mueller matrix for an $a = 0.015\lambda$, $m = 1.50 + 0.001i$ cylinder. We note that the Mueller matrix of this small cylinder is only slightly different than

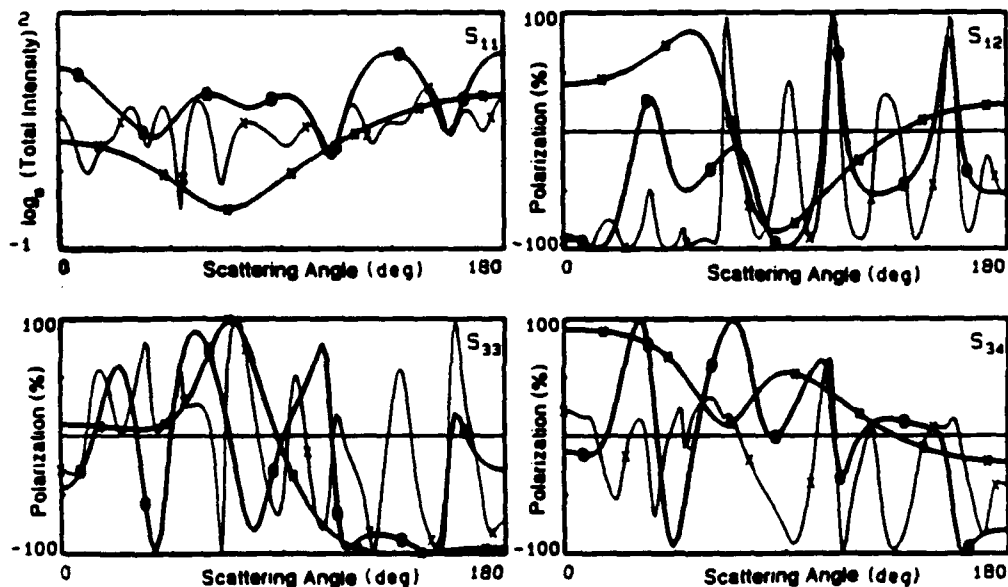


FIG. 5. The inelastic Mueller scattering matrix as a function of scattering angle for three $m_1 = m_2 = 1.5 + 0.001i$, $\lambda_1 = 1.0\lambda$, $\lambda_2 = 1.2\lambda_1$, $a = 0.3\lambda_1$ (*), $a = 1.0\lambda_1$ (○), and $a = 3.0\lambda_1$ (×). The wavelength $\lambda_2 = 1.2\lambda_1$.

nat of a small, Rayleigh particle. For a Rayleigh particle, matrix element S_{12} is zero at the end points, and element S_{33} starts at +100% and ends at -100% polarization. These elements are useful references of comparison for the inelastically scattered Mueller matrix elements.

A specific, but arbitrary, case of inelastic light scattered from a small fluorescing cylinder is shown in Fig. 4. For this case, $a=0.015\lambda_1$, $\lambda_2=1.2\lambda_1$, and $m_1=m_2=1.50+0.001i$. What is most apparent in this set of matrix elements is that they are almost constant, with the polarization matrix elements $S_{12}\approx 100\%$, $S_{33}\approx 0\%$, and $S_{34}\approx 0\%$. Matrix element S_{12} being nearly 100% means that nearly all the light is polarized parallel to the cylinder axis (TE). For the elastic scattering of Fig. 3, the light from this polarization is also constant as a function of scattering angle. If we were to examine just the TM-polarized light, we would see a dip in intensity near 90° similar to Rayleigh scattering (it is actually shifted toward the forward scatter slightly in the inelastic case), but the TE mode is so much more dominant in the inelastic case that we are unable to see any effects of the TM mode in the Mueller matrix of Fig. 4.

B. Cylinder size parameter

Figure 5 shows the light-scattering Mueller matrix of the $m_1=m_2=1.5+0.001i$ cylinder having three different radii: $a=0.3\lambda_1$, $a=1.0\lambda_1$, and $a=3.0\lambda_1$. The fluorescent wavelength is constant at $\lambda_2=1.2\lambda_1$. As the size of the cylinder increases, the frequency of oscillations in the matrix elements increases. This is similar to what occurs for elastic scattering. The most significant difference between the elastic and inelastic scattering matrix elements occurs in the total intensity: it does not necessarily reach the maximum value in the forward scatter ($\theta=0^\circ$). This

phenomenon is present in the scatter from all three cylinders of Fig. 5.

Of more interest, perhaps, are the absolute magnitudes of the total intensity of the fluorescent light. For elastic scattering, intensity increases as cylinder radius increases, but for coherent, inelastic scattering, the intensity does not increase, even though the size parameter has been increased by an order of magnitude. This is a result of the coupling that occurs between the wavelengths. As the cylinder radius approaches infinity, Eq. (17a) approaches zero, and A_n and D_n approach zero. This is analogous to taking the Fourier transform of a portion of a sine wave. For a very small portion (consider a δ function), all frequencies are represented approximately equally, but as the portion increases, we see more of the fundamental and less of the other frequencies, until only the fundamental frequency remains as the wave train extends to infinity.

C. Fluorescent wavelength

Another parameter which may be directly measured is the wavelength λ_2 , which is just one of the wavelengths in the fluorescent continuum. Figure 6 shows the light-scattering Mueller matrix of the $m_1=m_2=1.5+0.001i$, $a=\lambda_1$ cylinder emitting at three different wavelengths: $\lambda_2=1.2\lambda_1$, $\lambda_2=1.8\lambda_1$, and $\lambda_2=2.4\lambda_1$. It should be noted that the frequency of oscillations in the matrix elements decreases as the wavelength increases. This is similar to what occurs in elastic scattering. We compare these matrix elements with those of Fig. 7, for the same cylinder illuminated by a $\lambda_1=a/2$ plane wave. We note that the shapes of the matrix elements, that is, the position and amplitudes of the maxima or minima, are very similar to

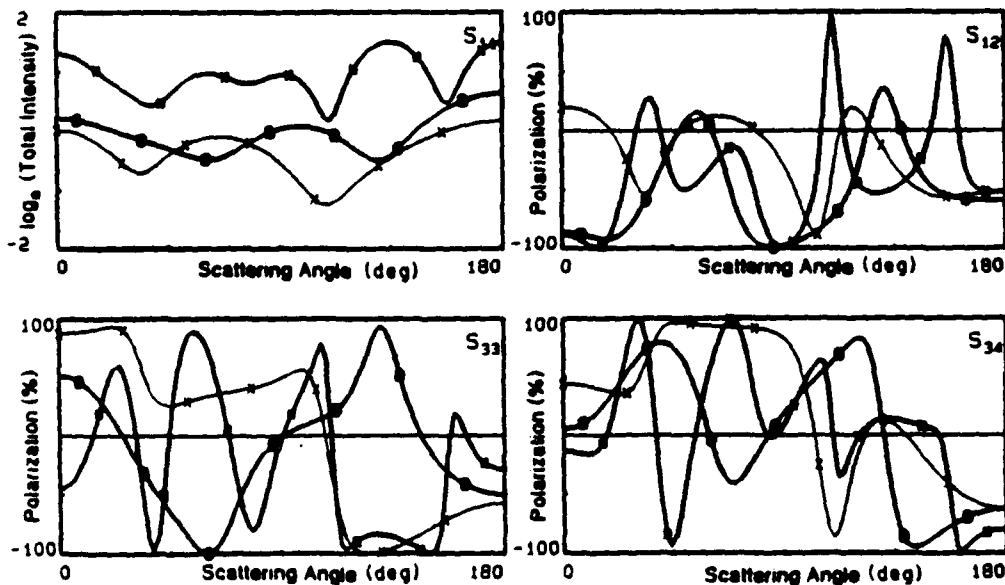


FIG. 6. The inelastic Mueller scattering matrix as a function of scattering angle from an $m_1=m_2=1.5+0.001i$, $a=\lambda_1$ radius fiber is measured at wavelength $\lambda_2=1.2\lambda_1$ (*), $\lambda_2=1.8\lambda_1$ (○), and $\lambda_2=2.4\lambda_1$ (×).

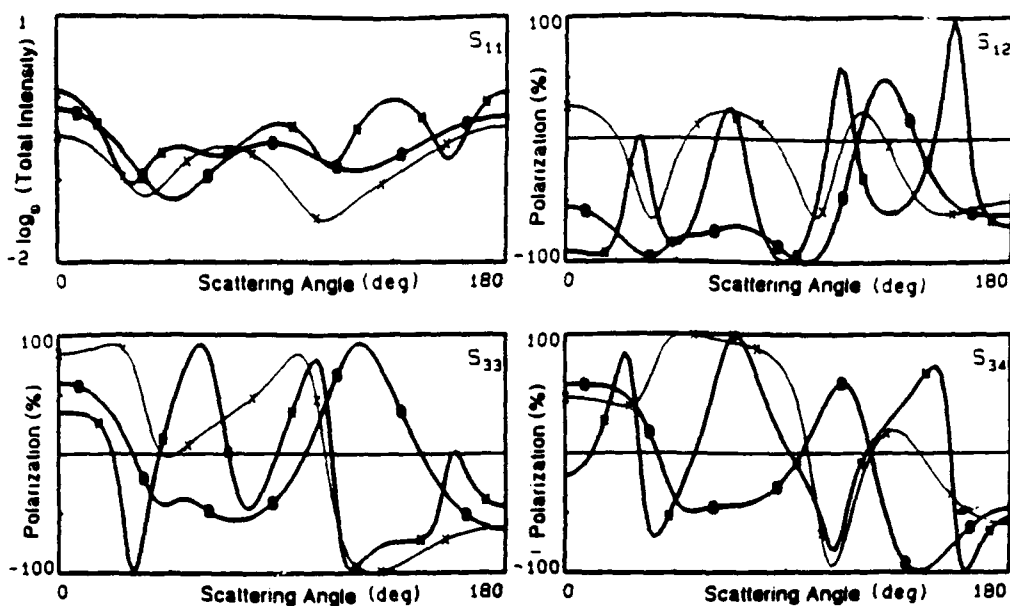


FIG. 7. The inelastic Mueller scattering matrix as a function of scattering angle from an $m_1 = m_2 = 1.5 + 0.001i$, $a = 2\lambda_1$ radius fiber is measured at wavelength $\lambda_2 = 1.2a$ (*), $\lambda_2 = 1.8a$ (○), and $\lambda_2 = 2.4a$ (X).

those of Fig. 6. From this we conclude that the shapes of the matrix elements are much more dependent on parameters other than the incident wavelength.

We can also study the scattered light as a function of the wavelength λ_2 by fixing the scattering angle and calculating the Mueller matrices as a function of wavelength λ_2 . Figure 8 shows the light-scattering Mueller matrix elements for an $m = 1.5 + 0.001i$, $a = \lambda_1$ cylinder as a function of λ_2 at three scattering angles: 0°, 90°, and 180°.

The horizontal axis is now a wavelength scale. The frequency of oscillations in these matrix elements is greatest when the difference between λ_1 and λ_2 is small. We compare these elements to those of Fig. 9 for the same cylinder system of Fig. 8 illuminated by $\lambda_1 = a/2$ light. The locations and amplitudes of maxima or minima in the matrix elements are very similar to those of Fig. 8 even though the frequency of the incident light has changed greatly.

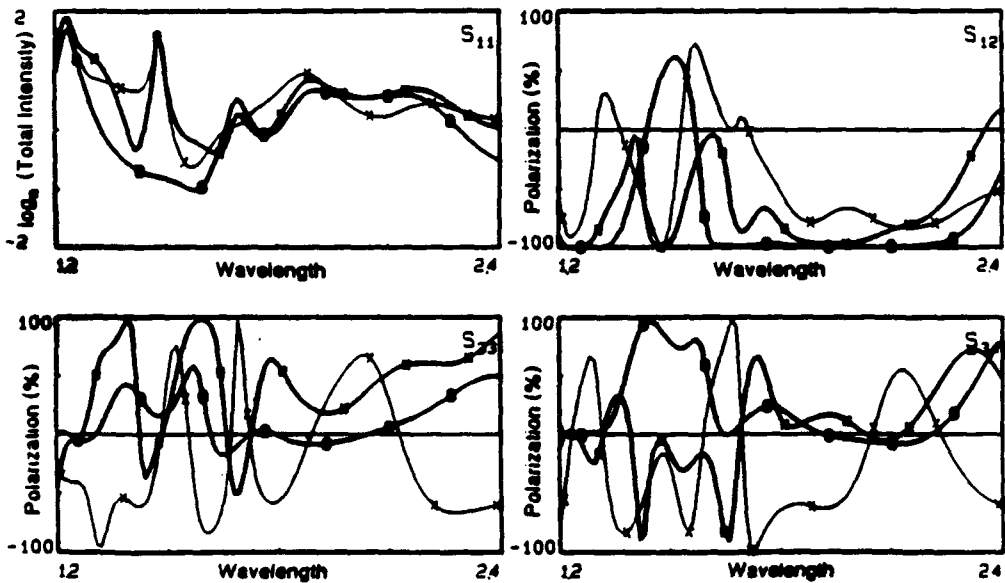


FIG. 8. The inelastic Mueller scattering matrix as a function of wavelength λ_2 . The light scattered from an $m_1 = m_2 = 1.5 + 0.001i$, $a = \lambda_1$ radius fiber is detected at angles $\theta = 0^\circ$ (*), $\theta = 90^\circ$ (○), and $\theta = 180^\circ$ (X) as wavelength increases from 1.2 to 2.4 times the fiber radius a .

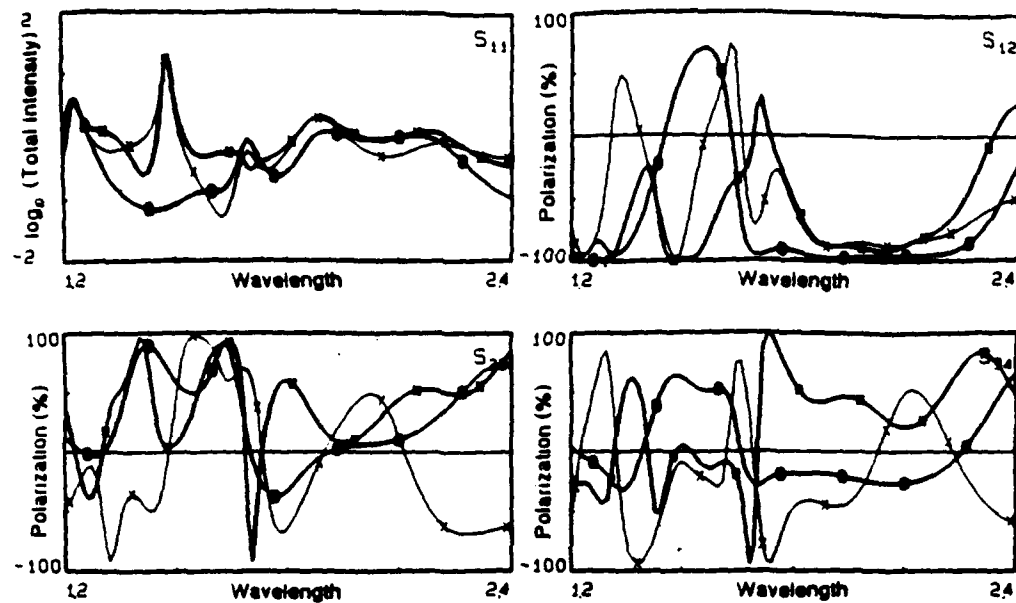


FIG. 9. The inelastic Mueller scattering matrix as a function of wavelength λ . The light scattered from an $m_1 = m_2 = 1.5 + 0.001i$, $a = 2\lambda_1$ radius fiber is detected at angles $\theta = 0^\circ$ (*), $\theta = 90^\circ$ (○), and $\theta = 180^\circ$ (X) as wavelength increases from 1.2 to 2.4 times the fiber radius a .

IV. CONCLUSION

These theoretical results demonstrate that the coherent, inelastically scattered light is a complicated function of many variables. In addition to the parameters involved in elastic scattering, we also have to take into account the wavelengths emitted and the wavelength-dependent optical properties of the fluorescing material. Direct experimental verification of these conclusions will need careful measurements of the low in-

tensity of radiation because the total intensity does not increase with cylinder radius as does the intensity of the elastically scattered light.

ACKNOWLEDGMENTS

This research was supported in part by the U.S. Air Force Office of Scientific Research (AFSC) and the Itek Corporation.

¹J. F. Owen, P. W. Barber, P. B. Dorain, and R. K. Chang, *Phys. Rev. Lett.* **47**, 1075 (1981).
²E. M. Sekerak, M.S. thesis, University of Arizona, 1989.
³D. Abramson, Ph.D. dissertation, University of Arizona, 1989.
⁴A. Biswas, H. Latifi, R. L. Armstrong, and R. G. Pinnick, *Opt. Lett.* **14**, 214 (1989).
⁵R. E. Benner, P. W. Barber, J. F. Owen, and R. K. Chang, *Phys. Rev. Lett.* **44**, 475 (1980).
⁶H. Chew, D. D. Cooke, and M. Kerker, *Appl. Opt.* **19**, 44 (1980).
⁷M. Kerker and S. D. Druger, *Appl. Opt.* **18**, 1172 (1979).
⁸P. Das and H. Metiu, *J. Chem. Phys.* **89**, 4680 (1985).
⁹S. C. Ching, H. M. Lai, and K. Young, *J. Opt. Soc. Am. B* **4**, 1995 (1987).
¹⁰Lord Rayleigh, *Philos. Mag.* **12**, 81 (1881).
¹¹C. Bohren and D. Huffman, *Absorption and Scattering of Light by Small Particles* (Wiley, New York, 1983).
¹²J. A. Stratton, *Electromagnetic Theory* (McGraw-Hill, New York, 1941).
¹³F. Bowman, *Introduction to Bessel Functions* (Dover, New York, 1958).
¹⁴W. H. Press, B. P. Flannery, S. A. Teukolsky, and W. T. Vetterling, *Numerical Recipes* (Cambridge University Press, Cambridge, 1989).
¹⁵*Handbook of Mathematical Functions*, edited by M. Abramowitz and I. Stegun (Dover, New York, 1972).

Coherent fluorescent emission and scattering from a uniform sphere

Gorden Videen, William S. Bickel, and Joseph M. Boyer

Physics Department, University of Arizona, Tucson, Arizona 85721

(Received 15 February 1991)

The coherent light inelastically scattered from an ideal fluorescent sphere illuminated by an electromagnetic wave is analyzed using an extension of Mie theory. Scattering coefficients are solved specifically for plane-wave illumination. The resulting inelastically scattered radiation is similar to that of elastically scattered radiation from a sphere. These results are illustrated by numerical calculations for several specific, but arbitrary, cases.

I. INTRODUCTION

Inelastically scattered light is subject to the morphology and optical properties of the particle that interacts with the incident electromagnetic radiation. Experimentally, fluorescent emission from uniform spherical particles was examined by Biswas *et al.* [1] and Benner *et al.* [2]. Theoretically, Raman and fluorescent emission by a molecule embedded in a dielectric sphere has been derived and examined [3-5]. For a uniform distribution of molecules within a sphere, the coherent process can be treated by adding the resulting amplitudes, molecule by molecule, over the cross section of the sphere. In another paper, we analyzed plane-wave illumination of a uniform fluorescent cylinder by examining the polarization induced at the new frequency within the cylinder [6]. This is the method used in this paper.

In this paper, we derive and examine the effects of coherent, inelastic scattering due to the geometry imposed by a uniform sphere composed of fluorescing material. The approach taken in this paper is an extension of Mie's solution to the elastically scattering light from a uniform sphere [7]. The derivation closely follows the derivation of Bohren and Huffman [8], and we represent the final scattered and radiated fields in terms of the Mueller matrix elements [9].

Inelastic scattering occurring in particles is a process that may be solved in three parts. First, the boundary conditions of the particle are used to determine the internal electromagnetic fields within the particle. Second, these internal fields are used to determine the fields produced by the fluorescing medium. And third, the boundary conditions of the particle are used to determine the inelastic fields emitted.

The fluorescence process outlined here is very similar to coherent Raman processes. For incoherent Raman processes, the internal fields are not intense enough to stimulate the individual molecules to emit as they are for coherent Raman processes, where more intense internal fields are generated, often by employing a second laser. Although our theory is limited as a model for Raman scatter because it incorporates only an incident field of one frequency, an extension of it to multifield interactions would follow the same basic procedure. However, we ex-

pect the main qualitative features of the scatter generated with this simplified model to remain unchanged.

Knowledge of the interaction of the incident electric fields and the fluorescing medium that produces the emitted fields is necessary to accurately determine the inelastically scattered radiation. We assume that the polarization within the fluorescing medium is proportional to the internal electric fields due to the incident electromagnetic field. We also assume all media are isotropic and homogeneous. With these assumptions, the derivation is straightforward.

II. THEORY

The starting point is to derive the internal fields within the uniform, fluorescing sphere having the same frequency of the incident radiation. This is done by applying the boundary conditions of the sphere on the electromagnetic field following the same procedure used to derive the scattered field.

A. The fields for the incident wavelength

Figure 1 shows the scattering geometry of the system. A sphere of radius a is centered on the origin. For wavelength λ_1 , the complex refractive index of the sphere is n_1 . The first step is to derive the internal electric fields of the sphere. The illuminating fields of the incident radia-

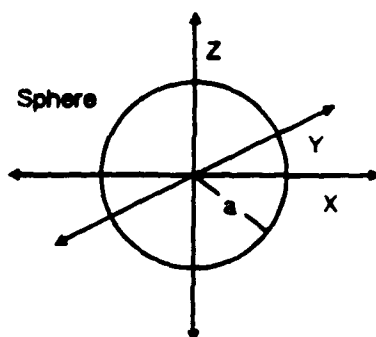


FIG. 1. The scattering geometry showing the fluorescing sphere of radius a centered on the origin.

may be expanded as follows (see, for instance, Ref.

$$\mathbf{E}_{\text{inc},1} = \sum_{n=0}^{\infty} \sum_{m=-n}^n a_{nm,1} \mathbf{M}_{nm,\rho_1}^{(1)} + b_{nm,1} \mathbf{N}_{nm,\rho_1}^{(1)} \quad (1a)$$

$$\mathbf{H}_{\text{inc},1} = \frac{k_1}{i\omega_1 \mu_1} \sum_{n=0}^{\infty} \sum_{m=-n}^n b_{nm,1} \mathbf{M}_{nm,\rho_1}^{(1)} + a_{nm,1} \mathbf{N}_{nm,\rho_1}^{(1)}, \quad (1b)$$

where $k_1 = 2\pi/\lambda_1$ is the wave number, ω_1 is the angular frequency, and μ_1 is the permeability of the incident medium at λ_1 . The vectors $\mathbf{M}_{nm,\rho_1}^{(1)}$ and $\mathbf{N}_{nm,\rho_1}^{(1)}$ are given

$$\begin{aligned} \mathbf{M}_{nm,\rho_1}^{(1)} &= \hat{\theta} \left[\frac{im}{\sin\theta} z_n^{(1)}(k_1 r) \bar{P}_n^{(m)}(\cos\theta) e^{im\phi} \right] \\ &\quad - \hat{\phi} \left[z_n^{(1)}(k_1 r) \frac{\partial}{\partial\theta} [\bar{P}_n^{(m)}(\cos\theta)] e^{im\phi} \right], \end{aligned} \quad (2a)$$

and

$$\begin{aligned} \mathbf{N}_{nm,\rho_1}^{(1)} &= \hat{r} \left[\frac{1}{k_1 r} z_n^{(1)}(k_1 r) n(n+1) \bar{P}_n^{(m)}(\cos\theta) e^{im\phi} \right] \\ &\quad + \hat{\theta} \left[\frac{1}{k_1 r} \frac{\partial}{\partial r} [r z_n^{(1)}(k_1 r)] \frac{\partial}{\partial\theta} [\bar{P}_n^{(m)}(\cos\theta)] e^{im\phi} \right] \\ &\quad + \hat{\phi} \left[\frac{1}{k_1 r} \frac{\partial}{\partial r} [r z_n^{(1)}(k_1 r)] \frac{im}{\sin\theta} \bar{P}_n^{(m)}(\cos\theta) e^{im\phi} \right]. \end{aligned} \quad (2b)$$

The superscript identifies the Bessel functions used to represent the fields. For example, $i=1$ corresponds with the use of the functions $z_n^{(1)}(\rho) = j_n(\rho)$, $i=2$ corresponds with the use of the functions $z_n^{(2)}(\rho) = y_n(\rho)$, and $i=3$ corresponds with the use of the functions $z_n^{(3)}(\rho) = h_n^{(1)}(\rho) = j_n(\rho) + iy_n(\rho)$. The functions $\bar{P}_n^{(m)}(\cos\theta)$ are the normalized associated Legendre polynomials defined by

$$\bar{P}_n^{(m)}(\cos\theta) = P_n^{(m)}(\cos\theta) \left(\frac{(2n+1)(n-m)!}{2(n+m)!} \right)^{1/2}. \quad (3)$$

The functions representing the incident radiation are of the form $u_{nm,\text{inc}} = j_n(k_1 r) \bar{P}_n^{(m)}(\cos\theta) e^{im\phi}$. The internal fields are also generated:

$$\mathbf{E}_{\text{int},1} = \sum_{n=0}^{\infty} \sum_{m=-n}^n c_{nm,1} \mathbf{M}_{nm,\rho_1}^{(1)} + d_{nm,1} \mathbf{N}_{nm,\rho_1}^{(1)}, \quad (4a)$$

and

$$c_{nm,1} = a_{nm,1} \frac{k_1 \mu_1 \psi_n(k_1 a) \xi_n(k_1 a) - k_1' \mu_1' \psi_n(k_1 a) \xi_n'(k_1 a)}{k_1' \mu_1' \psi_n(k_1 a) \xi_n(k_1 a) - k_1 \mu_1 \xi_n(k_1 a) \psi_n(k_1 a)},$$

$$\mathbf{H}_{\text{int},1} = \frac{k_1'}{i\omega_1 \mu_1'} \sum_{n=0}^{\infty} \sum_{m=-n}^n d_{nm,1} \mathbf{M}_{nm,\rho_1}^{(1)} + c_{nm,1} \mathbf{N}_{nm,\rho_1}^{(1)}, \quad (4b)$$

where $k_1' = k_1 n_1$ is the wave number inside the sphere medium for wavelength λ_1 , and μ_1' is the permeability of the sphere medium at wavelength λ_1 . The functions representing the internal fields are of the form $u_{nm,\text{int}} = j_n(k_1' r) \bar{P}_n^{(m)}(\cos\theta) e^{im\phi}$. The scattered fields are

$$\mathbf{E}_{\text{sca},1} = \sum_{n=0}^{\infty} \sum_{m=-n}^n e_{nm,1} \mathbf{M}_{nm,\rho_1}^{(3)} + f_{nm,1} \mathbf{N}_{nm,\rho_1}^{(3)}, \quad (5a)$$

and

$$\mathbf{H}_{\text{sca},1} = \frac{k_1}{i\omega_1 \mu_1} \sum_{n=0}^{\infty} \sum_{m=-n}^n f_{nm,1} \mathbf{M}_{nm,\rho_1}^{(3)} + e_{nm,1} \mathbf{N}_{nm,\rho_1}^{(3)}, \quad (5b)$$

The functions representing the scattered fields are of the form $u_{nm,\text{sca}} = h_n^{(1)}(k_1 r) \bar{P}_n^{(m)}(\cos\theta) e^{im\phi}$.

Four boundary conditions on \mathbf{E} and \mathbf{H} must be satisfied:

$$k_1 \psi_n(k_1 a) c_{nm,1} = k_1' \psi_n(k_1 a) a_{nm,1} + k_1' \xi_n(k_1 a) e_{nm,1}, \quad (6a)$$

$$\mu_1 \psi_n(k_1 a) c_{nm,1} = \mu_1' \psi_n(k_1 a) a_{nm,1} + \mu_1' \xi_n(k_1 a) e_{nm,1}, \quad (6b)$$

$$\mu_1 \psi_n(k_1 a) d_{nm,1} = \mu_1' \psi_n(k_1 a) b_{nm,1} + \mu_1' \xi_n(k_1 a) f_{nm,1}, \quad (6c)$$

and

$$k_1 \psi_n(k_1 a) d_{nm,1} = k_1' \psi_n(k_1 a) b_{nm,1} + k_1' \xi_n(k_1 a) f_{nm,1}. \quad (6d)$$

where

$$\psi_n(\rho) = \rho j_n(\rho) \quad \text{and} \quad \xi_n(\rho) = \rho h_n^{(1)}(\rho). \quad (7)$$

B. Plane-wave illumination

When the coefficients $a_{nm,1}$ and $b_{nm,1}$ are known, the other field components of Eq. (6) can be solved. For the case of plane-wave illumination along the positive z axis, polarized along the x axis, the coefficients can be derived as

$$a_{nm,1} = E_0 i^{n-1} \left(\frac{2n+1}{2n(n+1)} \right)^{1/2} (\delta_{m,-1} + \delta_{m,1}) \quad (8a)$$

and

$$b_{nm,1} = E_0 i^{n+1} \left(\frac{2n+1}{2n(n+1)} \right)^{1/2} (\delta_{m,-1} + \delta_{m,1}) \quad (8b)$$

The elastic-scattering coefficients and the internal field coefficients may be solved in terms of the coefficients of the incident field:

$$d_{nm,1} = b_{nm,1} \frac{k'_1 \mu'_1 \xi'_n(k_1 a) \psi_n(k_1 a) - k'_1 \mu'_1 \psi'_n(k_1 a) \xi_n(k_1 a)}{k'_1 \mu'_1 \xi'_n(k_1 a) \psi_n(k'_1 a) - k'_1 \mu'_1 \psi'_n(k'_1 a) \xi_n(k_1 a)}, \quad (9b)$$

$$e_{nm,1} = -a_{nm,1} \frac{k'_1 \mu'_1 \psi'_n(k'_1 a) \psi_n(k_1 a) - k'_1 \mu'_1 \psi'_n(k_1 a) \psi_n(k'_1 a)}{k'_1 \mu'_1 \psi'_n(k'_1 a) \xi_n(k_1 a) - k'_1 \mu'_1 \xi'_n(k_1 a) \psi_n(k'_1 a)}, \quad (9c)$$

and

$$f_{nm,1} = -b_{nm,1} \frac{k'_1 \mu'_1 \psi'_n(k'_1 a) \psi_n(k'_1 a) - k'_1 \mu'_1 \psi'_n(k'_1 a) \psi_n(k_1 a)}{k'_1 \mu'_1 \xi'_n(k_1 a) \psi_n(k'_1 a) - k'_1 \mu'_1 \psi'_n(k'_1 a) \xi_n(k_1 a)}. \quad (9d)$$

C. The fluorescent medium

The absorption of light in the fluorescent medium is proportional to the magnitude of the electromagnetic field. We agree with the assumption of Ref. [3], which states that the transmitted electric field within the sphere induces a polarization within the medium oscillating at a shifted frequency, ω_2 ; i.e., the distribution of excited fluorescent molecules emitting a particular wavelength λ_2 is given as follows:

$$P(r, \theta, \phi, t) = \alpha E_{int,1}(r, \theta, \phi) e^{-i\omega_2 t}, \quad (10)$$

where α is an excitation characteristic of the fluorescent medium (in the case of Raman scatter, α corresponds to a gain term). We consider the coherent field produced having the specific characteristic wavelength, angular frequency, permeability, and wave number in the incident medium of λ_2 , ω_2 , μ_2 , and k_2 , respectively. The refractive index, wave number, and permeability of the sphere at λ_2 are n_2 , k'_2 , and μ'_2 , respectively. We first expand the field oscillating at ω_2 into its components:

$$E_{fl,2} = \sum_{n=0}^{\infty} \sum_{m=-n}^n a_{nm,2} \mathbf{M}_{nm,\rho_2}^{(3)} + b_{nm,2} \mathbf{N}_{nm,\rho_2}^{(3)} \quad (11a)$$

and

$$\mathbf{H}_{fl,2} = \frac{k'_2}{i\omega_2 \mu'_2} \sum_{n=0}^{\infty} \sum_{m=-n}^n b_{nm,2} \mathbf{M}_{nm,\rho_2}^{(3)} + a_{nm,2} \mathbf{N}_{nm,\rho_2}^{(3)}. \quad (11b)$$

In order for the fields to behave as expanding spherical waves, the functions of the fields created by fluorescence are of the form $u_{nm,2} = h_n^{(1)}(k'_2 r) \tilde{P}_n^{(m)}(\cos\theta) e^{im\phi}$. The source of these fields is the electric polarization expressed in Eq. (10). The coefficients $a_{nm,2}$ and $b_{nm,2}$ can be determined by expanding the electric polarization in terms of the vector harmonics of generating function $u_{nm,2}$. Since the electric polarization is composed of vector harmonics of the generating function $u_{nm,int}$, we can start by expanding the internal electric-field vector harmonics in terms of the electric-field vector harmonics oscillating at ω_2 :

$$\mathbf{M}_{nm,\rho_1}^{(1)} = \sum_{n',m'} A_{n'm'} \mathbf{M}_{n'm',\rho_1}^{(3)} + B_{n'm'} \mathbf{N}_{n'm',\rho_1}^{(3)} \quad (12a)$$

and

$$\mathbf{N}_{nm,\rho_1}^{(1)} = \sum_{n',m'} C_{n'm'} \mathbf{M}_{n'm',\rho_1}^{(3)} + D_{n'm'} \mathbf{N}_{n'm',\rho_1}^{(3)}. \quad (12b)$$

The following orthogonal relationships exist for the vector harmonics [10]:

$$\int_0^{2\pi} \int_0^{\pi} \mathbf{M}_{nm,\rho_1}^{(1)} \cdot (\mathbf{M}_{n'm',\rho_2}^{(1)})^* \sin\theta d\theta d\phi = \delta_{m,m'} \delta_{n,n'} 2\pi n(n+1) z_n^{(i)}(\rho'_1) z_n^{(j)}(\rho'_2), \quad (13a)$$

$$\int_0^{2\pi} \int_0^{\pi} \mathbf{N}_{nm,\rho_1}^{(1)} \cdot (\mathbf{N}_{n'm',\rho_2}^{(1)})^* \sin\theta d\theta d\phi = \delta_{m,m'} \delta_{n,n'} 2\pi n(n+1) \left[\frac{z_n^{(i)}(\rho'_1) z_n^{(j)}(\rho'_2) n(n+1)}{\rho'_1 \rho'_2} + \frac{[\rho'_1 z_n^{(i)}(\rho'_1)]' [\rho'_2 z_n^{(j)}(\rho'_2)]'}{\rho'_1 \rho'_2} \right]. \quad (13b)$$

and

$$\int_0^{2\pi} \int_0^{\pi} \mathbf{M}_{nm,\rho_2}^{(1)} \cdot (\mathbf{N}_{n'm',\rho_2}^{(1)})^* \sin\theta d\theta d\phi = \int_0^{2\pi} \int_0^{\pi} \mathbf{N}_{nm,\rho_2}^{(1)} \cdot (\mathbf{M}_{n'm',\rho_2}^{(1)})^* \sin\theta d\theta d\phi = 0. \quad (13c)$$

By scalar multiplying (12a) and (12b) by $(\mathbf{M}_{nm,\rho_2}^{(1)})^*$ and integrating both equations over the fluorescing sphere, then repeating the process with $(\mathbf{N}_{nm,\rho_2}^{(1)})^*$, we can solve for the following coefficients:

$$A_{nm} = \frac{\int_{sph} \mathbf{M}_{nm,\rho_1}^{(1)} \cdot (\mathbf{M}_{nm,\rho_2}^{(1)})^* d\tau}{\int_{sph} \mathbf{M}_{nm,\rho_2}^{(1)} \cdot (\mathbf{M}_{nm,\rho_2}^{(1)})^* d\tau} = \frac{\int_0^a j_n(k'_1 r) j_n(k'_2 r) r^2 dr}{\int_0^a h_n^{(1)}(k'_2 r) j_n(k'_2 r) r^2 dr}, \quad (14a)$$

$$D_{nm} = \frac{\int_{\text{sph}} \mathbf{N}_{nm,\rho_1}^{(1)} \cdot (\mathbf{N}_{nm,\rho_2}^{(1)})^* d\tau}{\int_{\text{sph}} \mathbf{N}_{nm,\rho_2}^{(3)} \cdot (\mathbf{N}_{nm,\rho_1}^{(1)})^* d\tau} = \frac{\int_0^a [(n+1)j_{n-1}(k'_1 r)j_{n-1}(k'_2 r) + nj_{n+1}(k'_1 r)j_{n+1}(k'_2 r)]r^2 dr}{\int_0^a [(n+1)h_{n-1}^{(1)}(k'_1 r)j_{n-1}(k'_2 r) + nh_{n+1}^{(1)}(k'_1 r)j_{n+1}(k'_2 r)]r^2 dr}, \quad (14b)$$

$$B_n = C_n = 0. \quad (14c)$$

The integrals in equations (14a) and (14b) are Lommel's integrals and have the following solutions [11]:

$$\int_0^a j_n(k'_1 r)j_n(k'_2 r)r^2 dr = \frac{a^2}{(k'_1)^2 - (k'_2)^2} [k'_2 j_n(k'_2 a)j_n(k'_1 a) - k'_1 j_n(k'_1 a)j_n(k'_2 a)] \quad (15a)$$

and

$$\begin{aligned} \int_0^a j_n(k'_1 r)h_n(k'_2 r)r^2 dr = & \frac{a}{2(k'_2)^2} \{ (k'_2)^2 a^2 j_n(k'_2 a)h_n(k'_2 a) + k'_2 a j_n(k'_2 a)h'_n(k'_2 a) \\ & + [(k'_2)^2 a^2 - n(n+1)]j_n(k'_2 a)h_n(k'_2 a) \} - \frac{i(n+1)}{2(k'_2)^3}. \end{aligned} \quad (15b)$$

The coefficients of the emitted electromagnetic fields may be written as

$$a_{nm,2} = -\frac{a}{\epsilon'_2} c_{nm,1} \mathbf{A}_{nm} \quad (16a)$$

and

$$b_{nm,2} = -\frac{a}{\epsilon'_2} d_{nm,1} \mathbf{D}_{nm}, \quad (16b)$$

where ϵ'_2 is the cylinder permittivity at the emitted frequency. An induced field within the sphere is needed to satisfy the boundary conditions. This field corresponds to the field created by fluorescence reflecting off the linear surface of the sphere. Using functions of the form $u_{nm,\text{ind.}} = j_n(k'_2 r)P_n^{(1)}(\cos\theta)e^{im\phi}$, the induced field may be expressed as

$$\mathbf{E}_{\text{ind.2}} = \sum_{n=0}^{\infty} \sum_{m=-n}^n c_{nm,2} \mathbf{M}_{nm,\rho_2}^{(1)} + d_{nm,2} \mathbf{N}_{nm,\rho_2}^{(1)} \quad (17a)$$

and

$$\mathbf{H}_{\text{ind.2}} = \frac{k'_2}{i\omega_2 \mu'_2} \sum_{n=0}^{\infty} \sum_{m=-n}^n d_{nm,2} \mathbf{M}_{nm,\rho_2}^{(1)} + c_{nm,2} \mathbf{N}_{nm,\rho_2}^{(1)}. \quad (17b)$$

Finally, the scattered fields may be expressed as

$$\mathbf{E}_{\text{sca.2}} = \sum_{n=0}^{\infty} \sum_{m=-n}^n e_{nm,2} \mathbf{M}_{nm,\rho_2}^{(3)} + f_{nm,2} \mathbf{N}_{nm,\rho_2}^{(3)} \quad (18a)$$

$$e_{nm,2} = \frac{k_2 \mu_2 \psi_n(k'_2 a) \xi'_n(k'_2 a) - k_2 \mu_2 \psi'_n(k'_2 a) \xi_n(k'_2 a)}{k_2 \mu'_2 \psi_n(k'_2 a) \xi'_n(k'_2 a) - k'_2 \mu_2 \psi'_n(k'_2 a) \xi_n(k'_2 a)} \quad (20a)$$

and

$$f_{nm,2} = \frac{k_2 \mu_2 \psi_n(k'_2 a) \xi'_n(k'_2 a) - k_2 \mu_2 \psi'_n(k'_2 a) \xi_n(k'_2 a)}{k'_2 \mu_2 \psi_n(k'_2 a) \xi'_n(k'_2 a) - k_2 \mu'_2 \psi'_n(k'_2 a) \xi_n(k'_2 a)} \quad (20b)$$

and

$$\mathbf{H}_{\text{sca.2}} = \frac{k}{i\omega_2 \mu_2} \sum_{n=0}^{\infty} \sum_{m=-n}^n f_{nm,2} \mathbf{M}_{nm,\rho_2}^{(3)} + e_{nm,2} \mathbf{N}_{nm,\rho_2}^{(3)}. \quad (18b)$$

The generating functions of the scattered fields are of the form $u_{nm,\text{sca.2}} = h_n^{(1)}(k'_2 r)P_n^{(m)}(\cos\theta)e^{im\phi}$.

D. Boundary conditions at the wavelength of fluorescence

Four boundary conditions on \mathbf{E} and \mathbf{H} must be satisfied:

$$k_2 \psi_n(k'_2 a) c_{nm,2} + k_2 \xi_n(k'_2 a) a_{nm,2} = k'_2 \xi'_n(k'_2 a) e_{nm,2}, \quad (19a)$$

$$\mu_2 \psi'_n(k'_2 a) c_{nm,2} + \mu_2 \xi'_n(k'_2 a) a_{nm,2} = \mu'_2 \xi'_n(k'_2 a) e_{nm,2}. \quad (19b)$$

$$\mu_2 \psi_n(k'_2 a) d_{nm,2} + \mu_2 \xi_n(k'_2 a) b_{nm,2} = \mu'_2 \xi'_n(k'_2 a) f_{nm,2}. \quad (19c)$$

and

$$k_2 \psi'_n(k'_2 a) d_{nm,2} + k_2 \xi'_n(k'_2 a) b_{nm,2} = k'_2 \xi'_n(k'_2 a) f_{nm,2}. \quad (19d)$$

The scattering amplitude coefficients are

With analytical expressions for these coefficients, the solution to the scattered field from a coherently fluorescing sphere is complete.

E. Scattered light for plane-wave illumination

We now look at the specific case of light scattered into the far field by a fluorescing sphere illuminated by a plane wave. For large arguments, the first-order Hankel function is given asymptotically by the following:

$$h_n^{(1)}(\rho) \sim \frac{(-i)^n e^{i\rho}}{i\rho}, \quad |\rho| \gg 1. \quad (21)$$

We examine the light in two separate polarization states: the TE state corresponds with light polarized perpendicular to the scattering plane and the TM state corresponds with light polarized parallel to the scattering plane. The amplitude scattering matrix is given in the far field by

$$\begin{bmatrix} E_{TE, sca} \\ E_{TM, sca} \end{bmatrix} \sim \frac{e^{ik_2 r}}{-ik_2 r} \begin{bmatrix} S_1 & S_4 \\ S_3 & S_2 \end{bmatrix} \begin{bmatrix} E_{TE, inc} \\ E_{TM, inc} \end{bmatrix}, \quad (22)$$

where

$$S_1 = \sum_{n=1}^{\infty} -2i(-i)^n \left[\frac{\tilde{P}_n^1}{\sin\theta} f_{n1,2} + \frac{\partial}{\partial\theta} \tilde{P}_n^1(\cos\theta) e_{n1,2} \right], \quad (23a)$$

$$S_2 = \sum_{n=1}^{\infty} -2i(-i)^n \left[\frac{\tilde{P}_n^1}{\sin\theta} e_{n1,2} + \frac{\partial}{\partial\theta} \tilde{P}_n^1(\cos\theta) f_{n1,2} \right], \quad (23b)$$

and

$$S_3 = S_4 = 0. \quad (23c)$$

The four independent, nonzero Mueller matrix elements may be expressed by

$$S_{11} = \frac{1}{2}(|S_1|^2 + |S_2|^2), \quad (24a)$$

$$S_{12} = \frac{1}{2}(|S_2|^2 - |S_1|^2)/S_{11}, \quad (24b)$$

$$S_{33} = \text{Re}(S_1 S_2^*)/S_{11}, \quad (24c)$$

and

$$S_{34} = \text{Im}(S_2 S_1^*)/S_{11}. \quad (24d)$$

III. RESULTS

The numerical results presented here are for plane-wave incident radiation. We study in detail a few specific, but arbitrary, cases. Since photons of wavelength λ_1 are absorbed to create photons of wavelength λ_2 , it is unrealistic to consider the sphere to be composed of a dielectric medium. The imaginary part of the complex refractive index (which corresponds to the Einstein B coefficient) for the spheres is set at the arbitrary value of $\text{Im}(n_1) = \text{Im}(n_2) = 0.001$.

A. A small sphere

It is instructive to consider the scattering from a sphere of small $k_1 a$ (one whose fields do not change appreciably throughout its cross section) since the number of spherical harmonics needed to describe the fields is greatly reduced. Figure 2 shows the elastic light-scattering Mueller matrix for a sphere of $a = 0.001\lambda$, $n = 1.50 + 0.001i$. For such a small sphere (a Rayleigh particle), matrix element S_{11} is proportional to $1 + \cos^2\theta$, matrix element S_{12} is equal to $-\sin^2\theta/(1 + \cos^2\theta)$, element S_{33} is equal to

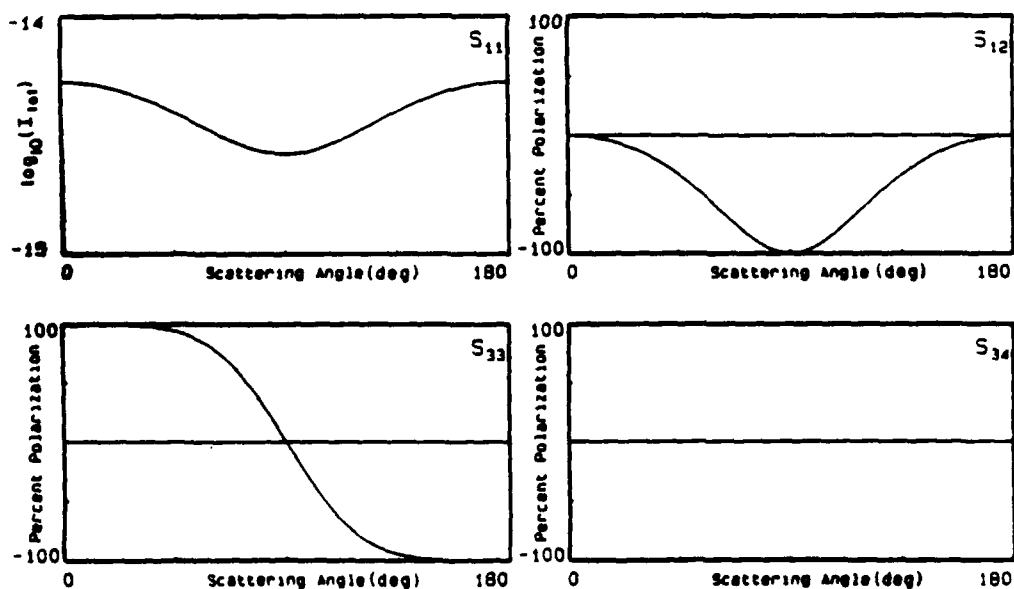


FIG. 2. The elastic Mueller scattering matrix for a small sphere: $a = 0.001\lambda$, $n = 1.50 + 0.001i$. I_{tot} represents total intensity

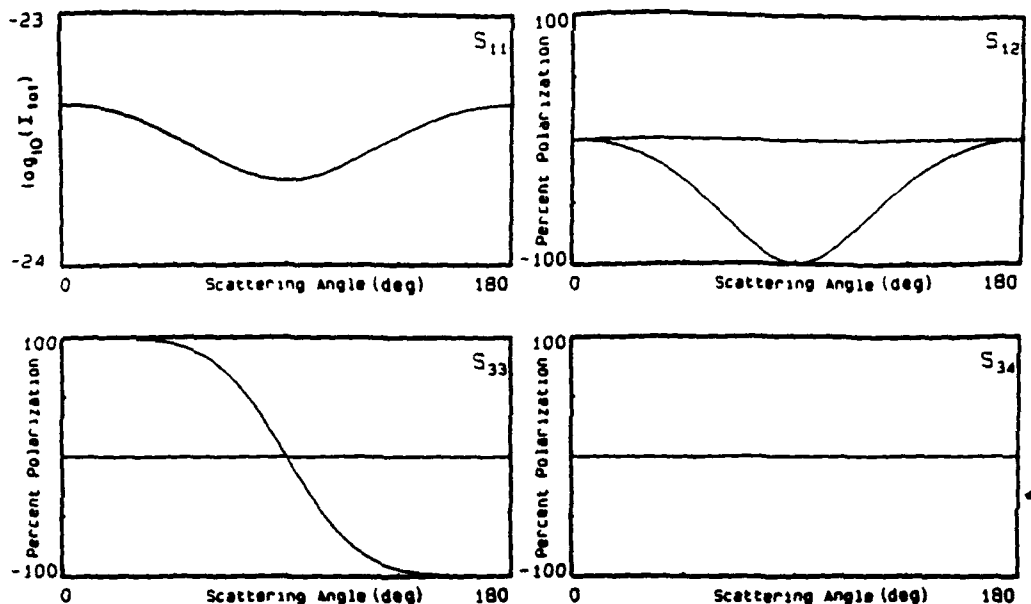


FIG. 3. The inelastic Mueller scattering matrix for a small sphere: $a = 0.001\lambda_1$, $\lambda_2 = 1.2\lambda_1$, $n_1 = n_2 = 1.50 + 0.001i$. I_{tot} represents total intensity.

$2\cos\theta/(1+\cos^2\theta)$, and element S_{34} is zero everywhere. These elements are useful references of comparison for the inelastically scattered Mueller matrix elements.

A specific, but arbitrary, case of inelastic light scattered from a small fluorescing sphere is shown in Fig. 3. For this case, $a = 0.001\lambda_1$, $\lambda_2 = 1.2\lambda_1$, and $n_1 = n_2 = 1.50 + 0.001i$. The shapes of the matrix elements of Fig. 3 are identical to the shapes of the matrix elements for the small, inelastic sphere of Fig. 2. The

only difference between these two sets of curves is the magnitude of matrix element S_{11} (note the total scattering has decreased by nine orders of magnitude).

B. Sphere-size parameter

Figure 4 shows the light-scattering Mueller matrix of three different $n_1 = n_2 = 1.5 + 0.001i$ spheres having radii $a = 0.3\lambda_1$, $1.0\lambda_1$, and $3.0\lambda_1$. The fluorescent wavelength

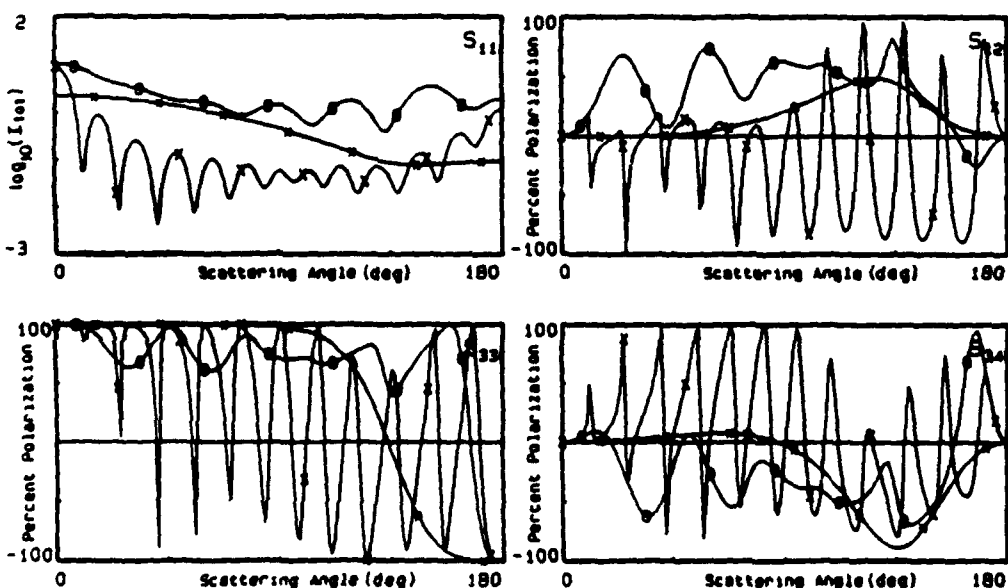


FIG. 4. The inelastic Mueller scattering matrix as a function of sphere radius. Curves are shown for three $n_1 = n_2 = 1.5 + 0.001i$ sphere radii: $a = 0.3\lambda_1$ (\bullet — \bullet), $a = 1.0\lambda_1$ (\circ — \circ), and $a = 3.0\lambda_1$ (\times — \times). The wavelength $\lambda_2 = 1.2\lambda_1$. I_{tot} represents total intensity.

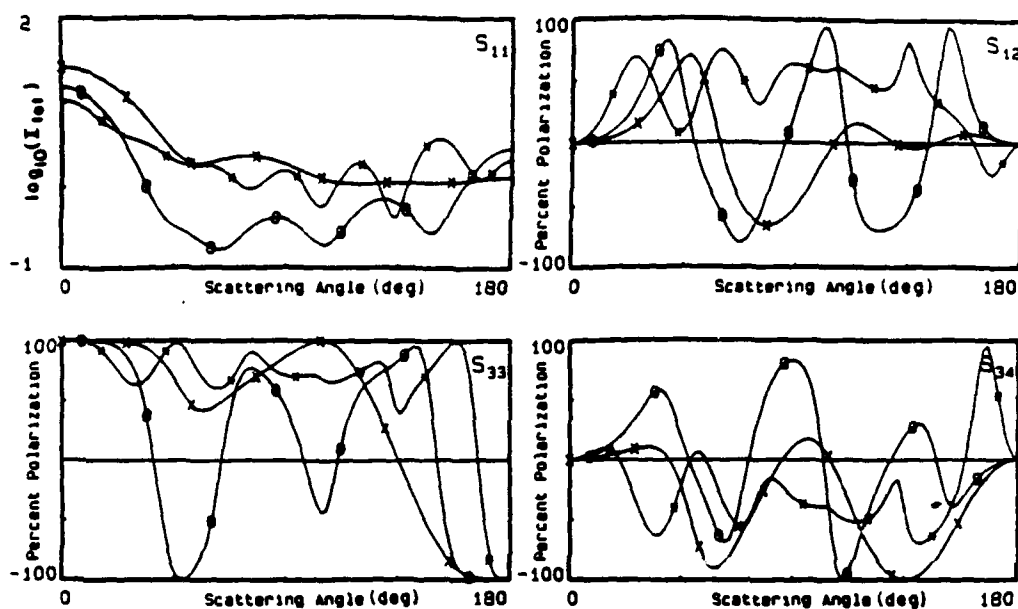


FIG. 5. The inelastic Mueller scattering matrix as a function of wavelength λ_2 . The light scattered from an $n_1 = n_2 = 1.5 + 0.001i$, $a = \lambda_1$ radius sphere is measured at wavelength $\lambda_2 = 1.2\lambda_1$ (\ast — \ast), $\lambda_2 = 1.8\lambda_1$ (\circ — \circ), and $\lambda_2 = 2.4\lambda_1$ (\times — \times). I_{tot} represents the total intensity.

is set at $\lambda_2 = 1.2\lambda_1$. As the size of the sphere increases, the frequency of oscillations in the matrix elements increases. This is similar to what occurs for elastic scattering. One major difference between the elastic and inelastic cases is illustrated in matrix element S_{11} . For elastic scattering, the total intensity of the scattered radiation increases significantly as the sphere radius increases. Such an increase does not necessarily occur for the case for coherent, inelastic scattering. Figure 4 shows that as the sphere radius is increased from $0.3\lambda_1$ to $1.0\lambda_1$, the total intensity has increased at all scattering angles, but as

the sphere radius is increased from $1.0\lambda_1$ to $3.0\lambda_1$, the total intensity has decreased at all scattering angles.

C. Fluorescent wavelength

Another parameter that may be directly measured is the wavelength λ_2 , which is a single wavelength selected from the fluorescent continuum. Figure 5 shows the light-scattering Mueller matrix of the $n_1 = n_2 = 1.5 + 0.001i$, $a = \lambda_1$ sphere emitting at three different wavelengths: $\lambda_2 = 1.2\lambda_1$, $\lambda_2 = 1.8\lambda_1$, and

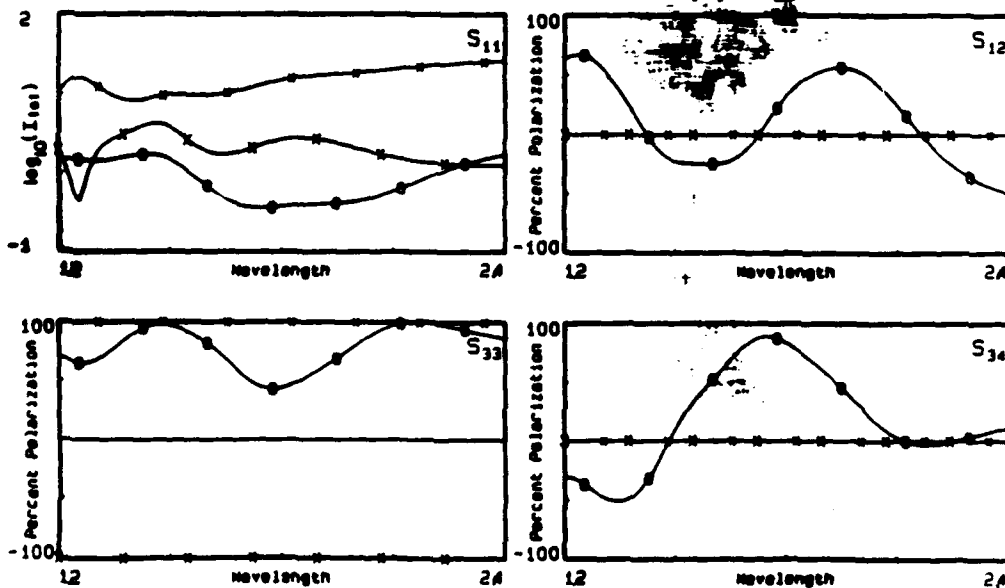


FIG. 6. The inelastic Mueller scattering matrix as a function of wavelength λ_2 . The light scattered from an $n_1 = n_2 = 1.5 + 0.001i$, $a = \lambda_1$ radius sphere is detected at angles $\theta = 0^\circ$ (\ast — \ast), $\theta = 90^\circ$ (\circ — \circ), and $\theta = 180^\circ$ (\times — \times) as wavelength λ_2 increases from 1.2 to 2.4 times the sphere radius a .

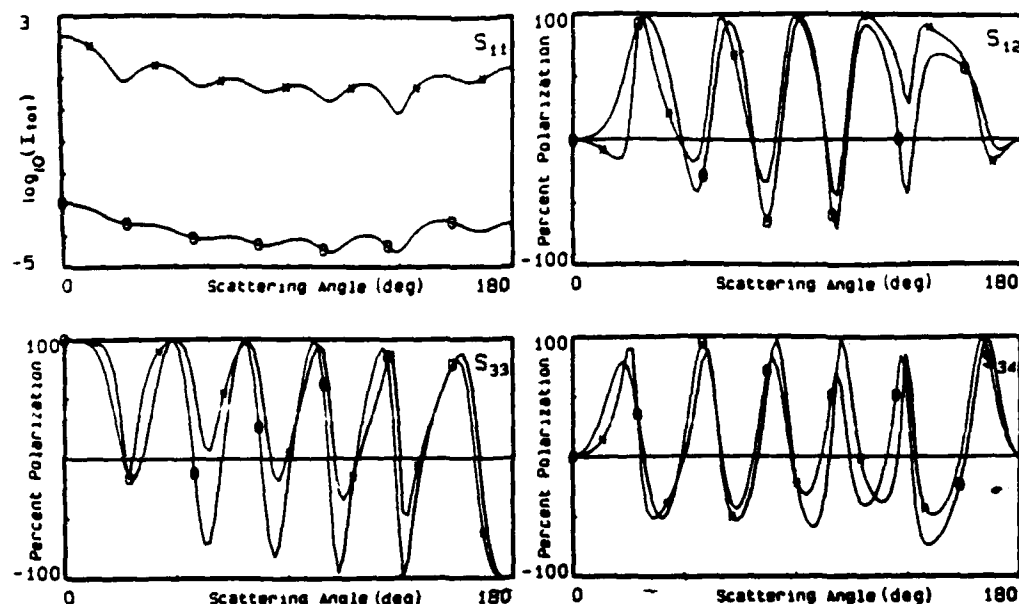


FIG. 7. The Mueller matrix for elastically (\bullet — \bullet) and inelastically (\circ — \circ) scattered light from an $n_1 = n_2 = 1.5 + 0.001i$, $a = \lambda_1$, radius sphere. The inelastically scattered light is detected at $\lambda_2 = 1.001\lambda_1$. I_{tot} represents the total intensity.

$\lambda_2 = 2.4\lambda_1$. It should be noted that the frequency of oscillations in the matrix elements decreases as the wavelength increases. This is similar to what occurs in elastic scattering.

We can also study the scattered light as a function of the wavelength λ_2 by fixing the scattering angle and calculating the Mueller matrices as a function of wavelength λ_2 . Figure 6 shows the light-scattering Mueller matrix elements for an $n_1 = n_2 = 1.5 + 0.001i$, $a = \lambda_1$ sphere as a function of λ_2 at three scattering angles: 0° , 90° , and 180° . The horizontal axis is now a wavelength scale varying from 1.2 to 2.4 times the sphere radius. Some features occur in these curves that occur in elastic scattering. Matrix elements S_{12} and S_{34} are zero at 0° and 180° , while matrix element S_{33} is 100% at 0° and -100% at 180° .

IV. CONCLUSIONS

To conclude, we show how the elastically scattered radiation differs from the inelastically scattered radiation. Figure 7 compares the Mueller matrix for elastically and inelastically scattered light from an $n_1 = n_2 = 1.5 + 0.001i$, $a = \lambda_1$, radius sphere. The inelastically scattered light is detected at $\lambda_2 = 1.001\lambda_1$. To the experimen-

talist, this is equivalent to illuminating the sphere at 400 nm and comparing the scatter at 400 nm (which is almost completely elastic) with the scatterer at 400.4 nm (which is completely inelastic). We note that the shapes of the two sets of elements are very similar, with the main difference being the amplitudes of the peaks. This difference is due to the difference between elastic- and inelastic-scattered light, not the small wavelength difference.

These theoretical results demonstrate that the coherent, inelastically scattered light is a complicated function of many variables. In addition to the parameters involved in elastic scattering, the wavelengths emitted and the wavelength-dependent optical properties of the fluorescing material must be considered. Direct experimental verification of these conclusions will need careful measurements of the low intensity of inelastic radiation because the total intensity does not increase with sphere radius as does the intensity of the elastically scattered light.

ACKNOWLEDGMENTS

This research was supported in part by the U.S. Air Force Office of Scientific Research (AFSC) and the ITEK Corporation.

- [1] A. Biswas, H. Latifi, R. L. Armstrong, and R. G. Pinnick, *Opt. Lett.* **14**, 214 (1989).
- [2] R. E. Benner, P. W. Barber, J. F. Owen, and R. K. Chang, *Phys. Rev. Lett.* **44**, 475 (1980).
- [3] H. Chew, P. J. McNulty, M. Kerker, *Phys. Rev. A* **13**, 396 (1976).
- [4] H. Chew, M. Sculley, M. Kerker, P. J. McNulty, and D. D. Cooke, *J. Opt. Soc. Am. A* **68**, 1686 (1978).
- [5] M. Kerker and S. D. Druger, *Appl. Opt.* **18**, 1172 (1979).
- [6] G. Videen, W. S. Bickel, and J. M. Boyer, *Phys. Rev. A* **43**, 5655 (1991).
- [7] G. Mie, *Ann. Phys.* **25**, 377 (1908).
- [8] C. Bohren and D. Huffman, *Absorption and Scattering of Light by Small Particles* (Wiley, New York, 1983).
- [9] W. S. Bickel and W. M. Bailey, *Am. J. Phys.* **53**, 468 (1985).
- [10] J. A. Stratton, *Electromagnetic Theory* (McGraw-Hill, New York, 1941).
- [11] F. Bowman, *Introduction to Bessel Functions* (Dover, New York, 1958).

Light-scattering Mueller matrix from a fiber as a function of MgO contamination

Gordon Videen and William S. Bickel

The light-scattering Mueller matrix for an $r = 0.345\text{-}\mu\text{m}$ -radius quartz fiber, illuminated at $\lambda = 0.4416\text{-}\mu\text{m}$, is examined as a function of contamination with MgO crystals. When the MgO contamination is low, the matrix elements resemble those of a fiber of slightly larger radius. The MgO contamination creates higher-frequency, smaller-amplitude oscillations in the matrix elements that mask the lower-frequency oscillations indicative of a perfect cylinder. The contamination also causes scatter outside the plane of incidence.

Key words: Mueller matrix, light scattering, fiber, contamination.

I. Introduction

The problem of light scattering from an infinitely long circular cylinder was solved independently by Lord Rayleigh¹ and by von Ignatowsky.² Theory was experimentally verified by Bell and Bickel,³ who measured the light-scattering Mueller matrix from a quartz fiber whose radius was approximately equal to the wavelength of the illuminating radiation. Certain modifications to the basic cylindrical system, such as cladding with another index material or giving the system an elliptical cross section, can be treated theoretically. These solutions have been discussed in several texts.⁴⁻⁶ When the scattering system geometry becomes irregular, that is, when structures or surfaces cannot be made to conform to a single orthogonal coordinate system, the theoretical solution becomes extremely difficult, if not impossible, to obtain. Theoretical progress toward solving for the light scattered from such systems needs experimental data so the theorist can be guided toward the simplifications that may be made while still yielding acceptable results.

In studying light scattering it is important to consider that no scattering system is perfect. Impurities in the material and distortions in geometry cause experimental measurements of scattered light to deviate from theory. Many systems, by their nature, are imperfect. The addition of contaminants to the scattering system (dust particles in air, minerals in water,

etc.) change the systems and their resulting scatter. Contamination monitoring is an especially difficult problem when the experimenter is not able to separate the sample to be monitored from other scatterers that might be present. For example, scattering signals from asbestos impurities could be dependent on the dust present or on humidity levels. The monitor cannot remove or ignore these other factors and so must deal with their contributions to the scattering signals. In the laboratory, greater control over the scattering system can be achieved.

The light-scattering Mueller matrix for a circular-cross-section, quartz ($n = 1.466 - 0.0i$ at $\lambda = 0.4416\text{-}\mu\text{m}$) fiber of known optical and geometrical parameters is predicted exactly by theory. This same fiber, coated by cubic MgO crystals ($n = 1.74 - 0.0i$ at $\lambda = 0.4416\text{-}\mu\text{m}$), has a different light-scattering Mueller matrix. To see how the contamination affected the scattering, we studied the light scattering as a function of MgO contamination of the fiber. By studying how a perfect quartz fiber's scatter changes when we contaminate it with particles of known characteristics, we may better understand how contaminants affect other, irregular, systems.

II. Light-Scattering Technique

The polar nephelometer used in this study employs the polarization modulation technique developed by Hunt and Huffman.⁷ A complete discussion of the nephelometer design and operation is given by them and also by Perry *et al.*⁸ and Bickel *et al.*⁹ This technique involves periodically modulating the incident beam's polarization state at $\omega_0 = 50\text{ kHz}$, using a photoelastic modulator, while observing the signals carried out by the fundamental frequency (ω_0) and the second harmonic ($2\omega_0$) of the scattered light. A lock-in amplifier

The authors are with the Department of Physics, University of Arizona, Tucson, Arizona 85721.

Received 29 October 1990.

0003-6935/91/273880-06\$05.00/0.

© 1991 Optical Society of America.

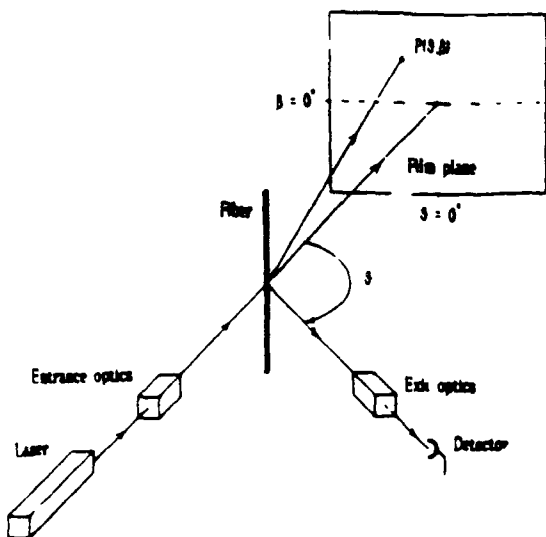


Fig. 1. Experimental apparatus used to measure the Mueller scattering matrix of a fiber. Laser light passes through the entrance optics and strikes the fiber at normal incidence. The scattered radiation passes through the exit optics, where it can be intercepted by a detector or a photographic plate to make a photograph.

is used to demodulate the signals. The experimental scattering matrix $S_{ij}(\theta)$ can be measured with the proper choice of exit optics.¹⁰ Normalization of the matrix elements is performed by servoing the photomultiplier tube (RCA 1P21) gain by means of a constant-current servo, which creates a constant dc output signal over the entire scan of the detector. The normalized output $S_{ij}(\theta)$ analog signals are collected and sent to a computer.

Figure 1 shows the experimental apparatus used to measure the $S_{ij}(\theta)$ of a fiber. The beam from the laser passes through the entrance optics and illuminates the fiber at normal incidence. The light scattered by the fiber may then either pass through various exit optics to a detector or pass directly to a photographic plate. A photographic plate can record the out-of-plane scattering, which does not occur for a perfect, uncontaminated fiber and which is usually missed by the polar nephelometer.

III. Initial System

The quartz fiber was made with the method developed by Bell and Bickel.³ The midsection of a quartz rod was heated by an oxygen-acetylene flame until it was molten. The rod was stretched slightly and slowly to make the midsection thinner. Just before the rod separated into two pieces, the ends were rapidly pulled

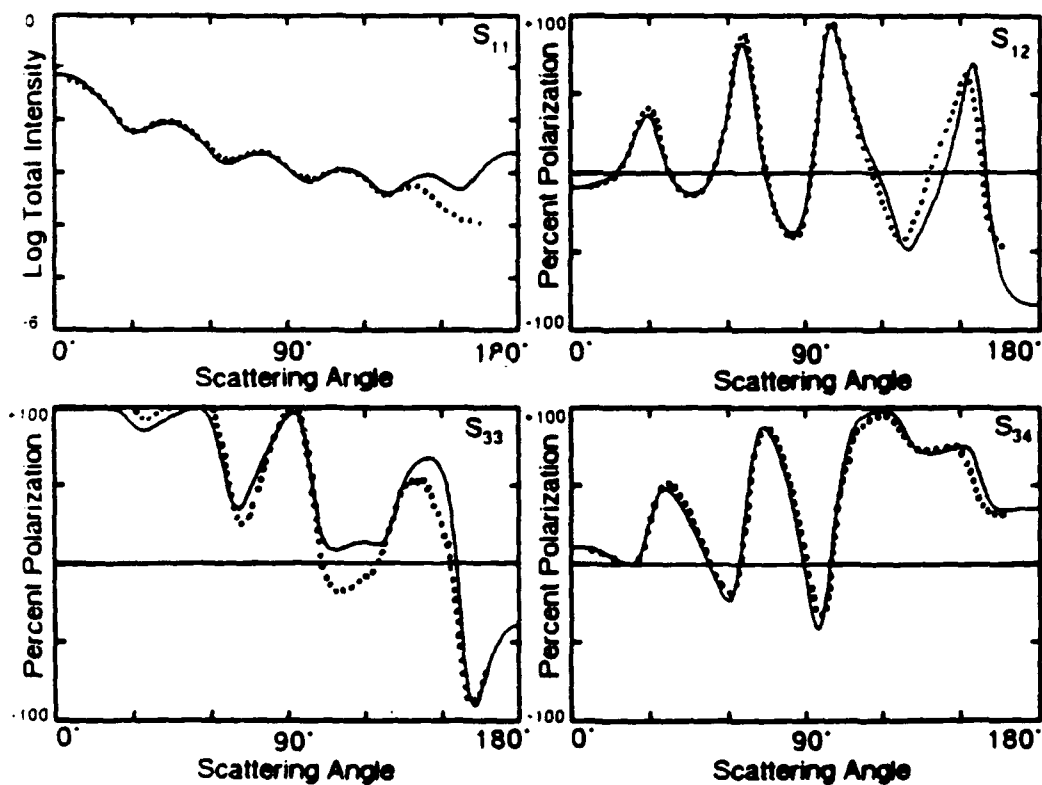


Fig. 2. Four experimentally measured Mueller scattering matrix elements for the initial fiber (dotted curves) and the theoretical matrix elements for an $r = 0.345\text{-}\mu\text{m}$ -radius quartz fiber (solid curves).

apart. This maneuver often produces fibers stretching from one or both ends of the rod. If no fibers are created, the process can be repeated.

Figure 2 compares the four unique, nonzero light-scattering Mueller matrix elements for the experimental fiber (dotted curves) with the theoretical matrix elements of an $r = 0.345\text{-}\mu\text{m}$ -radius quartz fiber (solid curves). The elements are nearly identical with differences most likely resulting from a slight nonuniformity of the fiber cross section. These matrix elements are the scattering signatures of the perfect fiber system. These elements will change as contaminants are added to the system.

IV. Contaminated System

Figure 3 shows the apparatus used for contaminating the quartz fiber with MgO crystals. The fiber is suspended vertically from a tube, 22 cm long and 8 cm in diameter, the top of which is blocked off except for a 2 cm \times 2 cm hole on one end opposite the fiber. The fiber is coated by burning a 2.5-cm-long strip (~ 24 mg) of magnesium ribbon (J. T. Baker Chemical Company) placed 2 cm below the lower end of the tube. The coating occurs as the smoke passes through the tube and out through the hole at the top. The ribbon burns for ~ 10 s, and after the smoke has cleared (~ 2 min), the contaminated fiber is removed. The fiber is placed under a microscope and photographed. Then it is placed in the nephelometer, where its scattering ma-

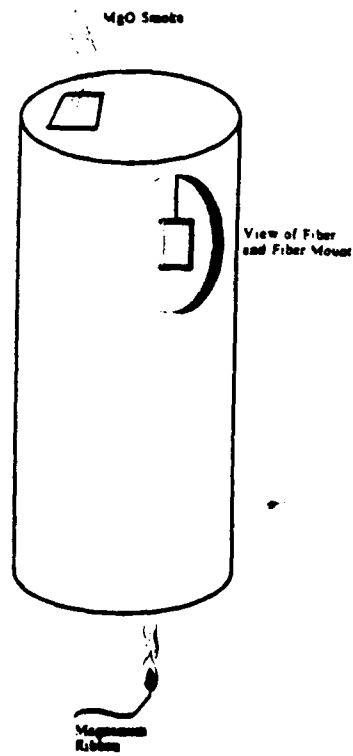


Fig. 3. Apparatus used to contaminate the quartz fibers with MgO crystals.

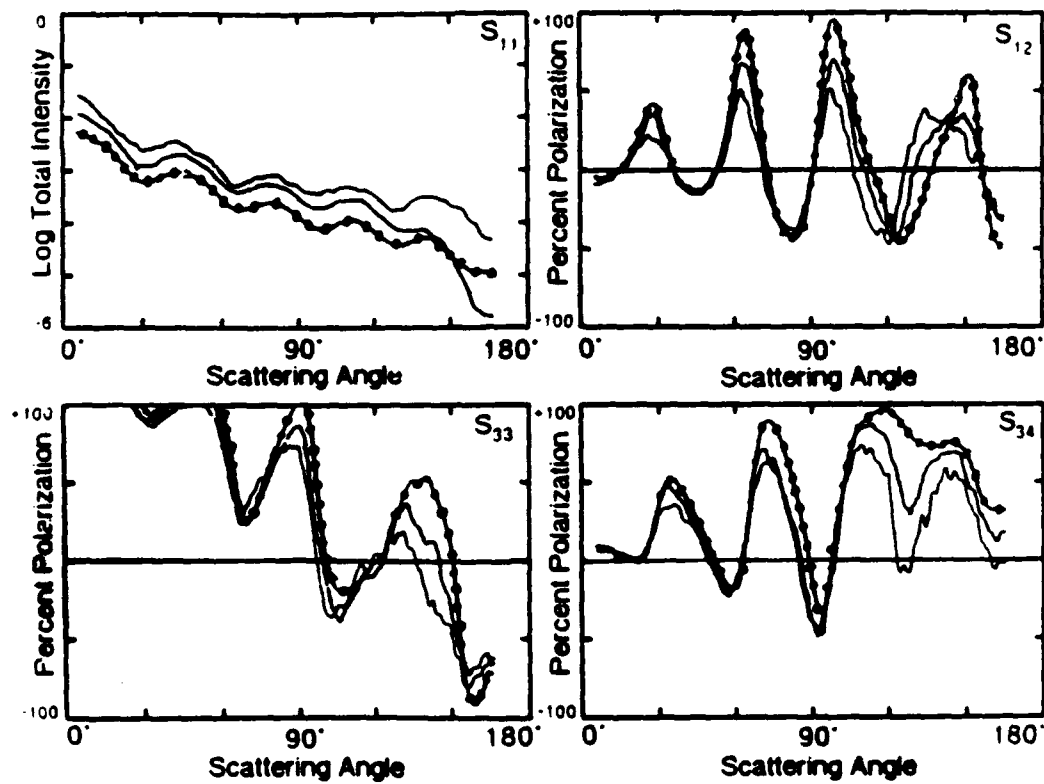


Fig. 4. Experimental light-scattering Mueller matrix of an $r = 0.345\text{-}\mu\text{m}$ -radius quartz fiber as a function of MgO contamination. The uncoated fiber elements are depicted by dots on solid curves. The other curves are for the fiber coated once and twice with MgO crystals.

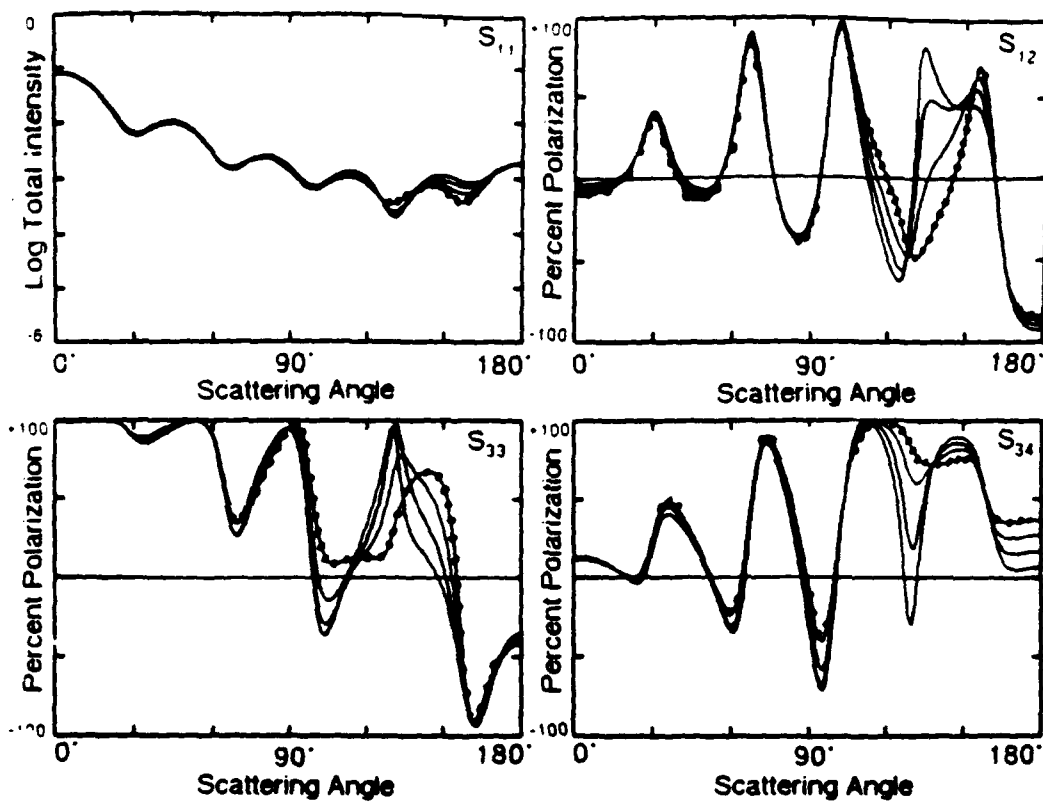


Fig. 5. Theoretical light-scattering Mueller matrix elements for a quartz fiber as a function of fiber radius. The elements for the initial $r = 0.345\text{-}\mu\text{m}$ -radius quartz fiber are shown by dots on solid curves. The other curves are for fiber radii of 0.350, 0.355, and 0.360 μm .

trix elements are measured. A photographic plate is used to measure the total intensity of the out-of-plane scatter. The process is then repeated, each time with additional coatings of contaminants added, until the light scattered is no longer significantly affected by the additional contaminants.

Figure 4 shows the light-scattering Mueller matrix of the fiber for three different levels of MgO contamination. The light-scattering total intensity matrix element (S_{11}) increases with increasing fiber contamination, while the magnitudes of the maxima/minima of the polarization matrix elements (S_{12} , S_{33} , and S_{34}) tend to decrease as the fiber becomes more contaminated. The frequency of the oscillations increases as the contamination increases. The matrix elements also display high-frequency, small-amplitude oscillations. These small (only a few percent) signal fluctuations are not noise since they are reproduced exactly by repetitive measurements of the fiber in exactly the same orientation. They change, however, if the laser beam strikes the fiber at a slightly different location or orientation.

Figure 5 shows the theoretical matrix elements for a quartz fiber as a function of fiber radius. A 0.345- μm -radius fiber (dots on solid curves) is shown; additional sets of elements are shown for fibers whose radii have increased by 0.005 μm . Figures 4 and 5 show many similarities. The low-frequency oscillation of the con-



Fig. 6. Photomicrograph of the fiber surface system after six coatings of MgO crystals.

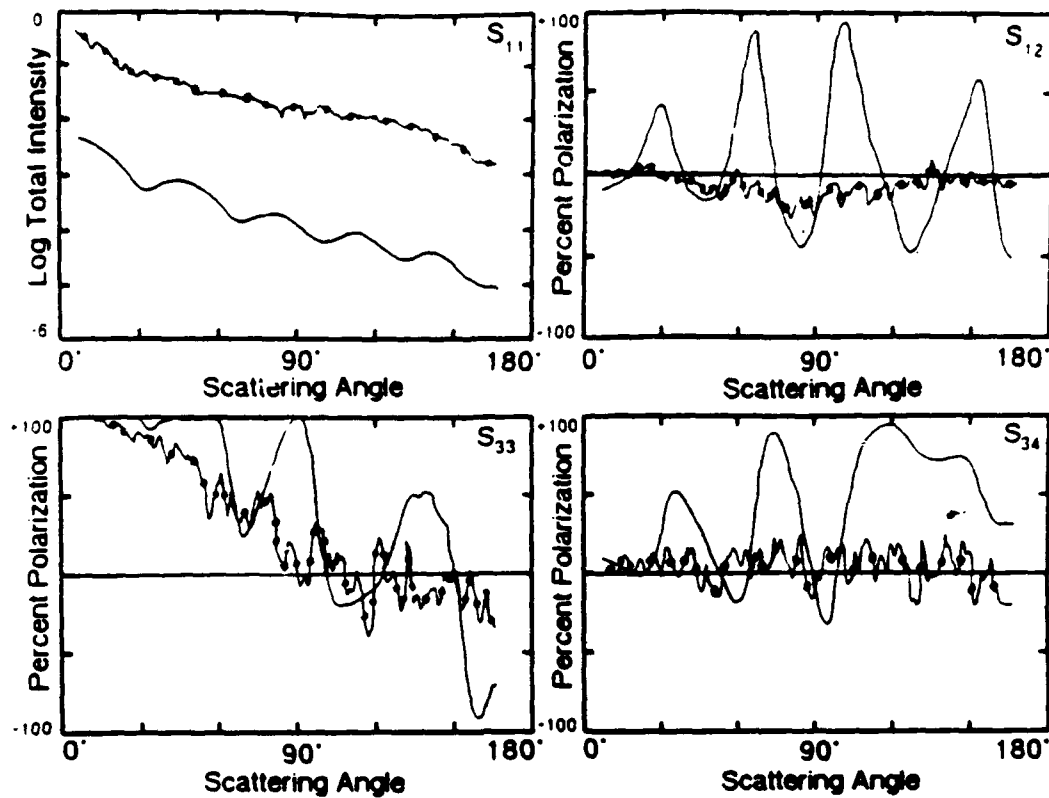


Fig. 7. Experimental light-scattering Mueller matrix of the initial uncoated fiber (solid curves) and the fiber after six coatings of MgO crystals (dotted curves).

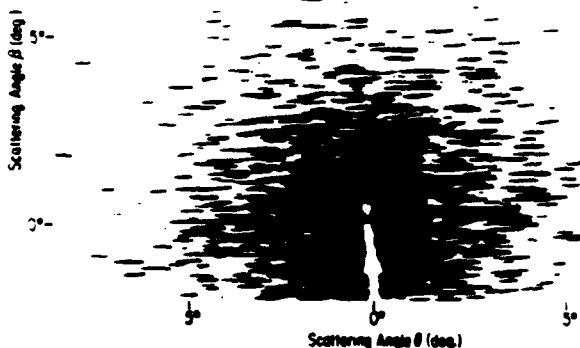


Fig. 8. Photograph of the light scattered by the fiber with six coatings of MgO crystals.

taminated fiber coincides with that of a fiber of slightly larger radius. Not only have the frequencies increased but the amplitudes of the maxima/minima of the contaminated fiber matrix elements coincide with the elements of the larger fibers. Note especially the shapes of the elements near $\theta = 130^\circ$.

Figure 6, a photomicrograph of the fiber system,

shows that after six coatings the MgO crystals extend many fiber diameters beyond the initial fiber boundary. Figure 7 shows the experimental light-scattering Mueller matrix of the uncoated fiber and of the fiber after six coatings of MgO crystals. The phase information that characterizes the initial uncoated fiber is no longer present for the coated fiber. Instead, high-frequency oscillations dominate the matrix elements. As the number of contaminants increases, matrix elements S_{12} and S_{34} tend toward zero. Matrix element S_{33} also tends toward zero, except in the forward-scattering region (near $\theta = 0^\circ$), where it is positively polarized.

The Mueller scattering matrix elements for a single sphere or cylinder obey the following relationship:

$$S_{12}^2 + S_{31}^2 + S_{34}^2 = 1$$

(note that we are using a normalized Mueller matrix representation). This relationship is obeyed by the uncoated fiber at all scattering angles. However, this relationship does not hold for the contaminated fiber, which has lost its efficiency in producing polarized light.

Figure 8 is a photograph of the scattering patterns created by the contaminated fiber shown in Fig. 6. A sheet of Kodak Panalure II photographic paper was placed 1 m away from the fiber. Both the fiber and the

photographic paper were normal to the incident beam. It is interesting that the pattern is especially intense in the forward scatter very near specular ($\theta = 0^\circ$, $\beta = 0^\circ$). Fiber asymmetry along the z axis causes out-of-plane scatter. This out-of-plane scatter is especially interesting because it is not a random speckle pattern. The speckles, elongated in the θ direction, betray the underlying cylindrical geometry. Although this is not evident in the matrix elements measured in the scattering plane (Fig. 7), it is evident in out-of-plane scatter.

V. Discussion

Adding contaminants to a perfect fiber changes its light-scattering Mueller matrix. Small amounts of contaminants tend to increase fiber size slightly, and this information appears in the matrix elements. Additional contamination drives the polarization elements (with the exception of S_{33} in the forward-scatter region) toward zero. Only the out-of-plane scatter contains a hint of a fiber system.

This research was supported in part by the U.S. Air Force Office of Scientific Research.

References

1. Lord Rayleigh, "On the Electromagnetic Theory of Light," *Philos. Mag.* 12, 81-101 (1881).
2. W. von Ignatowsky, "Reflexion elektromagnetischer Wellen an einem Draht," *Ann. Phys. (Leipzig)* 18, 495-522 (1905).
3. B. W. Bell and W. S. Bickel, "Single Fiber Light Scattering Matrix: an Experimental Determination," *Appl. Opt.* 20, 3874-3879 (1981).
4. C. Bohren and D. Huffman, *Absorption and Scattering of Light by Small Particles* (Wiley, New York, 1983).
5. H. C. van de Hulst, *Light Scattering by Small Particles* (Dover, New York, 1976).
6. M. Kerker, *The Scattering of Light and Other Electromagnetic Radiation* (Academic, New York, 1969).
7. A. J. Hunt and D. R. Huffman, "A New Polarization-Modulated Light Scattering Instrument," *Rev. Sci. Instrum.* 44, 1753-1762 (1973).
8. R. J. Perry, A. J. Hunt, and D. R. Huffman, "Experimental Determination of Mueller Scattering Matrices," *Appl. Opt.* 17, 2700-2710 (1978).
9. W. S. Bickel, J. F. Davidson, D. R. Huffman, and R. Kilkson, "Applications of Polarization Effects in Light Scattering: A New Biophysical Tool," *Proc. Natl. Acad. Sci. (USA)* 73, 486-490 (1976).
10. W. S. Bickel and W. M. Bailey, "Stokes Vectors, Mueller Matrices, and Polarized Scattered Light," *Am. J. Phys.* 53, 468-478 (1985).

Experimental light-scattering Mueller matrix for a fiber on a reflecting optical surface as a function of incident angle

Gorden Videen, William S. Bickel, Vincent J. Iafelice, and David Abramson

Department of Physics, University of Arizona, Tucson, Arizona 85721

Received December 31, 1990; revised manuscript received September 19, 1991; accepted September 20, 1991

The light-scattering Mueller matrix is experimentally determined for a 0.26- μm -radius quartz fiber mounted on an aluminum surface at five different incident angles. The results are compared with those for the experimental scattering elements of the lone fiber and the lone surface and with theoretical results derived from a simple fiber-surface model. The experimental matrix elements of the fiber-surface system do not resemble the matrix elements from any of these other systems.

INTRODUCTION

A perfect fiber (or sphere) on a perfect surface is the simplest solvable surface defect. We measured the Mueller scattering matrix for a fiber-surface system with a polar nephelometer. This scattering system incorporates two separate perfect systems whose scatter can be determined exactly by theory. Fresnel derived the scatter from a perfect plane surface before Maxwell developed his famous equations. Later in the 19th century, Rayleigh derived the scatter from a perfect cylinder.¹ Although the combination of a fiber-surface system is more difficult to solve theoretically, we can experimentally measure the scatter of the combined system just as easily as we can measure the scatter of the individual systems. The main experimental problem is to ensure that the surface, the fiber, and the fiber-surface system are of sufficiently high quality to give data accurate enough to warrant careful theoretical attention.

INSTRUMENTATION

The light-scattering apparatus used to measure the light-scattering Mueller matrix elements is shown schematically in Fig. 1. Light emitted from a He-Cd laser ($\lambda = 0.4416 \mu\text{m}$) passes through various entrance optics before striking the sample (either the fiber, the surface, or the fiber-surface system). Elements were measured for the lone fiber oriented along the z axis, perpendicular to the incident beam, and for the lone surface, with the plane of the surface defined by the z axis and a line at angle α measured from the incident beam. The angle α is the complement to the incident angle measured from the surface normal (see Fig. 1). Elements were then measured for the fiber-surface system with the fiber resting on the surface. The fiber is oriented parallel to the z axis, which is perpendicular to both the incident beam and the normal to the surface. Light from the scattering system passes through various exit optics before reaching the detector, which rotates through angle δ about the z axis.

The polar nephelometer used in this study employs the polarization modulation technique developed by Hunt and

Huffman.² Complete discussions of the nephelometer design and operation are given in Ref. 2 and also by Perry et al.³ and Bickel et al.^{4,5} The experimental scattering matrix measured by the nephelometer is signified by S_v .⁶ These elements are actually combinations of the general scattering matrix elements S_{ij} . Iafelice and Bickel⁶ determined that five elements are necessary to characterize the Mueller matrix for a near-perfect surface:

$$\begin{aligned} S_{11}^* &= S_{11}, & S_{12}^* &= S_{12}/S_{11}, \\ S_{21}^* &= (S_{12} + S_{21})/(S_{11} + S_{21}), \\ S_{31}^* &= (S_{13} + S_{31})/(S_{11} + S_{31}), \\ S_{34}^* &= (S_{14} + S_{34})/(S_{11} + S_{31}). \end{aligned} \quad (1)$$

For symmetric scatterers such as spheres and fibers, $S_{31} = S_{13} = S_{14} = 0$ and $S_{12} = S_{21}$. For these scatterers, the experimental scattering matrix reduces to the normalized scattering matrix:

$$\begin{aligned} S_{11}^* &= S_{11}, & S_{12}^* &= S_{12}/S_{11}, & S_{22}^* &= 1, \\ S_{33}^* &= S_{33}/S_{11}, & S_{34}^* &= S_{34}/S_{11}. \end{aligned} \quad (2)$$

SCATTERING SYSTEMS

The quartz fiber was made by using the method developed by Bell and Bickel.⁷ The radius of the fiber was determined by comparing the values of the experimentally measured matrix elements with theoretical values.⁸⁻¹⁰ A best fit of the experimental and theoretical curves occurred for a fiber radius of $0.260 \pm 0.005 \mu\text{m}$. The optical constants of the fiber were held constant (for quartz, the refractive index $n = 1.466 + 0.0i$ and permeability $\mu = \mu_0$). The experimental matrix elements for the quartz fiber (dotted curves) and the theoretical matrix elements for a 0.26- μm -radius quartz fiber (solid curves) are shown in Fig. 2. Repeated measurements of the fiber matrix elements coincide. Deviations occur because the fiber is not perfect.

The surface studied in this experiment is the same surface as that studied in great detail by Iafelice and Bickel.⁶

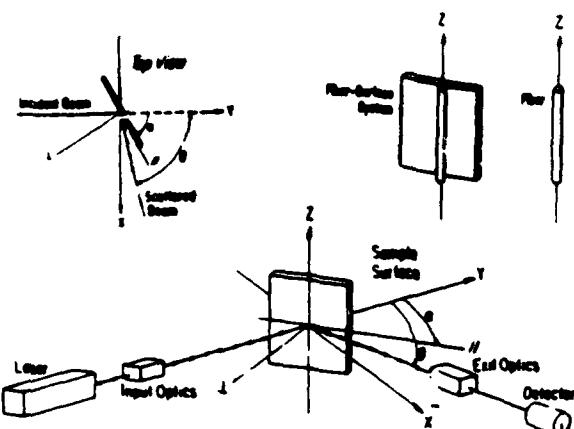


Fig. 1. Schematic of the light-scattering apparatus used to measure the Mueller matrix elements.

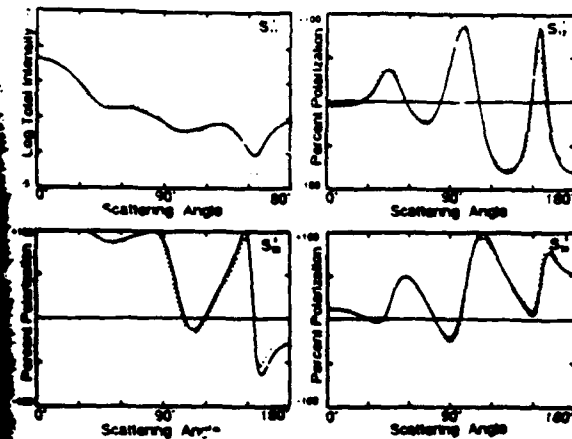


Fig. 2. The four unique experimental Mueller matrix elements for the quartz fiber (dotted curves) and the theoretical matrix elements for a 0.26- μm -radius quartz fiber (solid curves).

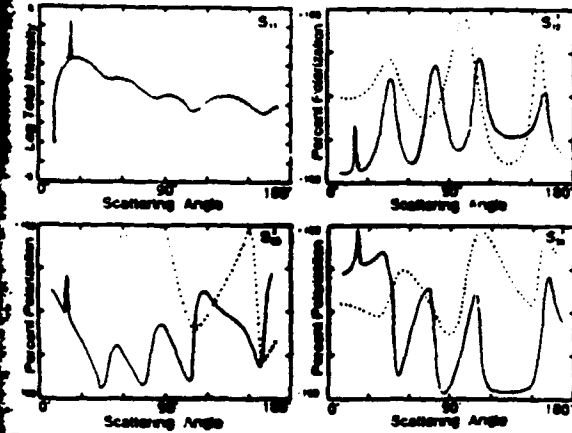


Fig. 3. The four unique experimental Mueller matrix elements for a fiber-surface system illuminated at near-grazing incidence ($\alpha = 11.25^\circ$) from an aluminum surface (solid curves). The experimental Mueller matrix elements for the fiber are also shown (dotted curves).

consists of an optically thick layer of aluminum coated on a diamond-polished synthetic sapphire substrate. The interferometrically measured rms roughness of the surface is $\sigma = 1.6 \pm 0.3$ nm.

Figure 3 shows the light-scattering Mueller matrix for the fiber-surface system measured at near-grazing incidence ($\alpha = 11.25^\circ$). Superimposed on the figure are the four scattering matrix elements for the lone

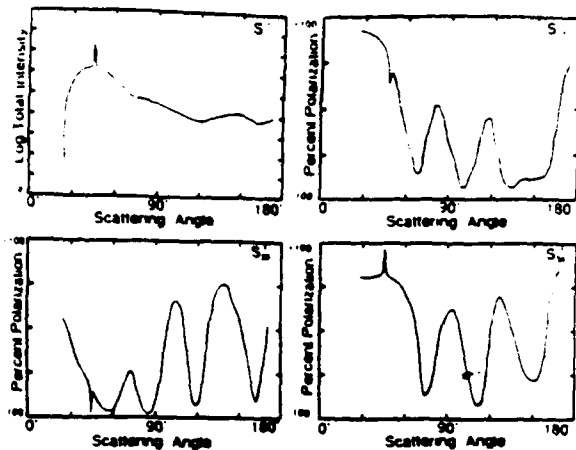


Fig. 4. The four unique Mueller matrix elements for a fiber-surface system illuminated at $\alpha = 22.5^\circ$ from an aluminum surface.

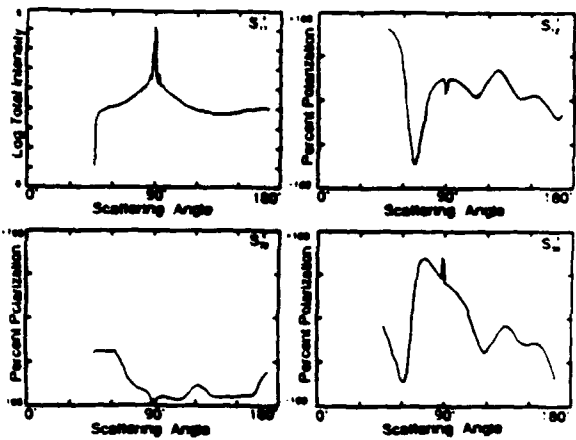


Fig. 5. The four unique Mueller matrix elements for a fiber-surface system illuminated at $\alpha = 45^\circ$ from an aluminum surface.

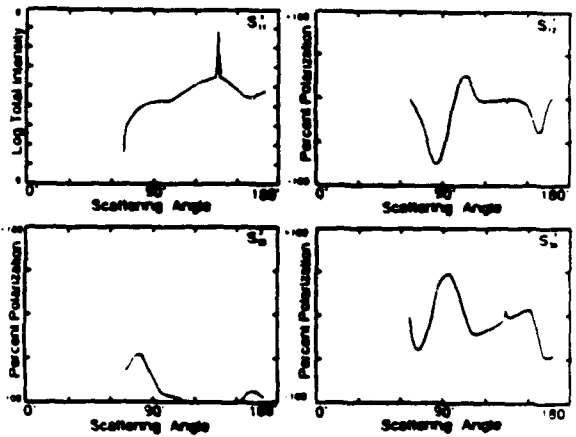


Fig. 6. The four unique Mueller matrix elements for a fiber-surface system illuminated at $\alpha = 67.5^\circ$ from an aluminum surface.

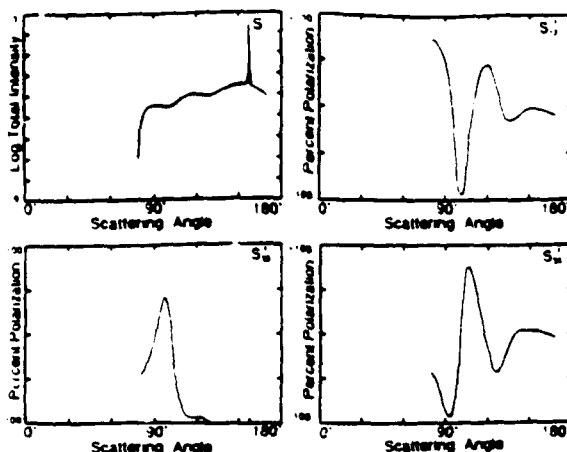


Fig. 7. The four unique Mueller matrix elements for a fiber-surface system illuminated at $\alpha = 78.75^\circ$ from an aluminum surface.

0.26- μ m-radius quartz fiber: S_{11}^* , S_{12}^* , S_{21}^* , and S_{34}^* . Measurements of the other matrix elements show that the relations expressed by Eqs. (2) are valid for the fiber-surface system and that only these four measurements are needed to characterize the scatter completely. Figures 4, 5, 6, and 7 show the fiber-surface matrix elements for $\alpha = 22.5^\circ$, 45° , 67.5° , and 78.75° , respectively. The intense specular peak that occurs when the scattering angle $\delta = 2\alpha$ causes sharp spikes on the polarization matrix elements. We note that as the illumination angle is varied, the matrix elements vary greatly and do not appear to approach a limiting value.

The experimental matrix elements of the fiber-surface system are dissimilar to the elements of both the lone fiber and the lone surface. The oscillation frequency of the elements of the fiber-surface system is much greater than that of the lone fiber or the lone surface. This is not surprising since the fiber-surface system approximates a double-fiber system: fiber and an image fiber whose dimensions are twice those of the lone fiber. In general, increasing the linear dimensions of a scattering system increases the oscillatory frequency of its scattering matrix elements. The large difference among the matrix elements of the fiber, the surface, and the fiber-surface system reveals that the three systems are fundamentally different. Therefore one cannot use the matrix elements of a lone fiber to predict the matrix elements of a fiber-surface system.

MODEL

The difference in oscillatory frequencies between the two systems cannot be accounted for simply by treating the fiber as a perturbation of the surface. A different model must be used to predict the scattering. Three models were proposed by Nahm and Wolfe to predict the scattering from spheres on a conducting plane.¹¹ Nahm and Wolfe concentrated on the total intensity matrix element S_{11} . Our polarization measurements contain additional information that does not play a part in bidirectional reflectance distribution function theory. Our treatment of this system uses a model similar to the double-interaction model. In this model, light reaches the detector by travel-

ing one of four different paths (Fig. 8). The light may either (I) strike the fiber and scatter directly to the detector; (II) reflect off the surface, strike the fiber, and scatter to the detector; (III) strike the fiber and scatter to the surface, where it is reflected to the detector; or (IV) reflect off the surface, strike the fiber, and scatter to the surface, where it is reflected to the detector. This model includes no interactions between the fiber and the surface, for instance, light scattered by the fiber that reflects off the surface before interacting with the fiber again. The resulting amplitude elements for these four rays can be derived as follows:

$$T_{n}^{(0)}(\delta) = T_n(\delta) + R_n(\pi/2 - \alpha) \exp i\delta(\alpha) T_n(\delta - 2\alpha) + R_n(\pi/2 - (\delta - \alpha)) \exp i\delta(\delta - \alpha) T_n(\delta - 2\alpha) + R_n(\pi/2 - (\delta - \alpha)) R_n(\pi/2 - \alpha) \exp i[\delta(\alpha) + \delta(\delta - \alpha)] T_n(\delta). \quad (3)$$

Here $T_n(\delta)$ is the scattering amplitude matrix element $T_1(\delta)$ or $T_2(\delta)$ ($n = 1$ is for the TE mode, and $n = 2$ is for the TM mode; see Ref. 8) for the cylinder with no surface present, and

$$\delta(\delta) = \frac{4\pi r \sin \delta}{\lambda} \quad (4)$$

is a phase difference resulting from the paths that the light may travel before reaching the detector. The Fresnel reflectance coefficients R_n are given by

$$R_1(\delta_i) = \frac{\mu_2 n_1 \cos \delta_i - \mu_1 n_2 [1 - (n_1/n_2)^2 \sin^2 \delta_i]^{1/2}}{\mu_2 n_1 \cos \delta_i + \mu_1 n_2 [1 - (n_1/n_2)^2 \sin^2 \delta_i]^{1/2}}, \quad (5)$$

$$R_2(\delta_i) = \frac{\mu_1 n_2 \cos \delta_i - \mu_2 n_1 [1 - (n_1/n_2)^2 \sin^2 \delta_i]^{1/2}}{\mu_1 n_2 \cos \delta_i + \mu_2 n_1 [1 - (n_1/n_2)^2 \sin^2 \delta_i]^{1/2}}, \quad (6)$$

where the subscripts on μ , and n , are the permeability and the complex refractive index for the medium on the incident side of the surface ($i = 1$) and the transmission side of the surface ($i = 2$).

Figure 9 shows the experimental Mueller scattering matrix and the theoretical results for a 0.26- μ m-radius quartz fiber resting on an aluminum surface ($n = 0.5 + 5.0i$)¹² calculated from the scattering amplitudes determined from Eq. (3). Although the experimental and

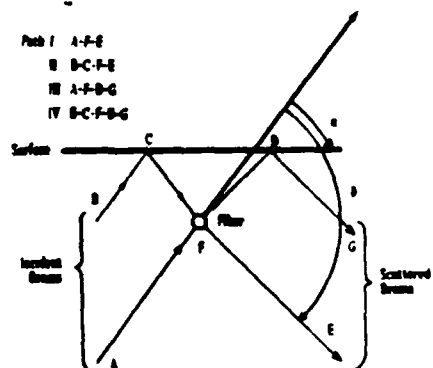


Fig. 8. Paths that an incident beam may follow to the fiber and after interaction before being detected on the incident side of the surface.

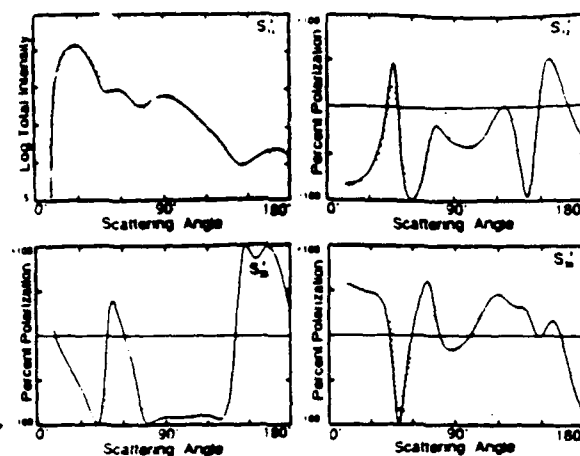


Fig. 3. The four unique Mueller matrix elements calculated for a fiber-surface system (quartz fiber of radius $0.26 \mu\text{m}$) illuminated at near-grazing incidence ($\alpha = 11.25^\circ$) from an aluminum surface (solid curves) are compared with the experimental Mueller matrix elements (dotted curves).

theoretical curves do not coincide, it is interesting to note a number of similarities. Most important is that the numbers of minima and maxima in the corresponding elements of both sets of curves are approximately equal. One of the crudest ways to estimate fiber (or sphere) diameter is to match the number of maxima or minima in a particular interval with theory (this is similar to determining slit width in a diffraction experiment). These data fit the fiber on the surface much better than they fit the lone fiber. The theory for total intensity matrix element S_{11} fits the experimental data quite well. Both show an intensity falloff of approximately 3 orders of magnitude from the specular peak to -180° . Although this model may predict the total intensity of the scattered light fairly well, it does not accurately predict the polarization states of the scattered light, especially with regard to polarization magnitudes. However, the numbers of maxima and minima compare favorably. Comparing polarization S_{11} 's is important from an experimental point of view because polarization curves from two scatterers that give virtually identical S_{11} can be quite different. It is important from a theoretical point of view because theories that can predict S_{11} cannot be taken for granted in predicting the correct polarization. That is the case here.

CONCLUSIONS

The light-scattering measurements and analysis of the fiber-surface system lead to the following conclusions:

1. The S_{ij} for a fiber-surface system in no way resembles the S_{ij} for the isolated fiber. This means that the matrix elements measured for a fiber (or sphere) on a surface are not useful in determining the properties of the defect without an appropriate theory.

2. S_{ij} are strongly dependent on the angle of incidence α . Studies of complete scattering as a function of incident angle may be necessary to characterize surface defects.

3. Polarization elements (other than S_{11}) carry sufficient extra information to warrant their measurement for a complete analysis of the surface.

4. The most stringent test of any theory that predicts scatter is whether it accurately predicts the polarizations. Often surfaces with very similar S_{11} will produce very different polarization curves.

ACKNOWLEDGMENTS

This research was supported in part by the U.S. Air Force Office of Scientific Research and Itek Corporation.

REFERENCES

1. Lord Rayleigh, "On the electromagnetic theory of light," *Philos. Mag.* 12, 81-101 (1881).
2. A. J. Hunt and D. R. Huffman, "A new polarization-modulated light scattering instrument," *Rev. Sci. Instrum.* 44, 1753-1762 (1973).
3. R. J. Perry, A. J. Hunt, and D. R. Huffman, "Experimental determinations of Mueller scattering matrices for nonspherical particles," *Appl. Opt.* 17, 2700-2710 (1978).
4. W. S. Bickel, J. F. Davidson, D. R. Huffman, and R. Kilkson, "Application of polarization effects in light scattering: a new biophysical tool," *Proc. Natl. Acad. Sci. USA* 73, 486-490 (1976).
5. W. S. Bickel and W. M. Bailey, "Stokes vectors, Mueller matrices, and polarized scattered light," *Am. J. Phys.* 53, 468-478 (1985).
6. V. J. Iafelice and W. S. Bickel, "Polarized light scattering matrix elements for select perfect and perturbed optical surfaces," *Appl. Opt.* 26, 2410-2415 (1987).
7. B. W. Bell and W. S. Bickel, "Single fiber light scattering matrix: an experimental determination," *Appl. Opt.* 20, 3874-3879 (1981).
8. C. P. Bohren and D. R. Huffman, *Adorption and Scattering of Light by Small Particles* (Wiley, New York, 1983).
9. H. C. van de Hulst, *Light Scattering by Small Particles* (Wiley, New York, 1967).
10. M. Kerker, *The Scattering of Light and Other Electromagnetic Radiation* (Academic, New York, 1969).
11. K. B. Nahm and W. L. Wolfe, "Light-scattering models for spheres on a conducting plane: comparison with experiment," *Appl. Opt.* 26, 2995-2999 (1987).
12. D. E. Gray, ed., *American Institute of Physics Handbook* (McGraw-Hill, New York, 1972).

Light-scattering resonances in small spheres

Gorden Videen and William S. Bickel

Physics Department, University of Arizona, Tucson, Arizona 85721

(Received 24 October 1991)

Two limiting expressions occur for scattering from very small spheres. One occurs when the refractive index becomes small (Rayleigh scattering), and the other occurs when the sphere becomes perfectly conducting (Thomson scattering). We explore the scatter from small spheres having real refractive indices. For such spheres, resonance conditions occur, and the resulting scattering coefficients are no longer proportional to the volume of a sphere.

PACS number(s): 42.25.Fx

INTRODUCTION

Electromagnetic scattering from small spheres was explored by Rayleigh [1] and Thomson [2], who calculated light-scattering expressions for two very different special cases: where the spheres have small refractive indices, and where they are perfect conductors, respectively. They did this before Mie [3] and Lorenz [4] derived a formalism for the scatter from arbitrary spheres. The range of validity of these special limits has been explored by Kerker, Scheiner, and Cooke [5]. They found that as the sphere size becomes smaller, Rayleigh theory is valid over a larger range of refractive index, and Thomson theory is valid over a smaller range of refractive index.

We might expect the scattering that occurs from small spheres that lie in the region between the Rayleigh and the Thomson limits to be composed of some combination of the modes present at these two limits. However, the extinction efficiencies of small, dielectric spheres as a function of refractive index (Fig. 1) are not smooth, but complicated by sharp resonances. Resonances in the light scattering from spheres have attracted a great deal of attention recently [6–16]. Resonances appear as strong, narrow enhancements in the scattering of a particle. The large internal fields that are built up within such particles can create interesting effects and have been used to investigate various phenomena such as fluorescent and Raman scattering [17–24].

It is well known that as the sphere size becomes small

with respect to the illuminating wavelength, the equations predicting the scatter are greatly simplified, since only a few sets of coefficients are necessary to characterize the scatter. We take advantage of these simplified expressions and derive the resonance conditions directly from the a_n and b_n coefficients [25–27] rather than from the A_n , B_n , C_n , D_n coefficients [28], which is the standard method. We then explore the scattering behavior and cross sections on and near resonance. Studying resonances in small spheres gives insight into the resonances that occur in larger spheres and even in more complicated particles.

We note that the resonance conditions in these small spheres are met when the sphere refractive index is large ($m > \pi/x$). Therefore, it would seem that this work would constitute only a theoretical exercise, which could only provide insight into other resonance situations. However, in a recent paper, Scully [29] has shown via quantum coherence that when operating near an atomic resonance between an excited state and a coherently prepared ground-state doublet, a large enhancement of the refractive index (by many orders of magnitude) may be achieved with zero absorption. In this case, the light-scattering resonances that we examine cannot only be realized, but may prove to be a useful tool in characterizing the optical properties of such materials.

SCATTERING COEFFICIENTS

The electromagnetic scattering a large distance from a sphere of radius r , illuminated by a unit-normalized plane wave traveling in the positive z direction, and polarized in the \hat{x} direction, may be expressed by two scattering amplitude functions given by

$$S_1 = \sum_{n=1}^{\infty} \frac{2n+1}{n(n+1)} \left[\frac{P_n^1(\cos\vartheta)}{\sin\vartheta} a_n + \frac{\partial}{\partial\vartheta} P_n^1(\cos\vartheta) b_n \right]. \quad (1a)$$

$$S_2 = \sum_{n=1}^{\infty} \frac{2n+1}{n(n+1)} \left[\frac{P_n^1(\cos\vartheta)}{\sin\vartheta} b_n + \frac{\partial}{\partial\vartheta} P_n^1(\cos\vartheta) a_n \right]. \quad (1b)$$

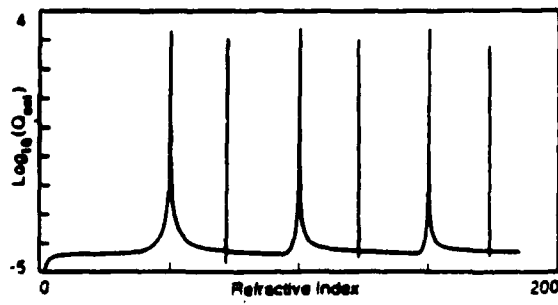


FIG. 1. Extinction efficiency for a small ($r = 0.01\lambda$) sphere as a function of real refractive index.

where S_1 is measured in the y - z plane and S_2 is measured in the x - z plane. The Mie scattering coefficients are given by

$$a_n = \frac{m\psi'_n(x)\psi_n(mx) - \psi'_n(mx)\psi_n(x)}{m\xi'_n(x)\psi_n(mx) - \psi'_n(mx)\xi_n(x)}, \quad (2a)$$

$$b_n = \frac{m\psi'_n(mx)\psi_n(x) - \psi'_n(x)\psi_n(mx)}{m\psi'_n(mx)\xi_n(x) - \xi'_n(x)\psi_n(mx)}, \quad (2b)$$

where m is the complex refractive index of the sphere, $x = 2\pi r/\lambda$, and ψ_n and ξ_n are the Riccati-Bessel functions.

First we examine what happens for the special limiting

$$a_1 \sim \frac{\cos(mx) \left[x \left[\frac{1+2m^2}{3m} \right] - x^3 \left[\frac{1+4m^2}{30m} \right] \right] + \sin(mx) \left[- \left[\frac{1+2m^2}{3m^2} \right] + x^2 \left[\frac{1+14m^2}{30m^2} \right] \right]}{\cos(mx) \left[x^{-2} \left[\frac{-i+im^2}{m} \right] - \left[\frac{i+im^2}{2m} \right] \right] + \sin(mx) \left[x^{-3} \left[\frac{i-im^2}{m^2} \right] + x^{-1} \left[\frac{i-im^2}{2m^2} \right] \right]}, \quad (5)$$

$$b_1 \sim \frac{\cos(mx)(x - x^3/6) + \sin(mx) \left[-1/m + x^2 \left[\frac{1+2m^2}{6m} \right] \right]}{\cos(mx)(-i+x) + \sin(mx) \left[x^{-1} \left[\frac{i-im^2}{m} \right] - 1/m - x \left[\frac{i+im^2}{2m} \right] \right]}.$$

Similarly, the second-order coefficients may be written as in Eq. (6).

Two additional limiting conditions exist for small spheres. One is the Rayleigh limit valid when $|m|x \ll 1$. In this case the scattering coefficients further reduce to

$$a_1 \sim -\frac{2ix^3}{3} \frac{m^2-1}{m^2+2}, \quad b_1 \sim 0, \quad (7)$$

$a_n \sim b_n \sim 0$ for $n > 1$.

The other limiting condition occurs when the sphere's refractive index approaches that of a perfect conductor $m \rightarrow i\infty$. In this case the scattering coefficients reduce to

$$a_1 \sim -\frac{2ix^3}{3}, \quad b_1 \sim \frac{ix^3}{3}, \quad (8)$$

$a_n \sim b_n \sim 0$ for $n > 1$.

Note that in both these limiting cases the scattering coefficients are proportional to x^3 . Figure 2 shows the angular scattering-intensity distributions for a Rayleigh and a Thomson sphere.

RESONANCES

We now examine the b_1 mode in more detail. When the refractive index m is increased along the real axis, the sine terms in Eq. (5) do not contribute to the scatter when $mx = N\pi$ where the index N is an integer. Resonances in the b_1 coefficients occur at approximately these locations. Two interesting results occur that are worth pointing out. The first is that the scattered fields are no longer propor-

case where the sphere size is small ($r \ll \lambda$). In this limiting case the scatter is determined primarily by the lowest-order terms of the series given by Eq. (1). The Riccati-Bessel functions for the $n = 1$ case are given by

$$\psi_1(\rho) = \frac{\sin \rho}{\rho} - \cos \rho, \quad \xi_1(\rho) = \exp(i\rho)(-i\rho^{-1} - 1). \quad (3)$$

For small arguments, these functions are approximately

$$\psi_1(\rho) \sim \frac{\rho^2}{3} - \frac{\rho^4}{30}, \quad \xi_1(\rho) \sim -\frac{i}{\rho} - \frac{i\rho}{2} + \frac{\rho^2}{3}. \quad (4)$$

For small x , the scattering coefficients given by Eq. (2) are approximately

$$a_1 \sim \frac{\cos(mx) \left[x \left[\frac{1+2m^2}{3m} \right] - x^3 \left[\frac{1+4m^2}{30m} \right] \right] + \sin(mx) \left[- \left[\frac{1+2m^2}{3m^2} \right] + x^2 \left[\frac{1+14m^2}{30m^2} \right] \right]}{\cos(mx) \left[x^{-2} \left[\frac{-i+im^2}{m} \right] - \left[\frac{i+im^2}{2m} \right] \right] + \sin(mx) \left[x^{-3} \left[\frac{i-im^2}{m^2} \right] + x^{-1} \left[\frac{i-im^2}{2m^2} \right] \right]}, \quad (5)$$

$$b_1 \sim \frac{\cos(mx)(x - x^3/6) + \sin(mx) \left[-1/m + x^2 \left[\frac{1+2m^2}{6m} \right] \right]}{\cos(mx)(-i+x) + \sin(mx) \left[x^{-1} \left[\frac{i-im^2}{m} \right] - 1/m - x \left[\frac{i+im^2}{2m} \right] \right]}.$$

tional to the sphere volume. As a result, the scattering efficiencies of such particles are greatly increased compared to particles just off resonance. Figure 3 shows the first b_1 resonance (following a previous convention [8]; this is written as b_1^1). For purposes of illustration, we chose to examine small spheres with an arbitrary but definite radius $r = 0.01\lambda$. The resulting resonances will necessarily occur only at large values of refractive index ($m = 50N$) due to the small size of these spheres.

The second interesting result is that the mode of oscil-

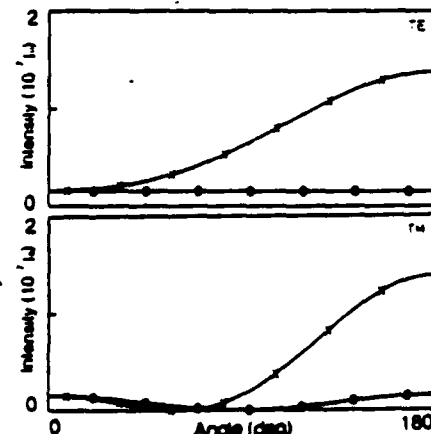


FIG. 2. Angular scattering-intensity distributions for an $r = 0.01\lambda$, $m = 2.0$ Rayleigh sphere (\circ), and an $r = 0.01\lambda$ Thomson sphere (\times).

$$(6)$$

$$\begin{aligned}
 \cos(mx) & \left[-x \left| \frac{2+3m^2}{5m^2} \right| + x^{-1} \left| \frac{6+29m^2}{210m^2} \right| + \sin(mx) \left| \frac{2+3m^2}{5m^3} \right| - x^{-2} \left| \frac{2+19m^2+14m^4}{70m^3} \right| \right] \\
 \cos(mx) & \left[x^{-4} \left| \frac{18i-18im^2}{m^2} \right| + x^{-2} \left| \frac{3i-3im^2}{m^2} \right| + \sin(mx) \left| x^{-5} \left| \frac{18i-18im^2}{-m^3} \right| + x^{-3} \left| \frac{-3i+9m^2-6im^4}{m^3} \right| \right. \right. \\
 \cos(mx) & \left. \left. -x/m + x^3 \left| \frac{3+2m^2}{30m} \right| + \sin(mx) \left| 1/m^2 - x^2 \left| \frac{1+4m^2}{10m^2} \right| + x^{-1} \left| \frac{3im^2-3i}{2m^2} \right| \right. \right] \\
 \cos(mx) & \left[x^{-2} \left| \frac{3i-3im^2}{m} \right| + \left| \frac{3i-im^2}{2m} \right| + \sin(mx) \left| x^{-1} \left| \frac{3im^2-3i}{m^2} \right| + x^{-1} \left| \frac{3im^2-3i}{2m^2} \right| \right. \right]
 \end{aligned}$$

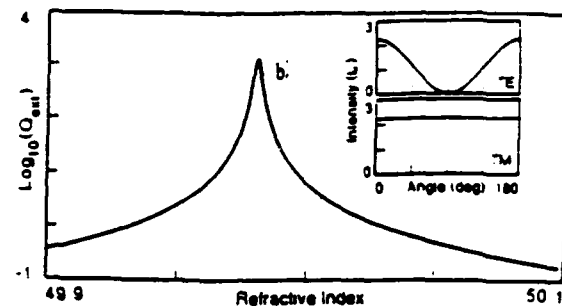


FIG. 3. Extinction efficiency for a small ($r=0.01\lambda$) sphere as a function of real refractive index near the b_1 resonance. Also shown are the scattering intensities for the TE and TM modes on the b_1 resonance ($m=49.98006$).

lation for the resonant sphere (b_1) is completely different than that for the Rayleigh sphere (a_1). The resulting field distributions (also shown in Fig. 3) for the b_1 -resonant sphere will necessarily be different from the Rayleigh sphere (shown in Fig. 2). The TE and TM Rayleigh-sphere intensities are proportional to the TM and TE b_1 -resonant sphere intensities, respectively. For the b_1 mode, the incident electromagnetic field induces a dipole moment *perpendicular* to the incident electric field.

The b_1 resonances do not account for all the resonances shown in Fig. 1. Resonances in the a_1 and b_2 modes occur when $\tan(mx)$ is approximately equal to mx [for large mx , this occurs approximately when $mx \sim (N + \frac{1}{2})\pi$]. The a_1 and b_2 resonances are shown in Fig. 4. These resonances are much narrower [half-width of the order $\Delta(mx)/(mx) \sim 10^{-7}$] than the b_1 resonances [half-width of the order $\Delta(mx)/(mx) \sim 10^{-5}$]. Resonances in the higher-order modes are not as prominent, since the resonant fields are proportional to x^k where $k \geq 3$.

Equations (5) and (6) not only can be used to predict where resonances occur, but can also provide information on the shapes of the resonances. We will now take a closer look at the b_1 resonance. If we express the complex refractive index as $m = m_r + im_i$, where m_r and m_i are both real quantities, we can expand the sine and cosine function about the resonance locations,

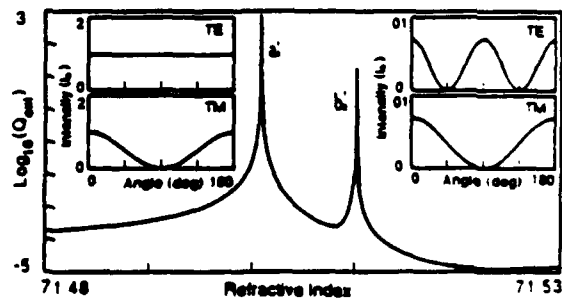


FIG. 4. Extinction efficiency for a small ($r=0.01\lambda$) sphere as a function of real refractive index near the a_1 and b_2 resonances. Also shown are the scattering intensities for the TE and TM modes on the a_1 ($m=71.50079$) and b_2 resonances ($m=71.51015$).

$$\begin{aligned}\sin(mx) &= (-1)^N \sin(mx - N\pi) \\ &\sim (-1)^N [i \sinh(m, x) + \Delta \cosh(m, x)], \\ \cos(mx) &= (-1)^N \cos(mx - N\pi) \\ &\sim (-1)^N [\cosh(m, x) - i \Delta \sinh(m, x)],\end{aligned}\quad (9)$$

where $m, x \sim N\pi$, and $\Delta = m, x - N\pi$. Near resonance, the scattering coefficient b_1 can be simplified:

$$\begin{aligned}b_1 &\sim \frac{\left[x \cosh(m, x) + i \left(\frac{x^2 m}{3} - \frac{1}{m} \right) \sinh(m, x) \right]}{\frac{m}{x} \sinh(m, x) - i \cosh(m, x)} \\ &\times \frac{1}{1 + \Delta/\bar{\Delta}}, \\ \text{where } \bar{\Delta} &= \frac{(x^2 - ix) \cosh(m, x) + m \sinh(m, x)}{-im \cosh(m, x)}\end{aligned}\quad (10)$$

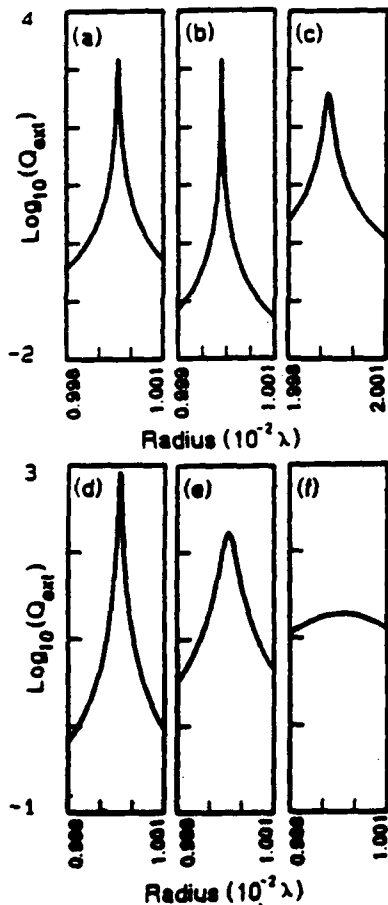


FIG. 5. Extinction efficiency near the b_1 resonances: (a) for an $m = 50.0$ sphere where $N = 1$; (b) for an $m = 100.0$ sphere where $N = 2$; (c) for an $m = 50.0$ sphere where $N = 2$; (d) for an $m = 50.0 + 0.01i$ sphere where $N = 1$; (e) for an $m = 50.0 + 0.01i$ sphere where $N = 1$; and (f) for an $m = 50.0 + 0.1i$ sphere $N = 1$. Radius $r = 0.01\lambda$.

Equation (10) may be simplified if we assume the absorption is small ($m, x \ll 1$),

$$b_1 \sim \frac{x}{x + mm_i} \frac{1}{1 + \frac{(\Delta + x/m)}{ix^2/m + im, x}}. \quad (11)$$

Multiplying Eq. (11) by its complex conjugate yields a Lorentzian function centered at $\Delta = -x/m$, with a half-width of $x^2/m + m, x$. We note that as the absorption is increased from zero, the amplitude of b_1 will decrease, and the half-width will increase. When $mm_i \gg x$, the amplitude will be proportional to $1/m$, and the half-width will be proportional to m_i . These dependencies were reached empirically for larger spheres having moderate refractive indices [9]. This type of analysis may also be performed for the a_1 and b_2 resonances.

The dependence of the line shapes on the size and refractive index is shown in Fig. 5. In Fig. 5(a), the $m = 50.0$ sphere passes through the b_1 resonance as its radius is increased. In Figs. 5(b) and 5(c), we can examine the b_1^2 resonances as the radius of an $m = 100.0$ sphere and an $m = 50.0$ sphere is increased, respectively. Going to a higher index by increasing the refractive index [Fig. 5(b)] results in a narrower resonance. Going to a higher index by increasing the size parameter [Fig. 5(c)] results in a broader resonance. The latter result has been discussed previously for spheres much larger than the wavelength [7, 10, 11]. Figure 5 also shows the shape and the width of the b_1^2 resonance as the refractive index is changed from $m = 50.0 + 0.001i$ [Fig. 5(b)] to

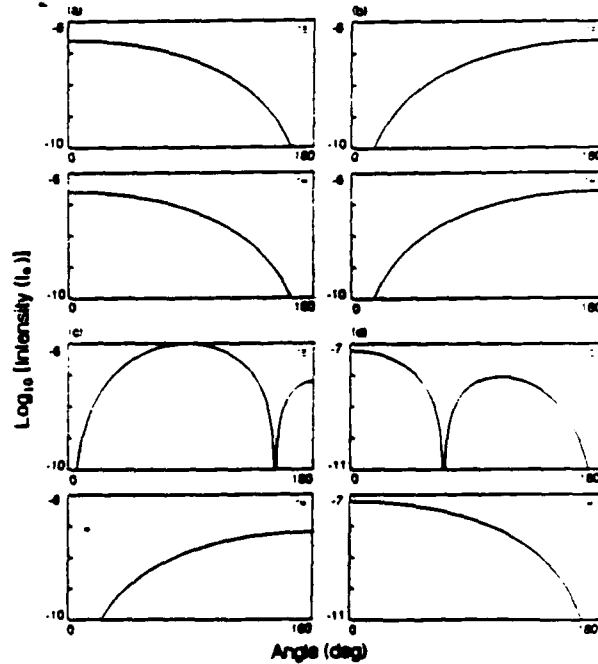


FIG. 6. Angular scattering-intensity distributions for a small ($r = 0.01\lambda$) sphere having refractive indices: (a) $m = 43.666 \cdot 10$, (b) $m = 59.226 \cdot 10$, (c) $m = 71.508 \cdot 44$, and (d) $m = 71.519 \cdot 92$.

$m = 50.0 + 0.01i$ [Fig. 5(e)] to $m = 50.0 + 0.1i$ [Fig. 5(f)]. These figures verify that increasing the imaginary part of the refractive index results in a reduction of the height and an increase in the width of the resonant peak. This conclusion has also been discussed when examining large spheres [7-9,13].

The angular intensity distributions for spheres having refractive indices between resonant values do not necessarily resemble the distributions of either a Rayleigh or a Thomson sphere. Figure 6 shows that cases exist when the forward scatter ($\theta \sim 0^\circ$) is down several orders of magnitude [in cases of Figs. 6(b) and 6(c), $a_1 + b_1 + 5b_2/3 \sim 0$] and when the backscatter ($\theta \sim 180^\circ$) is down several orders of magnitude [in cases of Figs. 6(a) and 6(d), $a_1 - b_1 + 5b_2/3 \sim 0$]. These are important points because most scattering studies of spheres would lead one to believe that the intensity in the forward-scattering or back-scattering directions would not extend several orders of magnitude below the scattered intensity at other scattering angles.

SUMMARY

For the limiting case when sphere size is much smaller than the incident wavelength, the equations describing the scatter are greatly simplified. When two additional limiting conditions on the refractive index are applied, these equations are simplified further. When the refractive index is increased along the real axis, resonance conditions develop that complicate the resulting scatter. Precisely because these resonances occur, no limiting condition can be reached as the complex refractive index is increased along the real axis. Resonances have been studied extensively for large spheres. Studying the resonances in smaller spheres in which the equations are greatly simplified gives insight to the resonance behavior occurring in larger spheres.

ACKNOWLEDGMENTS

This research was supported in part by the U.S. Air Force Office at Scientific Research (AFSC), the Petroleum Research Fund (PRF) and the Itek Corporation.

- [1] Lord Rayleigh, *Philos. Mag.* **41**, 107 (1871); **41**, 274 (1871); **41**, 447 (1871).
- [2] J. J. Thomson, *Recent Researches in Electricity and Magnetism* (Oxford University Press, London, 1893).
- [3] G. Mie, *Ann. Phys. (Leipzig)* **29**, 377 (1908).
- [4] L. Lorenz, *Oeuvres Scientifiques* (Johnson, New York, 1964).
- [5] M. Kerker, P. Scheiner, and D. D. Cooke, *J. Opt. Soc. Am.* **68**, 135 (1978).
- [6] P. Chýlek, *J. Opt. Soc. Am.* **66**, 285 (1976).
- [7] P. Chýlek, J. T. Kiehl, and M. K. W. Ko, *Phys. Rev. A* **18**, 2229 (1978).
- [8] P. Chýlek, J. T. Kiehl, and M. K. W. Ko, *Appl. Opt.* **17**, 3019 (1978).
- [9] H. S. Bennett and G. J. Rosasco, *Appl. Opt.* **17**, 491 (1978).
- [10] P. R. Conwell, P. W. Barber, and C. K. Rushforth, *J. Opt. Soc. Am. A* **1**, 62 (1984).
- [11] J. R. Probert-Jones, *J. Opt. Soc. Am. A* **1**, 822 (1984).
- [12] P. Chýlek, J. D. Pendleton, and R. G. Pinnick, *Appl. Opt.* **24**, 3940 (1985).
- [13] B. A. Hunter, M. A. Box, and B. Maier, *J. Opt. Soc. Am. A* **5**, 1281 (1988).
- [14] P. Chýlek and J. Zhan, *J. Opt. Soc. Am. A* **6**, 1846 (1989).
- [15] P. Chýlek, *J. Opt. Soc. Am. A* **7**, 1609 (1990).
- [16] J. A. Lock, *Appl. Opt.* **29**, 3180 (1990).
- [17] A. Ashkin and J. M. Dziedzic, *Phys. Rev. Lett.* **38**, 1351 (1977).
- [18] R. E. Benner, P. W. Barber, J. F. Owen, and R. K. Chang, *Phys. Rev. Lett.* **44**, 475 (1980).
- [19] A. Ashkin and J. M. Dziedzic, *Appl. Opt.* **20**, 1803 (1981).
- [20] J. F. Owen, P. W. Barber, P. B. Doran, and R. K. Chang, *Phys. Rev. Lett.* **47**, 1075 (1981).
- [21] R. Thurn and W. Kiefer, *Appl. Opt.* **24**, 1515 (1985).
- [22] J. B. Snow, S.-X. Qian, and R. K. Chang, *Opt. Lett.* **10**, 37 (1985).
- [23] R. G. Pinnick, A. Biswas, P. Chýlek, R. Armstrong, H. Latifi, E. Greegan, V. Srivastava, M. Jarzembski, and G. Fernandez, *Opt. Lett.* **13**, 494 (1988).
- [24] P. Chýlek, A. Biswas, M. Jarzembski, V. Srivastava, and R. Pinnick, *Appl. Phys. Lett.* **52**, 1642 (1988).
- [25] H. C. van de Hulst, *Light Scattering by Small Particles* (Dover, New York, 1981).
- [26] M. Kerker, *The Scattering of Light and Other Electromagnetic Radiation* (Academic, New York, 1969).
- [27] C. Bohren and D. Huffman, *Absorption and Scattering of Light by Small Particles* (Wiley, New York, 1983).
- [28] P. Chýlek, *J. Opt. Soc. Am.* **63**, 699 (1973).
- [29] M. O. Scully, *Phys. Rev. Lett.* **67**, 1855 (1991).

Polarized light scattered from rough surfaces

Gorden Videen, Jiunn-Yann Hsu, William S. Bickel, and William L. Wolfe

Optical Sciences Center, University of Arizona, Tucson, Arizona 85721

Received August 6, 1991; revised manuscript received January 21, 1992; accepted February 3, 1992

A facet model is used to predict the polarization states of light scattered from rough surfaces. The states are compared with experimentally determined elements from various types of rough substrates. The experimental data are found to be quite similar to what is predicted by the model.

INTRODUCTION

Before the development of Maxwell's equations and an electromagnetic theory of light, Fresnel was able to deduce the reflection and transmission coefficients for light interacting with a perfectly smooth surface. Since then researchers have been developing theories to obtain surface characteristics (such as the rms roughness) from the light scattered from the surface. These models often develop along a Fourier-transform approach. The bidirectional reflectance distribution function is a standard measurement of the scattered radiance divided by the incident irradiance on the surface.^{1,2} It usually does not take the polarization states of the source or of the scattered light into consideration. Therefore valuable information is missing. To characterize the light scattered from a system completely, one can measure the Mueller scattering matrix.³⁻⁷ This 4×4 matrix contains all the polarization scattering information.

Recently there has been considerable interest in light scattered from rough surfaces.⁸⁻¹² These studies include measurements of the scattered s- and p-polarization states. In only a few instances have authors characterized the polarization states more completely by expressing the resulting scattered light in the form of a Mueller matrix.¹⁴⁻¹⁶ The purpose of this paper is to take a closer look at the polarization state of the light. It is not our interest to examine the intensities, which have been examined in detail in the papers cited above. The simplest model that can predict the polarization state of light scattered from a rough surface uses a geometric-optics approach in which the light is Fresnel reflected from planar surface facets.¹⁷ Although the validity of this model is questionable in nearly all physical situations (it is valid only when the wavelength approaches zero), the model does have one distinct advantage in that the calculations are easily made. In this paper we discuss and develop this facet model. We then compare the Mueller scattering matrices predicted by this facet model with experimental matrices for several surfaces having various surface roughnesses.

FACET MODEL

Figure 1 shows the geometry of the scattering system. The scattering surface is located perpendicular to the

z axis in the *x*-*y* plane. The incident radiation is a plane wave traveling in the *x*-*z* plane, oriented at angle ϑ_{inc} with respect to the *z* axis. The wavelength, wave vector, and refractive index for the plane wave in the nonabsorbing, nonmagnetic incident medium above the surface are λ , \mathbf{k}_1 , and n_1 , respectively. The complex wave vector and refractive index for a plane wave of the same frequency in the medium below the surface are \mathbf{k}_2 and n_2 , respectively. A detector having area A_{det} at a point $P(r_{det}, \vartheta_{det}, \varphi_{det})$ detects light scattered into the solid angle $\Delta\Omega_{det}(r_{det}, \vartheta_{det}, \varphi_{det}, A_{det})$.

The facet model used in this study is based on a geometric-optics approach in which ray optics are valid. Light is assumed to travel in straight lines. When a ray of light intersects a surface, it is Fresnel reflected at that location in such a way that the incident angle at that location is equal to the reflection angle where these angles are measured from the normal to a tangent plane (or surface facet) at that location (Fig. 2). We further simplify our model by considering only the light scattered in the *x*-*z* plane ($\varphi_{det} = 0$) and ignoring rays that reflect off of more than one surface facet. These limitations eliminate the ability of the model to predict any cross polarization ($s \rightarrow p$ or $p \rightarrow s$) or effects such as enhanced backscatter. Of course it is possible to develop a physical theory that has more basis in reality, but it is always interesting to see how well a zeroth-order solution predicts experimental results. And perhaps for some applications the simplest solution is all that is required.

From Fig. 2 we see that only the facets oriented at angle δ with the incident light rays will reflect rays and contribute to the amplitude in the direction ϑ_{det} . Upon reflection, the light is attenuated by a Fresnel reflection factor¹⁸ that depends on the state of linear polarization of the incident light and complex refractive indices of the media above and below the surface:

$$R_{TG}(\delta) = \frac{n_1 \cos \delta - n_2 [1 - (n_1/n_2)^2 \sin^2 \delta]^{1/2}}{n_1 \cos \delta + n_2 [1 - (n_1/n_2)^2 \sin^2 \delta]^{1/2}}, \quad (1)$$

$$R_{TM}(\delta) = \frac{n_1 \cos \delta - n_2 [1 - (n_1/n_2)^2 \sin^2 \delta]^{1/2}}{n_1 \cos \delta + n_2 [1 - (n_1/n_2)^2 \sin^2 \delta]^{1/2}}, \quad (2)$$

where

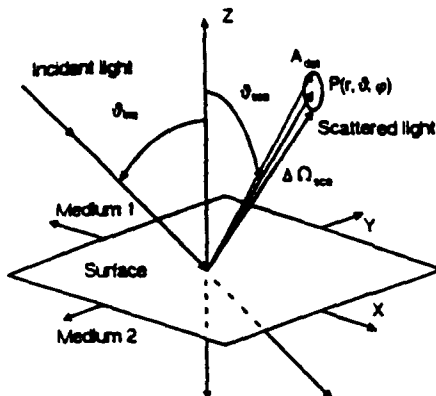


Fig. 1. Geometry of the light scattering at a surface.

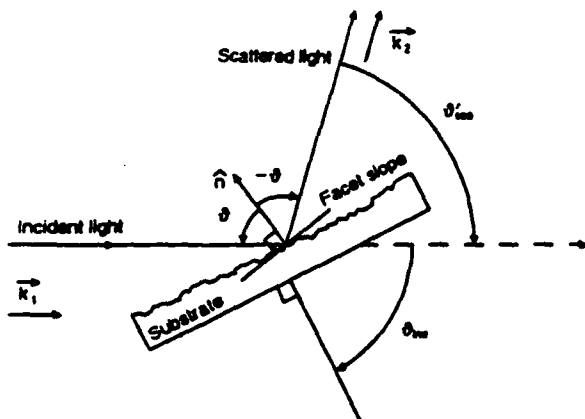


Fig. 2. Geometry of the facet reflection of a rough surface.

$$\theta = (\theta_{inc} - \pi)/2. \quad (3)$$

The subscripts TE and TM correspond to the incident electric- and magnetic-field vectors being transverse to the scattering plane (parallel to the y axis), respectively. We can calculate the electric-far-field amplitude by summing the contributions of the facets reflecting light in the direction θ_{inc}' (a time dependence of $\exp(i\omega t)$ is assumed):

$$E_{T,inc}^{(0)} = \frac{E_{T,inc}^{(0)} R_p(\theta)}{A_{inc}} \int \frac{k_1 \cdot \hat{n}(r)}{k_1} \times \exp(i(k_2 - k_1) \cdot r) \delta_{\alpha(\theta_{inc}' - \alpha)} ds, \quad (4)$$

where the $T^{(0)}$ is used to represent the TE or the TM mode of the scattered and the incident electric fields ($E_{T,inc}^{(0)}$ and $E_{T,scat}^{(0)}$, respectively), A_{inc} is the cross-sectional area of the incident beam upon the substrate, and $\hat{n}(r)$ is the unit normal at position r on the surface. The dot product is a geometric size factor, the exponential function accounts for the phase differences from rays reflecting at different locations on the surface, and the Kronecker delta function ensures that only rays obeying Snell's law contribute to

the amplitude. In terms of the scattering amplitude matrix, this may be expressed as

$$\begin{bmatrix} E_{TM}^{(0)} \\ E_{TE}^{(0)} \end{bmatrix} = \begin{bmatrix} S_2 & S_3 \\ S_4 & S_1 \end{bmatrix} \begin{bmatrix} E_{TM}^{(0)} \\ E_{TE}^{(0)} \end{bmatrix} \quad (5)$$

(note that $S_3 = S_4 = 0$ for light scattered in the x - z plane for the facet model, since there is no cross polarization). Of the 16 elements of the Mueller matrix, only 4 are nonzero or simple multiples of other elements in this case. We use a normalized Mueller scattering matrix given by

$$S_{11}' = S_{11} = \frac{1}{2} (|S_1|^2 + |S_2|^2), \quad (6)$$

$$S_{12}' = S_{12}/S_{11} = \frac{1}{2} (|S_1|^2 - |S_2|^2)/S_{11}, \quad (7)$$

$$S_{33}' = S_{33}/S_{11} = \text{Re}(S_1 S_2^*)/S_{11}, \quad (8)$$

$$S_{34}' = S_{34}/S_{11} = \text{Im}(S_1 S_2^*)/S_{11}. \quad (9)$$

When we normalize the polarization matrix elements by the total intensity matrix element S_{11} (expressing them as a percent polarization), the integral in Eq. (4) cancels from these elements and contributes only to the total intensity matrix element (S_{11}). The polarization matrix elements (which we want to examine) are not affected by this function. In our calculations of matrix element S_{11} , we arbitrarily set this integral to unity. For a perfectly conducting substrate ($n_s \rightarrow \infty$), the scatter would then be independent of the scattering angle. Any deviation in the scatter from a horizontal line (when plotted as a function of the scattering angle) is due to the complex refractive index of the substrate.

Finally, by expressing the matrix elements as a function of the scattering angle θ_{inc}' , which is measured from the path of the incident radiation, we find that the polarization state [Eqs. (7)–(9)] is independent of the incident angle θ_{inc} . The light-scattering Mueller matrices predicted by the facet model for a copper substrate ($n_s = 1.1 - 2.5i$ at $\lambda = 0.4416 \mu\text{m}$)¹⁹ and an aluminum substrate ($n_s = 0.5 - 5.0i$ at $\lambda = 0.4416 \mu\text{m}$),²⁰ both illuminated at $\theta_{inc} = 90^\circ$, are shown as a function of scattering angle θ_{inc}' in Fig. 3. We chose this incident angle (grazing incidence) because it provides the maximum amount of information in the graphs. Choosing a nongrazing incident angle would remove only the leftmost portions of the graphs (the forward scatter) owing to vignetting by the substrate. The differences between these two sets of matrix elements is due mainly to the differences in the absorption coefficients. These sets of matrix elements are compared with the experimentally measured matrix elements for the rough surfaces.

LIGHT-SCATTERING MEASUREMENT

The polar nephelometer used in this study employs the polarization modulation technique developed by Hunt and Huffman.²¹ A complete discussion of the nephelometer design and operation is given in Ref. 20 and also by Perry *et al.*,²² Bickel *et al.*,²³ Bell,²⁴ and Lafelice.²⁵ The measurement requires modulating the incident beam's polarization

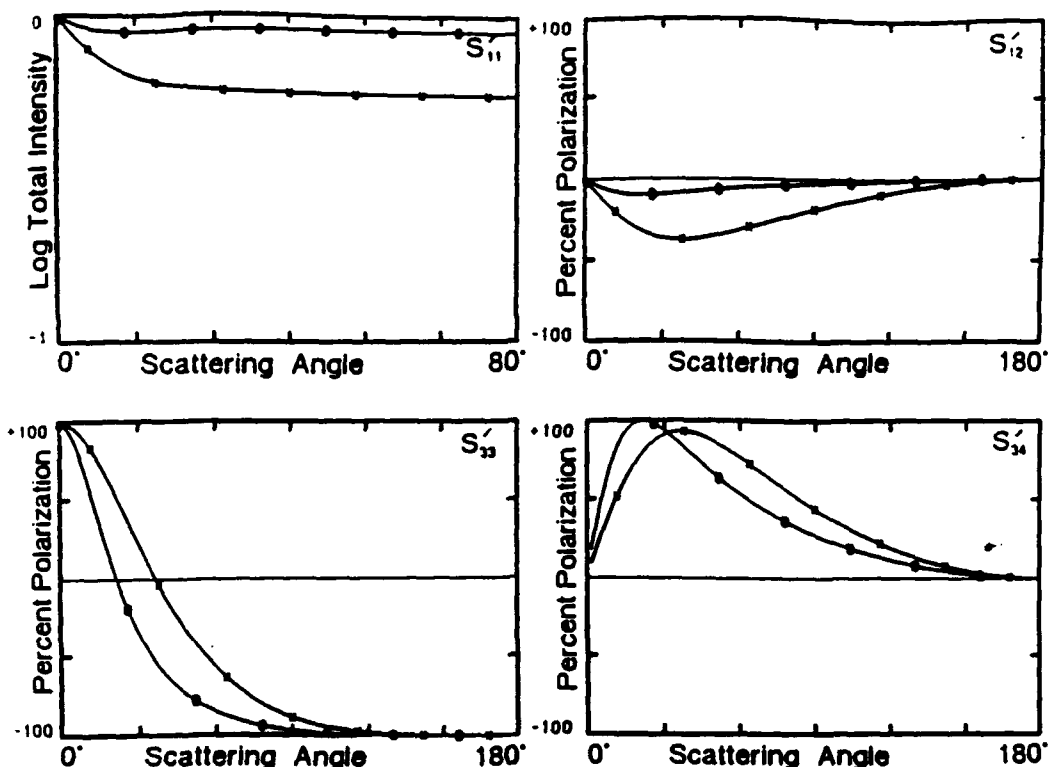


Fig. 3. Light-scattering Mueller matrix elements predicted by the facet model for a copper ($n = 1.1 - 2.5i$) substrate (x) and an aluminum ($n = 0.5 - 5.0i$) substrate (o) illuminated at $\theta_{inc} = 90^\circ$ and $\lambda = 0.4416 \mu\text{m}$.

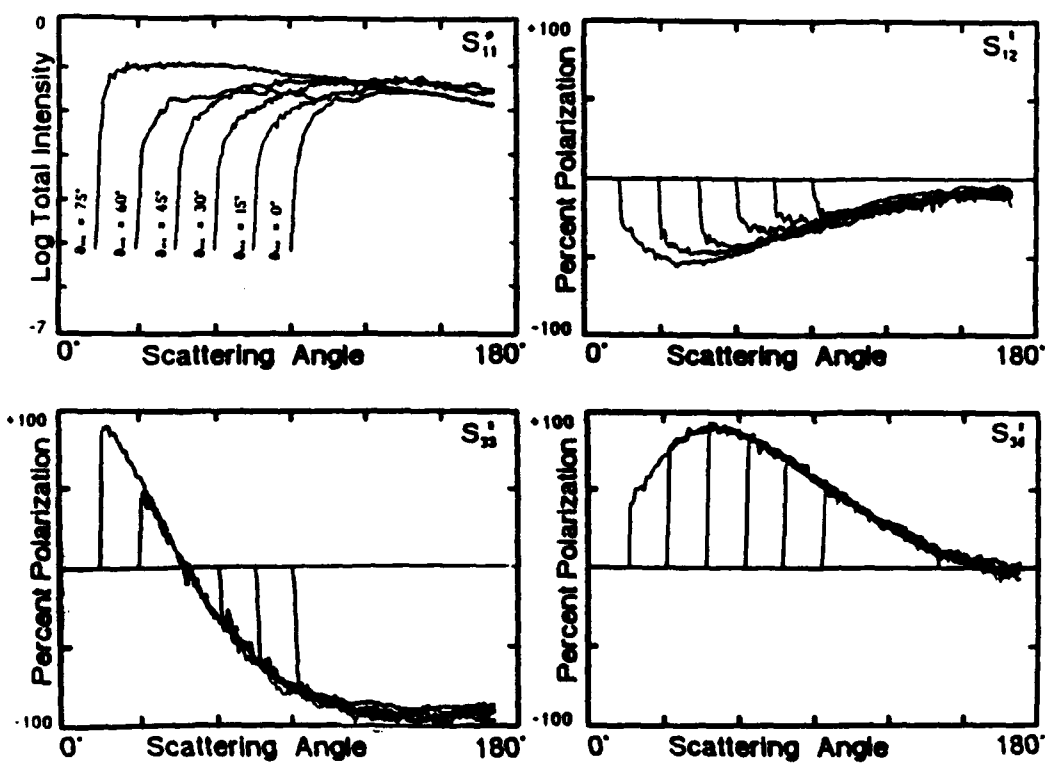


Fig. 4. Experimental light-scattering Mueller matrix elements of a rough copper substrate illuminated at $\theta_{inc} = 0^\circ, 15^\circ, 30^\circ, 45^\circ, 60^\circ$, and 75° ($\lambda = 0.4416 \mu\text{m}$).

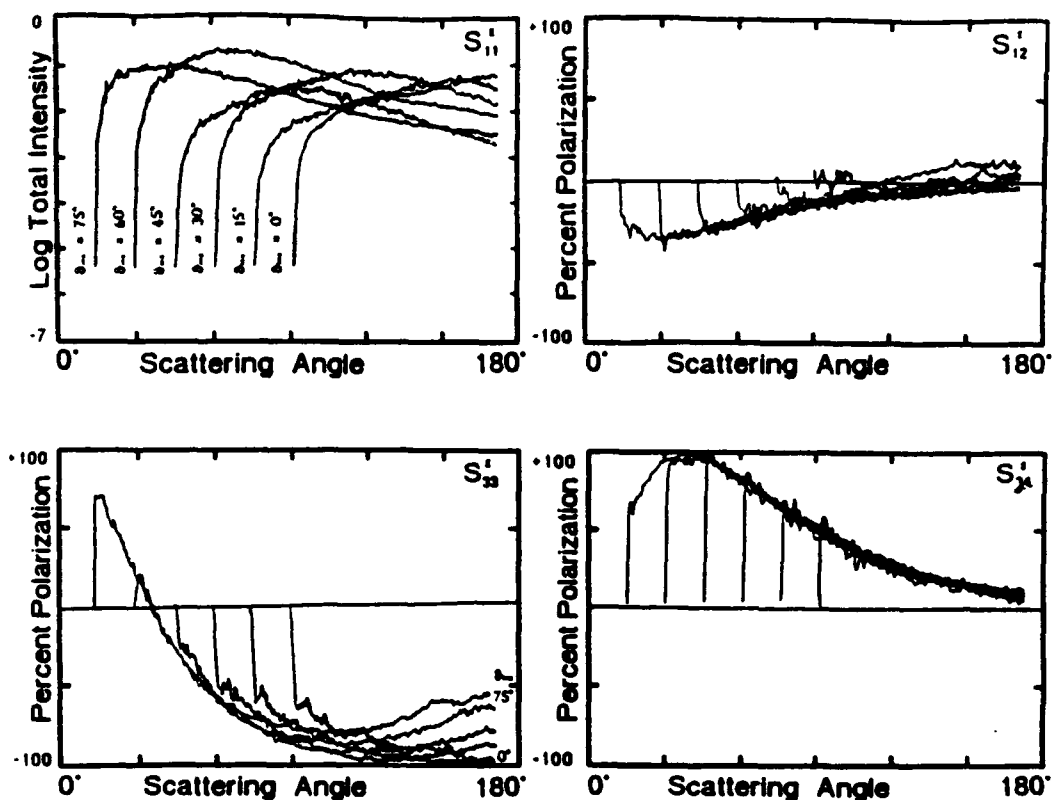


Fig. 5. Experimental light-scattering Mueller matrix elements of a rough aluminum substrate illuminated at $\theta_{\text{ill}} = 0^\circ, 15^\circ, 30^\circ, 45^\circ, 60^\circ$, and 75° ($\lambda = 0.4416 \mu\text{m}$).

state at $\omega_0 = 50 \text{ kHz}$ with a photoelastic modulator while observing the signals carried by the fundamental modulation frequency (ω_0) and second harmonic ($2\omega_0$) of the scattered light ($\lambda = 0.4416 \mu\text{m}$). A lock-in amplifier is used to demodulate the signals. The experimental scattering matrix $S_{ij}^*(\theta)$ can be measured with the proper choice of entrance and exit optics. Normalization of the matrix elements is performed by servoing the photomultiplier tube (RCA 1P21) gain via a constant-current servo, requiring a constant-dc output signal from the detector. This is performed over the entire scan of the detector. The normalized-output $S_{ij}^*(\theta)$ analog signals are collected and sent to a computer. The experimental matrix elements measured are actually combinations of the Mueller matrix:

$$S_{11}^* = S_{11}, \quad (10)$$

$$S_{12}^* = S_{12}/S_{33}, \quad (11)$$

$$S_{33}^* = (S_{12} + S_{34})/(S_{11} + S_{33}), \quad (12)$$

$$S_{34}^* = (S_{14} + S_{34})/(S_{11} + S_{33}). \quad (13)$$

Since there is no mixing of the *s*- and the *p*-polarization states in the facet model ($S_2 = S_4 = 0$), the matrix element $S_{11} = S_{12} = S_{14} = 0$. The normalized matrix elements predicted by the model are equivalent to the measured combinations of matrix elements ($S_{ij}^* = S_{ij}$).

SCATTERING FROM RANDOMLY SCRATCHED SUBSTRATES

The first sets of experimental data are from randomly scratched metal substrates. Figure 4 shows the four independent light-scattering Mueller matrix elements for a



Fig. 6. Micrograph of randomly sanded aluminum substrate.

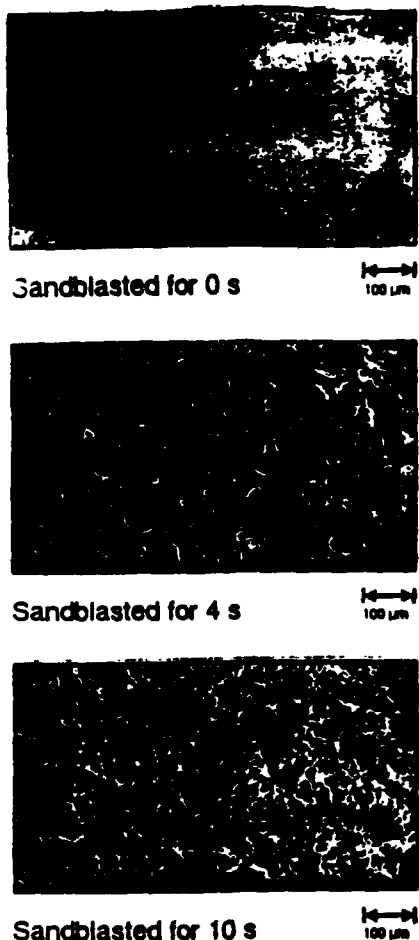


Fig. 7. Micrographs of three different substrates roughened by sandblasting.

randomly scratched copper substrate as a function of scattering angle ϑ_{sc} at six different incident angles ($\vartheta_{\text{inc}} = 0^\circ, 15^\circ, 30^\circ, 45^\circ, 60^\circ$, and 75°). Note that when $|\vartheta_{\text{sc}}| < 90^\circ$ (when there is no vignetting), the polarization elements shown in Fig. 4 are very similar to the polarization elements shown in Fig. 3 predicted by the facet model. Figure 5 shows the four independent light-scattering Mueller matrix elements for a randomly scratched aluminum substrate as a function of scattering angle ϑ_{sc} illuminated at the same incident angles as those of Fig. 4. Note that the peaks (in element S_{12}), valleys (in element S_{34}), and zero crossing points (in element S_{23}) for the aluminum substrate are shifted slightly toward smaller angles, as can be seen in the theoretical elements predicted in Fig. 3. Most notable in the experimental set of matrix elements is that element S_{23} shows more dependence on incident angle for the aluminum substrate than for the copper substrate. Note also that, as the incident angle is increased (toward grazing incidence), the percent polarization of element S_{23} rises toward zero in the backscatter ($\vartheta_{\text{sc}} \sim 180^\circ$). A micrograph of the aluminum substrate used in this study is shown in Fig. 6.

We note that the experimental matrix elements of the aluminum substrate resemble the theoretical matrix elements of the copper substrate of Fig. 3 better than they do the theoretical elements of the aluminum substrate. One possible reason for this is that our experimental substrate is not pure aluminum. When exposed to air, the sample is coated by a layer of aluminum oxide (this occurs much more rapidly for aluminum than for copper). One effect of this is a decrease in the absorption (the imaginary part of the complex refractive index). The effective complex refractive index of the oxidized aluminum substrate is closer to that of copper than pure aluminum.

SCATTERING AS A FUNCTION OF SURFACE ROUGHNESS

The last set of matrix elements is from aluminum substrates that were roughened to different amounts by sandblasting. Eleven nominally smooth mirror substrates were polished to high reflectivity. Substrate 0 remained a mirror and served as a reference, while the other 10 mirrors were sandblasted to increasing roughness (substrate 1 was blasted for 1 s, substrate 2 was blasted for 2 s, etc.). This created a family of related surfaces in which the roughness ranged from zero (a mirror) to saturation (when additional sandblasting did not change the surface). Micrographs of three of these surfaces are shown in Fig. 7.

Figure 8 shows the four independent light-scattering Mueller matrix elements for the reference (mirror) substrate as a function of scattering angle ϑ_{sc} at five different incident angles ($\vartheta_{\text{inc}} = 15^\circ, 30^\circ, 45^\circ, 60^\circ$, and 75°). S_{11} is characterized by a strong specular peak at the angle of reflection and a steep falloff in intensity away from the specular peak. The polarization matrix elements of this substrate only slightly resemble those predicted by the facet model shown in Fig. 3. Note that there is a strong dependence on incident angle in all three sets of polarization matrix elements in Fig. 8, not just S_{23} as was the case for the scratched substrate.

Figure 9 shows the four independent light-scattering Mueller matrix elements for substrate 4 (sandblasted for 4 s) as a function of scattering angle ϑ_{sc} at five different incident angles ($\vartheta_{\text{inc}} = 15^\circ, 30^\circ, 45^\circ, 60^\circ$, and 75°). This set of matrix elements resembles those of the facet model more closely (especially matrix element S_{34}). In the backscatter region, elements S_{12} and S_{23} still show a strong dependence on incident angle, becoming more positive as ϑ_{inc} is increased. Element S_{34} , however, is almost constant in the backscatter region as ϑ_{inc} is increased.

Figure 10 shows the four independent light-scattering Mueller matrix elements for substrate 10 (sandblasted for 10 s, almost to saturation) as a function of scattering angle ϑ_{sc} at five different incident angles ($\vartheta_{\text{inc}} = 15^\circ, 30^\circ, 45^\circ, 60^\circ$, and 75°). The scattering elements of this substrate are very similar to those predicted by the facet model. Again, however, a definite dependence on incident angle in the backscatter region of S_{23} , which is not predicted by the facet model, occurs. As seen in the matrix elements for the other aluminum samples, element S_{34} becomes more positive as ϑ_{inc} is increased.

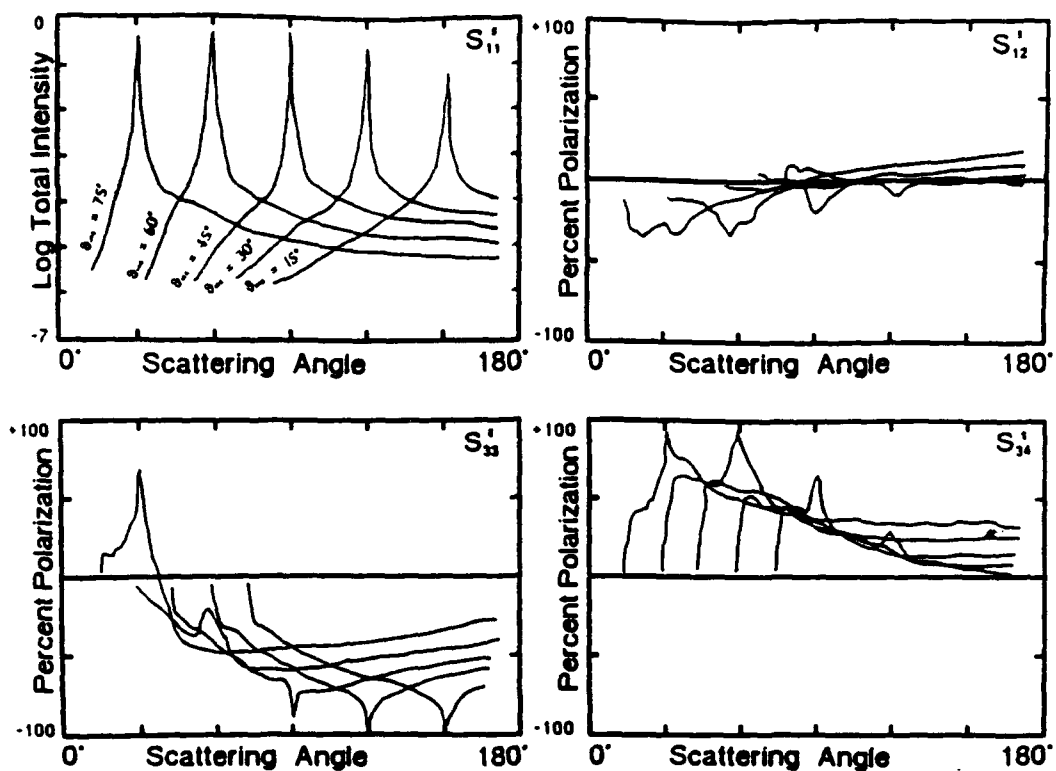


Fig. 8. Experimental light-scattering Mueller matrix elements of reference aluminum substrate 0 (mirror) illuminated at $\theta_{\text{inc}} = 15^\circ, 30^\circ, 45^\circ, 60^\circ$, and 75° ($\lambda = 0.4416 \mu\text{m}$). *ok*

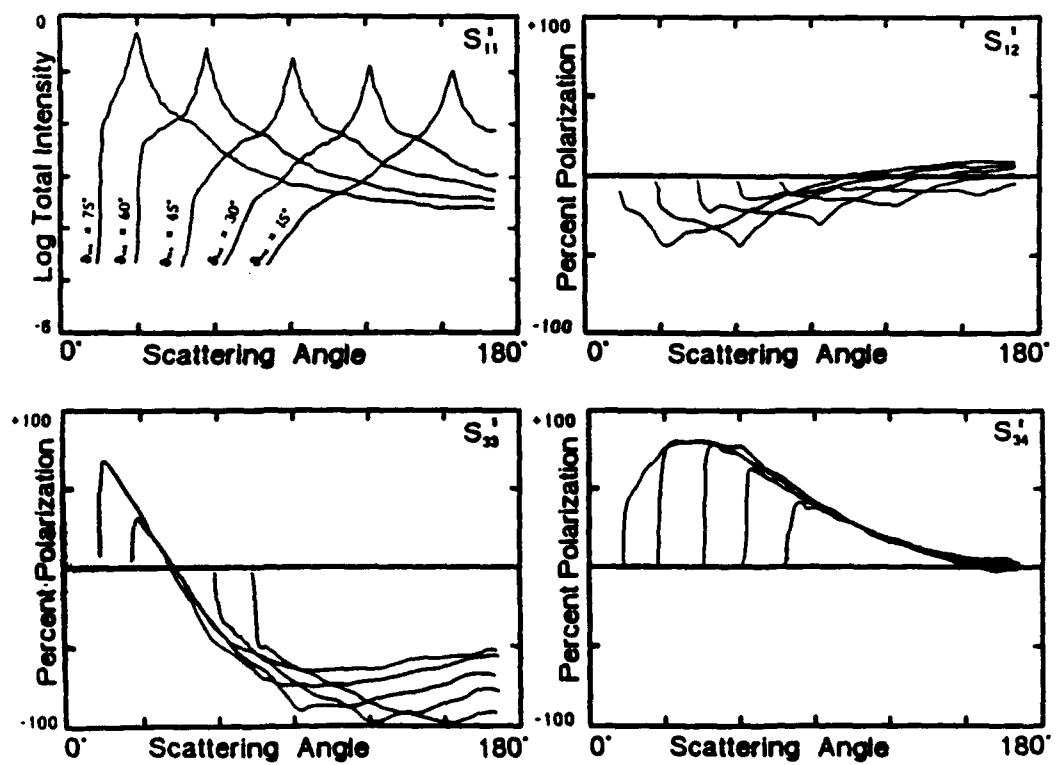


Fig. 9. Experimental light-scattering Mueller matrix elements of substrate 4 (slightly roughened) illuminated at $\theta_{\text{inc}} = 15^\circ, 30^\circ, 45^\circ, 60^\circ$, and 75° ($\lambda = 0.4416 \mu\text{m}$). *ok*

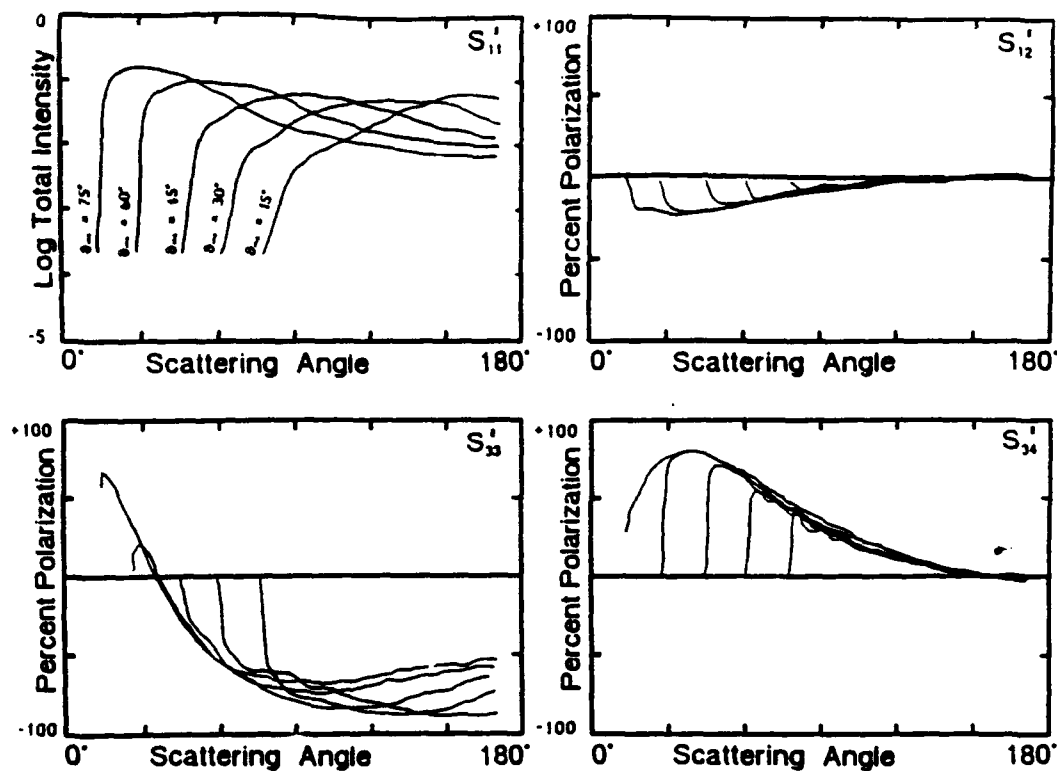


Fig. 10. Experimental light-scattering Mueller matrix elements of roughened substrate 10 illuminated at $\theta_{\text{inc}} = 15^\circ, 30^\circ, 45^\circ, 60^\circ$, and 75° ($\lambda = 0.4416 \mu\text{m}$). OK

CONCLUSION

In this study we used a facet model to predict the polarization states of light scattered from a rough surface. This model predicts that the polarization matrix elements depend solely on the complex refractive index of the surface and are entirely independent of the angle of surface illumination. We emphasize that this is a simple model that can explain only gross scattering features. It is inadequate in explaining the cross-polarization effects ($s \rightarrow p$ and $p \rightarrow s$) that occur in light scattered from rough surfaces. Nevertheless, we find that the experimental matrix elements from substrates of two different materials roughened in different ways agree quite well with this simple model.

ACKNOWLEDGMENTS

This research was supported in part by the U.S. Air Force Office of Scientific Research and by Itek.

REFERENCES

1. F. E. Nicodemus, "Directional reflectance and emissivity of an opaque surface," *Appl. Opt.* **4**, 767-773 (1965).
2. J. C. Stover, *Optical Scattering Measurement and Analysis* (McGraw-Hill, New York, 1990).
3. W. S. Bickel and W. M. Bailey, "Stokes vectors, Mueller matrices, and polarized light," *Am. J. Phys.* **53**, 468-478 (1985).
4. R. Anderson, "Matrix description of radiometric quantities," *Appl. Opt.* **30**, 858-867 (1991).
5. C. Bohren and D. Huffman, *Absorption and Scattering of Light by Small Particles* (Wiley, New York, 1983).
6. H. C. Van de Hulst, *Light Scattering by Small Particles* (Dover, New York, 1976).
7. M. Kerker, *The Scattering of Light and Other Electromagnetic Radiation* (Academic, New York, 1969).
8. V. Celli, A. A. Maradudin, A. M. Marvin, and A. R. McGurn, "Some aspects of light scattering from a randomly rough metal surface," *J. Opt. Soc. Am. A* **2**, 2225-2239 (1985).
9. K. A. O'Donnell and E. R. Méndez, "Experimental study of scattering from characterized random surfaces," *J. Opt. Soc. Am. A* **4**, 1194-1205 (1987).
10. E. Bahar and M. A. Fitzwater, "Depolarization and backscatter enhancement in light scattering from random rough surfaces: comparison of full wave theory with experiment," *J. Opt. Soc. Am. A* **6**, 33-43 (1989).
11. J. M. Soto-Crespo and M. Nieto-Vesperinas, "Electromagnetic scattering from very rough random surfaces and deep reflection gratings," *J. Opt. Soc. Am. A* **6**, 367-384 (1989).
12. M. J. Kim, J. C. Dainty, A. T. Friberg, and A. J. Sant, "Experimental study of enhanced backscattering from one- and two-dimensional random rough surfaces," *J. Opt. Soc. Am. A* **7**, 568-577 (1990).
13. M. Saillard and D. Maystre, "Scattering from metallic and dielectric rough surfaces," *J. Opt. Soc. Am. A* **7**, 982-990 (1990).
14. V. J. Iafelice and W. S. Bickel, "Polarized light-scattering matrix elements for select perfect and perturbed optical surfaces," *Appl. Opt.* **26**, 2410-2415 (1987).
15. W. S. Bickel, R. R. Zito, and V. J. Iafelice, "Polarized light scattering from metal surfaces," *J. Appl. Phys.* **51**, 5392-5398 (1987).
16. K. A. O'Donnell and M. E. Knotts, "Polarization dependence

of scattering from one-dimensional rough surfaces," *J. Opt. Soc. Am. A* **8**, 1126-1131 (1991).

17. P. Beckmann, *The Depolarization of Electromagnetic Waves* (Golem, Boulder, Colo., 1968).
18. J. D. Jackson, *Classical Electrodynamics* (Wiley, New York, 1962).
19. D. E. Gray, ed., *American Institute of Physics Handbook* (McGraw-Hill, New York, 1972).
20. A. J. Hunt and D. R. Huffman, "A new polarization-modulated light scattering instrument," *Rev. Sci. Instrum.* **44**, 1753-1762 (1973).
21. R. J. Perry, A. J. Hunt, and D. R. Huffman, "Experimental determinations of Mueller scattering matrices for nonspherical particles," *Appl. Opt.* **17**, 2700-2710 (1978).
22. W. S. Bickel, J. F. Davidson, D. R. Huffman, and R. Kilkson, "Application of polarization effects in light scattering: a new biophysical tool," *Proc. Natl. Acad. Sci. USA* **73**, 486-490 (1976).
23. B. W. Bell, "Single fiber light scattering matrix: an experimental determination," M.S. thesis (Optical Sciences Center, University of Arizona, Tucson, Ariz., 1981).
24. V. J. Iafelice, "Polarized light scattering matrix elements for select perfect and perturbed surfaces," M.S. thesis (Department of Physics, University of Arizona, Tucson, Ariz., 1985).

Scattering from a small sphere near a surface

Gorden Videen,* Mary G. Turner, Vincent J. Iafelice,
William S. Bickel and William L. Wolfe

Optical Sciences Center
University of Arizona
Tucson, Arizona 85721
(602) 621-1017

Abstract

We examine four different theories which predict the scattered radiation from a system composed of a small sphere and a plane and show that in the far field the scattering amplitude components predicted by these theories are essentially the same. We express the scattering intensities in Mueller matrix representation and examine the far-field Mueller matrix as a function of various parameters.

* Gorden Videen is now at Dalhousie University, Physics Department, Halifax N. S. Canada B3H 3JS

Introduction

Electromagnetic scattering from isolated systems has become well-established in the past century.¹⁻³ Lord Rayleigh did much to initiate this research when he solved for the scattered electromagnetic field from a small sphere or dipole to explain the color of skylight.⁴ The scattered electromagnetic fields surrounding an isolated cylinder were solved by Rayleigh⁵ in 1881 and by von Ignatowsky⁶ in 1905. The scattering from a sphere has been derived numerous times and its complex history has been analyzed extensively.^{2,7,8}

More recently, researchers have concentrated on scattering from more complex systems. Scattering by multiple cylinders by Twersky,⁹ using an order-of-scattering approach; Row,¹⁰ using a Green's function approach; and Olaofe;¹¹ and Yousif and Köhler^{12,13} by satisfying the boundary conditions at the cylinder surfaces. The two-sphere system has been examined by Liang and Lo¹⁴ and Bruning and Lo¹⁵ by satisfying boundary conditions at the surfaces of both spheres. The order-of-scattering approach has been examined by Fuller and Kattawar.^{16,17} Scattering systems composed of a cylinder, sphere or dipole resting on or near a plane surface have been explored by Rao and Barakat,¹⁸ Bobbert and Vlieger,¹⁹ Wind, Vlieger and Bedaux,²⁰ Nahm and Wolfe,²¹ Videen,²² Videen, Wolfe and Bickel,²³ Lindell *et al.*,²⁴ and Muinonen *et al.*²⁵

This last class of problems is closely related to the Sommerfeld^{26,27} half-space problem in which a radiating dipole is located near an interface. In the Sommerfeld problem, a dipole is oscillating vertically or horizontally to the interface, and is the source of the electromagnetic waves. In the scattering

problems, the source is typically at infinity producing plane waves at the interface. These interact with the surface interface and the object placed near it. This scattering system has been discussed extensively by Baños,²⁸ Wait,²⁹ and Rahmat-Samii, Mittra, and Parhami.³⁰

In this manuscript we investigate four different theories that predict the scattered far-field radiation from a small sphere placed near a surface and show that they all yield essentially the same results. Error analysis of the results are considered using an order-of-scattering approach. We then examine these results in the form of the Mueller matrix.³¹

The Solutions

We will be discussing four different solutions from different reference sources that have not used the same mathematical and physical conventions. We therefore adopted the following description and used it for this paper. Differences that arise in other manuscripts will be stated. Figure 1 shows the geometry of the system. A small sphere of refractive index m_{ss} and radius a is suspended a distance d above a surface separating two media: free space where $z > 0$ and a medium of complex refractive index m_{ss} where $z < 0$. The incident plane wave of amplitude E^{in} travels in the x - z plane and is electrically polarized either parallel to the y axis (TE) or parallel to the vector \hat{e} (TM) given by

$$\hat{e} = \hat{x} \cos\alpha - \hat{z} \sin\alpha \quad (1)$$

where α is the angle of incidence of the plane wave measured from the z axis.

To make the dipole approximation, it is necessary that $Im_{\alpha} \ll 1$. The time dependence used in this paper is $\exp(-i\omega t)$. The results will be in the form of the scattering amplitude matrix given by

$$\begin{pmatrix} E_{\theta}^{sc} \\ E_{\varphi}^{sc} \end{pmatrix} = \begin{pmatrix} S_2 & S_3 \\ S_4 & S_1 \end{pmatrix} \begin{pmatrix} E_{TM}^{inc} \\ E_{TE}^{inc} \end{pmatrix} \quad (2)$$

where E_{θ}^{sc} and E_{φ}^{sc} are the scattered electric field components in the θ and φ directions, respectively, and \mathbf{k} is the wave vector for the medium above the surface.

1. Sommerfeld-Rayleigh System

The first theoretical treatment we examine is a modification of the Sommerfeld half-space problem. Sommerfeld was able to solve for the electric fields from a radiating dipole located above an interface. In our scattering problem, the dipole is driven by the incident plane wave. Rayleigh was able to show that a plane wave induces a dipole moment in the direction of the incident electric field. We consider the radiation from a dipole in the x - z plane oriented at angle β from the z axis. The dipole moment is

$$\mathbf{p} = p(\hat{x} \sin\beta + \hat{y} \cos\beta) \delta(x) \delta(y) \delta(z - d). \quad (1.1)$$

Sommerfeld's far-field vector potential has the following form

$$\mathbf{A} = \Pi_{\theta} \hat{x} + \Pi_{\varphi} \hat{y} \quad (1.2)$$

where

$$\Pi_x = \frac{p}{4\pi\epsilon_0} \sin\beta \left[\frac{e^{ikr}}{r} + R_{TE}(\theta) \frac{e^{ikr'}}{r'} \right]$$

$$\Pi_z = \frac{p}{4\pi\epsilon_0} \left\{ \cos\beta \left[\frac{e^{ikr}}{r} - R_{TM}(\theta) \frac{e^{ikr'}}{r'} \right] + 2\sin\beta \cos\phi \sin\theta \cos\theta R_{TE}(\theta) \frac{e^{ikr'}}{r'} \right\} \quad (1.3)$$

and r' is measured from a source point located a distance d below the surface

$$r' = r + 2d\cos\theta \quad (1.4)$$

$$R_{TE}(\theta_i) = \frac{\cos\theta_i - [m_{sur}^2 - \sin^2\theta_i]^{1/2}}{\cos\theta_i + [m_{sur}^2 - \sin^2\theta_i]^{1/2}} \quad (1.5)$$

$$R_{TM}(\theta_i) = - \frac{m_{sur}^2 \cos\theta_i - [m_{sur}^2 - \sin^2\theta_i]^{1/2}}{m_{sur}^2 \cos\theta_i + [m_{sur}^2 - \sin^2\theta_i]^{1/2}} \quad (1.6)$$

$$R_{TE}(\theta_i) \approx \frac{\cos\theta_i - [m_{sur}^2 - \sin^2\theta_i]^{1/2}}{m_{sur}^2 \cos\theta_i + [m_{sur}^2 - \sin^2\theta_i]^{1/2}}. \quad (1.7)$$

The electric fields can be calculated from

$$\mathbf{E} = k^2 \mathbf{H} + \nabla (\nabla \cdot \mathbf{H}) \quad (1.8)$$

which yield the following electric far-field components

$$E_r = 0 \quad (1.9)$$

$$E_\theta = -k^3 \frac{p}{4\pi\epsilon_0} \frac{e^{ikr}}{kr} \left\{ \left[1 - R_{rw}(\theta) \exp(2ikdcos\theta) \right] \sin\theta \cos\beta - \left[1 + R_{rw}(\theta) \exp(2ikdcos\theta) \right] \cos\theta \cos\varphi \sin\beta \right\} \quad (1.10)$$

$$E_\varphi = -k^3 \frac{p}{4\pi\epsilon_0} \frac{e^{ikr}}{kr} \left[1 + R_{rw}(\theta) \exp(2ikdcos\theta) \right] \sin\varphi \sin\beta. \quad (1.11)$$

A dipole moment p is induced in the direction of the incident electric field with a magnitude

$$p = 4\pi\epsilon_0 \frac{m_{ph}^2 - 1}{m_{ph}^2 + 2} a^3 E^{inc}. \quad (1.12)$$

The field incident on the small sphere has two sources. One source is the incident plane wave (including the plane wave which reflects off the surface). The second source is the scattered field of the sphere-surface system. This scattered field is proportional to the induced dipole moment which is proportional to the sphere radius cubed, and at the sphere center is also proportional to $1/2kd$. This term is very small compared with the contribution of the incident plane wave source. We therefore neglect this scattered term and assume the dipole modes of the sphere are driven by the incident plane wave (including the plane wave which reflects off the surface). In sections 4 and 5 we consider this assumption in more detail. We consider two incident polarization states. A TE plane wave will induce a dipole moment in the sphere given by

$$p_{TE} = p \left[1 + R_{TE}(\pi - \alpha) \exp(-2ikd \cos \alpha) \right] \mathbf{g}. \quad (1.13)$$

A TM plane wave will induce a dipole moment in the sphere given by

$$p_{TM} = p \left[1 + R_{TM}(\pi - \alpha) \exp(-2ikd \cos \alpha) \right] \mathbf{g} \cos \alpha - p \left[1 - R_{TM}(\pi - \alpha) \exp(-2ikd \cos \alpha) \right] \mathbf{g} \sin \alpha. \quad (1.14)$$

The scattering amplitude matrix can now be calculated from 1.10 - 1.14:

$$S_1 = Ai \left[1 + R_{TE}(\pi - \alpha) \exp(-2ikd \cos \alpha) \right] \left[1 + R_{TE}(\theta) \exp(2ikd \cos \theta) \right] \cos \varphi \quad (1.15)$$

$$S_2 = Ai \left\{ \left[1 - R_{TM}(\pi - \alpha) \exp(-2ikd \cos \alpha) \right] \left[1 - R_{TM}(\theta) \exp(2ikd \cos \theta) \right] \sin \alpha \sin \theta + \left[1 + R_{TM}(\pi - \alpha) \exp(-2ikd \cos \alpha) \right] \left[1 + R_{TM}(\theta) \exp(2ikd \cos \theta) \right] \cos \alpha \cos \theta \cos \varphi \right\} \quad (1.16)$$

$$S_3 = Ai \left[1 + R_{TE}(\pi - \alpha) \exp(-2ikd \cos \alpha) \right] \left[1 + R_{TE}(\theta) \exp(2ikd \cos \theta) \right] \cos \theta \sin \varphi \quad (1.17)$$

$$S_4 = -Ai \left[1 + R_{TM}(\pi - \alpha) \exp(-2ikd \cos \alpha) \right] \left[1 + R_{TM}(\theta) \exp(2ikd \cos \theta) \right] \sin \varphi \cos \alpha \quad (1.18)$$

where

$$Ai = \frac{\exp(ikr)}{ikr} \frac{m_{ph}^2 - 1}{m_{ph}^2 + 2} (ka)^3 E^{inc}. \quad (1.19)$$

These four components represent the solution to the scattering problem and will be compared with solutions derived from the other theories.

2. Rayleigh limit of sphere-surface scattering

The second method we examine is a limiting approach of the light scattered from a sphere-surface system as the sphere becomes optically small. One of us (Videen) has derived an analytical solution for the scattered far fields from a sphere-surface system (ref. 22). The orientation of the scattering system is slightly different than the one used in section A. Figure 2 shows the scattering system used to predict the scatter from a sphere-surface system. A sphere of radius a is suspended a distance d below a surface separating two media: free space where $z < 0$ and a medium of complex refractive index m_{sr} where $z > 0$. The results may be expressed as

$$S_1 = \sum_{n=0}^{\infty} \sum_{m=-n}^n (-i)^n \exp(im\varphi) \left\{ \left[1 + R_{\text{sr}}(\pi-\theta)(-1)^{m+n} \exp(-2ikdcos\theta) \right] \frac{f_m^{\text{sr}} m}{\sin\theta} \tilde{P}_n^m(\cos\theta) \right. \\ \left. + \left[1 - R_{\text{sr}}(\pi-\theta)(-1)^{m+n} \exp(-2ikdcos\theta) \right] e^{\frac{\pi\epsilon}{m}} \frac{\partial}{\partial\theta} \tilde{P}_n^m(\cos\theta) \right\} E^{\text{sr}} \frac{\exp(ikr)}{-ikr} \quad (2.1)$$

$$S_2 = -i \sum_{n=0}^{\infty} \sum_{m=-n}^n (-i)^n \exp(im\varphi) \left\{ \left[1 - R_{\text{sr}}(\pi-\theta)(-1)^{m+n} \exp(-2ikdcos\theta) \right] \frac{e^{\frac{\pi\epsilon}{m}} m}{\sin\theta} \tilde{P}_n^m(\cos\theta) \right. \\ \left. + \left[1 + R_{\text{sr}}(\pi-\theta)(-1)^{m+n} \exp(-2ikdcos\theta) \right] f_m^{\text{sr}} \frac{\partial}{\partial\theta} \tilde{P}_n^m(\cos\theta) \right\} E^{\text{sr}} \frac{\exp(ikr)}{-ikr} \quad (2.2)$$

$$S_3 = -i \sum_{n=0}^{\infty} \sum_{m=-n}^n (-i)^n \exp(im\varphi) \left\{ \left[1 - R_{\text{sr}}(\pi-\theta)(-1)^{m+n} \exp(-2ikdcos\theta) \right] \frac{e^{\frac{\pi\epsilon}{m}} m}{\sin\theta} \tilde{P}_n^m(\cos\theta) \right. \\ \left. + \left[1 + R_{\text{sr}}(\pi-\theta)(-1)^{m+n} \exp(-2ikdcos\theta) \right] f_m^{\text{sr}} \frac{\partial}{\partial\theta} \tilde{P}_n^m(\cos\theta) \right\} E^{\text{sr}} \frac{\exp(ikr)}{-ikr} \quad (2.3)$$

$$S_4 = \sum_{n=0}^{\infty} \sum_{m=-n}^n (-i)^n \exp(im\varphi) \left\{ \left[1 + R_{TE}(\pi-\vartheta) (-1)^{n+m} \exp(-2ikd\cos\vartheta) \right] \frac{f_{nm}^{TM} m}{\sin\vartheta} \tilde{P}_n^m(\cos\vartheta) \right. \\ \left. + \left[1 - R_{TE}(\pi-\vartheta) (-1)^{n+m} \exp(-2ikd\cos\vartheta) \right] e_{nm}^{TM} \frac{\partial}{\partial \vartheta} \tilde{P}_n^m(\cos\vartheta) \right\} E^{inc} \frac{\exp(ikr)}{-ikr} \quad (2.4)$$

where

$$e_{nm}^{TE} = \left[[1 - R_{TE}(\alpha) (-1)^{n+m} \exp(2ikd\cos\alpha)] a_{nm}^{TE} \right. \\ \left. + R_{TE}(0^\circ) \sum_{n \neq m}^{\infty} (-1)^{n+m} [f_{nm}^{TE} D_n^{(n,m)} - e_{nm}^{TE} C_n^{(n,m)}] \right] Q_n^n \quad (2.5)$$

$$e_{nm}^{TM} = \left[[1 - R_{TM}(\alpha) (-1)^{n+m} \exp(2ikd\cos\alpha)] a_{nm}^{TM} \right. \\ \left. + R_{TM}(0^\circ) \sum_{n \neq m}^{\infty} (-1)^{n+m} [f_{nm}^{TM} D_n^{(n,m)} - e_{nm}^{TM} C_n^{(n,m)}] \right] Q_n^n \quad (2.6)$$

$$f_{nm}^{TE} = \left[[1 + R_{TE}(\alpha) (-1)^{n+m} \exp(2ikd\cos\alpha)] b_{nm}^{TE} \right. \\ \left. + R_{TE}(0^\circ) \sum_{n \neq m}^{\infty} (-1)^{n+m} [f_{nm}^{TE} C_n^{(n,m)} - e_{nm}^{TE} D_n^{(n,m)}] \right] Q_n^n \quad (2.7)$$

$$f_{nm}^{TM} = \left[[1 + R_{TM}(\alpha) (-1)^{n+m} \exp(2ikd\cos\alpha)] b_{nm}^{TM} \right. \\ \left. + R_{TM}(0^\circ) \sum_{n \neq m}^{\infty} (-1)^{n+m} [f_{nm}^{TM} C_n^{(n,m)} - e_{nm}^{TM} D_n^{(n,m)}] \right] Q_n^n. \quad (2.8)$$

and the Lorenz-Mie coefficients are represented by

$$Q_n^r = - \frac{k_{sph}\mu\psi_n(k_{sph}a)\psi_n(ka) - k\mu_{sph}\psi_n'(ka)\psi_n(k_{sph}a)}{k_{sph}\mu\psi_n(k_{sph}a)\xi_n(ka) - k\mu_{sph}\xi_n'(ka)\psi_n(k_{sph}a)} \quad (2.9)$$

$$Q_n^t = - \frac{k_{sph}\mu\psi_n'(ka)\psi_n(k_{sph}a) - k\mu_{sph}\psi_n'(k_{sph}a)\psi_n(ka)}{k_{sph}\mu\xi_n'(ka)\psi_n(k_{sph}a) - k\mu_{sph}\psi_n'(k_{sph}a)\xi_n(ka)} \quad (2.10)$$

$$a_{nm}^{TE} = \frac{2i^{n+2}}{n(n+1)} \frac{\partial \tilde{P}_n^m(\cos\alpha)}{\partial \alpha} \quad (2.11)$$

$$b_{nm}^{TE} = \frac{2i^{n+2}}{n(n+1)} \frac{m \tilde{P}_n^m(\cos\alpha)}{\sin\alpha} \quad (2.12)$$

$$a_{nm}^{TM} = i b_{nm}^{TE} \quad (2.13)$$

$$b_{nm}^{TM} = i a_{nm}^{TE} \quad (2.14)$$

$$C_n^{(n,m)} = C_n^{(n,m)} - \frac{2kd}{2n+3} \frac{n+m+1}{n+1} C_{n+1}^{(n,m)} - \frac{2kd}{2n-1} \frac{n-m}{n} C_{n-1}^{(n,m)} \quad (2.15)$$

$$D_n^{(n,m)} = \frac{-2ikd}{n(n+1)} m C_n^{(n,m)} \quad (2.16)$$

$$C_n^{(0,0)} = \sqrt{2n+1} h_n^{(1)}(2kd) \quad (2.17)$$

$$C_n^{(-1,0)} = -\sqrt{2n+1} h_n^{(1)}(2kd) \quad (2.18)$$

$$\sqrt{(n'-m+1)(n'+m)(2n+1)} c_n^{(n',m)} = \sqrt{(n-m+1)(n+m)(2n+1)} c_n^{(n,m-1)}$$

$$- 2kd \sqrt{\frac{(n-m+2)(n-m+1)}{(2n+3)}} c_{n+1}^{(n,m-1)} - 2kd \sqrt{\frac{(n+m)(n+m-1)}{(2n-1)}} c_{n-1}^{(n,m-1)} \quad (2.19)$$

$$c_n^{(n',m)} = c_n^{(n',-m)} \quad (2.20)$$

$$n' c_n^{(n'-1,0)} \sqrt{\frac{2n+1}{2n'-1}} - (n'+1) c_n^{(n'+1,0)} \sqrt{\frac{2n+1}{2n'+3}} =$$

$$(n+1) c_{n+1}^{(n',0)} \sqrt{\frac{2n'+1}{2n+3}} - n c_{n-1}^{(n',0)} \sqrt{\frac{2n'+1}{2n-1}} \quad (2.21)$$

where $\psi(r)$, and $\xi_n(r)$ are the Riccati-Bessel functions of the first and third kinds, respectively, and the primes denote their derivatives with respect to the argument. The functions $\tilde{P}_n^m(\cos\theta)$ are the normalized associated Legendre polynomials. These results may be simplified when the radius of the sphere becomes small in comparison to the incident wavelength. This can be taken care of by expanding the Bessel functions for small arguments:

$$j_n(\rho) \sim \rho^n \frac{1}{1 \cdot 3 \cdot 5 \dots (2n+1)} \quad (2.22)$$

$$h_n^{(0)}(\rho) \sim -i\rho^{-m} 1 \cdot 3 \cdot 5 \dots (2n-1). \quad (2.23)$$

With the sphere much smaller than λ we now can consider some specific ranges for the sphere-surface separation distance d . First we consider the case

when the separation distance $d \gg \lambda$. In this case the fields scattered by the small sphere (which decay as $1/2kd$) are negligible when compared with the fields of the incident plane-wave. The interaction which occurs between the sphere and image sphere are analytically represented by the summation terms of equations 2.5-2.8. We now consider these terms in detail. The translation coefficients $c_n^{(n,m)}$ are proportional to the spherical Hankel functions which decay as $1/(2kd)$. This dependence can be inferred from the addition theorem for spherical scalar wave functions.^{14,15} As a result, for large values of d the summation terms in equations 2.5-2.8 are negligible. This is confirmed numerically for several cases. Equations 2.5-2.8 may be expressed as

$$e_{nm}^{TE} = [1 - R_{TE}(\alpha)(-1)^{n+m} \exp(2ikd\cos\alpha)] a_{nm}^{TE} Q_i^* \quad (2.24)$$

$$e_{nm}^{TM} = [1 - R_{TM}(\alpha)(-1)^{n+m} \exp(2ikd\cos\alpha)] a_{nm}^{TM} Q_i^* \quad (2.25)$$

$$f_{nm}^{TE} = [1 + R_{TE}(\alpha)(-1)^{n+m} \exp(2ikd\cos\alpha)] b_{nm}^{TE} Q_i^* \quad (2.26)$$

$$f_{nm}^{TM} = [1 + R_{TM}(\alpha)(-1)^{n+m} \exp(2ikd\cos\alpha)] b_{nm}^{TM} Q_i^* \quad (2.27)$$

For small sphere radius a , the coefficients Q_i^* and Q_i^* are proportional to $(k_{sph}a)^{2n+1}$ or greater powers in $k_{sph}a$. Because of the dependence of the coefficients on sphere radius, only the first term ($n = 1$) is significant. This is equivalent to making an electric dipole approximation:

$$Q_i^* \sim 0 \quad (2.28)$$

$$Q_i^* \sim -\frac{2}{3} (ka)^3 \left[\frac{m_{sph}^2 - 1}{m_{sph}^2 + 2} \right]. \quad (2.29)$$

From 2.28 and 2.29, equations 2.1-2.4 reduce to

$$S_1 = \text{Ai} \left[1 + R_{T\ell}(\alpha) \exp(2ikd\cos\alpha) \right] \left[1 + R_{T\ell}(\pi-\theta) \exp(-2ikd\cos\theta) \right] \cos\varphi \quad (2.30)$$

$$S_2 = \text{Ai} \left\{ \left[1 - R_{T\ell}(\alpha) \exp(2ikd\cos\alpha) \right] \left[1 - R_{T\ell}(\pi-\theta) \exp(-2ikd\cos\theta) \right] \sin\alpha \sin\theta + \right. \\ \left. \left[1 + R_{T\ell}(\alpha) \exp(2ikd\cos\alpha) \right] \left[1 + R_{T\ell}(\pi-\theta) \exp(-2ikd\cos\theta) \right] \cos\alpha \cos\theta \cos\varphi \right\} \quad (2.31)$$

$$S_3 = \text{Ai} \left[1 + R_{T\ell}(\alpha) \exp(2ikd\cos\alpha) \right] \left[1 + R_{T\ell}(\pi-\theta) \exp(-2ikd\cos\theta) \right] \cos\theta \sin\varphi \quad (2.32)$$

$$S_4 = -\text{Ai} \left[1 + R_{T\ell}(\alpha) \exp(2ikd\cos\alpha) \right] \left[1 + R_{T\ell}(\pi-\theta) \exp(-2ikd\cos\theta) \right] \sin\varphi \cos\alpha. \quad (2.33)$$

Except for the system orientation, these results would be identical to those given in section 1 for the Sommerfeld-Rayleigh system. Recall that equations 2.30-2.33 were derived assuming a large sphere-surface separation, an assumption not actually necessary. For example, the coefficients $e_m^{\ell\alpha}$ and $f_m^{\ell\alpha}$ are proportional to $Q_m^{\ell\alpha}$ and $Q_m^{\ell\alpha}$, respectively, which are themselves proportional to $(k_{sph}a)^{2\ell+1}$. For equations 2.30-2.33 to be valid, the summation terms of equations 2.5-2.8 must be small compared with the plane wave expansion coefficients $a_m^{\ell\alpha}$ and $b_m^{\ell\alpha}$ (given by 2.11-2.14) which are independent of the sphere radius. All that is required for this to occur is for the translation coefficients to be well-behaved. The translation coefficients are a function of the spherical Hankel functions $h_m^{\ell\alpha}(2kd)$ which become large only when $4\pi d \ll \lambda$. Therefore, equations 2.30-2.33 are valid except when the sphere-surface separation d becomes much smaller than the wavelength.

3. EIT formulation

The third method we examine is the exact-image theory (EIT) developed by Lindell *et al* and Muinonen *et al*. The time-dependence used in these manuscripts is $\exp(i\omega t)$, so some minor adjustments will be needed. Some minor adjustments were made to their equations to account for a slightly different system orientation. Their results for a small sphere near a surface may be expressed as

$$\mathbf{E}_\theta^{ext} = \omega^2 \mu_0 \frac{\exp(-ikr)}{4\pi r} \left\{ \hat{\mathbf{z}} \cdot \mathbf{Q} \cdot \mathbf{E}^{inc} + \hat{\mathbf{z}} \cdot \mathbf{Q} \cdot \mathbf{R}_+ \cdot \mathbf{E}^{inc} \exp(2ikd\cos\alpha) + \hat{\mathbf{z}} \cdot \mathbf{R}_- \cdot \mathbf{Q} \cdot \mathbf{E}^{inc} \exp(-2ikd\cos\theta) + \hat{\mathbf{z}} \cdot \mathbf{R}_- \cdot \mathbf{Q} \cdot \mathbf{R}_+ \cdot \mathbf{E}^{inc} \exp(-2ikd(\cos\theta - \cos\alpha)) \right\} \quad (3.1)$$

$$\mathbf{E}_\phi^{ext} = \omega^2 \mu_0 \frac{\exp(-ikr)}{4\pi r} \left\{ \hat{\mathbf{p}} \cdot \mathbf{Q} \cdot \mathbf{E}^{inc} + \hat{\mathbf{p}} \cdot \mathbf{Q} \cdot \mathbf{R}_+ \cdot \mathbf{E}^{inc} \exp(2ikd\cos\alpha) + \hat{\mathbf{p}} \cdot \mathbf{R}_- \cdot \mathbf{Q} \cdot \mathbf{E}^{inc} \exp(-2ikd\cos\theta) + \hat{\mathbf{p}} \cdot \mathbf{R}_- \cdot \mathbf{Q} \cdot \mathbf{R}_+ \cdot \mathbf{E}^{inc} \exp(-2ikd(\cos\theta - \cos\alpha)) \right\} \quad (3.2)$$

The bold-faced cursive characters are dyadic functions given by

$$\mathbf{R}_+ = \hat{\mathbf{z}}\hat{\mathbf{z}} R_{\text{rr}}(\pi - \alpha) + \hat{\mathbf{y}}\hat{\mathbf{y}} R_{\text{rr}}(\pi - \alpha) - \hat{\mathbf{z}}\hat{\mathbf{z}} R_{\text{rr}}(\pi - \alpha) \quad (3.3)$$

$$\mathbf{R}_- = [\hat{\mathbf{z}}\hat{\mathbf{z}} R_{\text{rr}}(\theta) + \hat{\mathbf{p}}\hat{\mathbf{p}} R_{\text{rr}}(\pi - \alpha)] \cdot [\hat{\mathbf{z}}\hat{\mathbf{z}} + \hat{\mathbf{y}}\hat{\mathbf{y}} - \hat{\mathbf{z}}\hat{\mathbf{z}}] \quad (3.4)$$

$$\mathbf{Q} = [\hat{\mathbf{z}}\hat{\mathbf{z}} + \hat{\mathbf{y}}\hat{\mathbf{y}}] Q_r(2d) + \hat{\mathbf{z}}\hat{\mathbf{z}} Q_z(2d) \quad (3.5)$$

where

$$Q_1(2d) = \frac{B}{1 - \omega^2 \mu_0 B K_1(2d)} \quad (3.6)$$

$$Q_2(2d) = \frac{B}{1 + \omega^2 \mu_0 B K_2(2d)} \quad (3.7)$$

$$B = 4\pi\epsilon_0 \frac{m_{ph}^2 - 1}{m_{ph}^2 + 2} a^3 \quad (3.8)$$

$$K_1(r) = \left\{ -\frac{m_{sw}^2 - 1}{m_{sw}^2 + 1} \frac{\exp(-ikr)}{4\pi r} \left[\frac{1 + ikr + (ikr)^2}{(ikr)^2} \right] + \frac{8m_{sw}^2}{m_{sw}^4 - 1} \int_0^\infty \exp(-ik(z - ip/C)) \right. \\ \times \left. \left\{ 1 + \frac{(2m_{sw}^2 + 1)}{m_{sw}^2} \frac{1 + ik(z - ip/C)}{[ik(z - ip/C)]^2} \right\} \sum_{n=0}^{\infty} n \left(\frac{m_{sw}^2 - 1}{m_{sw}^2 + 1} \right)^n \frac{J_{2n}(p)}{p} dp \right\} \quad (3.9)$$

$$K_2(r) = -2 \left\{ -\frac{m_{sw}^2 - 1}{m_{sw}^2 + 1} \frac{\exp(-ikr)}{4\pi r} \left[\frac{1 + ikr}{(ikr)^2} \right] + \frac{8m_{sw}^2}{m_{sw}^4 - 1} \int_0^\infty \exp(-ik(z - ip/C)) \right. \\ \times \left. \left\{ \frac{1 + ik(z - ip/C)}{[ik(z - ip/C)]^2} \right\} \sum_{n=0}^{\infty} n \left(\frac{m_{sw}^2 - 1}{m_{sw}^2 + 1} \right)^n \frac{J_{2n}(p)}{p} dp \right\} \quad (3.10)$$

$$C = k(\mu_{sw}\epsilon_{sw} - 1)^{1/2}. \quad (3.11)$$

Evaluating the dyadic functions yields the following far-field solutions

$$S_1 = \frac{A'1 Q_1(2d)}{B} \left[1 + R_{11}(\pi - \alpha) \exp(2ikdcos\alpha) \right] \left[1 + R_{11}(\theta) \exp(-2ikdcos\theta) \right] \cos\phi \quad (3.12)$$

$$S_2 = \frac{A'1}{B} \left\{ \left[1 - R_{11}(\pi - \alpha) \exp(2ikdcos\alpha) \right] \left[1 - R_{11}(\theta) \exp(-2ikdcos\theta) \right] Q_1(2d) \sin\alpha \sin\theta + \right. \\ \left. \left[1 + R_{11}(\pi - \alpha) \exp(2ikdcos\alpha) \right] \left[1 + R_{11}(\theta) \exp(-2ikdcos\theta) \right] Q_1(2d) \cos\alpha \cos\theta \cos\phi \right\} \quad (3.13)$$

$$S_3 = \frac{A'iQ_1(2d)}{B} \left[1 + R_{re}(\pi - \alpha) \exp(2ikd \cos \alpha) \right] \left[1 + R_{re}(\theta) \exp(-2ikd \cos \theta) \right] \cos \theta \sin \varphi \quad (3.14)$$

$$S_4 = \frac{-A'iQ_1(2d)}{B} \left[1 + R_{re}(\pi - \alpha) \exp(2ikd \cos \alpha) \right] \left[1 + R_{re}(\theta) \exp(-2ikd \cos \theta) \right] \sin \varphi \cos \alpha \quad (3.15)$$

$$A' = \frac{\exp(-ikr)}{ikr} \frac{m_{ph}^2 - 1}{m_{ph}^2 + 2} (ka)^3 E^m. \quad (3.16)$$

Except for the time dependence and factors of $Q_1(2d)/B$ and $Q_1(2d)/B$, these solutions would be identical to those given in the previous sections. So let us examine these factors a little more closely. These factors depend on the functions K_1 and K_2 (given by equation 3.9 and 3.10) which are a result of the scattered fields interacting with the small sphere. Recall that in the previous sections we assumed that this contribution was negligible so that $Q_1(2d) \sim Q_2(2d) \sim B$. We now examine this approximation in more detail. The contributions of K_1 and K_2 will be greatest when the permittivity of the medium below the surface approaches infinity. In this case, 3.9 and 3.10 simplify to

$$K_1(r) = -\frac{\exp(-ikr)}{4\pi r} \left[\frac{1 + ikr + (ikr)^2}{(ikr)^2} \right] \quad (3.17)$$

$$K_2(r) = 2 \frac{\exp(-ikr)}{4\pi r} \left[\frac{1 + ikr}{(ikr)^2} \right]. \quad (3.18)$$

Equations 3.6 and 3.7 may now be expressed as

$$Q_1(2d) \approx B \left[1 - \exp(-2ikd) \left[1 + 2ikd + (2ikd)^2 \right] \left[\frac{m_{ph}^2 - 1}{m_{ph}^2 + 2} \right] \frac{a^3}{(2d)^3} \right]^{-1}, \quad (3.19)$$

$$Q_s(2d) = B \left[1 - 2\exp(-2ikd) \left[1 + 2ikd \right] \left[\frac{m_{sph}^2 - 1}{m_{sph}^2 + 2} \right] \frac{a^3}{(2d)^3} \right]^{-1}. \quad (3.20)$$

The derivation following from 3.8 has two requirements: the sphere radius is much smaller than the incident wavelength ($a \ll \lambda$) and the sphere radius is much smaller than the wavelength inside the sphere ($m_{sph}a \ll \lambda$). For sphere-surface separations on the order of λ or greater, we have $Q_s(2d) \sim Q_d(2d) \sim B$. This is a direct result of the first requirement, in which, $a \ll d$. We now consider a worst case scenario for our approximation. We note that if the sphere-surface separation is equal to the sphere radius these equations further simplify to

$$Q_s(2d) = B \left[1 - \frac{1}{8} \left[\frac{m_{sph}^2 - 1}{m_{sph}^2 + 2} \right] \right]^{-1} \quad (3.21)$$

$$Q_d(2d) = B \left[1 - \frac{1}{4} \left[\frac{m_{sph}^2 - 1}{m_{sph}^2 + 2} \right] \right]^{-1}. \quad (3.22)$$

The second requirement, that $m_{sph}a \ll \lambda$, helps ensure that we can assume $Q_s(2d) \sim Q_d(2d) \sim B$, saying that the sphere refractive index cannot be large. For a numerical example, this assumption is good to within 10% for a lossless dielectric sphere of refractive index $m_{sph} = 1.6$. Although this accuracy does not seem outstanding we should remember that this is the worst case in which the medium below the surface is a perfect conductor and the sphere-surface separation is much smaller than the wavelength.

4. Projection model

The three theoretical methods thus far discussed all yield the same results. We now discuss one more approach which is particularly insightful. The method is based on the double interaction model of Nahm and Wolfe and dipole scattering discussed by van de Hulst. In the double interaction model, the scattered light from a sphere near a surface can reach a detector by one of four paths. It may 1.) strike the sphere directly and scatter directly to the detector; 2.) strike the sphere directly, scatter to the surface which reflects light to the detector; 3.) reflect off the surface, strike the sphere and scatter to the detector; or 4.) reflect off the surface, strike the sphere, scatter to the surface which reflects light to the detector (see Fig. 3). The light scattered by the sphere, reflecting off the surface and striking the dipole is assumed to be very small compared with the incident fields and contribute only negligibly to the scattered fields. Assuming the small sphere is a dipole, the magnitude of the scattered electric field is proportional to the dipole moment projected onto a plane perpendicular to the radius vector. Although it is not necessary, for the purpose of this discussion, we restrict our detector to the x-z plane ($\phi = 0^\circ$). We sum the four components of the TE mode that make up matrix element S_1 as

$$\begin{aligned}
 S_1 &= A_1 \left[1 + R_{tt}(\pi-\alpha) \exp(-2ikd\cos\alpha) + R_{tt}(\theta) \exp(2ikd\cos\theta) \right. \\
 &\quad \left. + R_{tt}(\pi-\alpha) R_{tt}(\theta) \exp(2ikd(\cos\theta - \cos\alpha)) \right] \\
 &= A_1 \left[1 + R_{tt}(\pi-\alpha) \exp(-2ikd\cos\alpha) \right] \left[1 + R_{tt}(\theta) \exp(2ikd\cos\theta) \right] \quad (4.1)
 \end{aligned}$$

Similarly, we sum the four components of the TM mode that make up element S_2 as

$$\begin{aligned}
 S_2 = & \text{Ai} \left[\cos(\theta-\alpha) - R_{TM}(\pi-\alpha)\cos(\pi-\theta-\alpha)\exp(-2ikdcos\alpha) - R_{TM}(\theta)\cos(\pi-\theta-\alpha)\exp(2ikdcos\theta) \right. \\
 & \left. + \cos(\theta-\alpha)R_{TM}(\pi-\alpha)R_{TM}(\theta)\exp(2ikd(\cos\theta-\cos\alpha)) \right] \\
 = & \text{Ai} \left\{ \left[1 - R_{TM}(\pi-\alpha)\exp(-2ikdcos\alpha) \right] \left[1 - R_{TM}(\theta)\exp(2ikdcos\theta) \right] \sin\alpha\sin\theta + \right. \\
 & \left. \left[1 + R_{TM}(\pi-\alpha)\exp(-2ikdcos\alpha) \right] \left[1 + R_{TM}(\theta)\exp(2ikdcos\theta) \right] \cos\alpha\cos\theta \right\}. \quad (4.2)
 \end{aligned}$$

Since $\phi = 0^\circ$, elements $S_3 = S_4 = 0$. Although this solution is derived using a very simple model, the results are identical to equations 1.15 - 1.19 ($\phi = 0^\circ$).

5. Multiple scattering interactions

We derived the first-order terms in the scattering amplitude matrix in the first section in equations 1.15-1.19 where order refers to the number of interactions that a beam of light undergoes with the small sphere before being scattered to the far field. The order-of-scattering approach can be used to add correcting terms to these results. Using this approach, the scattered field from one portion of the system is considered to be an incident field on another portion of the system. Then the scattered field from this portion of the system is calculated and the process is repeated until the desired accuracy is achieved. To perform a rigorous order-of-scattering analysis requires perform-

ing translations of the scattered fields and the resulting equations are similar to those in section 2, containing the same translation coefficients. Such a derivation is not our intent. Insight into the problem can be gained by considering the interaction which occurs between the scattered dipole radiation terms which are spherical waves reflecting off the plane surface and interacting with the dipole. Since the sphere is much smaller than the wavelength, we can assume the field to be approximately constant over the volume of the sphere and avoid the cumbersome translation. It is relatively straightforward to calculate the effect of the second order terms. This case includes the fields scattered from the small sphere, striking the plane surface and inducing a dipole moment in the small sphere. From equations 1.12-1.19 we get

$$p_{TE2} = 4\pi\epsilon_0 \left[\frac{m_{ph}^2 - 1}{m_{ph}^2 + 2} \right]^2 k^3 a^4 \frac{\exp(2ikd)}{2kd} \left[1 + R_T(\pi-\alpha) \exp(-2ikd\cos\alpha) \right] R_T(0) E^{\infty} \mathbf{y} \quad (5.1)$$

for the TE case and

$$p_{TM2} = 4\pi\epsilon_0 \left[\frac{m_{ph}^2 - 1}{m_{ph}^2 + 2} \right]^2 k^3 a^4 \frac{\exp(2ikd)}{2kd} \left[1 + R_T(\pi-\alpha) \exp(-2ikd\cos\alpha) \right] R_T(0) E^{\infty} \mathbf{z} \cos\alpha \quad (5.2)$$

for the TM case. Since the scattered fields are proportional to the dipole moment induced in the small sphere, it is apparent that the second order dipole moment will have only a negligible effect since it is proportional to $k^2 a^3/d$ times the first order dipole moment.

We can include the effects of all the higher order scattering interaction terms since the induced dipole moment is due to the incident field and the scattered field from the small sphere (from equations 1.12-1.19):

$$\mathbf{p}_{\text{rr}} = p \left[1 + R_{\text{rr}}(\pi-\alpha) \exp(-2ikd \cos \alpha) \right] \mathbf{\hat{y}} + p_{\text{rr}} \frac{m_{\text{sp}}^2 - 1}{m_{\text{sp}}^2 + 2} k^3 a^3 \frac{\exp(2ikd)}{2kd} R_{\text{rr}}(0) \quad (5.3)$$

$$\begin{aligned} \mathbf{p}_{\text{rm}} = p \left[1 + R_{\text{rm}}(\pi-\alpha) \exp(-2ikd \cos \alpha) \right] \mathbf{\hat{x}} \cos \alpha - p \left[1 - R_{\text{rm}}(\pi-\alpha) \exp(-2ikd \cos \alpha) \right] \mathbf{\hat{z}} \sin \alpha \\ + p_{\text{rm},x} \frac{m_{\text{sp}}^2 - 1}{m_{\text{sp}}^2 + 2} k^3 a^3 \frac{\exp(2ikd)}{2kd} R_{\text{rm}}(0) \end{aligned} \quad (5.4)$$

where $p_{\text{rm},x}$ is the x component of \mathbf{p}_{rm} . These two equations yield dipole moments of the form

$$\mathbf{p}_{\text{rr}} = \left[1 - \frac{m_{\text{sp}}^2 - 1}{m_{\text{sp}}^2 + 2} k^3 a^3 \frac{\exp(2ikd)}{2kd} R_{\text{rr}}(0) \right]^{-1} p \left[1 + R_{\text{rr}}(\pi-\alpha) \exp(-2ikd \cos \alpha) \right] \mathbf{\hat{y}} \quad (5.5)$$

$$\begin{aligned} \mathbf{p}_{\text{rm}} = \left[1 - \frac{m_{\text{sp}}^2 - 1}{m_{\text{sp}}^2 + 2} k^3 a^3 \frac{\exp(2ikd)}{2kd} R_{\text{rm}}(0) \right]^{-1} p \left[1 + R_{\text{rm}}(\pi-\alpha) \exp(-2ikd \cos \alpha) \right] \mathbf{\hat{x}} \cos \alpha \\ - p \left[1 - R_{\text{rm}}(\pi-\alpha) \exp(-2ikd \cos \alpha) \right] \mathbf{\hat{z}} \sin \alpha \end{aligned} \quad (5.6)$$

Note that the first terms in the expansions of equations 5.5 and 5.6 are the second order correction terms of equations 5.1 and 5.2. The scattering coefficients can be expressed as

$$S_1 = iAC [1 + R_{rt}(\pi-\alpha)\exp(2ikdcos\alpha)] [1 + R_{rt}(\theta)\exp(-2ikdcos\theta)] \cos\varphi \quad (5.7)$$

$$S_2 = iA \left\{ C [1 - R_{rt}(\pi-\alpha)\exp(2ikdcos\alpha)] [1 - R_{rt}(\theta)\exp(-2ikdcos\theta)] \sin\alpha \sin\theta + \right. \\ \left. [1 + R_{rt}(\pi-\alpha)\exp(2ikdcos\alpha)] [1 + R_{rt}(\theta)\exp(-2ikdcos\theta)] \cos\alpha \cos\theta \cos\varphi \right\} \quad (5.8)$$

$$S_3 = iAC [1 + R_{rt}(\pi-\alpha)\exp(2ikdcos\alpha)] [1 + R_{rt}(\theta)\exp(-2ikdcos\theta)] \cos\theta \sin\varphi \quad (5.9)$$

$$S_4 = -iAC [1 + R_{rt}(\pi-\alpha)\exp(2ikdcos\alpha)] [1 + R_{rt}(\theta)\exp(-2ikdcos\theta)] \sin\varphi \cos\alpha \quad (5.10)$$

$$C = \left[1 - \frac{m_{sph}^2 - 1}{m_{sph}^2 + 2} k^2 a^3 \frac{\exp(2ikd)}{2kd} R_{rt}(0) \right]^{-1} \quad (5.11)$$

since $R_{rt}(0) = R_{rt}(0)$. Note that the correction term C varies only slightly from 1 since $k^2 a^3 / d \ll 1$. This appears to contradict the analysis of section 3 where the scattered fields could vary by as much as 10%. It should be noted that the analysis in section 3 was for a very small separation distance d ; whereas the analysis in this section was derived from the radiation terms of the dipole scatter and is invalid for small separations d . In the near-field scatter from a small sphere, there are scattering terms proportional to $(kr)^{-2}$ which become significant along with a radial component. These terms were not considered in this analysis.

Results

Up to this point we have derived the far-field electric fields for a small sphere near an interface using four different formal solutions. We now examine the results of these derivations which are expressed by equations 1.15-1.19. Rather than examine just the intensities of the TE and TM components, we will put the results in Mueller matrix form, since the 16-element Mueller matrix contains the phase information of the scattered fields. We will also restrict ourselves to the plane of incidence ($\phi = 0^\circ$). The particular Mueller matrix formulation we use is given by

$$S_{11} = \frac{1}{2} [|S_{11}|^2 + |S_{21}|^2],$$

$$S_{21} = \frac{1}{2} [|S_{11}|^2 - |S_{21}|^2] / S_{11},$$

$$S_{31} = \text{Re}(S_{11}S_{11}^*) / S_{11}, \text{ and}$$

$$S_{41} = -\text{Im}(S_{11}S_{11}^*) / S_{11}. \quad (S.1)$$

With the detector in the plane of incidence ($\phi = 0^\circ$), the other scattering $S_{ij}(\theta)$ are either zero or simple multiples of these elements. It should be noted that the results derived do not include the specular component of the scattered field.

The first set of scattering $S_{ij}(\theta)$ we consider are shown in Figure 4. The system is illuminated at normal incidence ($\alpha = 180^\circ$) and optical constants

of the medium below the plane are chosen to correspond with an aluminum surface ($m_{\text{sub}} = 0.5 + 5.0i$ at $\lambda = 0.4416\mu\text{m}$). Scattering $S_{\text{u}}(\theta)$ are shown for four different sphere-surface distances d . Note that when the system is illuminated at normal incidence, equations 4.1 and 4.2 reduce to two periodic functions in d . One of the functions is independent of θ and determines the maximum amplitude of the signal. This amplitude cycles through maximum and minimum values with a period of $d = \lambda/2$. If the medium below the surface is a lossless dielectric, then $R_{\text{r}}(\alpha)$ is real and amplitude minima occur when $d = n\lambda/2$ and amplitude maxima occur when $d = \lambda/4 + n\lambda/2$. If the medium below the surface is lossy, then $R_{\text{r}}(\alpha)$ is complex and a phase difference will be introduced. The parameters chosen in Fig. 4 introduce only a slight phase difference. Matrix element $S_{\text{u}}(\theta)$ shows that the highest signal intensities (of the four curves shown) occur when $d = \lambda/4$ and the lowest signal intensities occur when $d = \lambda/2$.

The oscillatory structure in the matrix elements of Fig. 4 is also periodic in d and is very nearly periodic in θ . From equations 4.1 and 4.2, we would expect the total intensity, $S_{\text{u}}(\theta)$, to be at minima values approximately when $2d\cos\theta = n\lambda$ (where n is an integer) for a dielectric medium below the surface. For the $d = \lambda/2$ curves of Fig. 4, we would expect a minimum to occur at $\theta = 0^\circ$. The minima have been displaced slightly because the medium below the substrate is slightly conducting. Note that spikes and inflection points occur in the polarization matrix elements at the angular locations where the intensity signals are at minima.

Another set of matrix elements is shown in Figure 5 for the same systems as Fig. 4, but illuminated at near-grazing $\alpha = 101^\circ$. In Fig. 4, where the illumination was at normal incidence, the sets of matrix elements were very similar. Changing the incident angle away from normal incidence breaks the symmetry and increases the complexity of the matrix elements.

Conclusion

Four theoretical models were examined and found to predict the same scattering signals from a small sphere suspended above a plane surface interface. The approximation breaks down when the sphere-surface separation also becomes much smaller than the wavelength. In this case the maximum error in the approximation is on the order of 10% of the theoretical value.

Acknowledgements

This research was supported in part by the Air Force Office of Scientific Research and by the Itek Corporation.

References

1. H. C. van de Hulst, Light Scattering by Small Particles (Wiley, New York, 1957).
2. M. Kerker, The Scattering of Light and Other Electromagnetic Radiation (Academic, New York, 1969).
3. C. F. Bohren and D. R. Huffman, Absorption and Scattering of Light by Small Particles (Wiley, New York, 1983).
4. Lord Rayleigh, "On the scattering of light by small particles," Phil. Mag., 41, 447-454 (1871).
5. Lord Rayleigh, "On the electromagnetic theory of light," Phil. Mag., 12, 81-101 (1881).
6. W. von Ignatowsky, "Reflexion elektromagnetischer Wellen an einem Draht," Ann. Physik, 18, 495- 522 (1905).
7. N. A. Logan, "Early history of the Mie solution," J. Opt. Soc. Am. 52, 342-343 (1962).
8. N. A. Logan, "Survey of some early studies of the scattering of plane waves by a sphere," Proc. IEEE 53, 773-785 (1965).
9. V. Twersky, "Multiple scattering of radiation by an arbitrary configuration of parallel cylinders," J. Acoust. Soc. Am. 24, 42-46 (1952).
10. R. V. Row, "Theoretical and experimental study of electromagnetic scattering by two identical conducting cylinders," J. Appl. Phys. 26, 666-675 (1955).
11. G. O. Olafse, "Scattering by two cylinders," Radio Sci. 5, 1351-1360 (1970).
12. H. A. Yousif and S. Köhler, "Scattering by two penetrable cylinders at oblique incidence. I. The analytical solution," J. Opt. Soc. Am. A 5, 1085-1096 (1988).

13. H. A. Yousif and S. Köhler, "Scattering by two penetrable cylinders at oblique incidence. II. Numerical examples," *J. Opt. Soc. Am. A*, 5, 1097-1104 (1988).
14. C. Liang and Y. T. Lo, "Scattering by two spheres," *Radio Science*, 2, 1481-1495 (1967).
15. J. H. Brunning and Y. T. Lo, "Multiple scattering of EM waves by spheres Part I — multipole expansion and ray-optical solution," *IEEE Trans. Antennas Propag. AP-19*, 378-390 (1971).
16. K. A. Fuller and G. W. Kattawar, "Consummate solution to the problem of classical electromagnetic scattering by an ensemble of spheres. I: Linear chains," *Opt. Lett.*, 13, 90-92 (1988).
17. K. A. Fuller and G. W. Kattawar, "Consummate solution to the problem of classical electromagnetic scattering by an ensemble of spheres. II: Clusters of arbitrary configuration," *Opt. Lett.*, 13, 1063-1065 (1988).
18. T. C. Rao and R. Barakat, "Plane-wave scattering by a conducting cylinder partially buried in a ground plane I. TM case," *J. Opt. Soc. Am. A*, 6, 1270-1280 (1989).
19. P. A. Bobbert and J. Vlieger, "Light scattering by a sphere on a substrate," *Physica*, 137A, 209-241 (1986).
20. M. M. Wind, J. Vlieger, and D. Bedeaux, "The polarizability of a truncated sphere on a substrate I," *Physica* 141A, 33-57 (1987).
21. K. Nahm and W. L. Wolfe, "Light-scattering models for spheres on a conducting plane: comparison with experiment," *Appl. Opt.* 26, 2995-2999 (1987).

22. G. Videen, "Light scattering from a sphere on or near a surface," *JOSA A* 8, 483-489 (1991); *Errata, JOSA A* 9, 844-845 (1992).
23. G. Videen, W. L. Wolfe, and W. S. Bickel, "The light-scattering Mueller matrix for a surface contaminated by a single particle in the Rayleigh limit," *Opt. Eng.* 31, 341-349 (1992).
24. I. V. Lindell, A. H. Sihvola, K. O. Muinonen, and P. W. Barber, "Scattering by a small object close to an interface. I. Exact-image theory formulation," *JOSA A* 8, 472-476 (1991).
25. K. O. Muinonen, A. H. Sihvola, I. V. Lindell, and K. A. Lumme, "Scattering by a small object close to an interface. II. Study of backscattering," *JOSA A* 8, 477-482 (1991).
26. A. N. Sommerfeld, "Ueber die Ausbreitung der Wellen in der drahtlosen Telegraphie," *Ann. Physik*, 28, 665-695 (1909).
27. A. N. Sommerfeld, "Ueber die Ausbreitung der Wellen in der drahtlosen Telegraphie," *Ann. Physik*, 81, 1135-1153 (1926).
28. A. Baños, Dipole Radiation in the Presence of a Conducting Half-Space (Pergamon Press, Oxford, 1966).
29. J. R. Wait, Electromagnetic Wave Theory (Harper and Row, New York, 1985).
30. Y. Rahmat-Samii, R. Mittra, and P. Parhami, "Evaluation of Sommerfeld integrals for lossy half-space problems," *Electromagnetics* 1, 1-28 (1981).
31. W. S. Bickel and W. M. Bailey, "Stokes vectors, Mueller matrices, and polarized scattered light," *Am. J. Phys.* 53, 468-478 (1985).
32. B. Friedman and J. Russek, "Addition theorems for spherical waves," *Quart. Appl. Math.* 12, 13-23 (1954).

Figure Captions

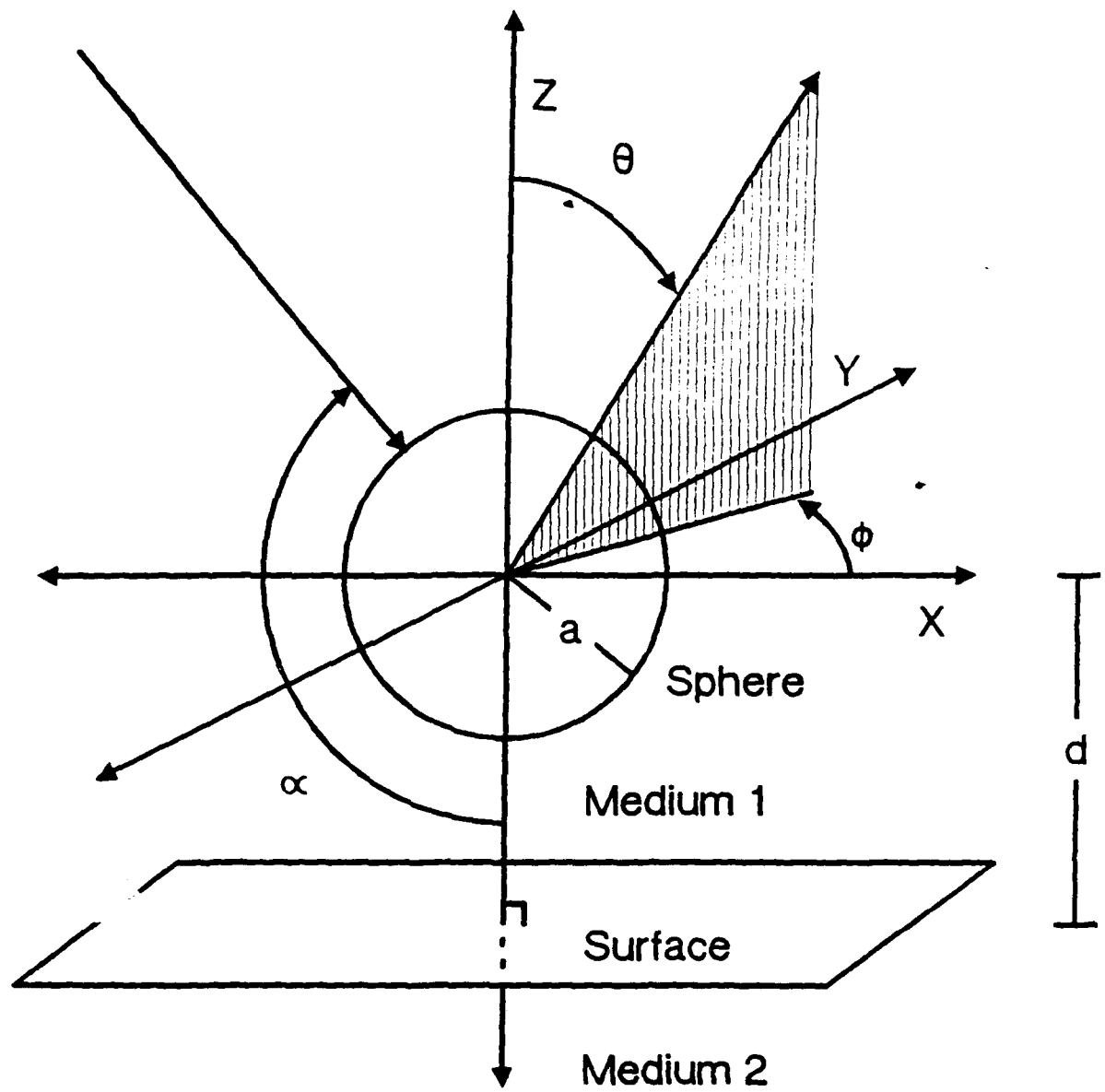
Fig. 1. The geometry of the scattering system. A sphere of radius a is located a distance d above a surface. A plane wave travels in the x - z plane at angle α with respect to the z axis.

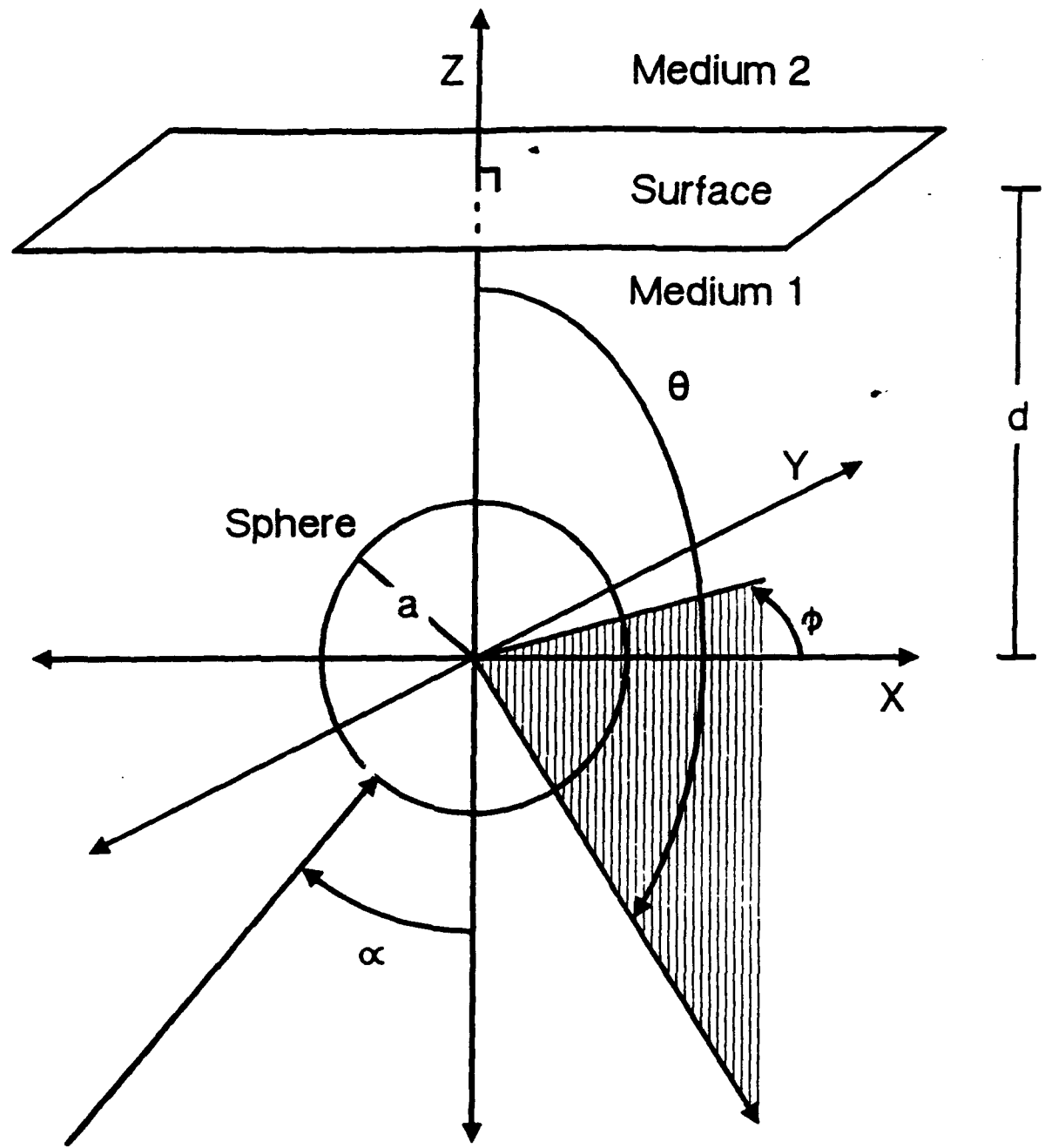
Fig. 2. The geometry of the scattering system. A sphere of radius a is located a distance d below a surface. A plane wave travels in the x - z plane at angle α with respect to the z axis.

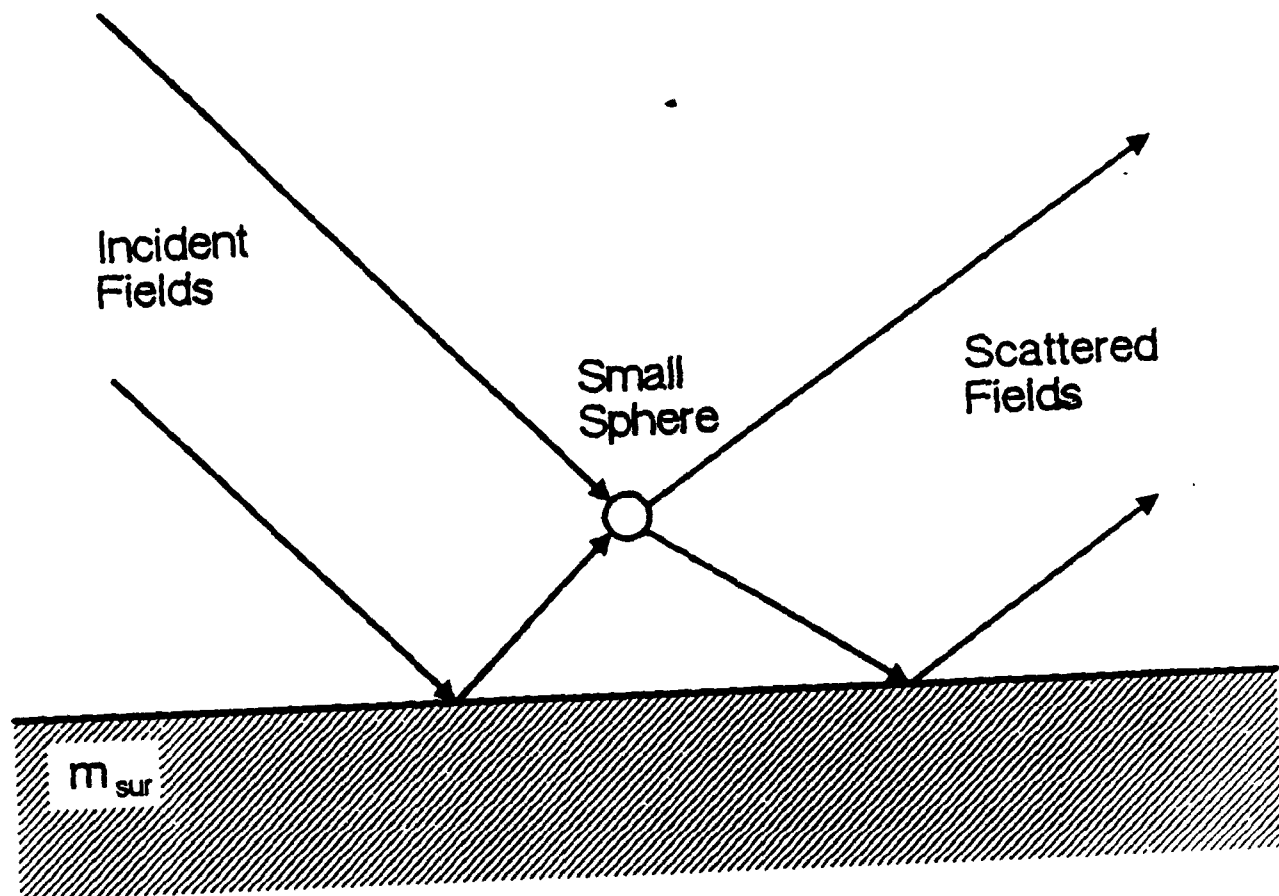
Fig. 3. The geometry of the scattering system showing the four paths light may travel to reach the detector in the double interaction model.

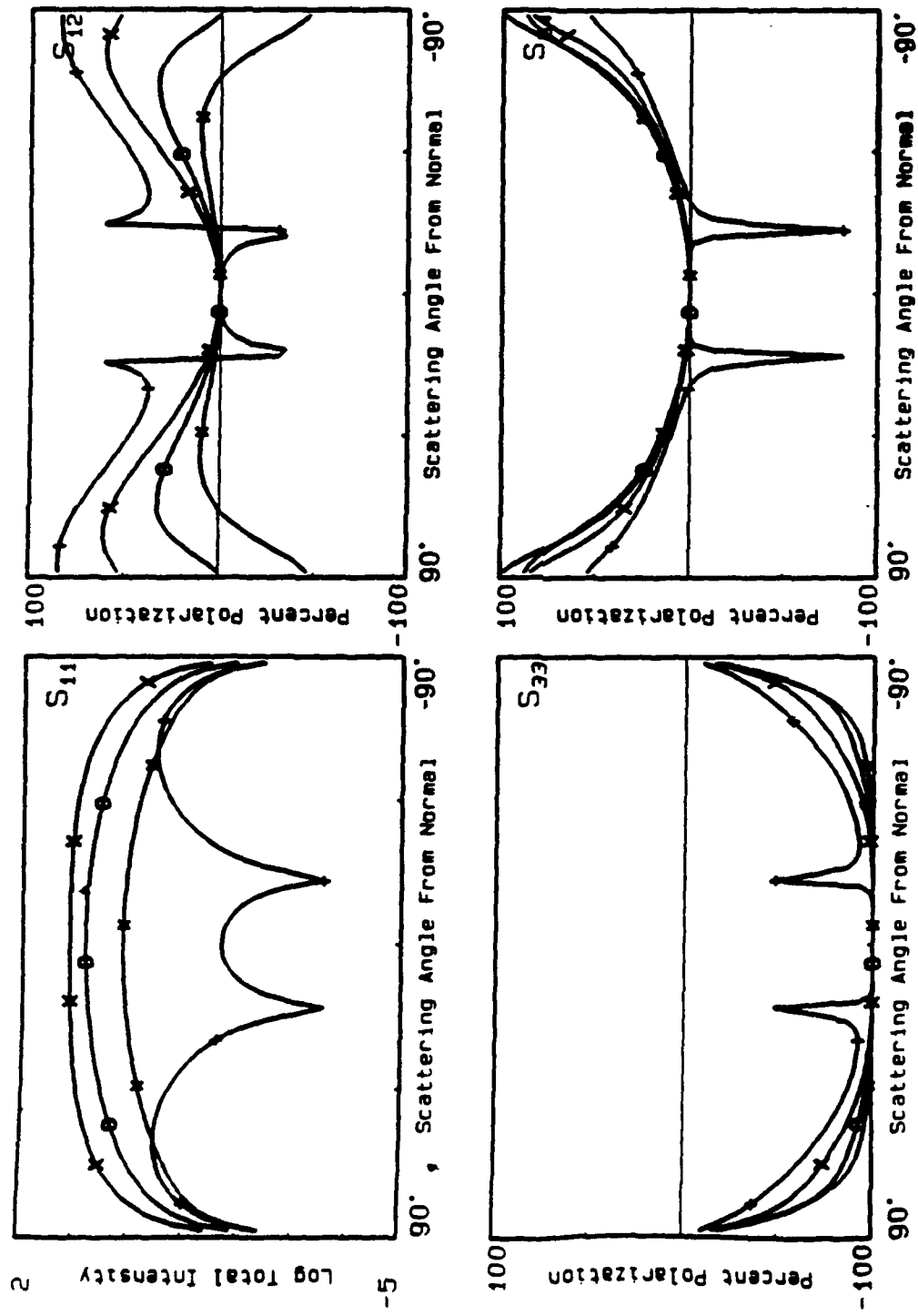
Fig. 4. The Mueller matrix elements from a small sphere at four separations from a surface of index $n = 0.5 + 5.0i$ illuminated at normal incidence ($\alpha = 180^\circ$, $A = 1$). \bullet $d = \lambda/16$. O $d = \lambda/8$. X $d = \lambda/4$. \longleftrightarrow $d = \lambda/2$.

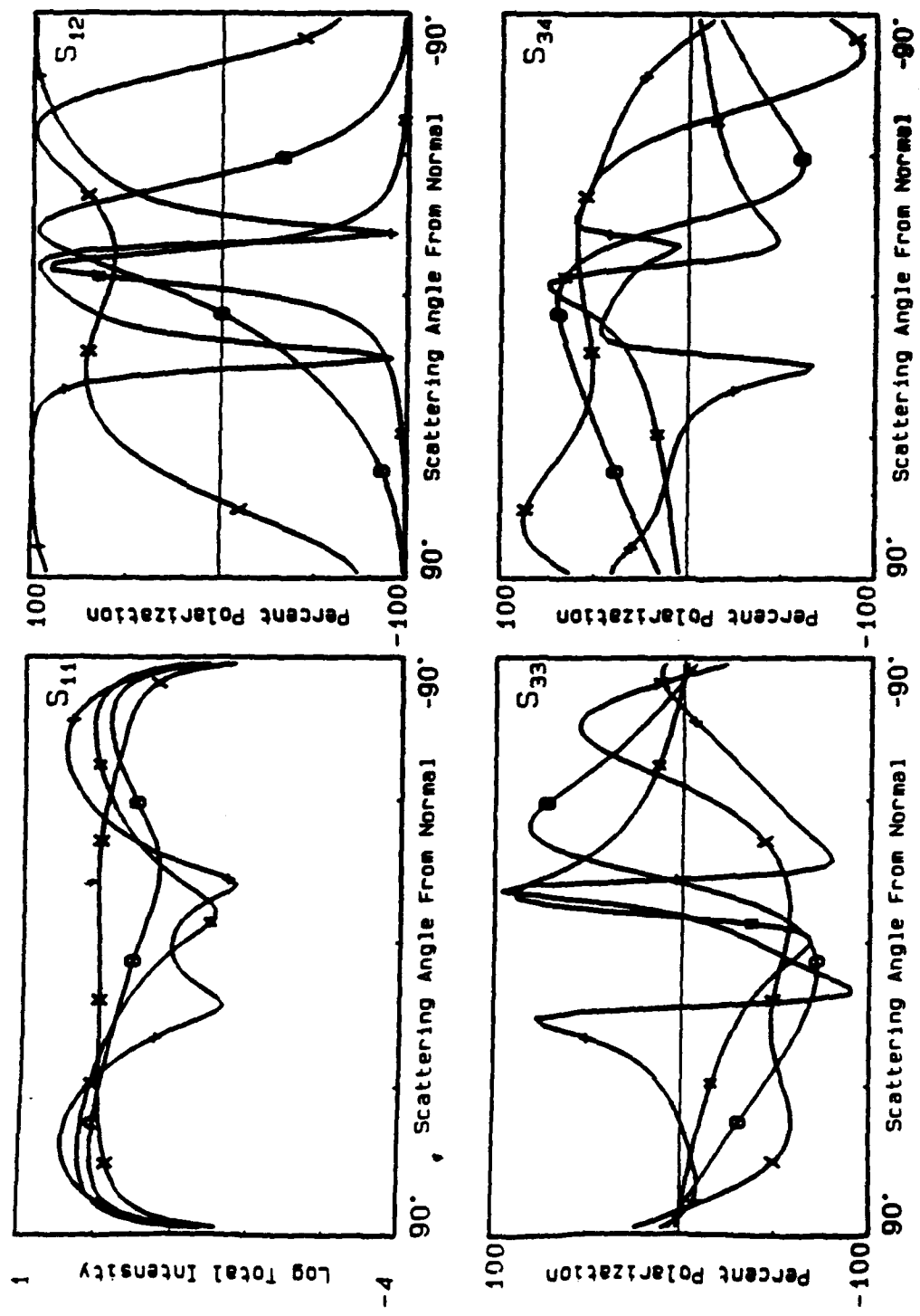
Fig. 5. The Mueller matrix elements from a small sphere at four separations from a surface of index $n = 0.5 + 5.0i$ illuminated at $\alpha = 101^\circ$. ($A = 1$). \bullet $d = \lambda/16$. O $d = \lambda/8$. X $d = \lambda/4$. \longleftrightarrow $d = \lambda/2$.











Stokes vectors, Mueller matrices and polarized scattered light: experimental applications to optical surfaces and all other scatterers

William S. Bickel and Gorden Videen

University of Arizona, Department of Physics
Tucson, Arizona 85721

ABSTRACT

We discuss scattering in the context of the Stokes vectors and Mueller matrices that characterize the interaction. In order to study surface structures using light-scattering techniques it is useful to examine the nature of light scattered from perfect and perturbed mirror surfaces.

1. INTRODUCTION

A highly motivated, systematic, and fundamental approach to surface scattering requires that the initial surfaces be fundamental and that the contamination to produce the surface scattering be known and controlled. With this in mind any rough surface can be considered to be a perturbed perfect surface that has reached its final condition through some continuum contamination process.

The powerful Stokes vector, Mueller matrix light-scattering techniques can be applied directly to study surfaces. Scattering from perfect surfaces can be theoretically predicted and experimentally measured. Experimentalists have an advantage in that they can measure what theorists cannot calculate. If the data are to be used to check theory, the experimentalist must relate the light scattering signal to the exact structure and orientation of the surface that scattered the light.

Consider how a perfect optical surface (lens) is treated by taking into account its geometrical and diffraction-limited properties. Geometrical optics is used to predict where a point on the object will be focused to a point on the image. Diffraction theory will predict how the image point is

actually a diffraction pattern; i. e., not all light from the object point ends up at the image point. Nevertheless, the diffraction-limited image is exactly predicted by theory and its intensity distribution is related to fundamental constants. The problem arises when the perfect diffraction-limited optic and its image is perturbed by a defect in or on the optic. This defect scatters light into all directions — out of the paths so well defined by geometrical and diffraction optics.

The question is where does this scattered light go and what does it do to the image (information). There will be a loss of image intensity, but more troublesome is the light initially intended for one part of the image that is scattered to another part of the image causing loss of contrast and image definition. We can write that the object (point A) is transformed into a diffuse diffraction-limited geometrical image (point A') by a transformation matrix [L, D, S] where L is the geometrical function of the lens, D is the diffraction function and S is the scattering function which contains all of the scattering parameters of the defect.

2. POLARIZED LIGHT SCATTERING

What is S? If the defect were a perfect sphere the scatter from it is nothing more than the diffraction by a spherical object — a problem solved by Gustav Mie in 1908.¹ As the sphere becomes more irregular in shape and inhomogeneous in optical constants, exactly solvable sphere diffraction goes over to the statistical aspects of irregular particle scatter.² A scatterer is said to be characterized by its scattering properties when we know how it will rearrange the properties of light incident on it. For example, consider perfect sphere scattering. A sphere with radius r , refractive index n and absorption μ has a scattering matrix [S]. When it is illuminated with light of intensity I_0 , wavelength λ_0 , polarization Π_0 , at angle θ_0 , it creates a scattered field of I_s , λ_s , Π_s , and θ_s . We can write $(I_s, \lambda_s, \Pi_s, \theta_s) = [S](I_0, \lambda_0, \Pi_0, \theta_0)$ where [S] is exactly known for spheres. The matrix [S] can be calculated only for certain highly symmetric cases. It can be approximated for slightly distorted systems, but can only be measured for truly irregular particles. Therefore, in order to learn how a defect on or in a surface (an irregular, imperfect surface) will affect all aspects of the incident light, it is better to measure what happens exactly instead of relying on approximation and theoretical models. Generally two things

are required of scattering experiments: 1. produce a defect and measure its scatter; or 2. measure the scatter and predict the defect — the inversion process. Before we extract information from light-scattering data it is important to be sure that we have all the information available.

3. POLARIZED SCATTERING NEPHELOMETER

The experimental set-up that can measure the polarized intensities scattered by the scatterer [S] into the angles θ and ϕ is shown in Fig. 1. The input optics can be selected to be an open hole [o], or horizontal linear polarizer [h], or $+45^\circ$ linear polarizer [+] or a right-handed circular polarizer [r]. The exit optics choices are the same and can be chosen independently of the input optics and can swing with the detector through the scattering angle θ from 0° to 180° .³

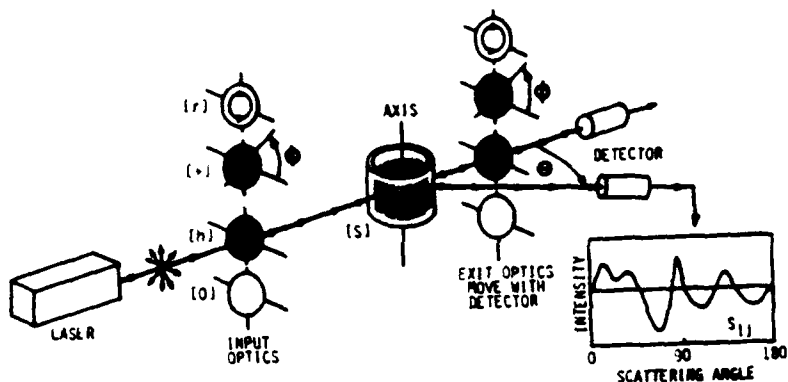


Fig. 1. Arrangement of entrance-exit polarizers to measure the matrix elements of a scatterer.

The following example shows how to determine what scattering matrix elements S_{ij} are involved when a particular set of input-output polarizers are used to prepare and analyze the scattered light. For our first choice we assume that the arbitrary scatterer (defect) is illuminated with horizontally-polarized light [h]. The scattered Stokes vector will be $[V.] = [S] \cdot [h]$ or

$$\begin{pmatrix} S_{11} & S_{12} & S_{13} & S_{14} \\ S_{21} & S_{22} & S_{23} & S_{24} \\ S_{31} & S_{32} & S_{33} & S_{34} \\ S_{41} & S_{42} & S_{43} & S_{44} \end{pmatrix} \begin{pmatrix} 1 \\ 1 \\ 0 \\ 0 \end{pmatrix} = \begin{pmatrix} S_{11} + S_{33} \\ S_{21} + S_{41} \\ S_{31} + S_{23} \\ S_{41} + S_{13} \end{pmatrix}.$$

We see that the scatterer [S] mixes the initial pure polarization state [h] to produce a scattered Stokes vector with mixed polarizations. The first component ($S_{11} + S_{12}$) is the total intensity and is a sum of two matrix elements. If this scattered light is now passed through a +45° linear polarizer [+] we get $[V_1] = [+] [V_1]$. Specifically we have

$$\begin{pmatrix} S_{11} + S_{12} + S_{31} + S_{21} \\ 0 \\ S_{11} + S_{12} + S_{31} + S_{21} \\ 0 \end{pmatrix} = \begin{pmatrix} 1 & 0 & 1 & 0 \\ 0 & 0 & 0 & 0 \\ 1 & 0 & 1 & 0 \\ 0 & 0 & 0 & 0 \end{pmatrix} \begin{pmatrix} S_{11} + S_{12} \\ S_{21} + S_{31} \\ S_{31} + S_{21} \\ S_{41} + S_{42} \end{pmatrix}.$$

The first component of the final Stokes vector is now a mixture of four matrix elements. The element sum ($S_{11} + S_{12} + S_{31} + S_{21}$) is the total intensity that will be measured by the detector. We put the result of all such calculations from all 16 Stokes vector combinations into a final array shown in Fig. 2. The main point of Fig. 2 is that there are $4 \times 4 = 16$ measurements to be made to completely characterize the polarized light scattered from the defect. These measurements can be routinely made by nephelometers that incorporate the various polarizers in their entrance-exit optics. The 16 matrix elements are needed to completely characterize the scattered light or to use in the inversion process to determine the properties of the scatterer.

S_{11} *	S_{12} — *	S_{31} / *	S_{41} O *
** S_{11}	— * $S_{12} + S_{31}$ * $S_{12} + S_{21}$	/ * $S_{31} + S_{21}$ \\ * $S_{31} + S_{41}$	O * $S_{41} + S_{31}$ O * $S_{41} + S_{21}$
S_{21} * —	S_{22} — —	S_{32} / —	S_{42} O —
* — $S_{11} + S_{21}$ * — $S_{11} + S_{31}$	— — $S_{12} + S_{21} + S_{31} + S_{41}$ — $S_{12} + S_{21} + S_{31}$ — $S_{12} + S_{21} + S_{41}$ — $S_{12} + S_{31} + S_{41}$ — $S_{12} + S_{21} + S_{31} + S_{41}$	/ — $S_{31} + S_{21} + S_{31} + S_{41}$ \\ — $S_{31} + S_{21} + S_{31}$ \\ — $S_{31} + S_{21} + S_{41}$ \\ — $S_{31} + S_{31} + S_{41}$ \\ — $S_{31} + S_{21} + S_{31} + S_{41}$	O — $S_{41} + S_{21} + S_{31} + S_{41}$ O — $S_{41} + S_{21} + S_{31}$ O — $S_{41} + S_{21} + S_{41}$ O — $S_{41} + S_{31} + S_{41}$ O — $S_{41} + S_{21} + S_{31} + S_{41}$
S_{31} * /	S_{32} — /	S_{41} / —	S_{42} O /
* / $S_{11} + S_{31}$ * / $S_{11} + S_{41}$	— / $S_{12} + S_{21} + S_{31} + S_{41}$ — $S_{12} + S_{21} + S_{31}$ — $S_{12} + S_{21} + S_{41}$ — $S_{12} + S_{31} + S_{41}$ — $S_{12} + S_{21} + S_{31} + S_{41}$	/ — $S_{31} + S_{21} + S_{31} + S_{41}$ \\ — $S_{31} + S_{21} + S_{31}$ \\ — $S_{31} + S_{21} + S_{41}$ \\ — $S_{31} + S_{31} + S_{41}$ \\ — $S_{31} + S_{21} + S_{31} + S_{41}$	O / $S_{41} + S_{21} + S_{31} + S_{41}$ O / $S_{41} + S_{21} + S_{31}$ O / $S_{41} + S_{21} + S_{41}$ O / $S_{41} + S_{31} + S_{41}$ O / $S_{41} + S_{21} + S_{31} + S_{41}$
S_{41} * O	S_{42} — O	S_{31} / O	S_{21} O O
* O $S_{11} + S_{41}$ * O $S_{11} + S_{21}$	— O $S_{12} + S_{21} + S_{31} + S_{41}$ — O $S_{12} + S_{21} + S_{31}$ O $S_{12} + S_{21} + S_{41}$ O $S_{12} + S_{31} + S_{41}$ O $S_{12} + S_{21} + S_{31} + S_{41}$	/ O $S_{31} + S_{21} + S_{31} + S_{41}$ \\ O $S_{31} + S_{21} + S_{31}$ \\ O $S_{31} + S_{21} + S_{41}$ \\ O $S_{31} + S_{31} + S_{41}$ \\ O $S_{31} + S_{21} + S_{31} + S_{41}$	O O $S_{41} + S_{21} + S_{31} + S_{41}$ O O $S_{41} + S_{21} + S_{31}$ O O $S_{41} + S_{21} + S_{41}$ O O $S_{41} + S_{31} + S_{41}$ O O $S_{41} + S_{21} + S_{31} + S_{41}$

Fig. 2. Matrix array showing matrix element combinations measured with various arrangements of input and output polarizers.

4. SURFACE ORIENTATION

The geometrical orientation of the rough surface with respect to the entrance-exit beams must be addressed early because there are an infinite number of possible orientations, all of which might give a different S_{θ} for the same surface. Figure 3 shows some of the geometrical parameters involved in surface scattering studies. The laser beam, after preparation into a definite polarization state, strikes the surface at angle α and is scattered into all 4π . The light scattered into angle θ is analyzed with the polarization exit optics and detected by the photomultiplier. The angle τ is a surface tilt measured in the surface plane. Our work has shown that geometry is important and that no universal scaling factor exists and that no best orientation exists for all cases.

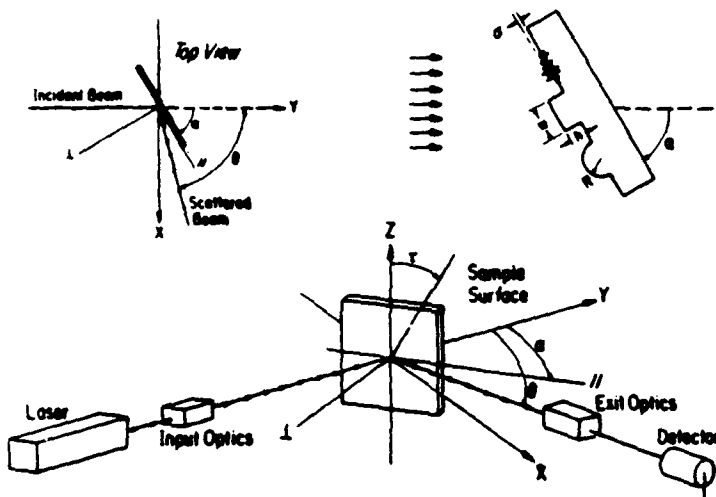


Fig. 3. Optical and sample arrangement for surface scattering measurements.

5. SURFACE SCATTERING

We now show some general results of scattering from some surfaces to show how light-scattering nephelometry and BRDF are related.^{1,6} Figure 4 shows four matrix elements for a reflective aluminum surface. The 4 order of magnitude angular decrease of the total intensity matrix element $S_{\theta\theta}$ is an indication of the quality of the reflecting surface. Note that even though the total scattered intensity is down by over 5 orders of magnitude near $\theta = 150^\circ$ (back-scatter) the polarization of the scattered light is significant as demonstrated by matrix S_{33} and S_{14} .

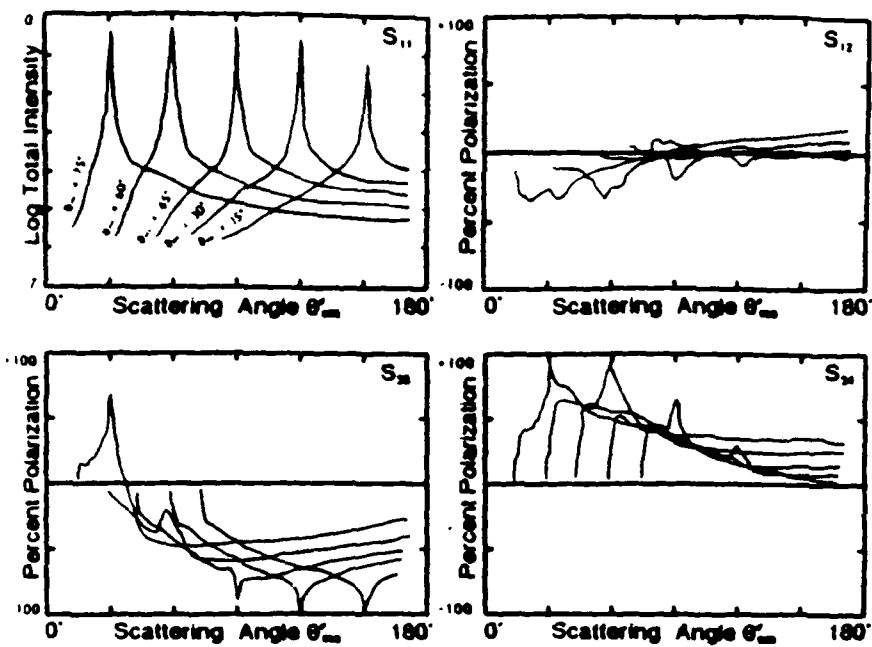


Fig. 4. Four Mueller matrix elements for a reflecting aluminum surface.

Figure 5 shows the matrix elements for the same surface but now roughened to saturation. Further roughening will not change the surface character. All hints of the location of the specular peak are gone. S_{11} as well as S_{33} are independent of surface orientation; and polarizations, as indicated by all matrix elements, remain large.

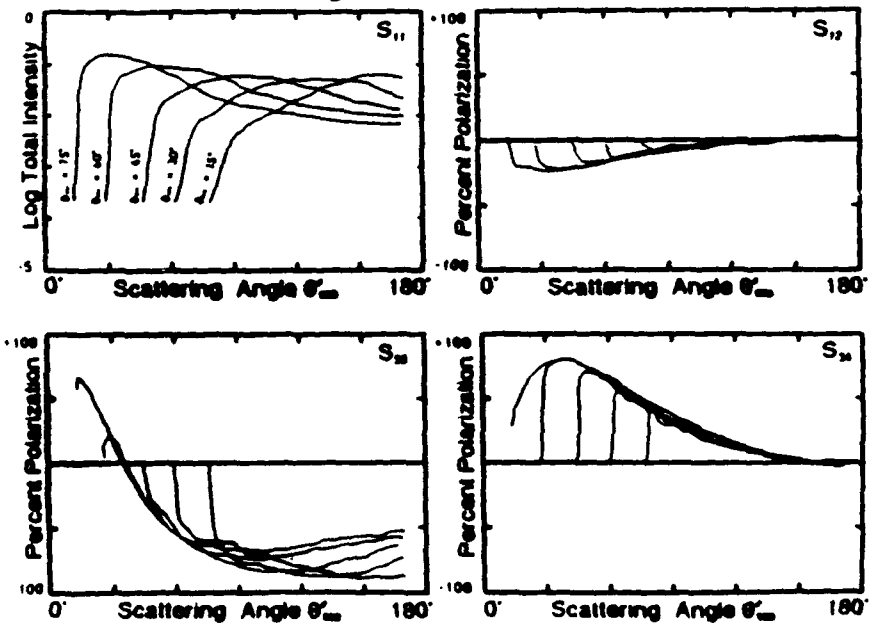


Fig. 5. Four Mueller matrix elements for a saturated rough aluminum surface.

Now we show how dramatically the S_{11} from surface defects depend on the angle at which the surface (and its defect) is illuminated. Figure 6 shows the matrix element S_{33} for a rectangular line ($h = 0.46\mu\text{m}$, $w = 1.10\mu\text{m}$) on a smooth aluminum surface illuminated at near-grazing incidence and at normal incidence. Normal incidence not only restricts the angular range over which the data is received but it also wipes out all the phase information needed to characterize the defect.

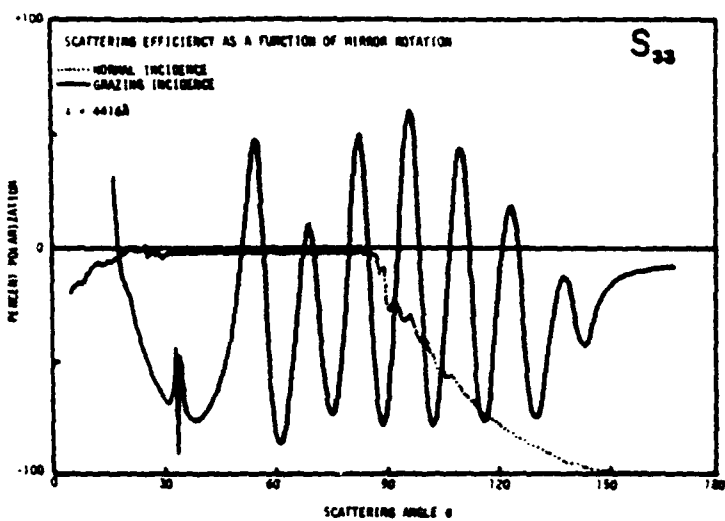


Fig. 6. Matrix element S_{33} for a rectangular line on a mirror surface measured at two different angles of incidence.

8. CONCLUSIONS

One general goal of light scattering is to develop an algorithm to put into a computer which will predict either the scattered field (from particle properties) or particle properties (from the scattered field). The data (particle properties or scattered field) must be determined experimentally. We must determine how much scattering data is needed, how good it must be and how well it describes the scatterer in a practical way. We also must determine the amount of information contained in the various matrix elements and whether signal changes can be related to changes in the optical or geometrical properties. We see that polar nephelometry gives sixteen matrix element signals. The record shows that polar nephelometry, ellipsometry, BRDF, and other optical techniques can all complement each other and yield important information

about surface scattering when used with care, keeping in mind their limitations and range of validity.

9. ACKNOWLEDGMENTS

This research was funded by the Army Armament Research and Development Command, the U. S. Air Force Office of Scientific Research (AFSC) and the Itek Corporation. We thank Vincent J. Iafelice for many helpful discussions.

10. REFERENCES

1. G. Mie, "Beitrage zur Optik trüber Medien speziell kolloidaler Metallösungen," *Ann. Phys.*, 25, 377-445 (1908).
2. W. S. Bickel, H. A. Yousif, and W. M. Bailey, "Masking of information in light scattering signals from complex scatterers," *Aerosol Sci. and Technol.* 1, 329-335 (1982).
3. A. J. Hunt and D. R. Huffman, "A new polarization modulated light scattering instrument," *Rev. Sci. Instrum.*, 44, 1753-1762 (1973).
4. W. S. Bickel and W. M. Bailey, "Stokes vectors, Mueller matrices, and polarized scattered light," *Am. J. Phys.* 53, 468-478 (1985).
5. V. J. Iafelice, The Polarized Light Scattering Matrix Elements for Select Perfect and Perturbed Optical Surfaces, M. S. thesis, University of Arizona 1985.
6. R. Anderson, "Matrix description of radiometric quantities," *Appl. Opt.* 30, 858-867 (1991).

The light-scattering Mueller matrix for a surface contaminated by
a single particle in the Rayleigh limit

Gorden Videen, William L. Wolfe, and William S. Bickel

Optical Sciences Center
University of Arizona
Tucson, Arizona, 85721

Abstract

A ray-tracing model was used to derive the light-scattering Mueller matrix element curves for a dipole near a perfect surface as a function of angle of incidence, scattering angle and surface index of refraction. This system represents a fundamental system composed of a perfect plane surface and the perfect (Rayleigh) scatterer.

Subject terms: dipole, contamination, light-scattering, Mueller matrix, surface.

INTRODUCTION

Mie theory,¹ which can be used to predict exactly the scattering from spheres of all types, has recently been the subject of a great deal of modification. The modification is brought about by examining the simple sphere when it comes into contact with the perfect surface. The impetus has come from contamination studies, often centered around wafer-producing technology in the electronic and computer sciences, but the applications are numerous, ranging from degradation of optical modulation transfer functions to energy losses in laser systems.

The modification to Mie theory investigates how the scattering system, composed of a single sphere, is changed when the system is composed of a sphere and a surface. Since each system taken independently has been solved exactly, the sphere by Mie and the surface by Fresnel, a logical first order solution would be to combine these two systems into something similar to what Nahm and Wolfe² refer to as the double-interaction model. This model ignores the interaction term between the sphere and the surface. For Rayleigh scattering, the scattering intensity is proportional to $(r/\lambda)^4$, and the effect of the interaction term when compared to the other terms is negligible. Therefore, when the sphere is driven to the Rayleigh limit, $r \ll \lambda$, this model should be able to predict the scattering exactly.

THEORY

Theoretically, we treat the system as a dipole illuminated by two plane waves, one incident and one reflected off the surface. The scattered radiation is also in two parts, one directly from the dipole and one reflected off the surface. Figure 1 shows the various paths by which light can be scattered into the detector and the convention used for measuring angles. All angles are measured from the normal to the surface. Figure 2 shows the four paths that a beam may travel for scattering on the incident side of the detector. Path 1

is the direct path and is what comes from Mie theory. The beam whose angle of incidence with the surface normal is θ_i excites the dipole, which scatters radiation through angle θ to the detector. Path II shows the beam reflecting off the surface before striking the dipole. Radiation is then scattered directly to the detector. Path III shows the beam striking the dipole directly, with the scattered radiation striking the surface before reaching the detector. Path IV shows the beam reflecting off the surface before striking the dipole whose scattered radiation also reflects off the mirror before reaching the detector.

Before looking at the polarizations, we will complete this analysis by looking at the scattering that penetrates the surface, where $\cos\theta > 90^\circ$. Although most of the interest seems to be in the case where the surface is highly reflecting, the transmission case is such a simple extension that it should not be neglected. Figure 3 shows the two paths that a beam may travel in reaching a detector. Path V shows the beam striking the dipole directly with the scattered radiation being refracted by the surface to the detector. Path VI shows the beam reflecting off the surface before striking the dipole, with the scattered radiation being refracted by the surface before propagating to the detector. For a high index surface, all refracted beams lie very near the normal. To facilitate viewing the information, the transmitted portion of the graphs are plotted as a function of the beam angle incident on the surface. This is equivalent to making the reflecting medium a thin slab of material with air on either side, and putting an anti-reflection coating on the exiting surface. The beam angle incident on the front surface is equal to the beam angle leaving the rear surface. Since we are going to calculate the Mueller matrix elements, we need to consider the TE and TM polarizations independently.

To calculate the Mueller matrix, we first calculate the scattering amplitude matrix which is explained by Bohren and Huffman¹ and others.^{2,3} For

our purposes we define the scattering amplitude matrix by the following equation:

$$\begin{pmatrix} E_{\text{TM}}^{\text{inc}} \\ E_{\text{TE}}^{\text{inc}} \end{pmatrix} = \begin{pmatrix} S_2 & S_3 \\ S_4 & S_1 \end{pmatrix} \begin{pmatrix} E_{\text{TM}}^{\text{sc}} \\ E_{\text{TE}}^{\text{sc}} \end{pmatrix}, \quad (1)$$

where the vectors represent the incident and scattered electric fields for the TE and TM polarizations. If we place our detector in the plane of incidence (defined by the incident beam and the normal to the surface), it can be shown that the matrix elements S_2 and S_4 are identically zero. We can now examine the TE mode and calculate the element S_1 .

THE TE MODE

The vibration of the dipole for the TE mode is perpendicular to the plane of incidence. As a result, the radiation from a dipole in this mode has no angular dependence in this plane and is therefore slightly easier to understand than the TM mode. Since all the beams have the same temporal dependence, we can normalize the beam from path I, and represent all other beams in terms of this beam's amplitude and phase. A beam following path II will be out of phase with the normalized beam when it reaches the dipole by an amount $\delta(\theta_0, d)$, where

$$\delta(\theta_0, d) = -\frac{2\pi}{\lambda} 2d \cos\theta_0, \quad (2)$$

d is the distance between the dipole and the mirror, and λ is the wavelength of the light. Furthermore, the amplitude and the phase are affected by the Fresnel reflectance factor³, $R\pi(\theta_0)$, where

$$R\pi(\theta_0) = \frac{Z_2 \cos\theta_0 - Z_1 [1 - (n_1/n_2)^2 \sin^2\theta_0]^{1/2}}{Z_2 \cos\theta_0 + Z_1 [1 - (n_1/n_2)^2 \sin^2\theta_0]^{1/2}}, \text{ and} \quad (3)$$

$$\frac{Z_1}{Z_2} = \frac{\mu_1 \epsilon_0}{\mu_2 \epsilon_0}. \quad (4)$$

The subscripts, 1 and 2, correspond to different sides of the surface. In our case, the plane wave is traveling from material 1 and striking material 2. For

most cases, the light initially travels through air or vacuum with $n_1 \approx 1$ and $\mu_1 \approx \mu_0$. Path III is similar to path I, but the phase difference and reflectance factor are a function of $\pi - \theta$. Finally, for path IV we have to consider the phases and reflectance factors of both the previous paths. The net result of the four beams at the detector is the following:

$$S_1(\theta) = 1 + R_{\pi}(\theta_0)e^{i\delta(\theta_0, d)} + R_{\pi}(\pi - \theta)e^{i\delta(\pi - \theta, d)} + R_{\pi}(\theta_0)R_{\pi}(\pi - \theta)e^{i(\delta(\theta_0, d) + \delta(\pi - \theta, d))}, \quad (5)$$

where $\cos\theta < 0$.

We now consider the transmission of the TE mode. Path V, like path I undergoes no phase lags. However, one must consider the effect of the Fresnel transmission factor on the scattered beam which is given by

$$T_{\pi}(\theta) = \frac{2Z_1 \cos\theta}{Z_1 \cos\theta + Z_2 [1 - (n_1/n_2)^2 \sin^2\theta]^{1/2}}. \quad (6)$$

The beam following path VI undergoes the same phase lag on the incident beam as that of path II. The scattering amplitude matrix element for the transmitted beam can be expressed as follows:

$$S_1(\theta) = [1 + R_{\pi}(\theta_0)e^{i\delta(\theta_0, d)}] T_{\pi}(\theta), \quad (7)$$

where $\cos\theta > 0$. With the scattering amplitude matrix element for the TE mode solved, we now examine the TM mode.

THE TM MODE

The terms used to calculate the scattering matrix for the TM mode are almost identical to those of the TE mode. The Fresnel coefficients of reflection and transmission of the surface are slightly different and may be written as follows:

$$R_{\pi\mu}(\theta) = \frac{Z_1 \cos\theta - Z_2 [1 - (n_1/n_2)^2 \sin^2\theta]^{1/2}}{Z_1 \cos\theta + Z_2 [1 - (n_1/n_2)^2 \sin^2\theta]^{1/2}}, \text{ and} \quad (8)$$

$$T_m(\theta) = \frac{2 Z \cos \theta}{Z \cos \theta + Z_1 [1 - (n_1/n_2)^2 \sin^2 \theta]^{1/2}}. \quad (9)$$

The major difference is the angular-dependent dipole scattering that occurs for this mode. Bickel and Bailey⁷ provide an inciteful discussion of the reason why the scattering of this mode is proportional to the cosine of the angle between the incident and the scattered beam. As the detector scans in the plane of incidence, the amount of dipole vibration that the detector sees corresponds to the projection of the dipole in the detector plane. This causes the cosine dependence. With a bit of trigonometry, we can derive the following equations for the scattering amplitude matrix element $S_2(\theta)$:

$$S_2(\theta) = \cos(\theta - \theta_0) + \cos(\pi - \theta - \theta_0) R_m(\theta_0) e^{i\delta(\theta_0, d)} + \cos(\pi - \theta - \theta_0) R_m(\pi - \theta) e^{i\delta(\pi - \theta, d)} + \cos(\theta - \theta_0) R_m(\theta_0) R_m(\pi - \theta) e^{i(\delta(\theta_0, d) + \delta(\pi - \theta, d))}, \quad \text{for } \cos \theta < 0 \text{ and,} \quad (10)$$

$$S_2(\theta) = [\cos(\theta - \theta_0) + \cos(\pi - \theta - \theta_0) R_m(\theta_0) e^{i\delta(\theta_0, d)}] T_m(\theta), \quad \text{for } \cos \theta > 0. \quad (11)$$

With both polarizations taken into account, we now direct our attention to the scattering Mueller matrix elements.

THE MUELLER MATRIX

From the relations given by Bohren and Huffman, we can use the scattering amplitude matrix elements to calculate the Mueller scattering matrix elements. In the plane of incidence, only four of the sixteen elements of the Mueller matrix are of interest. These are

$$\begin{aligned} S_{11} &= \frac{1}{2} [|S_d|^2 + |S_u|^2], \\ S_{22} &= \frac{1}{2} [|S_d|^2 - |S_u|^2] / S_{11}, \\ S_{12} &= \text{Re}(S_d S_d^*) / S_{11}, \text{ and} \\ S_{21} &= \text{Im}(S_d S_d^*) / S_{11}. \end{aligned} \quad (12)$$

When we consider only the scatter in the plane of incidence, the other scattering elements are either zero or simple multiples of these elements.

Using these expressions, the four Mueller matrix elements were calculated for a dipole with no surface. The surface can be removed by setting the surface index equal to 1. These elements are shown in Figure 4. It is noted that the scattering angle θ goes from 0° to 360° . As expected, symmetries occur about $\theta = 180^\circ$. This is a fundamental case discussed in many of the references, especially Bickel and Bailey. These scattering elements are useful references and will be compared with those generated when a surface is placed near the dipole.

SCATTERING AS A FUNCTION OF PARTICLE-SURFACE SEPARATION

Figure 5 shows the four scattering Mueller matrix elements as a function of dipole-surface separation for a beam incident at normal incidence and a surface of index $n = 10.0 - 0.0i$. Such a surface could be made with a series of $1/4$ -wave dielectric layers on a glass substrate. It is more instructive to look at the effects of a high index dielectric surface initially (rather than a simple glass plate or a metallic surface) because a high index interface gives interfering beams that are of nearly equal amplitude. Also, a metal interface creates phase shifts upon reflection. Before examining Figure 5 in detail, it is instructive to examine the scattering amplitude matrix elements. To provide some insight for the TE case, we rewrite the scattering amplitude matrix element (equation 5) in the following form:

$$S_n(\theta) = [1 + R_n(\theta, d)e^{i\theta(\theta, d)}][1 + R_n(\pi - \theta)e^{i\theta(\pi - \theta, d)}]. \quad (13)$$

The first term which is independent of θ controls the amplitude of the overall pattern. As the dipole-surface separation is increased, a stationary detector at θ will witness the intensity element $S_n(\theta)$ fluctuating sinusoidally with distance due to the first term. For a beam incident along a normal to a dielectric surface illuminating a particle next to the surface ($d \approx 0$), the intensity mea-

sured by a fixed detector will be in a trough (minima) since there is a phase change at the surface. As the particle moves away from the surface, the signal increases until it is $1/4$ wave from the surface, at which point the signal has cycled into a peak (maxima) since $\delta(\theta, d) = -\pi$. At $1/2$ wave from the surface, the signal has returned to the trough. The intensity difference between a peak and a trough can be calculated using

$$\Delta I = \log\left\{\left|1 + R(0)\right|^2\right\} - \log\left\{\left|1 - R(0)\right|^2\right\}. \quad (14)$$

For $n = 10.0 - 0.0i$, this yields $\Delta I = 2$ or a two order of magnitude change in the scattering by moving the particle $1/4$ wave. This is most easily seen in the transmission region ($\theta = 0^\circ$) of the S_n curves of figure 5.

The second term in the $S(\theta)$ equation, controls the shape of the pattern. If the first order approximation assumes $R(\theta)$ to be constant, then the pattern behaves sinusoidally with $\delta(\theta, d)$. At $\theta = 180^\circ$, we not only see the pattern fluctuating two orders of magnitude with the amplitude envelope, but also varying another two orders of magnitude due to the scattering (second) term of equation 13, for a total fluctuation of four orders of magnitude. For other scattering angles, the fluctuation of the amplitude envelope and the fluctuation at a particular scattering angle will be out of phase and will tend to cancel each other. For a dipole-surface separation of $3\lambda/4$ and the detector placed at $\theta = 180^\circ$, $\delta(\theta, d) = 3\pi$. At this location, there is a peak in the scattering intensity. A trough will appear at any scattering angle where the phase, $\delta(\theta, d) = 2m\pi$, where m is a positive integer not greater than $\delta(180^\circ, d)/2\pi$ ($3/2$ in this case). Keeping d constant with $m = 1$, we can solve our phase equation, $\delta(\theta, d) = 2\pi$, for scattering angle θ , yielding 132° and 228° . At about these locations in Figure 5 we see troughs whose value hasn't changed much from the amplitude envelope of the half wave separation. These nodes move in to the center of the pattern (toward 180°) as the dipole-surface distance increases. Another set of troughs (for $m = 0$) is just beginning to form for $\delta(\theta, d) = 0$ which corresponds to $\theta = 90^\circ$ and 270° , but they are not as apparent at this

point because the Fresnel reflection term dominates.

The response of the polarization matrix elements (S_{11} , S_{22} , and S_{33}) is not as dramatic as the total intensity matrix element, S_{11} . Spikes tend to appear on these elements where there are troughs in the total intensity element. These spikes seem similar to those that appear in the Rayleigh-Gans limit of single sphere scattering.¹ S_{11} has an interesting feature: for very small dipole-surface separations ($d \approx \lambda/1000$), the polarization has switched sign. This appears to be a function of the refractive index of the surface which we now consider.

Figure 6 shows the S_{11} scattering as a function of dipole separation from a surface of index $n = 28.0 - 95.0i$, an index roughly corresponding to aluminum at $10\mu\text{m}$ wavelength. First note that the transmission portions of the polarization elements carry very little information; i.e., they are either zero or 100% over the entire range. This is not too disturbing since the skin depth of this metal would effectively prevent most transmission measurements. This information loss also occurs for high index dielectric surfaces, but is more apparent in figure 6 because the reflectance of aluminum is greater than the dielectric of figure 5. An interesting feature has cropped up in matrix element $S_{11}(\delta)$ at normal incidence when $d = \lambda/2$. At $\delta = 180^\circ$; where a node occurred for the dielectric surface of figure 5, a small maximum exists. Reflections from a metallic surface change the state of the incident beam from linear polarization to elliptical polarization. As a result of these reflections, the shape and position of the nodes are different than the nodes for a dielectric surface. The nodes and spikes for aluminum are sharper than for the dielectric, but this is a function of the reflectance: the aluminum is more reflecting, so the spikes are sharper. Other than the small displacements of the maxima/minima and the loss of information in matrix element S_{11} for large dipole-surface separations, it is hard to distinguish the scattering from the metal surface of figure 6 from the high-index dielectric surface of figure 5.

Figure 7 shows the S_w scattering as a function of dipole distance from a surface of index $n = 1.5 - 0.01$, which roughly corresponds with glass in the visible spectrum. For a low-index surface, the matrix element curves are much smoother, and very closely resemble the curves for a dipole without a surface shown in Figure 4. As the dipole-surface distance is increased, the elements change, while retaining this general shape.

SCATTERING AS A FUNCTION OF INCIDENT ANGLE

We now consider the final remaining parameter for dipole-surface scattering, the incident angle of the incoming radiation. We examine the specific, but arbitrary, case for the particle near the surface at $d = \lambda/10$. This case could represent a $2\mu\text{m}$ diameter dust particle on a surface illuminated with $10.6 \mu\text{m}$ light. Although a radius of $\lambda/10$ borders on the Rayleigh limit, it has practical applications.

Figure 8 shows the S_w scattering as a function of incident illumination angle for a dipole located $\lambda/10$ from a surface of index $n = 10.0 - 0.01$. First we note the lack of symmetry in the elements. Prior to this study, all the elements have been symmetric about $\theta = 180^\circ$. As θ_i is increased first to 30° and then to 60° , the elements vary significantly from those of the isolated dipole of figure 4. Specular peaks occur in those directions where the beam takes a direct path and does not interact with the particle. These occur at $\theta = \theta_i$ on the transmission side of the surface and $\theta = \pi - \theta_i$ on the reflection side of the surface. It may seem surprising to find that the peak of the scattered radiation is not necessarily at the specular beam on the reflecting side of the surface.

Established patterns in the polarization matrix elements for scattering from a single, isolated sphere no longer hold when the incident beam is no longer normal to the surface. Element S_w which, for an isolated sphere, is equal to zero both at specular and at 180° from specular, no longer obeys this

rule. For a high-index surface the signal does tend to -100% for scattering along the surface ($\theta = \pm 90^\circ$). Element $S_{\parallel\parallel}$, which for an isolated sphere is equal to 100% at specular and -100% in the backscatter (180° from specular) no longer obeys these rules either. For a highly reflecting surface it does tend to zero along the surface ($\theta = \pm 90^\circ$). Element $S_{\parallel\perp}$, which for a lone sphere is equal to zero at specular and 180° from specular, now tends to zero only along the surface ($\theta = \pm 90^\circ$). These tendencies can be derived from the scattering amplitude matrix elements. When $\theta = \pm 90^\circ$, $R(\theta) = -1$ and $S(\theta, d) = 0$, the elements reduce to zero. For surfaces of high index of refraction, the Fresnel reflection coefficient $R_{\text{II}}(\theta)$ approaches -1 more rapidly than $R_{\text{I}}(\theta)$, which goes to zero at Brewster's angle. As a result of this dissimilarity, the beam is almost entirely TM polarized, and the Mueller matrix element $S_{\parallel\parallel}$ will go to 100%. The other polarization elements must go to zero at this point. Since $S_{\parallel\perp}$ and $S_{\perp\perp}$ go to zero along the surface, element $S_{\perp\parallel}$ goes to zero along the surface.

Figure 9 shows the scattering as a function of incident angle for a dipole $\lambda/10$ from a surface of index $n = 28.0 - 95.0i$. These curves are similar to the curves of Figure 8 where $n = 10.0 - 0.0i$. The only differences are the magnitudes in some locations and the loss of information in the reflected portion of the $S_{\parallel\parallel}$ matrix element. The change to a higher, complex index has had very little effect on the elements.

Figure 10 shows the scattering as a function of incident angle for a dipole $\lambda/10$ from a surface of index $n = 1.5 - 0.0i$. The matrix elements for a low-index surface are expected to retain the shape of the elements for the isolated dipole shown in Figure 4. The peaks in the elements are very near the same angular locations that they would be with no surface present. The maxima/minima of matrix elements $S_{\parallel\parallel}$ and $S_{\perp\perp}$ reveal the incident angle of the incident radiation. The trough located 90° from specular in the $S_{\parallel\parallel}$ curve is still close to 90° from specular. The maxima/minima of the $S_{\parallel\perp}$ curves also become shifted toward the specular and backscatter locations as the incident angle is changed.

CONCLUSION

Determining the nature of systems by studying the light scattered from them demands an understanding of how basic properties of the systems affect the scattering. Reducing the size of the particle to the Rayleigh limit eliminates the effects of the particle's geometry and refractive index from the problem. This effectively reduces the number of parameters to three: the complex index of refraction of the surface, the particle-surface separation, and the incident illumination angle. Understanding the trends in a simple system consisting of only three parameters leads to a better understanding of what happens in more complex systems. If we are unable to comprehend how a simple system scatters light, we cannot hope to understand the scattering from a system that is more complex.

Finally, it may be asked if any of our conclusions are valid for a particle of finite size. Figure 11 compares two sets of curves. One is the set of Mueller matrix elements for a dipole separated $d = \lambda/10$ from an aluminum mirror illuminated at an angle of incidence of 30° . The other is a set of theoretical Mueller matrix elements for the same system with the dipole replaced by a $\lambda/10$ radius sphere of index 1.5 resting on the surface. The theoretical system has been derived by solving the boundary conditions at both the sphere and the surface. Its solution is the subject of another paper.⁷ The two curves are quite similar, with differences arising from the geometry and refractive index of the finite-size sphere. The scattering from such a system can be measured. Weber and Hirleman made scattering measurements from a single sphere of radius $\sim\lambda/2$ using a He-Ne laser for illumination.⁸ A higher power laser in the infrared region would facilitate the measurements. On a more practical note, this model could be used to measure sub-wavelength contaminant sizes and/or densities by placing detectors at appropriate scattering locations and monitoring signal changes in the matrix elements as the surface is scanned.

REFERENCES

1. G. Mie, "Beitrage zur Optik truber Medien speziell kolloidaler Metallosungen," *Ann. Phys.*, 25, 377-445 (1908).
2. K. Nahm and W. Wolfe, "Light-scattering models for spheres on a conducting plane: comparison with experiment," *Appl. Opt.* 26, 2995-2999 (1987).
3. J. D. Jackson Classical Electrodynamics, Wiley, New York (1962).
4. C. Bohren and D. Huffman, Absorption and Scattering of Light by Small Particles, Wiley, New York (1983).
5. H. C. Van de Hulst, Light Scattering by Small Particles, Dover, New York (1957, 1976).
6. M. Kerker, The Scattering of Light and Other Electromagnetic Radiation, Academic, New York (1969).
7. W. S. Bickel and W. M. Bailey, "Stokes vectors, Mueller matrices, and polarized light," *Am. J. Phys.* 53, 468-478 (1985).
8. W. S. Bickel, J. Watkins, and G. Videen, "The light-scattering Mueller matrix elements for Rayleigh, Rayleigh-Gans, and Mie spheres," *Am. J. Phys.* 55, 559-561 (1987).
9. G. Videen, "The light scattering from a sphere on or near a surface," submitted to *JOSA A*, (1990).
10. D. C. Weber and E. D. Hirleman, "Light scattering signatures of individual spheres on optically smooth conducting surfaces," *Appl. Opt.* 27, 4019-4026 (1988).

Figure Captions

Fig. 1. The geometry of a dipole-surface scattering system: the dipole, represented by a circle, rests a distance, d , from a surface of index n . The incident angle θ_i and the scattering angle θ are measured from the surface normal.

Fig. 2. The paths that an incident beam may follow to the dipole and after interaction before being detected on the incident side of the surface.

Fig. 3. The paths that a beam may follow before being detected on the transmitted side of the surface.

Fig. 4. The Mueller matrix elements for an isolated dipole.

Fig. 5. The Mueller matrix elements as a function of dipole distance from a surface of index $n = 10.0 - 0.01$ illuminated at normal incidence. \bullet — \bullet Distance = $\lambda/1000$. \circ — \circ Distance = $\lambda/4$. \times — \times Distance = $\lambda/2$. \longleftrightarrow Distance = $3\lambda/4$.

Fig. 6. The Mueller matrix elements as a function of dipole distance from a surface of index $n = 28.0 - 95.01$ illuminated at normal incidence. \bullet — \bullet Distance = $\lambda/1000$. \circ — \circ Distance = $\lambda/4$. \times — \times Distance = $\lambda/2$. \longleftrightarrow Distance = $3\lambda/4$.

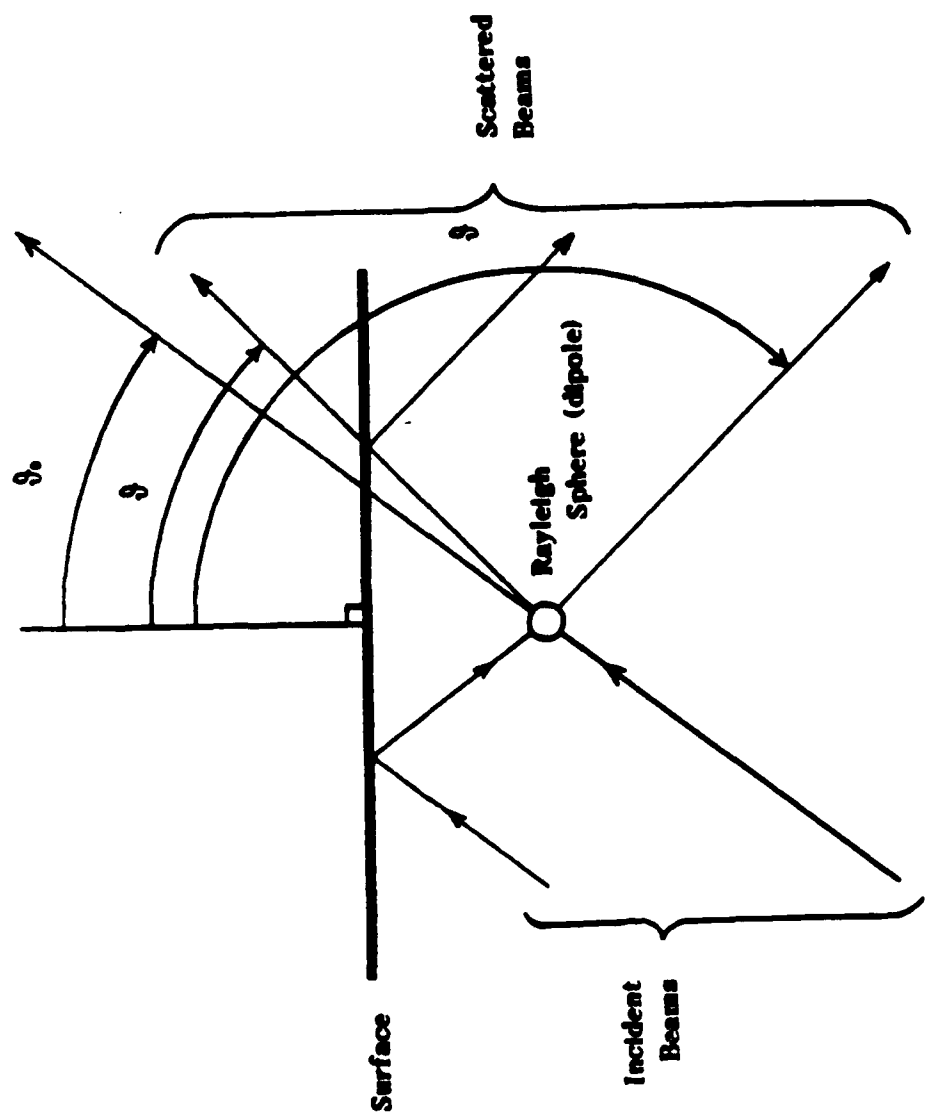
Fig. 7. The Mueller matrix elements as a function of dipole distance from a surface of index $n = 1.5 - 0.01$ illuminated at normal incidence. \bullet — \bullet Distance = $\lambda/1000$. \circ — \circ Distance = $\lambda/4$. \times — \times Distance = $\lambda/2$. \longleftrightarrow Distance = $3\lambda/4$.

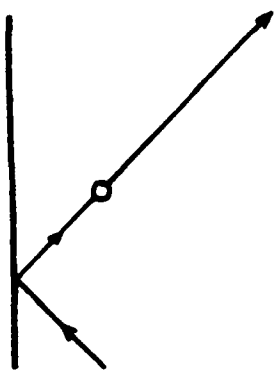
Fig. 8. The Mueller matrix elements as a function of incident angle of illumination for a dipole a distance $\lambda/10$ from a surface of index $n = 10.0 - 0.01$. \bullet — \bullet $\theta_i = 0^\circ$. \circ — \circ $\theta_i = 30^\circ$. \times — \times $\theta_i = 60^\circ$.

Fig. 9. The Mueller matrix elements as a function of incident angle of illumination for a dipole a distance $\lambda/10$ from a surface of index $n = 28.0 - 95.0i$. $\bullet - \bullet$ $\theta_i = 0^\circ$, $\circ - \circ$ $\theta_i = 30^\circ$, $\times - \times$ $\theta_i = 60^\circ$.

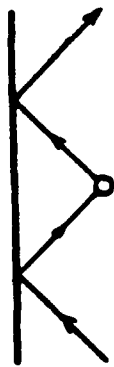
Fig. 10. The Mueller matrix elements as a function of incident angle of illumination for a dipole a distance $\lambda/10$ from a surface of index $n = 1.5 - 0.01$. \bullet $\delta_s = 0^\circ$, \circ $\delta_s = 30^\circ$, \times $\delta_s = 60^\circ$.

Fig. 11. The Mueller matrix elements as a function of incident angle of illumination for a particle $\lambda/10$ from a surface of index $n = 28.0 - 95.0i$ and incident angle of 30° . — A dipole. $\circ - \circ$ A sphere of index $n = 1.55 - 0.0i$ and radius $\lambda/10$.

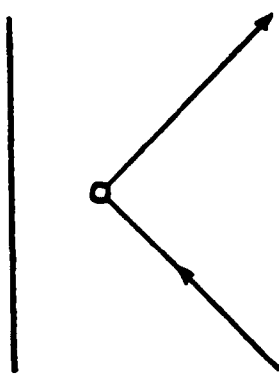




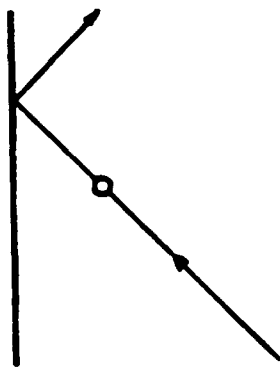
Path II



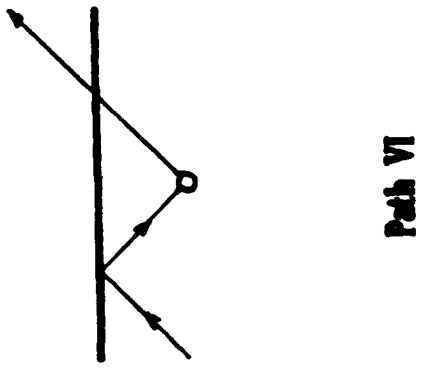
Path IV



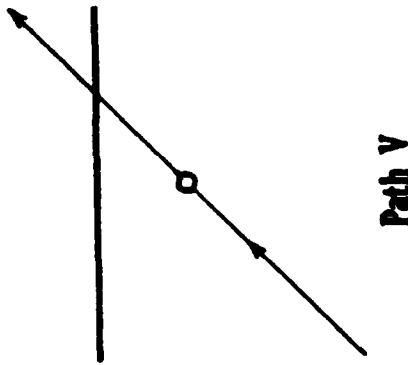
Path I



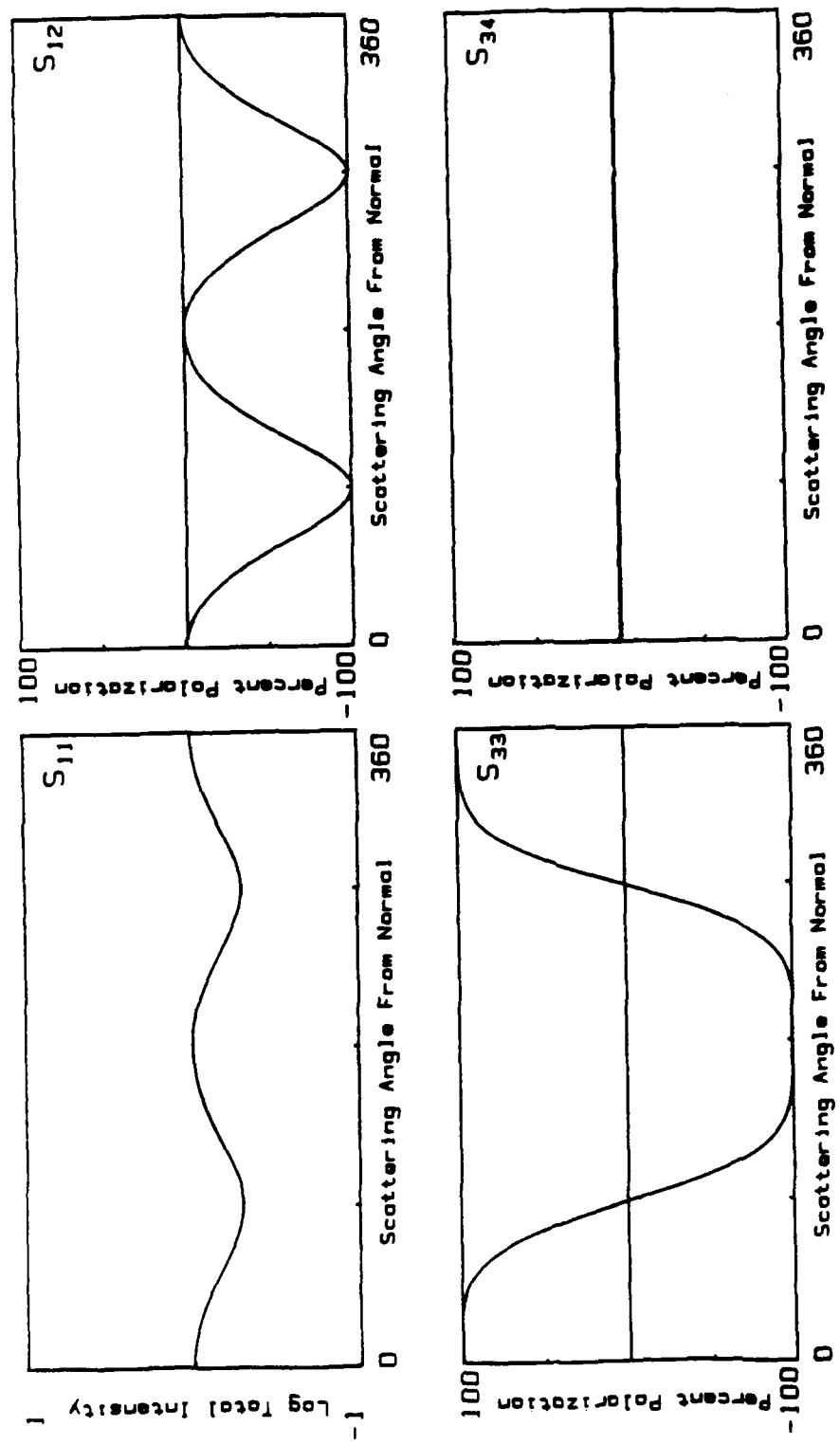
Path III

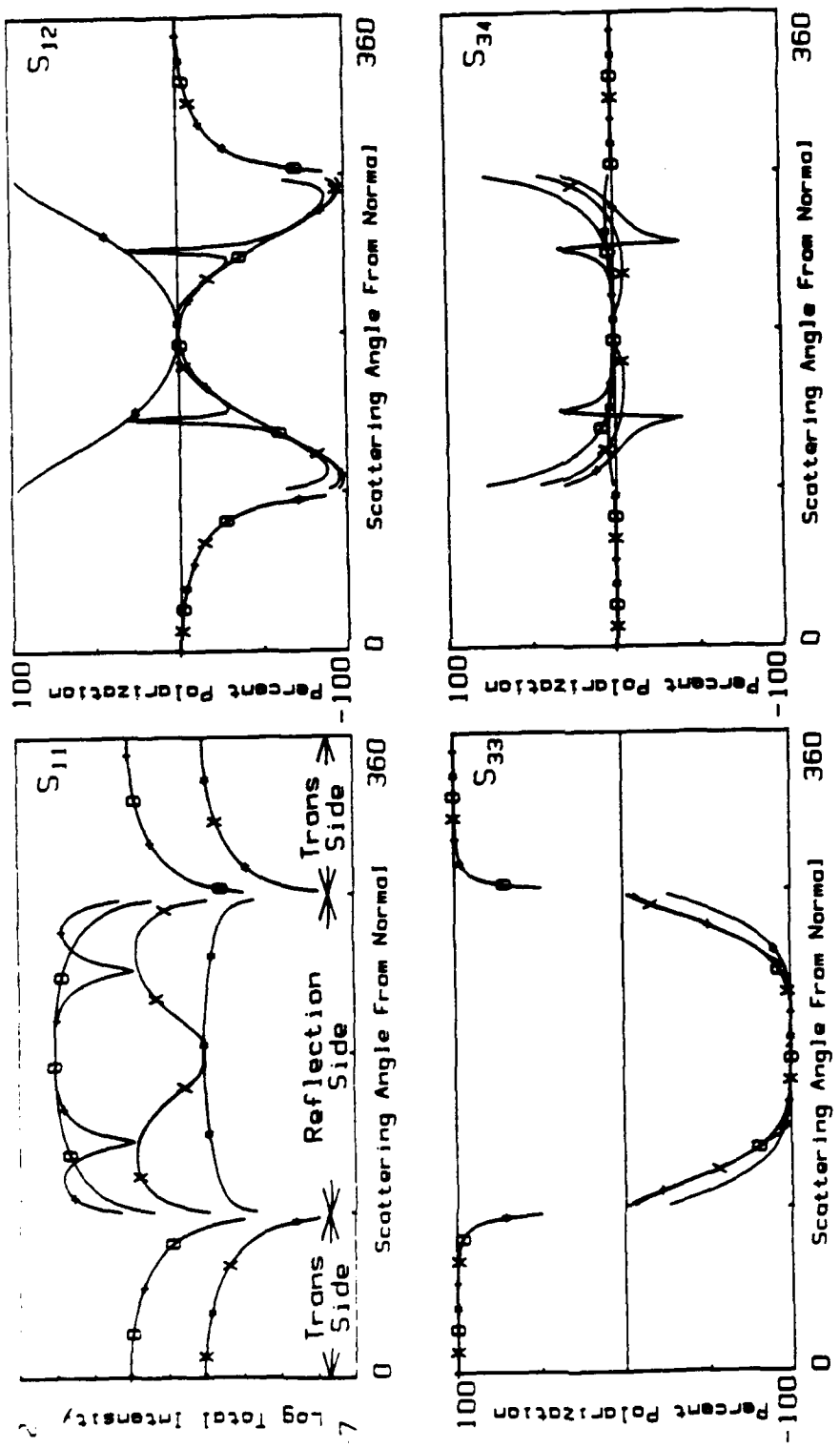


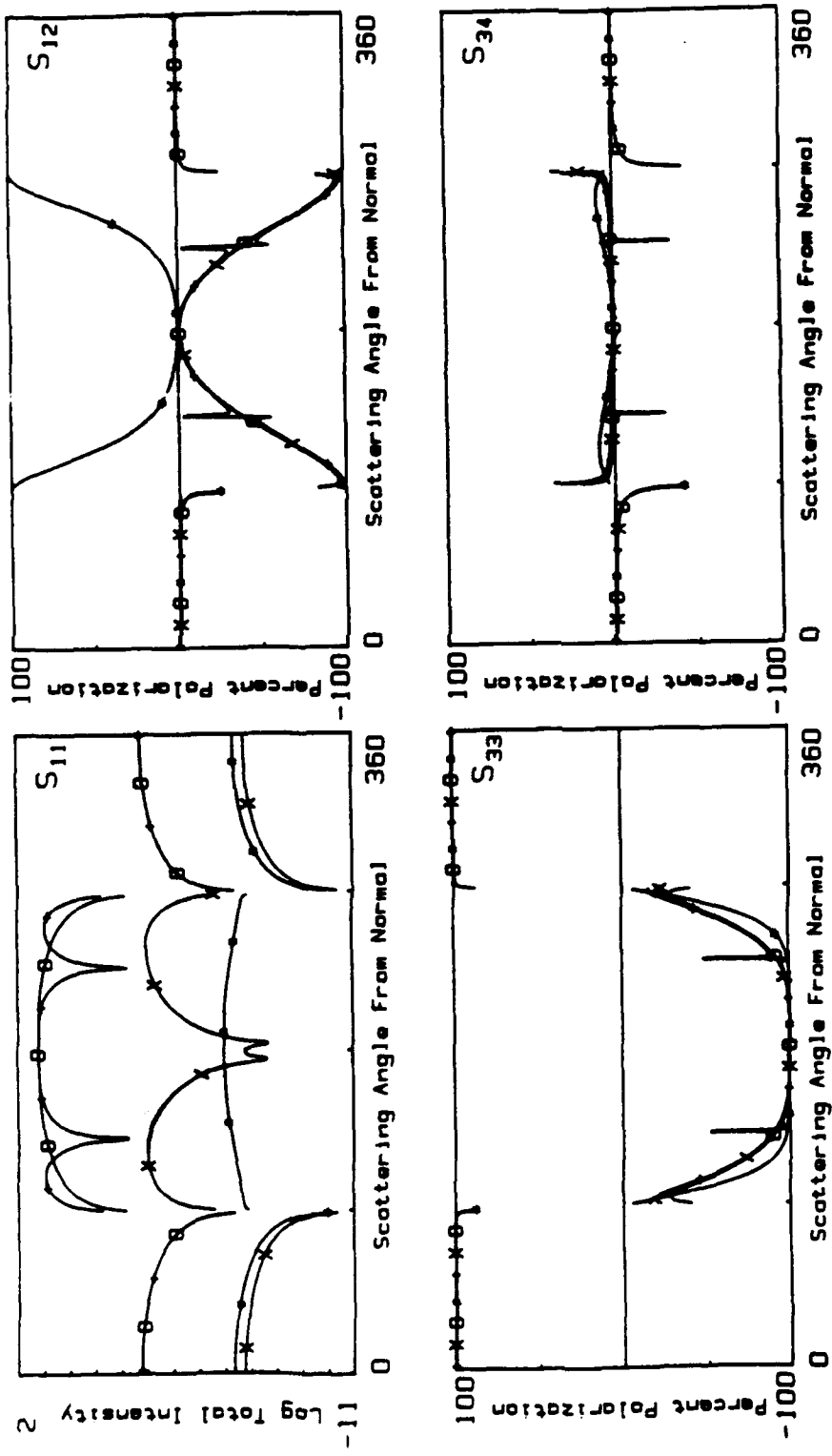
Path VI

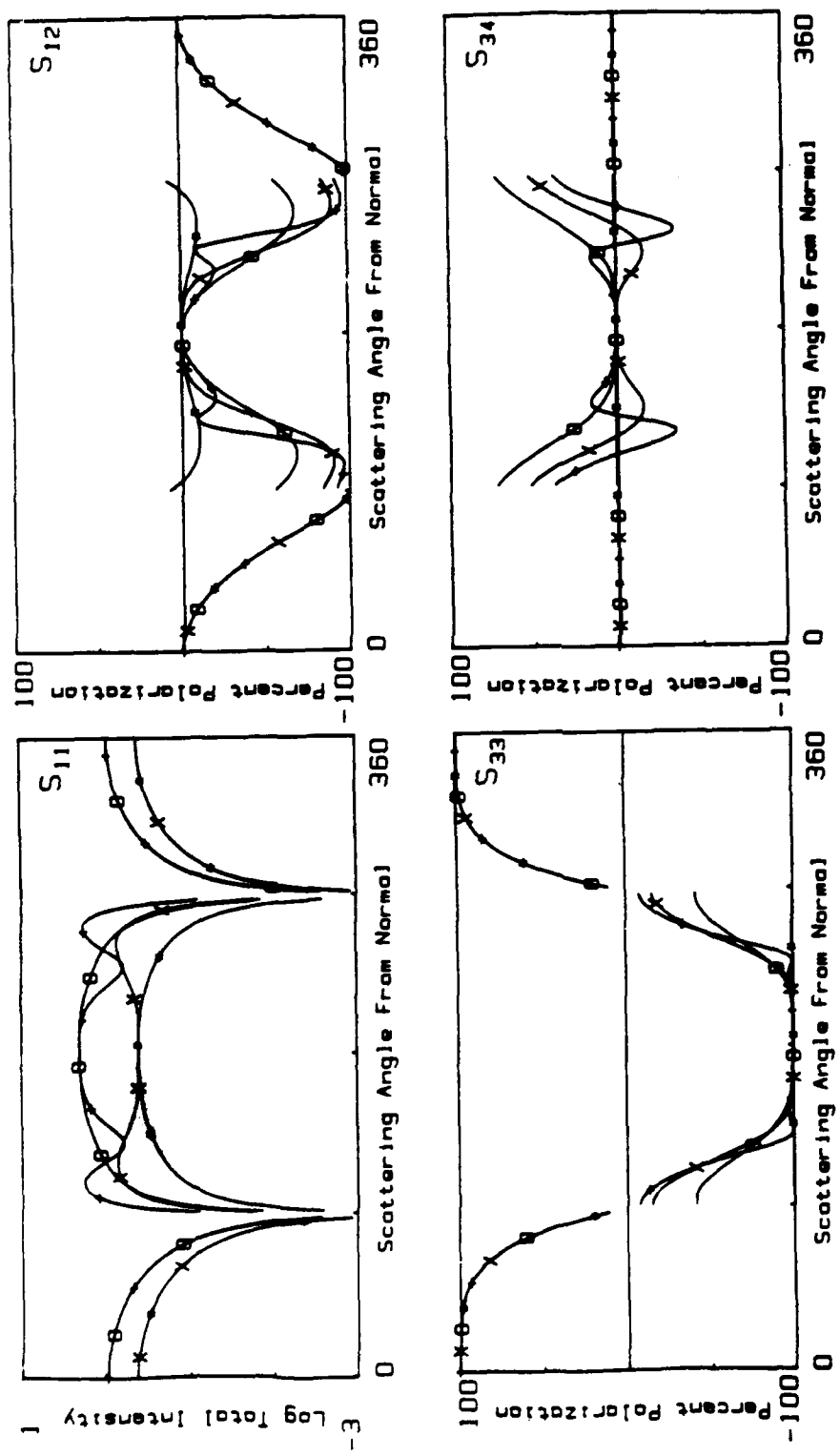


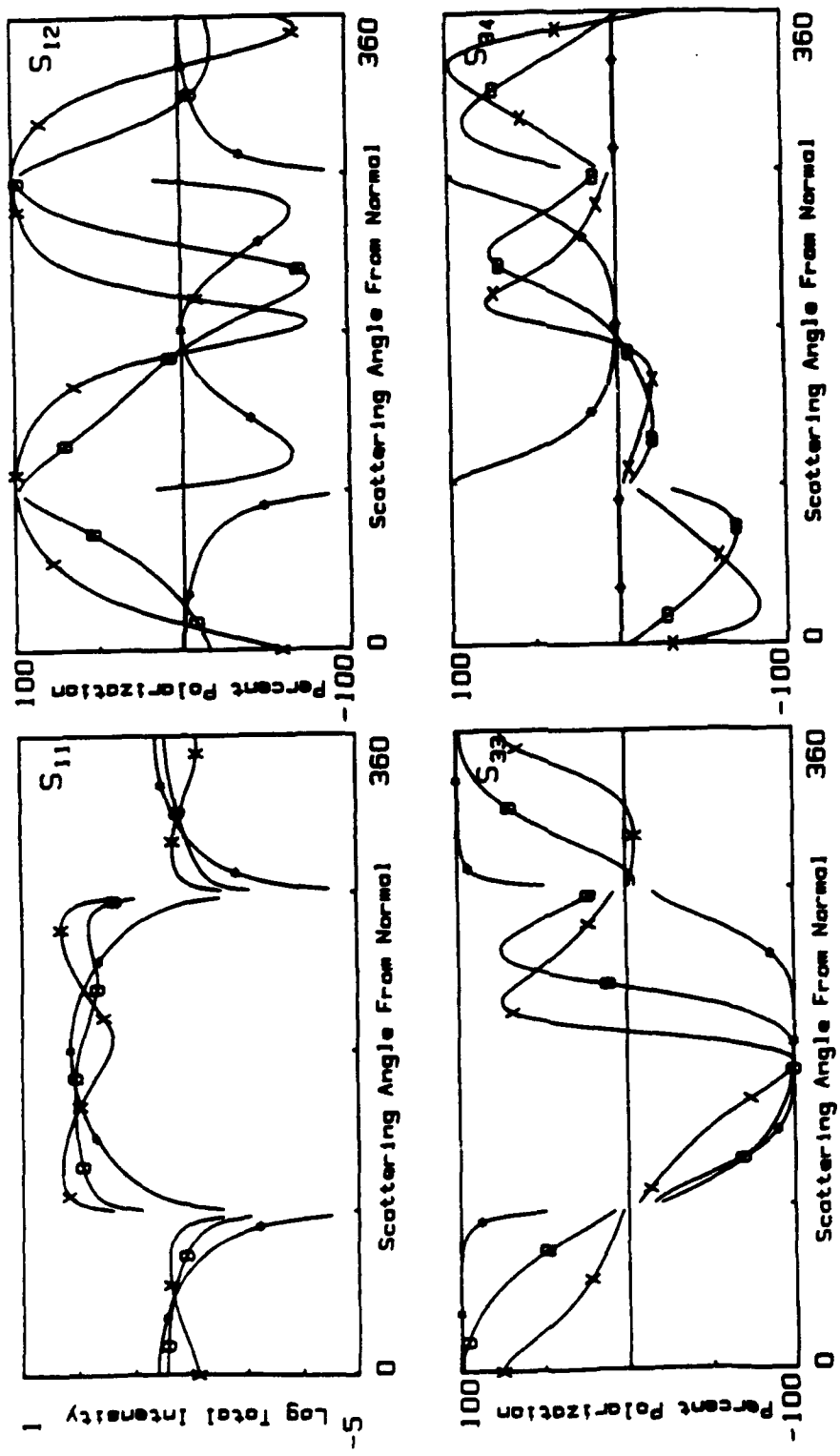
Path V

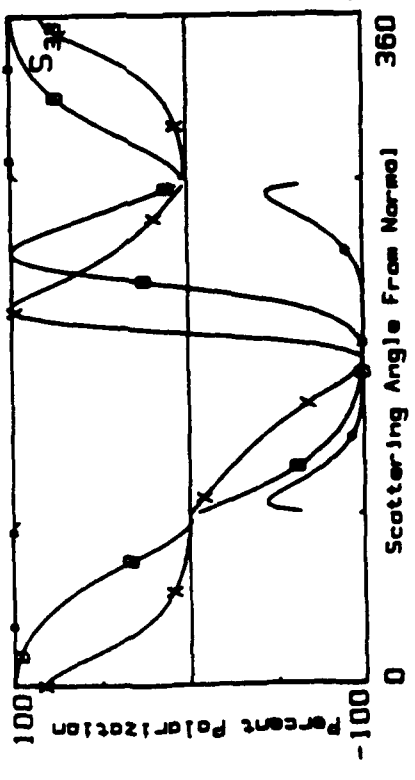
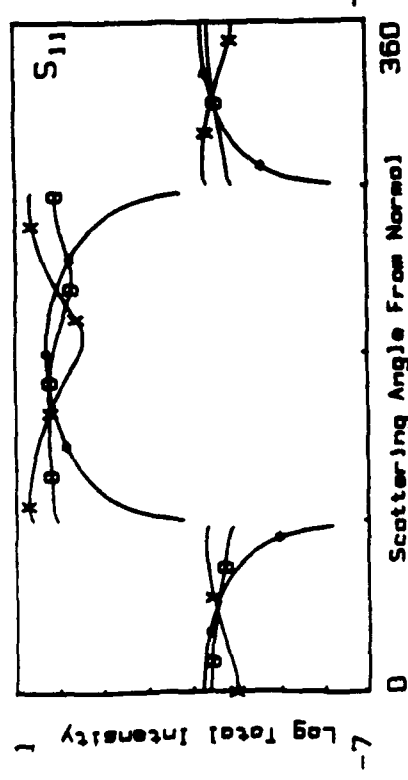
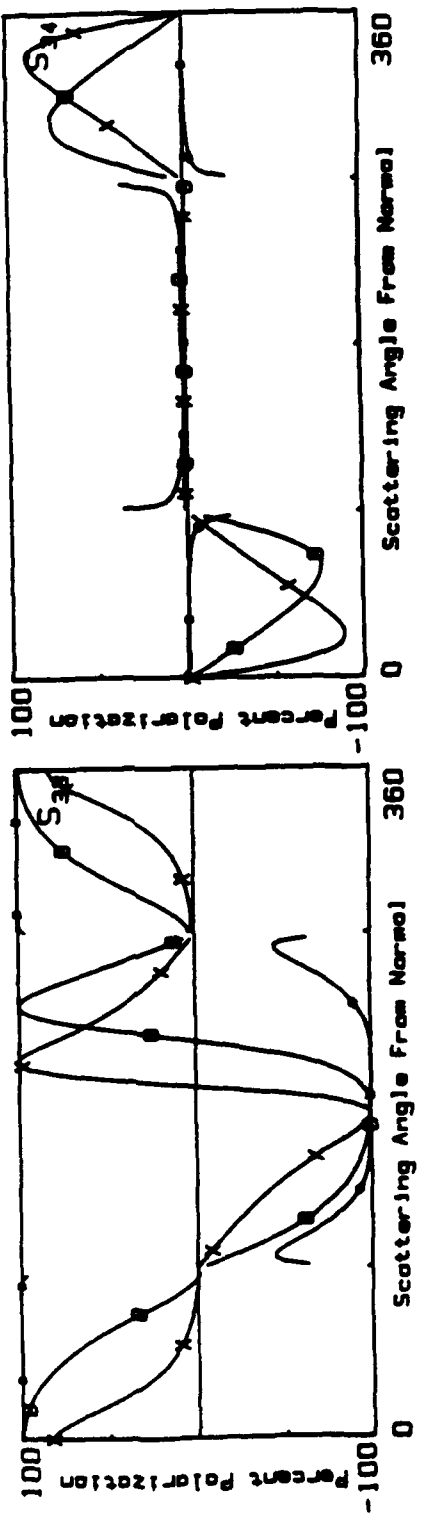
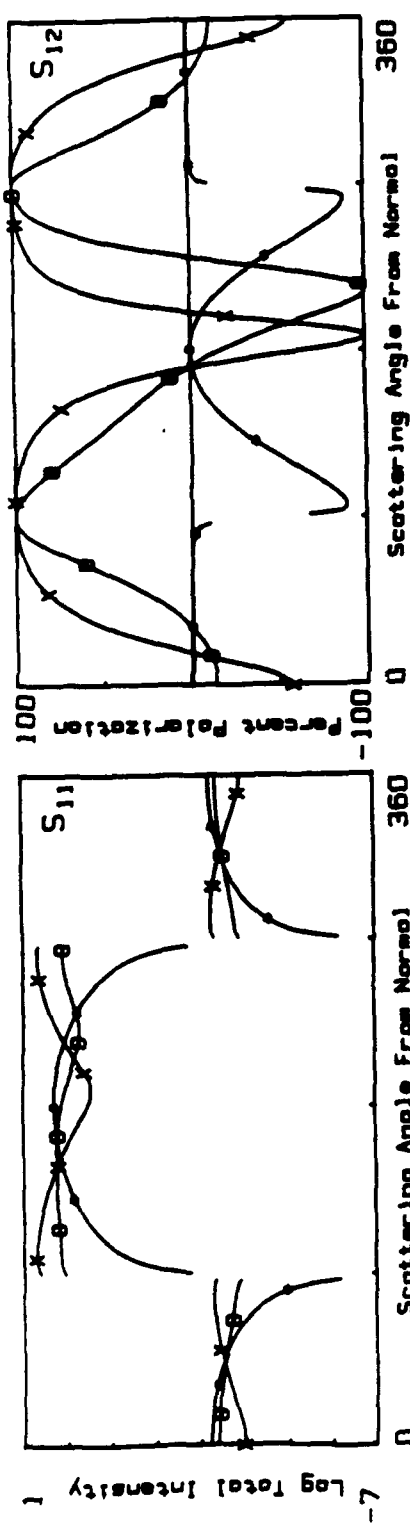


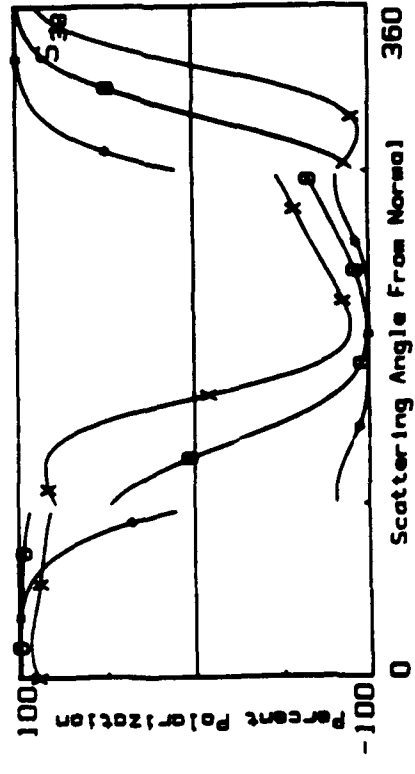
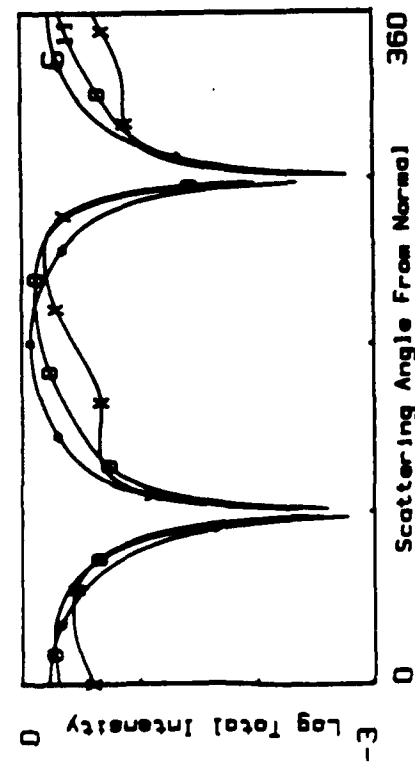
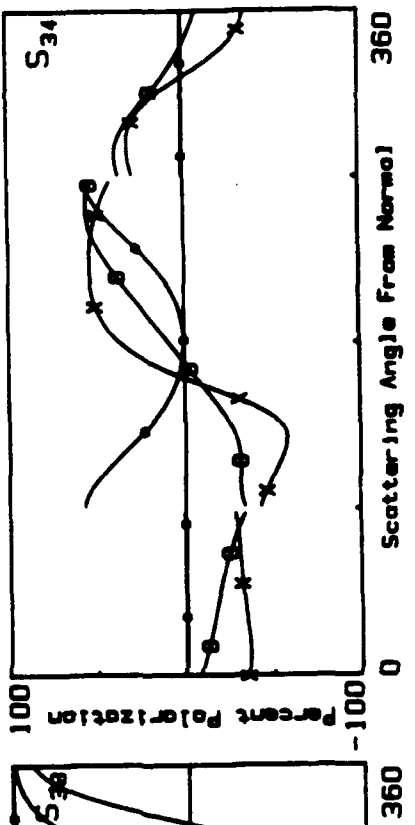
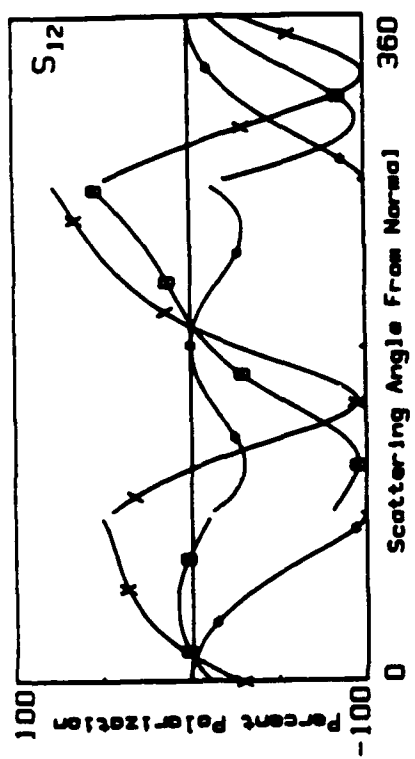


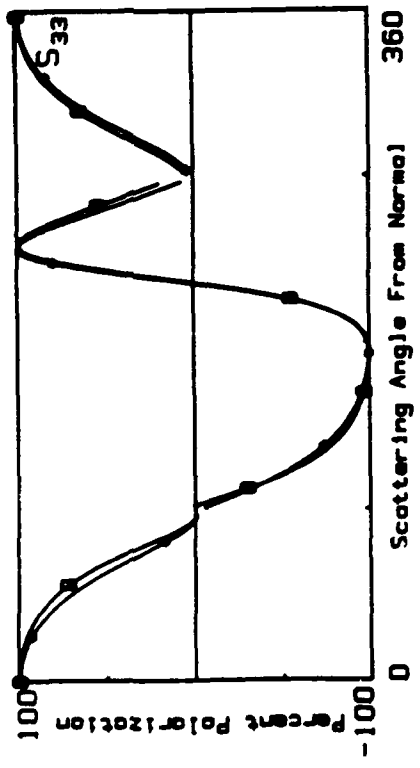
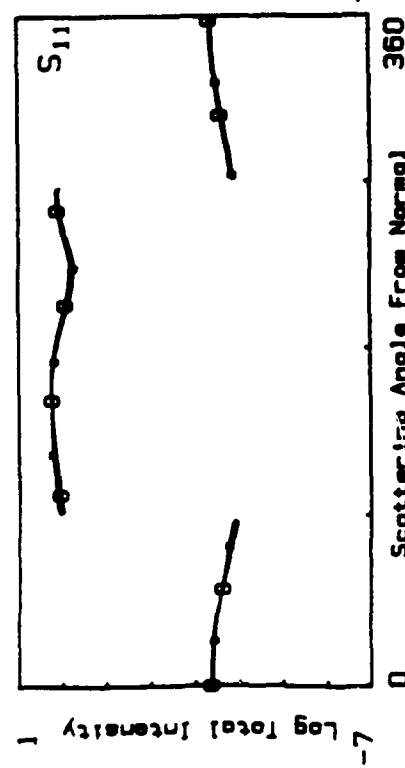
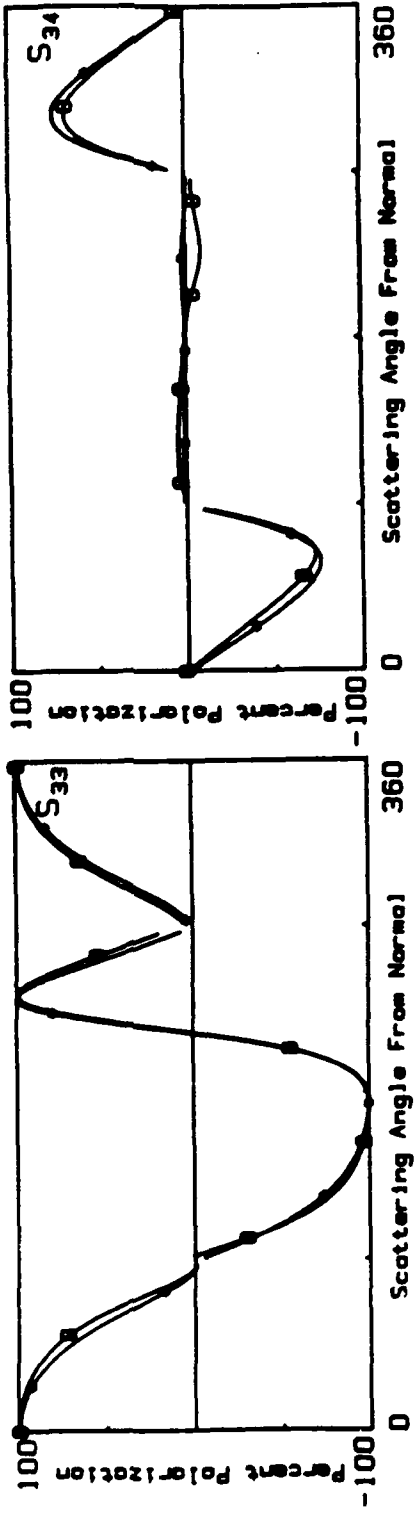
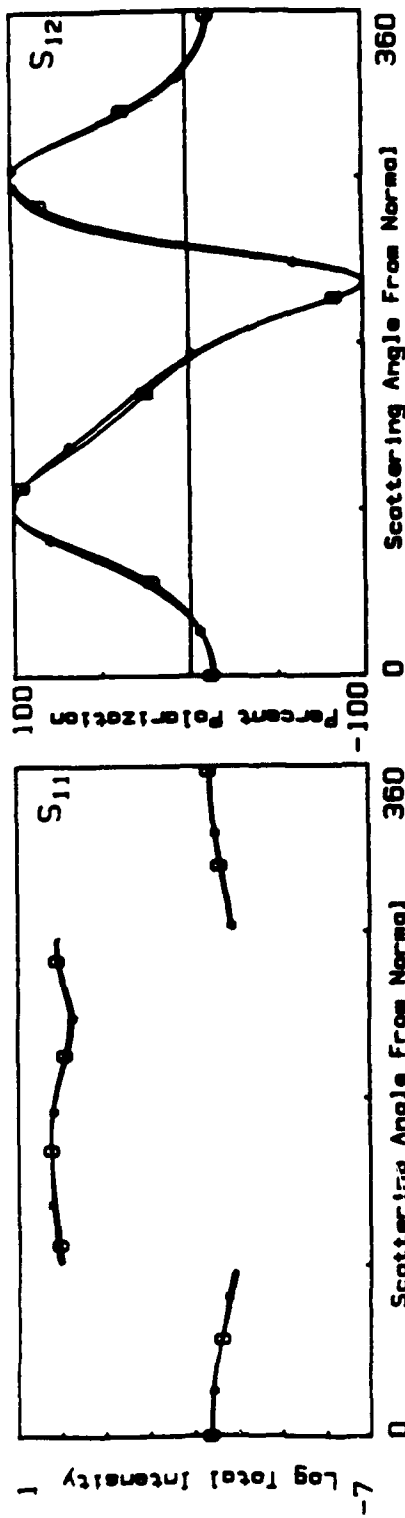












(17)

SUBMITTED TO J. OPT SOC AM

Sent

Feb 21, 91

1

Electromagnetic scattering from a sphere: the near-field region

Gorden Videen, Joseph M. Boyer, and William S. Bickel

Physics Department

University of Arizona

Tucson, Arizona 85721

(602) 621-2534

Abstract

Although the general case of electromagnetic waves scattered from a sphere when illuminated by a plane wave was formulated by Mie more than half a century ago, almost all measurements and calculations of the total scatter have concentrated on the far-field region. We examine the electric and magnetic field topographies as well as the scattering Mueller matrices in the near-field region of a Mie sphere.

I. Introduction

In the nineteenth and early twentieth centuries, one of the most important problems in the application of Maxwell's theory to phenomenon taking place in nature was the interaction of electromagnetic waves with matter. An important example is the work of Rayleigh¹ in explaining the blue color of the sky in terms of scattering from particles small in comparison with the optical wavelengths. An analysis of electromagnetic waves scattered from a sphere was published by Clebsch in 1863,² and like Fresnel's reflection equations, his solutions appeared before the development of Maxwell's equations. Although the radiation scattered by a sphere was solved by Mie in 1908,³ and refined by Debye in 1909⁴ when he investigated the incident electromagnetic wave pressure on particles, the result was also obtained by Lorenz in 1898.⁵ The geometry of spherical systems is especially appealing because spheres possess high symmetry and they occur naturally, being a condition of minimum potential energy. Extensive applications to atmospheric sciences occur where rainbows, planetary atmospheres and other systems are explored in books by van de Hulst,⁶ Kerker,⁷ and Bohren and Huffman.⁸

The relations of Mie's general theory are relatively simple when the distance kR to the sphere lay in the electromagnetic far-field region where only scattered fields decaying as $1/kR$ are significant. Fifty years after Mie presented his theory, King and Wu⁹ lamented the fact that "sufficient data do not seem to be available to construct a complete representation about a conducting sphere" as that shown for an infinitely-long, conducting cylinder (in referring to figures in the text showing the near-field region of the cylinder).

In the same text, they devoted an appendix to plots of surface currents on perfectly-conducting spheres of increasing size illuminated by incident plane waves which were obtained from a large, state-of-the-art military computer program directed by Nelson Logan for USAF Cambridge Research Center.

Most theoretical work and scattering applications consider only the far field, optically represented as the Fraunhofer region. For instance, all three scattering programs in the book by Bohren and Huffman (ref. 8) calculate the far fields. One notable exception is the work of Aden² who ingenuously measured the near-zone fields of metal and water spheres along the back-scatter direction in the microwave region of the spectrum. With the advent of better computers, the entire electromagnetic fields can now be calculated easily. It is instructive to see what happens as the detectors move into the near-field region, optically represented as the Fresnel region. We want to know the error involved in assuming a far-field solution when we know our detector is not at infinity. We also want to know just how the near-field region differs from the far-field region.

In experiments where scattering systems are illuminated with visible wavelengths ($\lambda = 0.6328\mu\text{m}$, for instance), a detector mechanism only one meter distant, would certainly seem to be operating in the far-field region. At this distance, changing the scatterer-detector distance by a factor of two would not change the relative shape of a scattering signal, therefore the de-

tector is considered to be in the far field for all practical considerations. Indeed, Bell's³ measurements of the light-scattering Mueller matrix for a fiber, seemed to verify this (although his optical system was typical, it certainly was not universal).

In this paper we explore the near-field region of a Mie scatterer. First we will calculate the entire field. We will then calculate the scatter that would be measured in the far-field region, and compare the results with what would be measured in the near-field region.

II. Mie Theory

Figure 1 shows the arrangement of the scattering system. A sphere of radius a , and complex refractive index n' is centered on the origin. A plane wave, electrically polarized in the x direction, propagates in the positive z direction. We detect the electric and magnetic fields at position R, θ, ϕ from the center of the sphere (R is the sphere-detector distance).

We report only the primary results of Mie theory since formal derivations exist in many of the cited texts. The electric and magnetic components of the fields incident upon the sphere are

$$\mathbf{E}_{in} = \sum_{n=0}^{\infty} \sum_{m=-n}^n a_{nm} \mathbf{M}_{nm}^{(in)} + b_{nm} \mathbf{N}_{nm}^{(in)}, \text{ and} \quad (1a)$$

$$\mathbf{H}_{in} = \frac{k}{i\omega\mu} \sum_{n=0}^{\infty} \sum_{m=-n}^n b_{nm} \mathbf{M}_{nm}^{(in)} + a_{nm} \mathbf{N}_{nm}^{(in)}, \quad (1b)$$

where $k = 2\pi/\lambda$ is the wavenumber, ω is the angular frequency, and μ is the permeability of the incident medium at λ . The vectors $\mathbf{M}_\infty^{(j)}$ and $\mathbf{N}_\infty^{(j)}$ are given by

$$\mathbf{M}_\infty^{(j)} = \hat{\mathbf{z}} \left[\frac{im}{\sin\theta} z_n^{(j)}(kr) \tilde{P}_n^{(j)}(\cos\theta) e^{im\phi} \right] -$$

$$\hat{\mathbf{y}} \left[z_n^{(j)}(kr) \frac{\partial}{\partial\theta} \left(\tilde{P}_n^{(j)}(\cos\theta) \right) e^{im\phi} \right], \text{ and} \quad (2a)$$

$$\mathbf{N}_\infty^{(j)} = \hat{\mathbf{r}} \left[\frac{1}{kr} z_n^{(j)}(kr) n(n+1) \tilde{P}_n^{(j)}(\cos\theta) e^{im\phi} \right] +$$

$$\hat{\mathbf{z}} \left[\frac{1}{kr} \frac{\partial}{\partial r} (rz_n^{(j)}(kr)) \frac{\partial}{\partial\theta} \left(\tilde{P}_n^{(j)}(\cos\theta) \right) e^{im\phi} \right] +$$

$$\hat{\mathbf{y}} \left[\frac{1}{kr} \frac{\partial}{\partial r} (rz_n^{(j)}(kr)) \frac{im}{\sin\theta} \tilde{P}_n^{(j)}(\cos\theta) e^{im\phi} \right]. \quad (2b)$$

The superscript identifies the Bessel functions used to represent the fields. For example, $j = 1$ corresponds with the use of the functions $z_n^{(1)}(\rho) = j_n(\rho)$, $j = 2$ corresponds with the use of the functions $z_n^{(2)}(\rho) = y_n(\rho)$, and $j = 3$ corresponds with the use of the functions $z_n^{(3)}(\rho) = h_n^{(3)}(\rho) = j_n(\rho) + iy_n(\rho)$. The functions $\tilde{P}_n^{(j)}(\cos\theta)$ are the normalized associated Legendre polynomials defined by

$$\tilde{P}_n^{(j)}(\cos\theta) = P_n^{(j)}(\cos\theta) \sqrt{\frac{(2n+1)(n-m)!}{2(n+m)!}}. \quad (3)$$

For an incident electromagnetic plane wave traveling along the positive z axis and polarized along the x axis, the coefficients are

$$a_{nm} = E_0 i^{n-m} \sqrt{\frac{2n+1}{2n(n+1)}} (\delta_{m-1} + \delta_{m+1}), \text{ and} \quad (4a)$$

$$b_{nm} = E_0 i^{n+1} \sqrt{\frac{2n+1}{2n(n+1)}} (\delta_{m,-1} - \delta_{m,1}), \quad (4b)$$

where E_0 is the maximum amplitude of the electric field. Internal fields are also generated when $k' \rightarrow \infty$:

$$\mathbf{H}_{int} = \sum_{n=0}^{\infty} \sum_{m=-n}^n c_{nm} \mathbf{M}_{nm}^{(1)} + d_{nm} \mathbf{M}_{nm}^{(2)}, \text{ and} \quad (5a)$$

$$\mathbf{H}_{int} = \frac{k'}{i\omega\mu'} \sum_{n=0}^{\infty} \sum_{m=-n}^n d_{nm} \mathbf{M}_{nm}^{(1)} + c_{nm} \mathbf{M}_{nm}^{(2)}, \quad (5b)$$

where $k' = kn'$ is the wavenumber of the sphere medium for incident wavelength λ , n' is the sphere refractive index and μ' is the permeability of the sphere medium at wavelength λ . The scattered fields are

$$\mathbf{H}_{sc} = \sum_{n=0}^{\infty} \sum_{m=-n}^n e_{nm} \mathbf{M}_{nm}^{(3)} + f_{nm} \mathbf{M}_{nm}^{(4)}, \text{ and} \quad (6a)$$

$$\mathbf{H}_{sc} = \frac{k}{i\omega\mu} \sum_{n=0}^{\infty} \sum_{m=-n}^n f_{nm} \mathbf{M}_{nm}^{(3)} + e_{nm} \mathbf{M}_{nm}^{(4)}, \quad (6b)$$

By applying boundary conditions, the scattering coefficients may be solved in terms of the coefficients of the incident field:

$$e_{nm} = -a_{nm} \frac{k'\mu\psi_n'(ka)\psi_n(ka) - k\mu'\psi_n'(ka)\psi_n(k'a)}{k'\mu\psi_n'(ka)\xi_n(ka) - k\mu'\xi_n'(ka)\psi_n(k'a)}, \text{ and} \quad (7a)$$

$$f_{nm} = -b_{nm} \frac{k'\mu\psi_n'(ka)\psi_n(k'a) - k\mu'\psi_n'(ka)\psi_n(ka)}{k'\mu\xi_n'(ka)\psi_n(k'a) - k\mu'\psi_n'(ka)\xi_n(ka)}. \quad (7b)$$

where $\psi_r(\rho) = \rho j_r(\rho)$, and $\xi_r(\rho) = \rho h_r'''(\rho)$. These coefficients can be reduced to much simpler expressions when the refractive index of the sphere approaches large values, in which case

$$e_{nm} = -a_{nm} \frac{\psi_r(ka)}{\xi_r(ka)}, \text{ and} \quad (8a)$$

$$f_{nm} = -b_{nm} \frac{\psi_r'(ka)}{\xi_r'(ka)}. \quad (8b)$$

We will detect the fields in two different planes, one in the y-z plane ($\varphi = 90^\circ$) which lies perpendicular to the incident electric field (the TE plane, or H-plane), and the other in the x-z plane ($\varphi = 0^\circ$) which lies perpendicular to the incident magnetic field (the TM plane, or E-plane). We can represent the fields in the form of matrices:

$$\begin{pmatrix} E_\varphi \\ E_\theta \\ E_r \end{pmatrix} = \begin{pmatrix} S_1 & S_2 \\ S_2 & S_1 \\ S_1 & S_2 \end{pmatrix} \begin{pmatrix} E_{Tz} \\ E_{T\theta} \end{pmatrix}, \quad \begin{pmatrix} H_\varphi \\ H_\theta \\ H_r \end{pmatrix} = \begin{pmatrix} S_1' & S_2' \\ S_2' & S_1' \\ S_1' & S_2' \end{pmatrix} \begin{pmatrix} H_{Tz} \\ H_{T\theta} \end{pmatrix}, \text{ where} \quad (9)$$

$$S_1 = \sum_{n=1}^{\infty} 2i \left[\frac{iE_r'(kR)\tilde{P}_r'(\cos\theta)}{kR\sin\theta} f_{n1} - h_r'''(kR) \frac{\partial}{\partial\theta} \tilde{P}_r'(\cos\theta) e_{n1} \right], \quad (10a)$$

$$S_2 = \sum_{n=1}^{\infty} 2 \left[\frac{ih_r''(kR)\tilde{P}_r'(\cos\theta)}{\sin\theta} e_{n1} + \frac{\xi_r'(kR)}{kR} \frac{\partial}{\partial\theta} \tilde{P}_r'(\cos\theta) f_{n1} \right], \quad (10b)$$

$$S_0 = \sum_{n=1}^{\infty} 2n(n+1) \frac{h_n^{(1)}(kR)}{kR} \tilde{P}_n'(\cos\theta) f_{n1}, \quad (10c)$$

$$S_1' = \frac{k}{\omega\mu} \sum_{n=1}^{\infty} 2 \left[\frac{\xi_n'(\cos\theta) \tilde{P}_n'(\cos\theta)}{kR \sin\theta} e_{n1} + i h_n^{(1)}(kR) \frac{\partial}{\partial\theta} \tilde{P}_n'(\cos\theta) f_{n1} \right], \quad (10d)$$

$$S_2' = \frac{k}{\omega\mu} \sum_{n=1}^{\infty} 2 \left[\frac{i h_n^{(1)}(kR) \tilde{P}_n'(\cos\theta)}{\sin\theta} f_{n1} + \frac{\xi_n'(\cos\theta)}{kR} \frac{\partial}{\partial\theta} \tilde{P}_n'(\cos\theta) e_{n1} \right], \quad (10e)$$

$$S_3' = \frac{k}{\omega\mu} \sum_{n=1}^{\infty} 2n(n+1) \frac{h_n^{(1)}(kR)}{kR} \tilde{P}_n'(\cos\theta) e_{n1}, \text{ and} \quad (10f)$$

$$S_3 = S_4 = S_5 = S_6 = S_7' = S_8' = 0. \quad (10g)$$

These expressions hold for the fields everywhere. To get to the far-field region we let $kR \rightarrow \infty$, where these expressions are further reduced by taking advantage of the asymptotic behavior of the spherical Hankel function:

$$h_n^{(1)}(\rho) \sim \frac{(-i)^n e^{i\rho}}{i\rho}, \quad \text{and} \quad \xi_n'(\rho) = (-i)^n e^{i\rho}, \quad \text{for } |i\rho| \gg 1 \text{ yield} \quad (11)$$

$$S_1 = \sum_{n=1}^{\infty} -2(-i)^n \frac{e^{ikR}}{kR} \left[\frac{\tilde{P}_n'(\cos\theta)}{\sin\theta} f_{n1} + \frac{\partial}{\partial\theta} \tilde{P}_n'(\cos\theta) e_{n1} \right], \quad (12a)$$

$$S_2 = \sum_{n=1}^{\infty} 2(-i)^n \frac{e^{ikR}}{kR} \left[\frac{\tilde{P}_n'(\cos\theta)}{\sin\theta} e_{n1} + \frac{\partial}{\partial\theta} \tilde{P}_n'(\cos\theta) f_{n1} \right], \quad (12b)$$

$$S_4 = \sum_{n=1}^{\infty} 2n(n+1)(-i) \frac{e^{ikR}}{i(kR)^2} \tilde{P}_n'(\cos\theta) f_{n1}, \quad (12c)$$

$$S_4' = \frac{k}{\omega\mu} S_4, \quad (12d)$$

$$S_4' = - \frac{k}{\omega\mu} S_4, \text{ and} \quad (12e)$$

$$S_4' = \frac{k}{\omega\mu} \sum_{n=1}^{\infty} 2n(n+1)(-i) \frac{e^{ikR}}{i(kR)^2} \tilde{P}_n'(\cos\theta) e_{n1}. \quad (12f)$$

As the sphere-detector distance is increased, matrix elements S_4 and S_4' (which vary as $1/R^2$) approach zero more rapidly than do the other matrix elements (which vary as $1/R$). We see here another significance of the far field. The E and H field vectors are not only orthogonal to one another and to propagation direction \mathbf{R} , but are also in time and spatial phase so as to compose a wave front moving at the speed of light in the wave medium (equations 12c,d).

III. How far is far?

Equations 9-12 can be used to determine whether the radiation from a scattering system is in the near or far field. As an example we start by examining the scattered fields from a dielectric (quartz) sphere of refractive index $n' = 1.55 + 0.0i$ in the optical region of the spectrum ($\lambda = 0.6328\mu\text{m}$ HeNe laser radiation). We arbitrarily choose the radius of the sphere to be

$a = 0.525\mu\text{m}$, a size large enough to provide some oscillatory structure on the scattering curves.

A. The Electric Fields

Figure 2 shows the intensity of the electric fields as a function of scattering angle at four different observation distances. The TE curves correspond to measurements when the incident electric field is transverse to the scattering plane (a measurement of $S_e^*S_e$). The TM curves correspond to measurements of the non-radial component of the electric field when the incident magnetic field is transverse to the scattering plane (a measurement of $S_a^*S_a$). The RD curves correspond to measurements of the radial component of the electric field when the magnetic field is transverse to the scattering plane (a measure of $S_r^*S_r$). Four sets of curves are shown respectively for sphere-detector distances of $R = 1\lambda$, $R = 3\lambda$, $R = 9\lambda$, and $R = \infty$. To facilitate comparison, the elements have all been normalized for sphere-detector distance [multiplied by $(kR)^2$ for TE and TM and $(kR)^4$ for RD]. Note that at the endpoints ($\theta = 0^\circ$ and $\theta = 180^\circ$) the TE elements are equal to the TM elements and the RD elements are zero.

These curves show that at optical wavelengths, the far field is not very far away from the scatterers. This is shown by the fact that three curves ($R = 3\lambda$, $R = 9\lambda$, and $R = \infty$) in each set of four have very similar shape and almost coincide, while the fourth curve ($R = 1\lambda$) is quite different. When the sphere-detector distance is only $R = 3\lambda$, the matrix elements are already simi-

lar to those for $R = \infty$. When $R = 9\lambda$ (less than $6\mu\text{m}$ at optical wavelengths!) the elements are almost indistinguishable from far-field elements. This shows that near-field phenomena occurs only very close to the particle, and that it is very difficult to measure near-field signals in scattering experiments at optical wavelengths. An infinitely-small, non-interfering detector would have to probe the field at $R \sim \lambda$.

B. The Magnetic Fields

We next look at the magnetic fields and compare them with the electric fields for the same system. Figure 3 shows the intensities of the magnetic fields as a function of scattering angle at four different observation distances (note that TE corresponds to $S_e^{-}S_e'$, TM to $S_s^{-}S_s'$, and RD to $S_s^{-}S_s'$). Four sets of curves are shown respectively for the same sphere-detector distances of $R = 1\lambda$, $R = 3\lambda$, $R = 9\lambda$, and $R = \infty$ used to calculate the electric field intensities of Fig. 2. To facilitate comparison, the elements have all been normalized for sphere-detector distance and for field strength (multiplied by $\omega\mu/k$). As with the electric field curves, three curves ($R = 3\lambda$, $R = 9\lambda$, and $R = \infty$) in each set of four have very similar shape and almost coincide, while the fourth curve ($R = 1\lambda$) is quite different. Only in the far field when $R = \infty$ does the magnetic field behavior approach that of the electric field, the ratio between them being $\omega\mu/k$. The TE and TM electric and magnetic field intensity curves are identical in the far field. Since the radial component approaches zero much more rapidly (as $1/R^4$) than the other components (which decay as $1/R^2$), it does not contribute to the intensity in the far fields.

C. The Matrix Elements

Finally, we generate the Mueller matrix elements¹³ from the above expressions for the fields and examine their behavior as a function of sphere-detector distance R . The Mueller matrix, which is defined in terms of the electric field components S_x and S_y , is especially attractive experimentally because it completely quantifies the polarization state of the system. The matrix does not, however, include the radial component of the system. This component which decays as $1/R^2$ contributes only to the total field and not to radiation from the system since the radiation term decays as $1/R$. An ideal (infinitely-small, perfectly-impedance-matched) detector placed in the near-field region cannot distinguish between the radiation terms and the total electric field. Only four elements of the 16-element matrix are non-zero and unique. Only these are necessary to characterize a symmetric scatterer like a sphere. These four Mueller matrix elements for the $a = 0.525\mu\text{m}$ radius quartz sphere calculated from the data shown in Figs. 2 and 3 are presented in Figure 4.

The Mueller matrix is an especially useful diagnostic tool for experimentalists because it is self-calibrating. The polarizations are independent of intensity. It is important to emphasize the value of the matrix elements as discriminators of small differences. The electric fields measured at $R = 1\lambda$ in Fig. 2 can easily be distinguished from the others measured at $R = 3\lambda$, $R = 9\lambda$, and $R = \infty$. However they are proportional to the source intensity and detector efficiency. If these parameters are unknown, the absolute intensities are un-

known and the similarity in shapes will prevent discrimination of these four curves. The situation is entirely different with the Mueller matrix elements of Fig. 4. Although the curves are similar, they are distinguishable. A detector measuring element S_{11} near 135° can easily distinguish all the elements at the four different sphere-detector distances, and the signal is completely independent of the source intensity.

IV. What about conductivity?

Earlier in the paper we simplified the equations representing the scattering amplitude coefficients by letting the sphere refractive index approach infinity. Making the sphere a perfect conductor provides an interesting example because it provides one limit to which the refractive index of the sphere may approach. Another interesting example, known as the Rayleigh-Gans region, occurs when the refractive index of the sphere approaches the refractive index of the encompassing medium. In this limit, where the refractive index of the sphere is identical to the refractive index of the encompassing medium, the sphere disappears. It is optically invisible and no scatter can occur. The intensities of the electric fields as a function of scattering angle at different sphere-detector distances for a perfectly-conducting, $a = 0.525\mu\text{m}$ radius sphere illuminated at $\lambda = 0.6328\mu\text{m}$ are shown in Figure 5 and the corresponding intensities of the magnetic fields are shown in Figure 6. The curves for the conducting sphere are much smoother than those for the dielectric sphere (shown in figures 2 and 3) because the fields are unable to penetrate the conducting sphere. The scatter from a perfectly-conducting sphere and a

dielectric sphere can be compared to the reflection of a light source from a metal mirror (with one boundary) and a sheet of glass having two boundaries. The metal mirror provides a well-defined reflection, but the intensity of the light reflecting from the sheet of glass will oscillate through maxima/minima due to interference occurring between the fields which reflect off the front and rear boundaries of the glass. These oscillations are perhaps more pronounced in the Mueller scattering matrix shown in Fig. 7.

Finally we should see if the approximation of large refractive index has any physical significance. To do this we examine the scatter from an $a = 0.525\mu\text{m}$ radius partially-conducting sphere of aluminum ($n = 1.1 + 6.0i$) illuminated at $\lambda = 0.6328\mu\text{m}$ as a function of scattering angle at four different sphere-detector distances R . The matrix elements for this system are shown in Figure 8. They are very similar to the elements of Figure 7 for perfectly conducting spheres. Therefore, even though the refractive index of aluminum is finite, its scattering properties can be estimated by considering scattering in the limiting case of a perfect conductor.

V. The Total Field

The near field can be distinguished from the far field by placing a "perfect" detector within a few wavelengths of a sphere whose size is comparable with the wavelength of the illuminating radiation. Unfortunately the detector will measure a mixture of the scattered fields and the incident fields since there is no way to filter out the incident fields from the scattered

fields. Therefore the incident fields must be included in measurements taken in the near field.

This does not occur experimentally for most scattering measurements since they are made in the far-field region. The laser illumination, though not an infinite plane wave, is very nearly constant over the scattering system (sphere). Also, because the laser beam has a small diameter ($\sim 1000a$), the angular subtense of the incident field is very narrow, occurring mostly in the forward scatter ($\theta \sim 0^\circ$). Therefore it is not collected by the detector system at large angles. Even though such systems are not illuminated by an infinite plane wave (the laser beam intensity cross-section is approximately Gaussian), the resulting scatter is very nearly what is predicted with plane-wave illumination (ref. 13).

In order to study the interference of the scattered radiation with the incident plane wave we investigate a system with a simple scattered radiation pattern: an $a = 0.25\lambda$ radius, perfectly-conducting sphere. Now we can distinguish between the effects due to the fields scattering from the sphere and the effects due to the fields interfering with the plane wave. Figure 9 shows the intensities of the electric fields for this system as a function of scattering angle at four different sphere-detector distances. Reducing the size of the sphere relative to the incident wavelength reduces the oscillatory frequencies in the scattering as a function of scattering angle and the total amount of scattered radiation. The interference effects are best seen when the scattered intensities are comparable to the incident plane wave intensities

where the measurements are made. We keep in mind that the plane wave intensity does not depend on detector position; whereas, the total scattered radiation decays as $1/R^2$. The curves of Figure 9 are for a sphere whose scattered fields have only a small angular dependence.

Figure 10 shows the interference of the scattered electric fields with the incident plane wave from an $a = 0.25\lambda$ radius, perfectly-conducting sphere as a function of scattering angle at four different sphere-detector distances. The intensity on these graphs is not normalized for distance. At a sphere-detector distance of infinity, the fields give the well-known "Rayleigh curves" and are due entirely to the plane wave ($I_{Rz} = 1$, $I_{Rw} = \cos^2\theta$, and $I_{Ro} = \sin^2\theta$). As the sphere-detector distance is reduced, oscillations about these values appear in the interference patterns.

VI. Topographical Plots

It is apparent that the near-field interference is very complex and rich with structure. In order to view this complexity from a different vantage point, we generated the topography of the electric and magnetic field intensities in figures 11 and 12, respectively. These plots show the intricacies of the near-field and elucidate certain features which are not apparent on the other figures. Intensity is shown in the vertical axis. The sphere lies on the z axis and the scatter is shown only to the left of the z axis (in the x-z or y-z plane).

There are several points to make from these plots. First, the internal fields within the perfectly-conducting sphere are zero. Second, boundary conditions force the electric fields parallel to the surface (TE and TM of Figure 11) and the magnetic fields perpendicular to the surface (RD of Figure 12) to zero. In these three plots, the fields outside the sphere approach zero as the sphere-detector distance approaches the sphere radius ($R \rightarrow a$). In the other three plots (RD of Figure 11 and TE and TM of Figure 12), there are discontinuities in the field intensities at the boundary of the sphere. To satisfy the boundary condition at the sphere surface, a surface current is induced on the sphere equivalent to the magnetic field at the surface of the sphere. Third, all radial fields along the z axis are zero. Fourth, the TE fields are identical to the TM fields along the z axis. Fifth, the TE and TM field intensities decay as $1 + 1/R^2$. And sixth, standing waves appear in the intensity distribution.

The standing waves that appear in figures 11 and 12 are the result of the scattered spherical waves interfering with the incident plane waves. To gain insight into the origin and implication of these standing waves, we examine the scalar components along the z axis. The amplitude of the unit-normalized incident plane wave is of the form $e^{i\omega t}$. The scattered spherical waves are of the form $Ae^{i\omega z}$ for negative values of z and $Be^{i\omega z}$ for positive values of z where A and B contain additional phase and amplitude information (the spherical amplitudes must decay as $1/R$, for instance). In the negative z direction, the sum of these exponentials ($e^{i\omega t} + Ae^{i\omega z}$) indicates a decaying standing wave and a traveling wave, while in the positive z direction the sum ($e^{i\omega t} + Be^{i\omega z}$) indicate only a traveling wave. Figure 13 shows the electric and magnetic fields

along the z axis for a perfectly-conducting, $a = 0.25\lambda$ radius sphere. The standing waves appear in the back-scatter region (negative z). Note that the electric field standing waves, which have a node ($I = 0$) at the sphere surface, are 180° out of phase with the magnetic field standing waves which have an antinode ($I \sim 3.75$) at the sphere surface. The spatial frequency of the standing waves is twice the frequency of the incident radiation.

We now consider the shapes of the nodal and antinodal regions in the scattering plane. These regions are produced by the interference effects of the incident plane wave and the scattered spherical waves. Antinodal regions occur in regions where these two sets of waves meet in phase, and nodal regions occur in regions where they meet out of phase. We are looking, in effect, at contours in space where the distance from some reference plane wave is equal to the distance from the center of the spherical plane waves. This is precisely the definition of a paraboloid. Figure 14 shows contour maps of the TE electric field intensities and the TM magnetic field intensities for a perfectly-conducting, $a = 0.25\lambda$ radius sphere interfering with the incident plane wave is shown in Figure 14. The parabolically-shaped standing-wave patterns are clearly seen.

VII. Discussion

We have examined electromagnetic waves scattered from spheres in the near-field and found that the field distributions quickly approach those of the far-field (within about 10 wavelengths for spheres whose radius is approx-

imately the wavelength of the incident radiation). We examine the near-field region where the scattered fields cannot be separated from the incident fields. The most striking feature of the near-field region is the parabolically-shaped standing waves that form in the backscatter region.

Acknowledgements

We thank Steve Robinson and Jim Dugan for many enlightening discussions. This research was supported in part by the Air Force Office of Scientific Research and by an Itek fellowship.

References

1. Lord Rayleigh, "On the Scattering of Light by Small Particles," *Phil. Mag.* 41, 447-454 (1871).
2. Clebsch, A., "Ueber die Reflexion an einer Kugelfläche," *J. reine angew. Math.* 61, 195-262 (1863).
3. Mie, G., "Beitrage zur Optik trüber Meiden speziell kolloidaler Metallosungen," *Ann. Physik*, 25, 377-445 (1908).
4. Debye, P., "Der Lichtdruck auf Kugeln von beliebigem Material," *Ann. Physik*, 30, 57-136 (1909).
5. Lorenz, L., Oeuvres Scientifiques (Copenhagen, 1898).
6. van de Hulst, H. C., Light Scattering by Small Particles (Dover, New York, 1981).
7. Kerker, M., The Scattering of Light and Other Electromagnetic Radiation, (Academic Press, New York, 1969).
8. Bohren, C. and Huffman, D., Absorption and Scattering of Light by Small Particles (Wiley, New York, 1983).
9. King, R. W. P., Scattering and Diffraction of Waves (Harvard University Press, 1959).
10. Boyer, J. M. and Coleman, R., "Investigations on the future development and verification of the E.W.F. theory" NASA Technical Report NAS-8-11138, **GMSFC, Huntsville, Alabama** (1964).
11. Boyer, J. M., "A radio wave mechanism to account for the known distribution van Allen belts about the earth," *Nature* 190, 597-599 (1961).
12. Aden, A. L., "Electromagnetic scattering from spheres with sizes comparable to the wavelength," *J. Appl. Phys.*, 22, 601-605 (1951).

13. Bell, B. W. and Bickel W. S., "Single fiber light scattering matrix: an experimental determination," *Appl. Opt.* 20, 3874-3879 (1981).
14. Bickel, W. S., and Bailey, W. M. , "Stokes vectors, Mueller matrices, and polarized light," *Am. J. Phys.* 53, 468-478 (1985).

Figure Captions

Fig. 1. The scattering geometry showing the sphere of radius a centered on the origin.

Fig. 2. The normalized scattering electric field intensities for an $a = 0.525\mu\text{m}$ radius quartz sphere illuminated by $\lambda = 0.6328\mu\text{m}$ light for sphere-detector distances of $R = 1\lambda$ (---o---), $R = 3\lambda$ (O—O), $R = 9\lambda$ (X—X), and $R = \infty$ (↔↔).

Fig. 3. The normalized scattering magnetic field intensities for an $a = 0.525\mu\text{m}$ radius quartz sphere illuminated by $\lambda = 0.6328\mu\text{m}$ light for sphere-detector distances of $R = 1\lambda$ (---o---), $R = 3\lambda$ (O—O), $R = 9\lambda$ (X—X), and $R = \infty$ (↔↔).

Fig. 4. The scattering Mueller matrix for an $a = 0.525\mu\text{m}$ radius quartz sphere illuminated by $\lambda = 0.6328\mu\text{m}$ light for sphere-detector distances of $R = 1\lambda$ (---o---), $R = 3\lambda$ (O—O), $R = 9\lambda$ (X—X), and $R = \infty$ (↔↔).

Fig. 5. The normalized scattering electric field intensities for an $a = 0.525\mu\text{m}$ radius, perfectly-conducting sphere illuminated by $\lambda = 0.6328\mu\text{m}$ light for sphere-detector distances of $R = 1\lambda$ (---o---), $R = 3\lambda$ (O—O), $R = 9\lambda$ (X—X), and $R = \infty$ (↔↔).

Fig. 6. The normalized scattering magnetic field intensities for an $a = 0.525\mu\text{m}$ radius, perfectly-conducting sphere illuminated by $\lambda = 0.6328\mu\text{m}$ light for sphere-detector distances of $R = 1\lambda$ (---o---), $R = 3\lambda$ (O—O), $R = 9\lambda$ (X—X), and $R = \infty$ (↔↔).

Fig. 7. The scattering Mueller matrix for an $a = 0.525\mu\text{m}$ radius, perfectly-conducting sphere illuminated by $\lambda = 0.6328\mu\text{m}$ light for sphere-detector distances of $R = 1\lambda$ (—*—), $R = 3\lambda$ (O—O), $R = 9\lambda$ (X—X), and $R = \infty$ (↔).

Fig. 8. The scattering Mueller matrix for an $a = 0.525\mu\text{m}$ radius aluminum sphere illuminated by $\lambda = 0.6328\mu\text{m}$ light for sphere-detector distances of $R = 1\lambda$ (—*—), $R = 3\lambda$ (O—O), $R = 9\lambda$ (X—X), and $R = \infty$ (↔).

Fig. 9. The normalized scattering electric field intensities for an $a = 0.25\lambda$ radius, perfectly-conducting sphere at sphere-detector distances of $R = 0.5\lambda$ (—*—), $R = 0.75\lambda$ (O—O), $R = 1.0\lambda$ (X—X), and $R = \infty$ (↔).

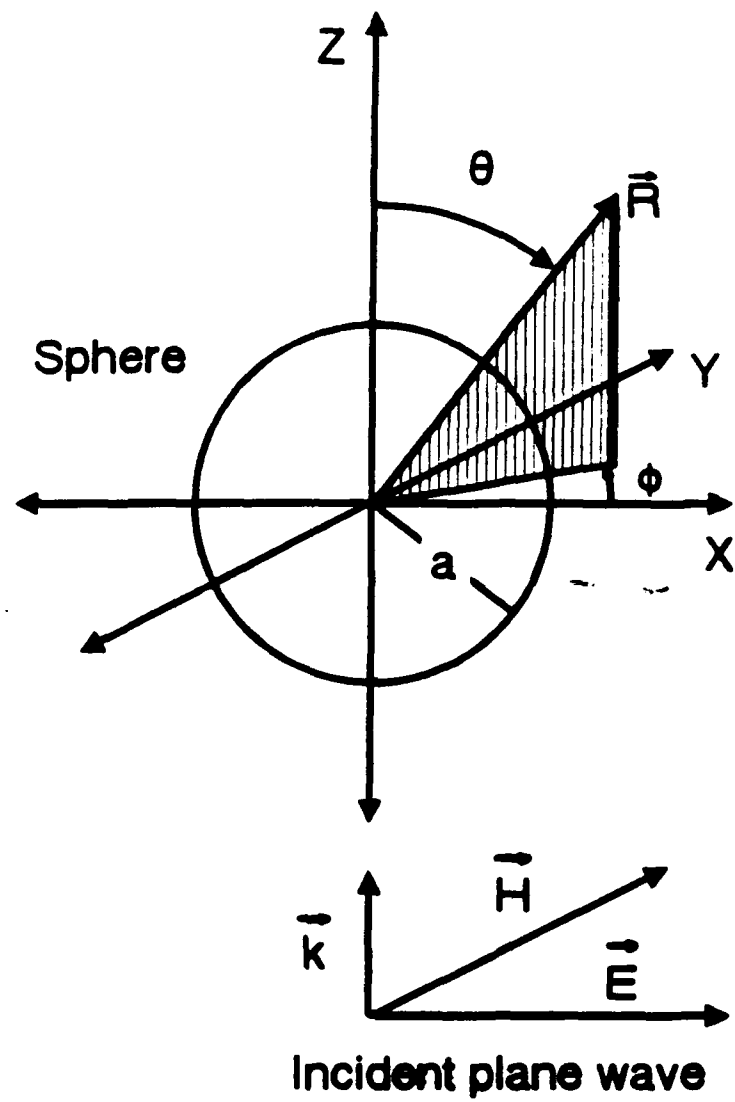
Fig. 10. The normalized scattering electric field intensities for an $a = 0.25\lambda$ radius, perfectly-conducting sphere interfering with the incident plane wave at sphere-detector distances of $R = 0.5\lambda$ (—*—), $R = 0.75\lambda$ (O—O), $R = 1.0\lambda$ (X—X), and $R = \infty$ (↔).

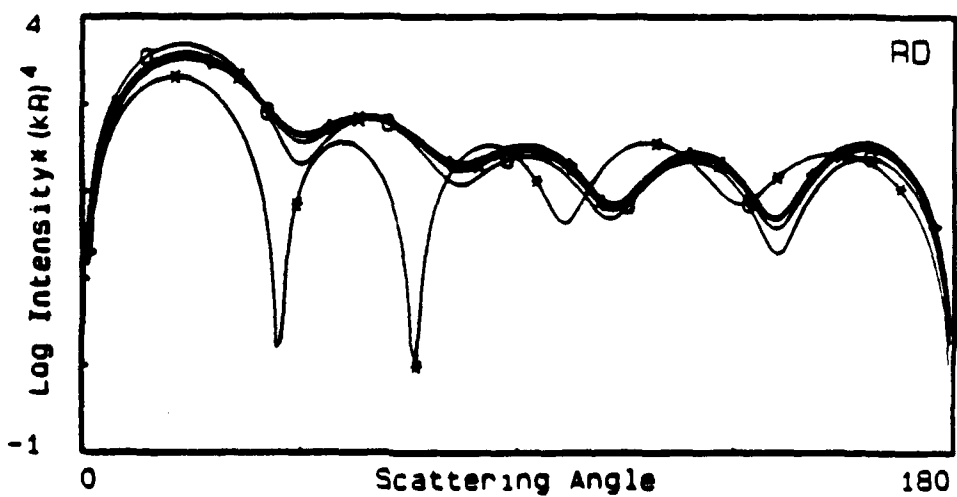
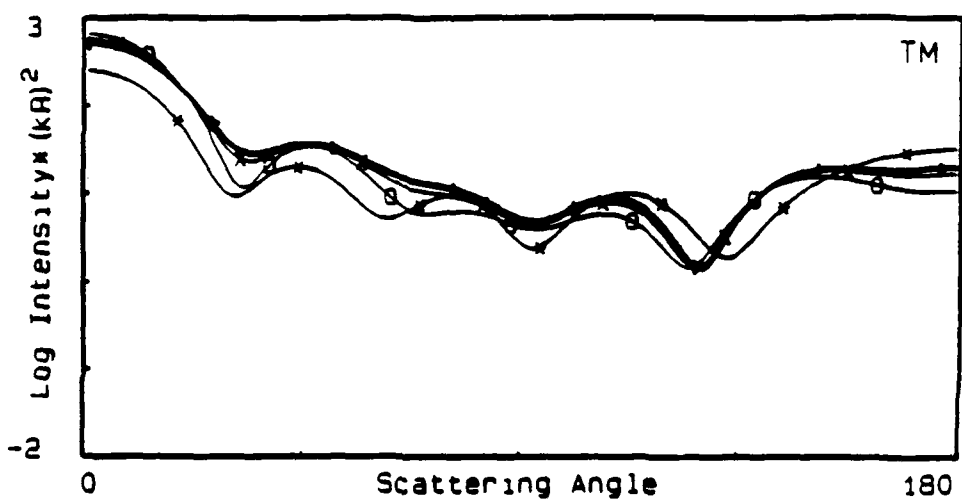
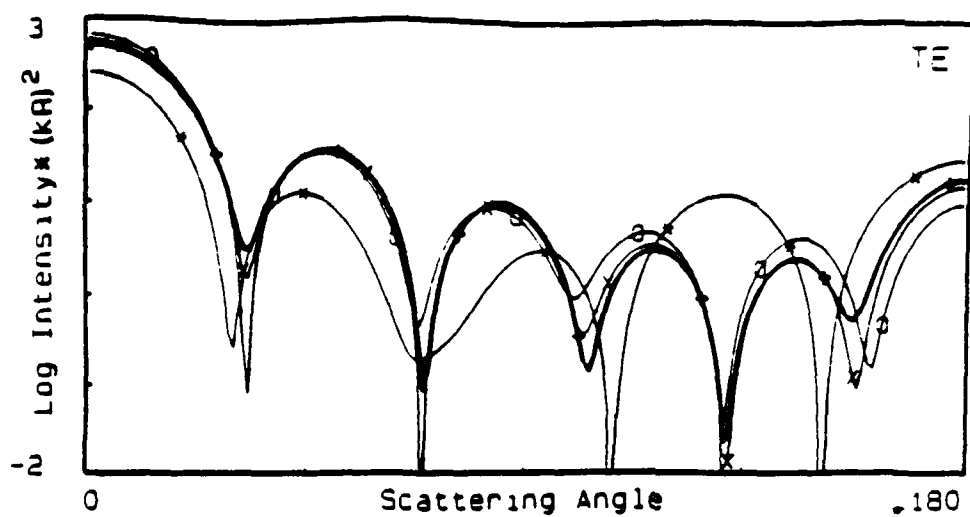
Fig. 11. The normalized topography of near-zone electric field intensities for an $a = 0.25\lambda$ radius, perfectly-conducting sphere interfering with the incident plane wave.

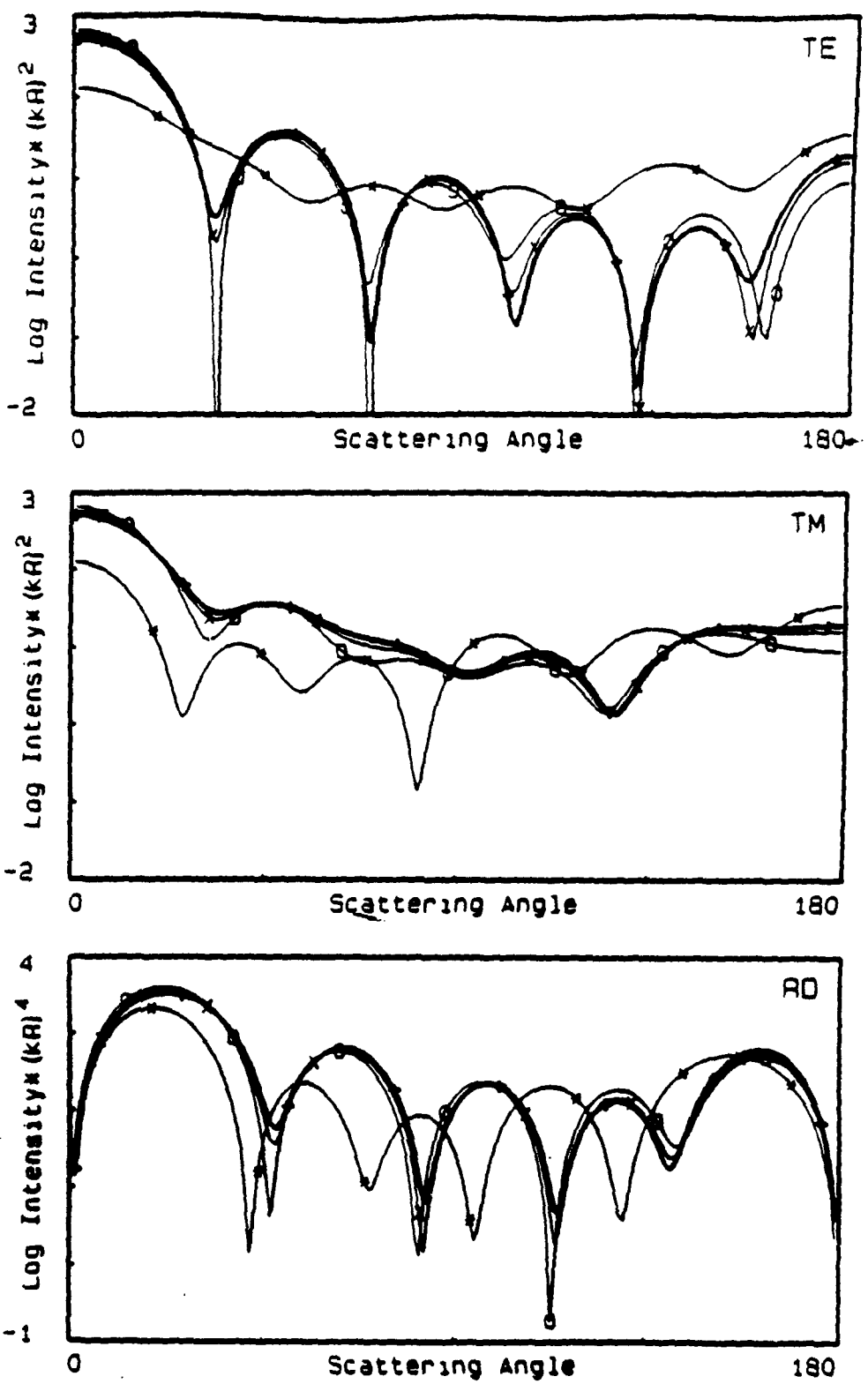
Fig. 12. The normalized topography of near-zone magnetic field intensities for an $a = 0.25\lambda$ radius, perfectly-conducting sphere interfering with the incident plane wave.

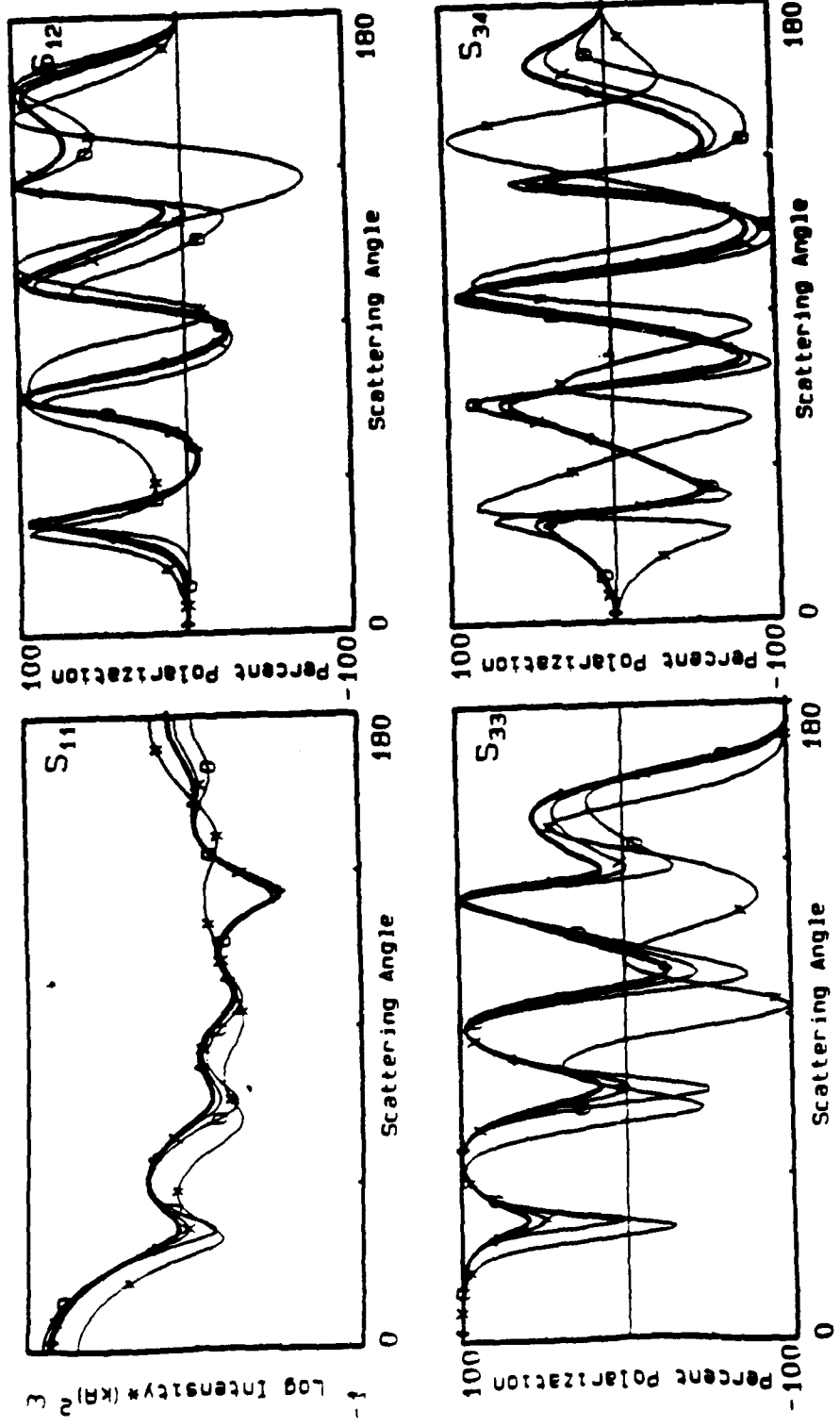
Fig. 13. The normalized scattering electric and magnetic field intensities for an $a = 0.25\lambda$ radius, perfectly-conducting sphere interfering with the incident plane wave measured on the z axis.

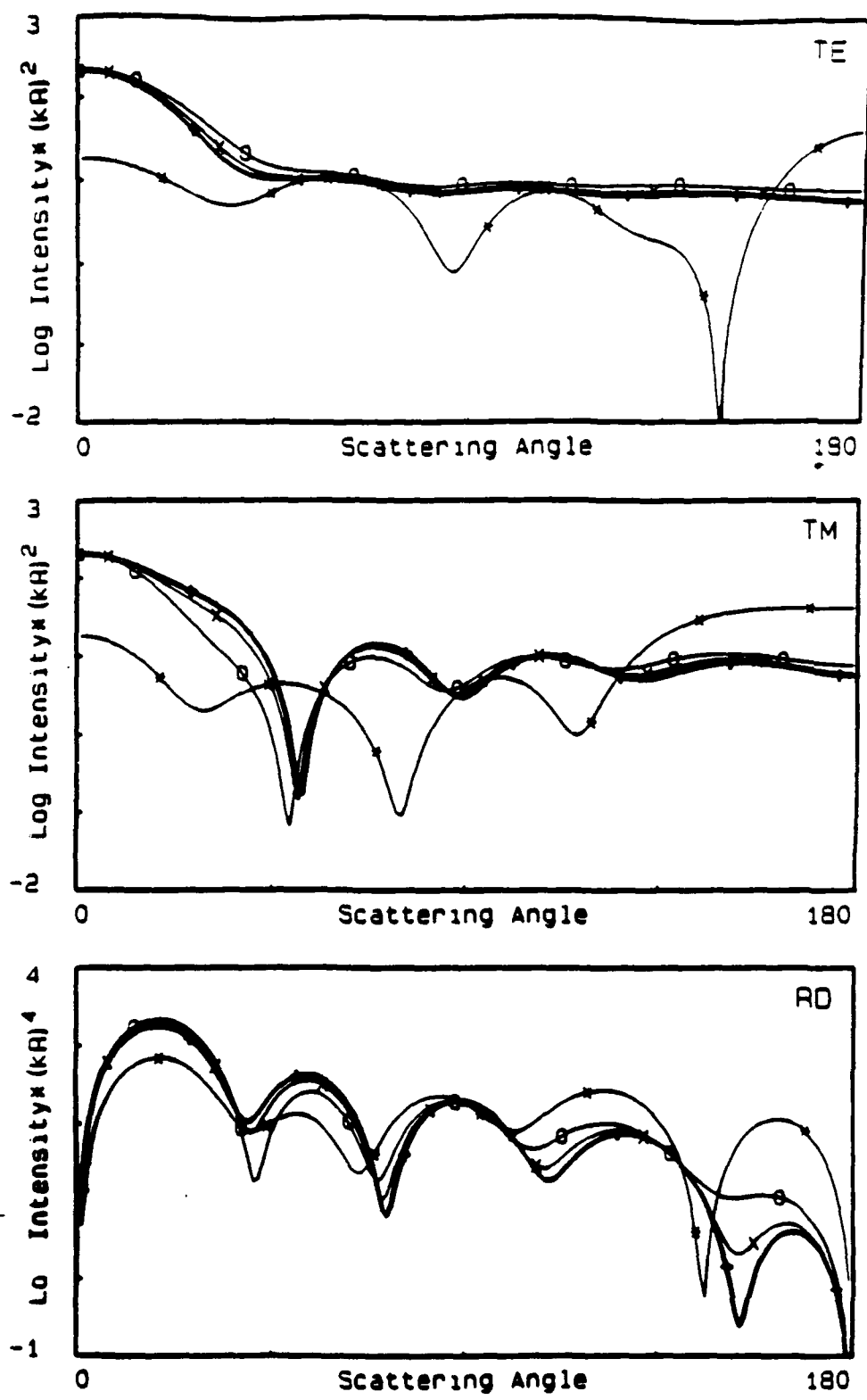
Fig. 14. Contour maps of the normalized scattering electric (TE) and magnetic (TM) field intensities for an $a = 0.25\lambda$ radius, perfectly-conducting sphere interfering with the incident plane wave.

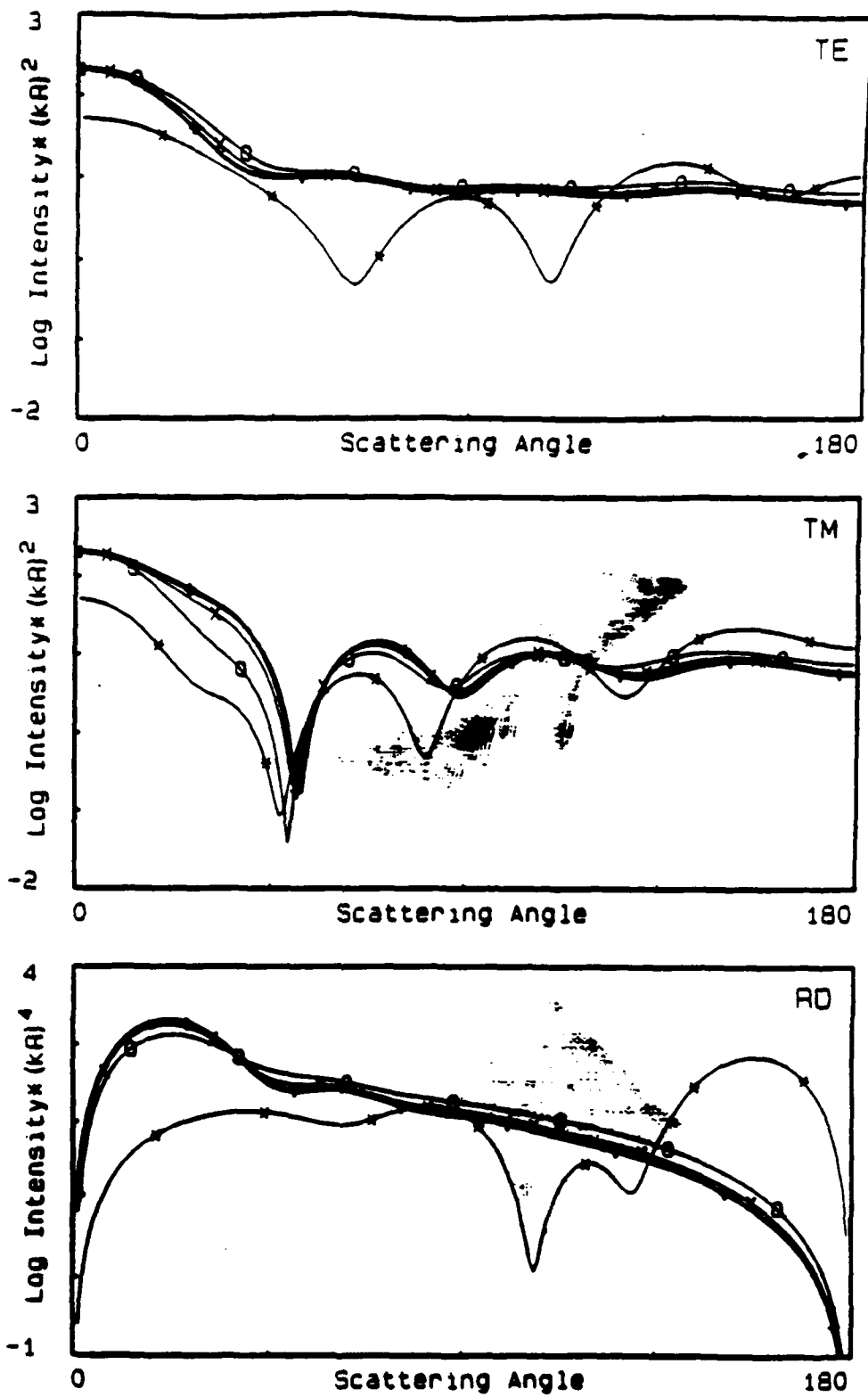


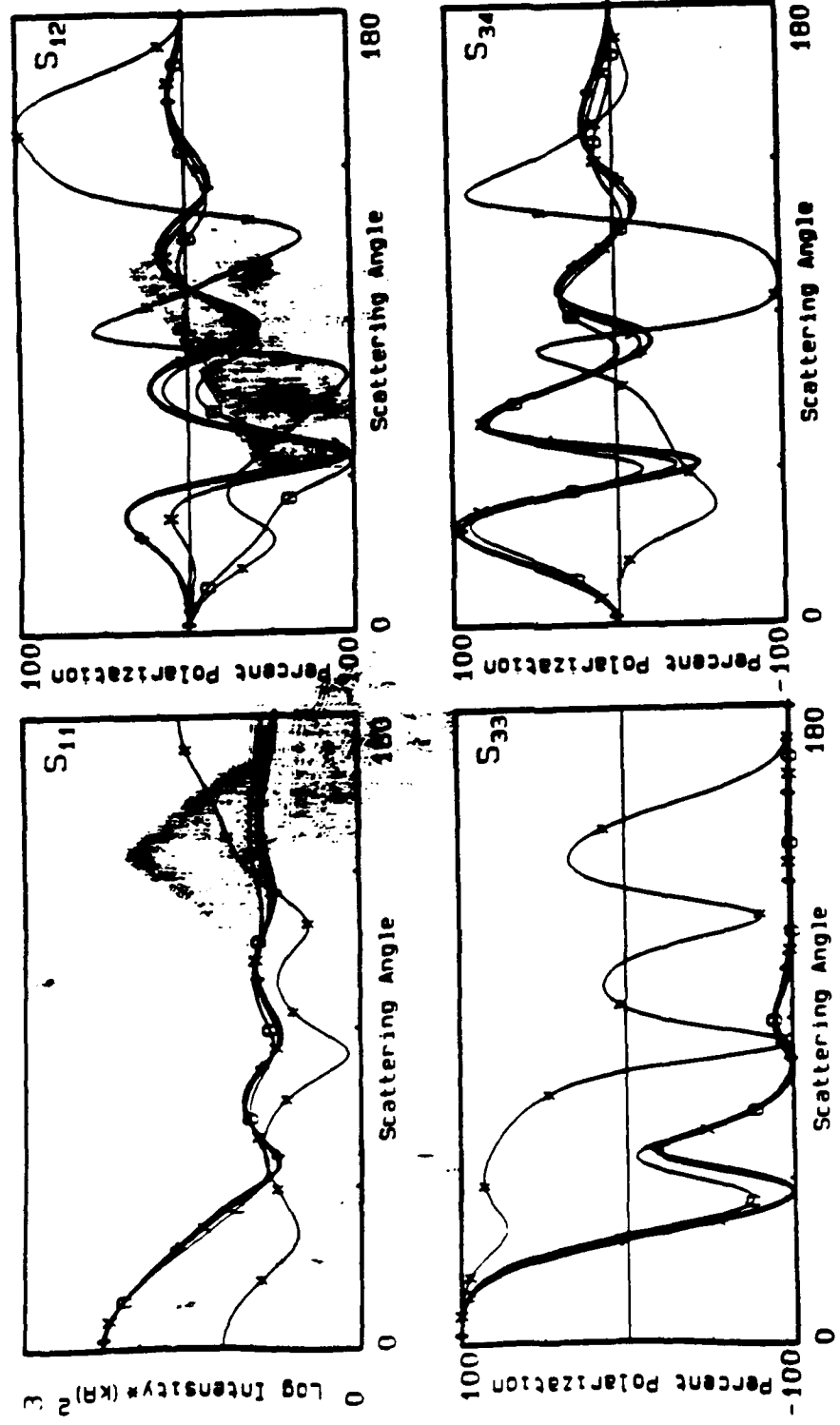


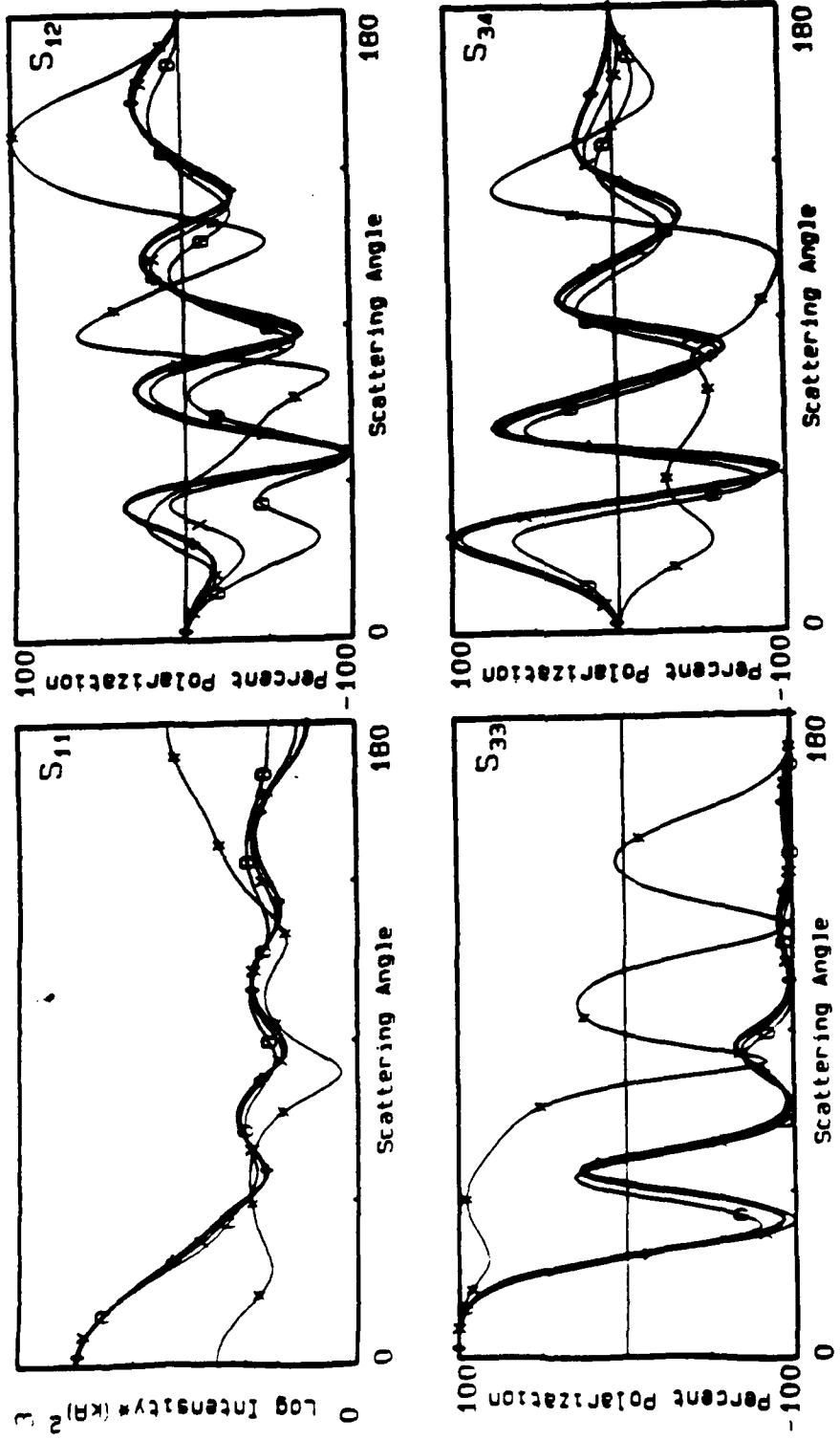


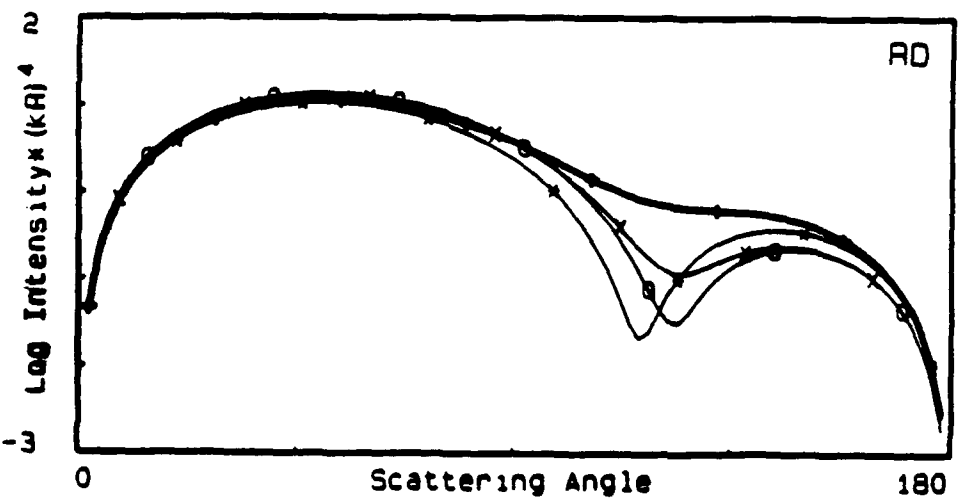
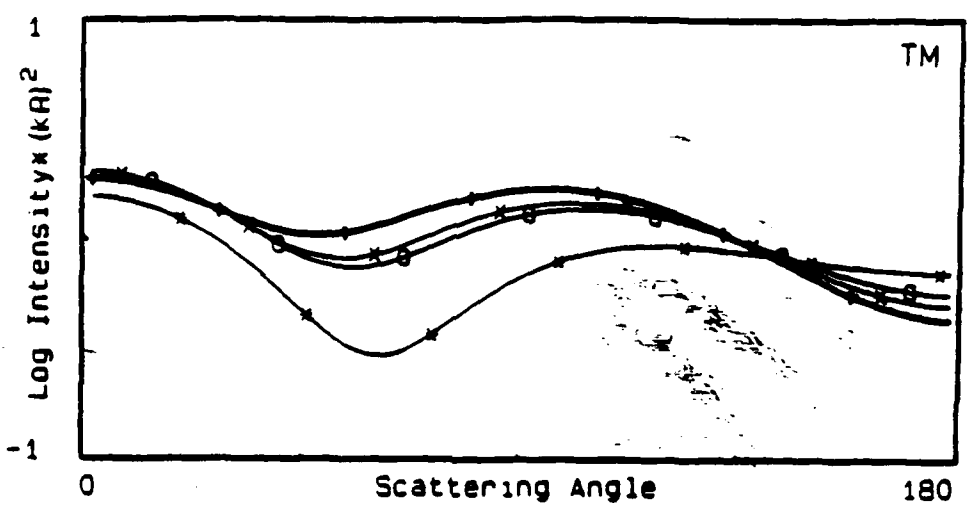
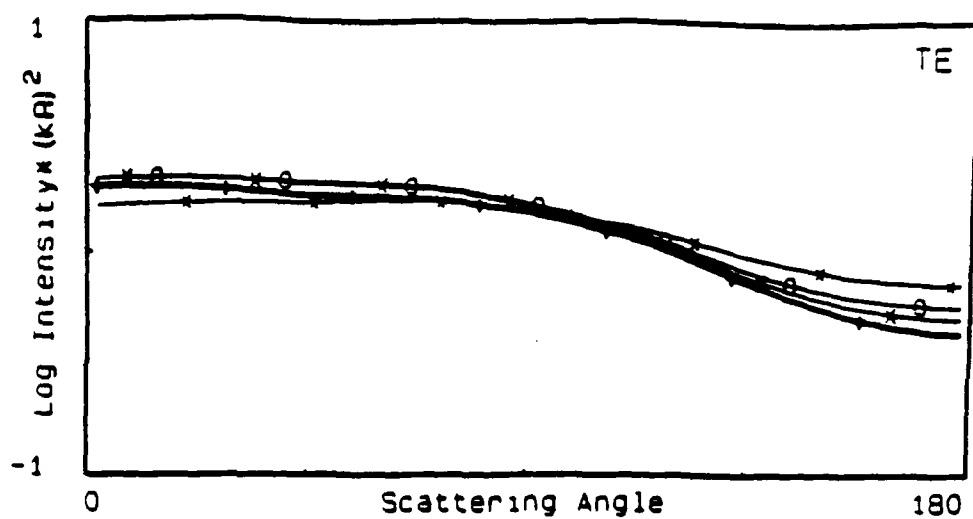


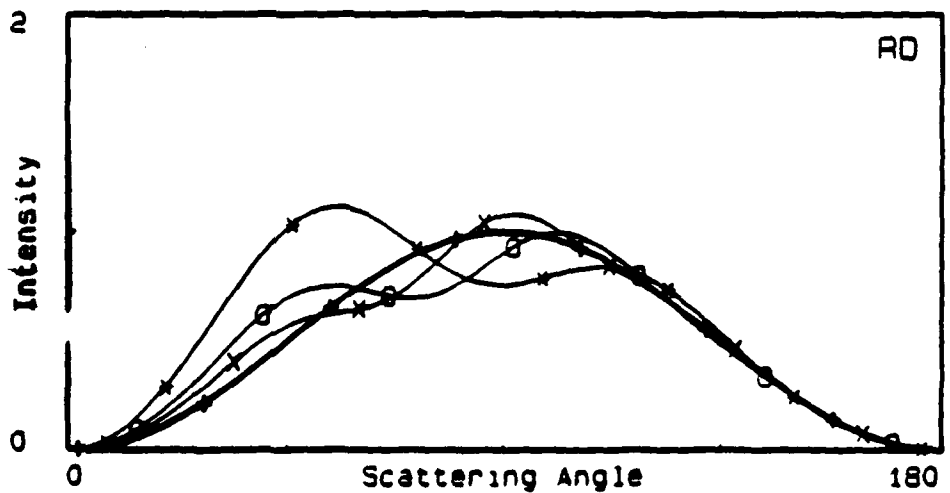
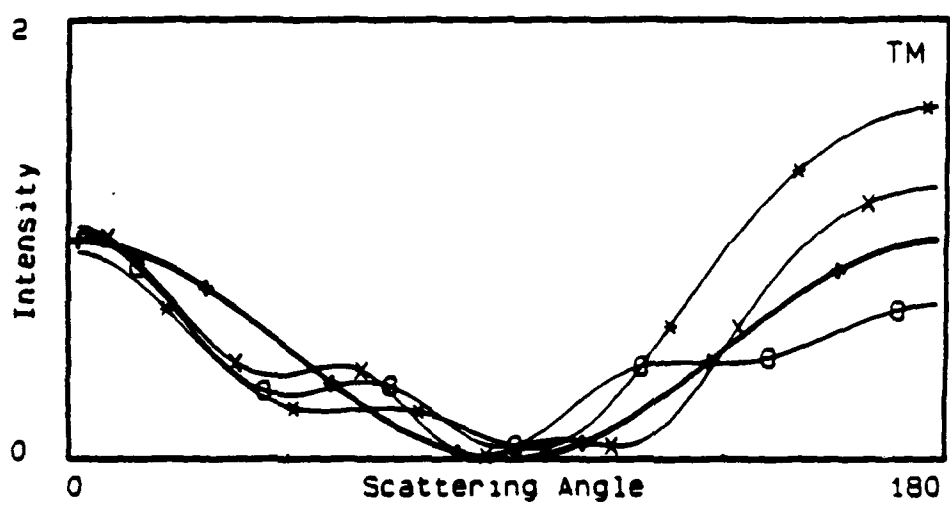
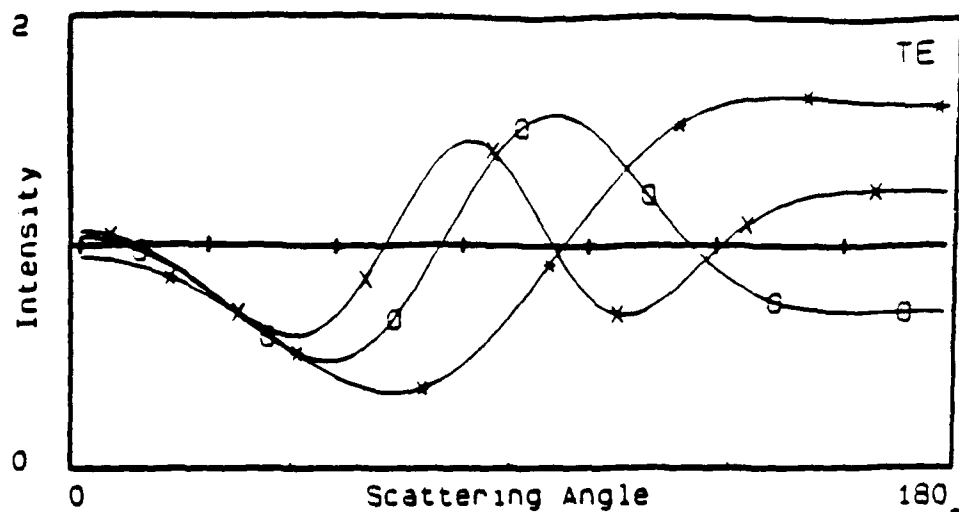


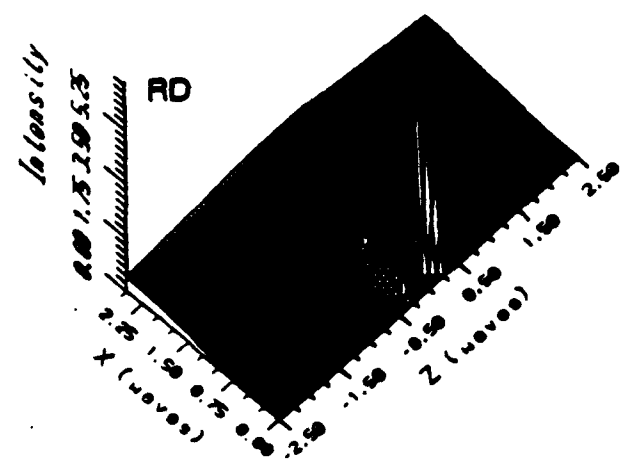
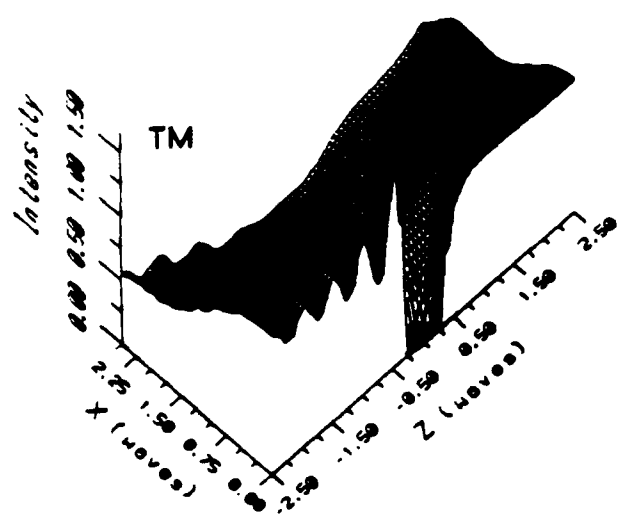
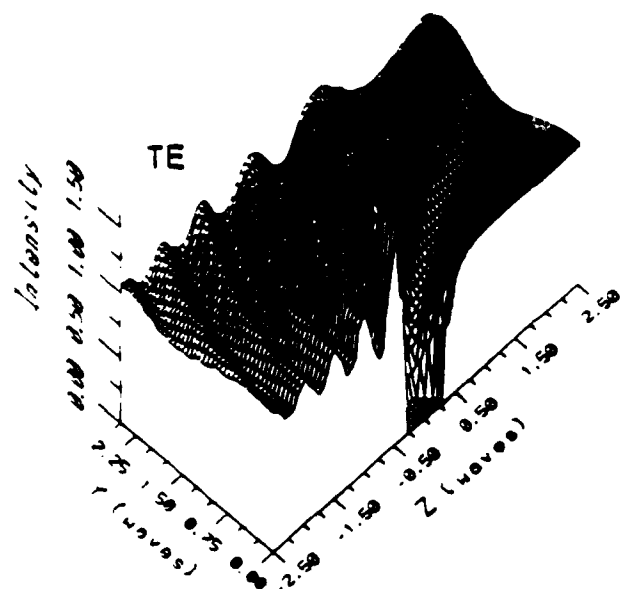


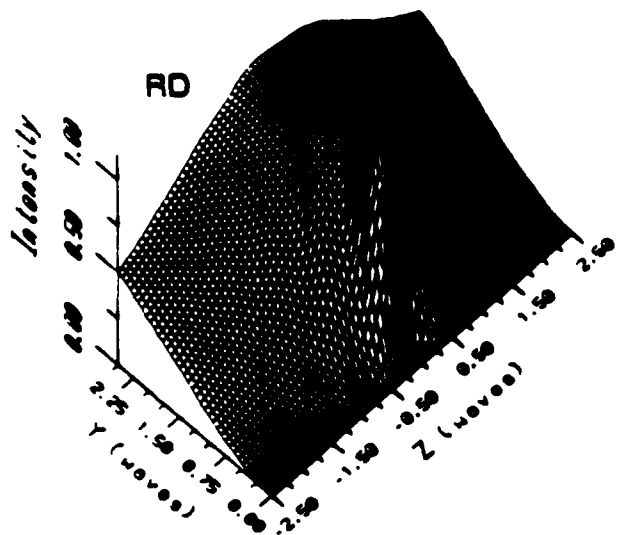
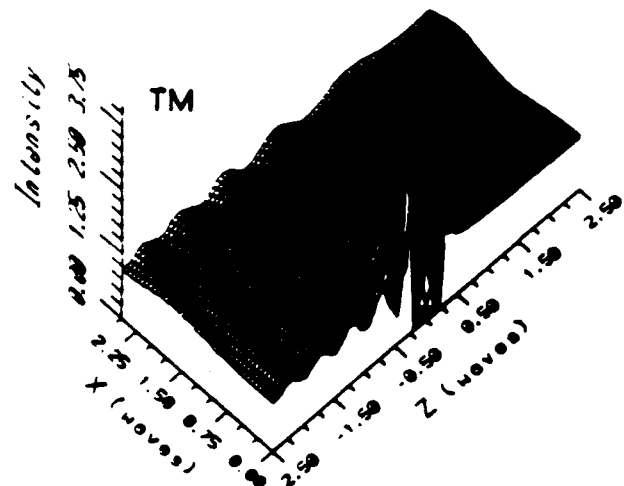
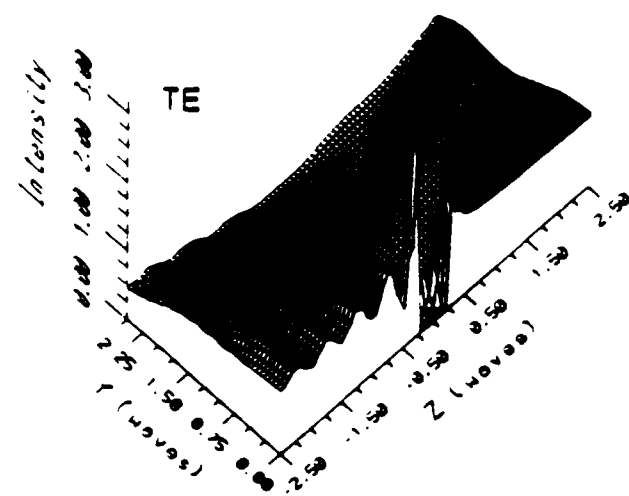


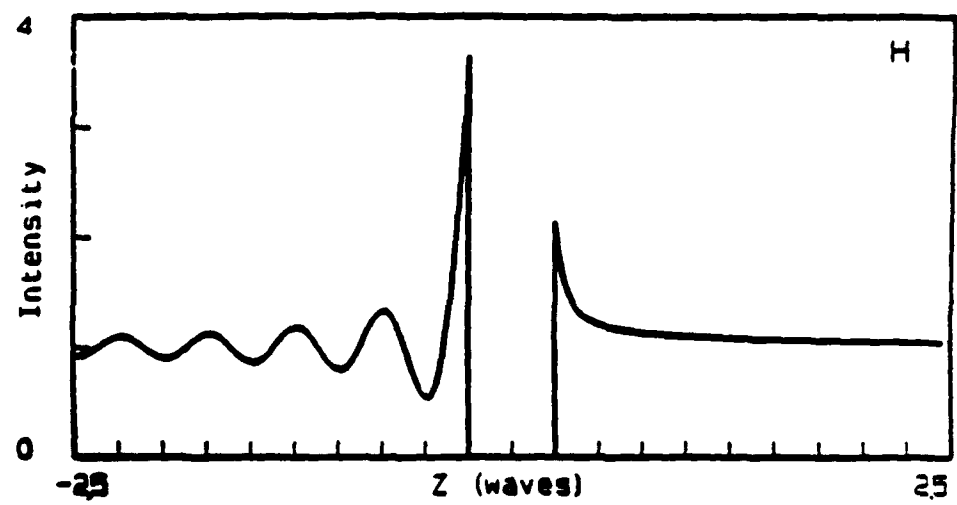
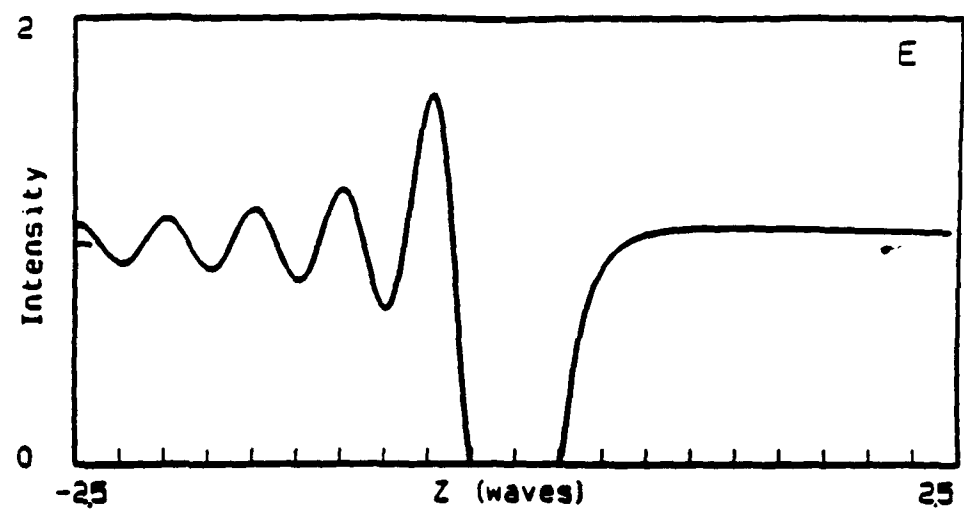


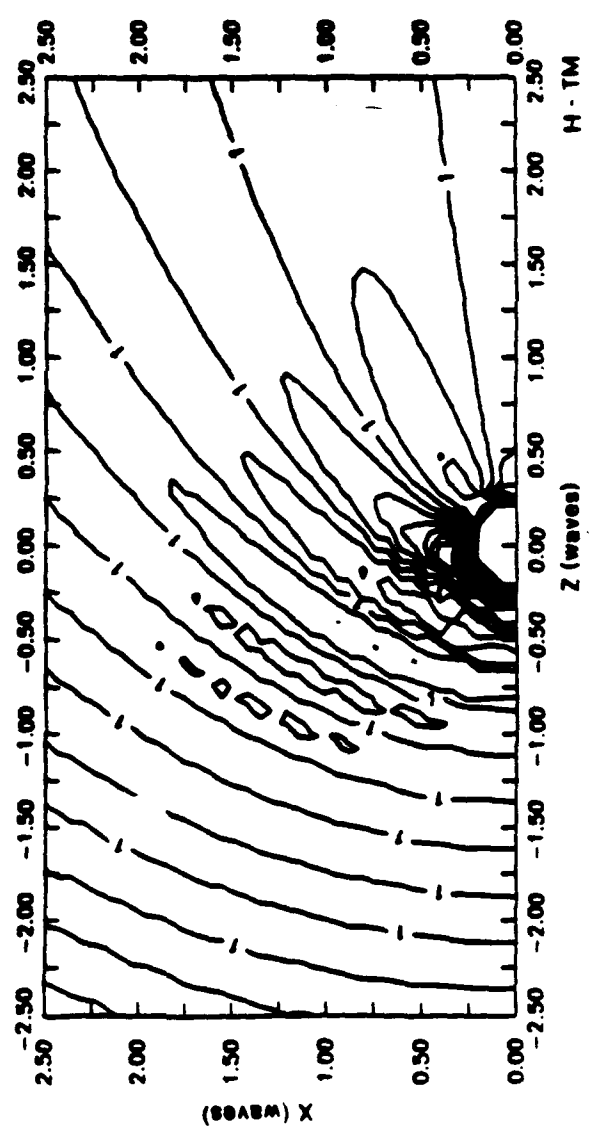
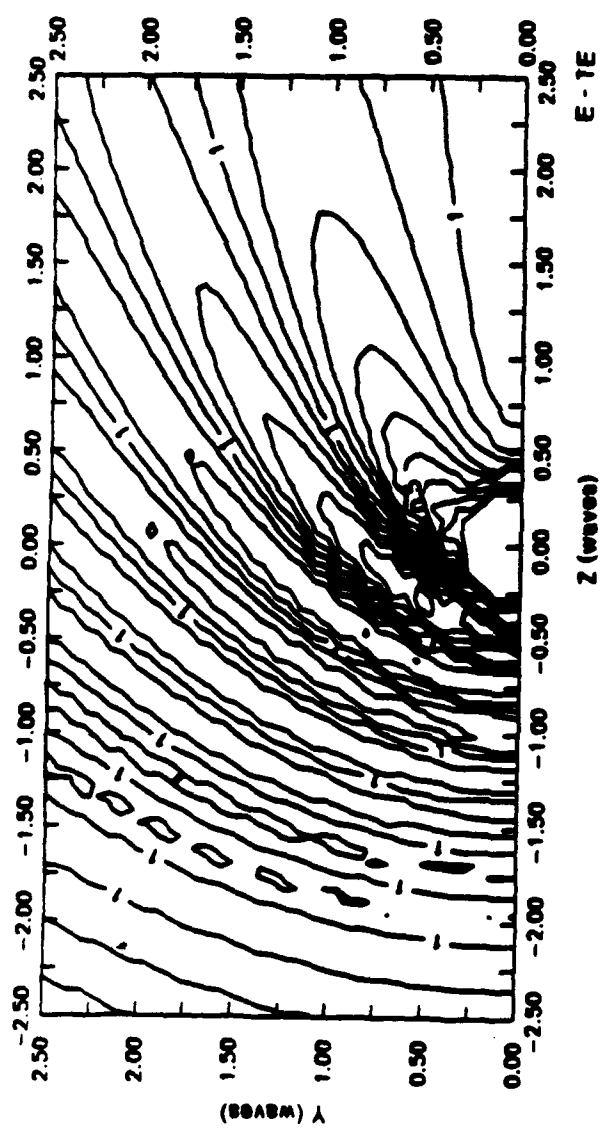












LIGHT SCATTERING FROM A SPHERE ON OR NEAR AN INTERFACE

by
Gorden Wayne Videen

Copyright © Gorden Wayne Videen 1992

**A Dissertation Submitted to the Faculty of the
COMMITTEE ON OPTICAL SCIENCES (GRADUATE)
In Partial Fulfillment of the Requirements
For the Degree of
DOCTOR OF PHILOSOPHY
In the Graduate College
THE UNIVERSITY OF ARIZONA**

1992

**THE POLARIZED LIGHT SCATTERING MATRIX
ELEMENTS
FOR ROUGH SURFACE**

by

Jiunn-Yann Hsu

**A Thesis Submitted to the Faculty of the
DEPARTMENT OF PHYSICS
In Partial Fulfilment of the Requirements
For the Degree of
MASTER OF SCIENCE
In the Graduate College
THE UNIVERSITY OF ARIZONA**

1992